Effect of Processing Techniques on the Secondary Intermetallic Phases and Thermomechanical Behaviour of 6xxx Series Aluminium



Tahsina Smith

St. Catherine's College

University of Oxford

A thesis submitted for the degree of

Doctor of Philosophy

Hilary 2019

Acknowledgement

This thesis would have never come to an end without the kindness and patience of the people around me, and I would very much like to thank Keyna O'Reilly for supervising, advising, and correcting my infinite iterations of drafts; Kumar Sundaram for guiding me through the thesis and paper write up process and making it enjoyable; Andrew Lui for teaching me the key experimental techniques that I have been using throughout this project; Lauri Walton for the endless hours of sample prep in the workshop; Marina Galano and Marion Beckett for always being very encouraging and supportive.

I must also mention Paul Bastock from the Optoelectronics Research Centre (University of Southampton) for kindly agreeing to let me use the Pyris Diamond TMA equipment that made it possible for me to get the set of thermomechanical results. Thank you ever so much for your assistance and generosity.

The group of friends and family who persistently bullied, supported, encouraged and inspired me into writing up this thesis: Aoife Kelly, Mujtaba Zaka, Rizvi Rahman, Yuki Kawaguchi; Granny and Grandad Witt, Debbie and Adrian Smith; my little brother Sam Smith; Ammi (Shireen) and Abbu (Rakib) Khan. And the people who kept me motivated and sane when things got too much: my three sisters Rabab Khan, Bosede Lawal, and Rumman Khan. A special thanks to Lara for keeping me company and distracted while I tried to correct the final draft.

And finally, thank you Phil, you made it all possible.

Abstract

For this project, an AlMgSi alloy with small additions of Fe was examined. It is established that the presence of Fe introduces secondary intermetallic phases α-AlFeSi and β-AlFeSi. It is also known that introduction of 5:1 Al-Ti-B type grain refiner encourages the formation of β-AlFeSi, while the introduction of Zr encourages the formation of α-AlFeSi.

The overall objective of this investigation was to establish the role of secondary intermetallic phases α-AlFeSi and β-AlFeSi on the hot tearing properties of a 6xxx series aluminium alloy. The approach was to isolate 'phase identity' and consequently phase morphology as the variables between two alloys that were being tested. This was achieved by processing a base 6063 alloy, and then making small additions of Zr and 5:1 Al-Ti-B type grain refiner to encourage the specific intermetallic phase identities. To maintain consistent non-dendritic grains of comparable size, the alloys were processed using semisolid technique, which also ensured the alloys experienced the same cooling conditions.

The microstructures of the resultant alloys were then characterised in terms of grain and cell sizes using macro-etched and annodised surfaces, intermetallic phase morphology and phase interconnectivity in both topographical examinations and overall 3D structures using optical microscopy and scanning electron microscopy. The intermetallic phase selections of all alloys were also determined using X-ray diffraction analysis, and their thermodynamic behaviours were observed using differential scanning calorimetry analysis.

Finally, the alloys with highest and lowest levels of α-AlFeSi were selected for thermomechanical examinations.

The most notable ones were found in the alloy containing Al-Ti-B type grain refiner: the morphology resembled that of a 6-petal flower. Despite in-depth examination no initiation point could be clearly established. Chemically verified Ti-B particles were not observed in association with these ‘flower’-like structures. The thermomechanical tests revealed that the alloy with β-AlFeSi phase present was more susceptible to hot tearing.

Contents

Chapter 1 Introduction 5
1.1 Objectives 5
1.1.1 Consistent α-Al Grain Size 5
1.1.2 Intermetallic Phase Identity, Quantity & Morphology Verification 6
1.1.3 ThermoMechanical Analysis 6
1.2 Outline of Thesis 7
Chapter 2 Literature Review 8
2.1 6xxx Aluminium Alloys 8
2.1.1 Effects of Mg and Si Additions 8
2.1.2 Effect of Fe Additions 10
2.1.3 Effects of Ti and B Additions 10
2.1.4 Effect of Zr Additions 11
2.2 Semisolid Alloy Processing 11
2.2.1 Non-Agitation Process 14
2.2.2 Component Shaping Technologies 16
2.2.3 Semisolid Processing Technique vs Conventional Casting 21
2.3 Solidification 21
2.3.1 Nucleation 22
2.3.2 Growth 27
2.3.3 Development of the Equiaxed Microstructure 32
2.4 Secondary Intermetallic Phases 36
2.4.1 Fe-rich Phases in 6xxx Al Alloys 36
2.4.2 Impact of Intermetallic Phases on Al Alloys 39
2.4.3 Stability of β-AlFeSi in 6xxx Al Alloys 39
2.4.4 Solidification Reactions 40
2.4.5 The Al-Mg-Fe-Si Alloy Systems 41
2.4.6 Observation of TiB_2 in Alloys 44
2.4.7 Intermetallic Phase Selection Mechanisms 53
2.5 ThermoMechanical Behaviour of Al Alloys 55
2.5.1 Hot Tearing 55
2.5.2 Criteria for Predicting Hot Tear Formation 57

2.5.3 Semisolid Tensile Tests 62
2.5.4 Development of Tensile Strength at Elevated Temperatures 67
2.5.5 Alloy Composition 69
2.5.6 Post Hot Tear Fracture Surface Examinations 69
2.6 Summary 70
Chapter 3 Experimental Procedures 72
3.1 Alloy preparation 72
3.1.1 Solid Fraction Estimations 72
3.1.2 Base Alloy (BA) 73
3.1.3 Grain Refined Alloy (GR) 77
3.1.4 Zr Containing Alloy (ZR) 78
3.1.5 Alloy Addition Calculations 78
3.1.6 TP-1 sample casts 80
3.2 Optical Emission Spectroscopy (OES) 84
3.3 Slurry and TP-1 Sample Segmenting 85
3.4 Macro-etching 86
3.5 Micro-etching 88
3.6 Intermetallic Phase Extraction 89
3.7 X-ray Diffraction (XRD) Identification 93
3.7.1 Sample preparation 94
3.7.2 Identification of phases 95
3.7.3 Phase content quantification 96
3.8 MTDATA Analysis 98
3.9 Differential Scanning Calorimetry (DSC) 98
3.10 Scanning Electron Microscopy (SEM) 101
3.10.1 Sample Preparation for SEM 102
3.10.2 Topographical Examination 105
3.10.3 TiB_2 Particle Location 106
3.10.4 Element Mapping 108
3.11 ThermoMechanical Analysis (TMA) 109
3.11.1 Equipment Calibration 110
3.11.2 Sample Preparation 110
3.11.3 Technique Development 111
3.11.4 Test Conditions 118
3.11.5 Test Data Analysis 119
3.11.6 Fracture Surface Analysis 120

Chapter 4 Results 121
4.1 Alloy Composition 121
4.2 Macro-etch 122
4.3 Micro-etching (anodising) 135
4.4 Thermodynamic Behaviour 144
(a) MTDATA Analysis and DSC Curves for BA 144
(b) MTDATA Analysis and DSC Curves for GR 146
(c) MTDATA Analysis and DSC Curves for ZR 148
(d) Summary 151
4.5 Intermetallic Phase Identification 154
4.5.1 Intermetallic Phase Selection along the Radius and Length of BA200 155
4.5.2 Intermetallic Phase Selection in BA Alloys 158
4.5.3 Intermetallic Phase Selection in GR Alloys 159
4.5.4 Intermetallic Phase Selection in ZR Alloys 160
4.5.5 Summary 161
4.6 Intermetallic Phase Morphology (2D) 162
4.6.1 Base Alloy (BA200) 162
4.6.2 Grain Refined Alloy (GR200) 166
4.6.3 Zr Added Alloy (ZR200) 168
4.6.4 Summary 170
4.7 Extracted Intermetallic Phase Morphology (3D) 171
4.7.1 Base Alloy (BA200) 171
4.7.2 Extracted Intermetallic Phase Examination: Grain Refined Alloy 177
4.7.3 Extracted Intermetallic Phase Examination: Zr Added Alloy 188
4.7.4 Summary 191
4.8 ThermoMechanical Analysis (TMA) 193
4.8.1 GR200 (~50wt.% α-AlFeSi content) 193
4.8.2 ZR200 (~80wt.% α-AlFeSi content) 197
4.9 Fracture Surface Analysis of TMA Samples 200
4.9.1 GR595 200
4.9.2 GR610 200
4.9.3 GR625 203
4.9.4 ZR595 206
4.9.5 ZR610 210
4.9.6 ZR625 213

Chapter 5 Discussion 215
5.1 Primary Al Grain Size Analysis 215
5.1.1 TP-1 Casting Process 216
5.1.2 New Rheocasting Process 220
5.1.3 Microstructure of BA400, GR400 and ZR400 221
5.1.4 Non-Dendritic Microstructure Formation Mechanism 223
5.2 Intermetallic Phases 225
5.2.1 Intermetallic Phase Selection Mechanism 226
5.2.2 2D Phase Morphology 228
5.2.3 3D Phase Morphology of BA200, GR200 and ZR200 229
5.2.4 Phase Formation Mechanism 231
5.2.5 Ti-Rich Particles and Clusters 248
5.3 ThermoMechanical Analysis 249
5.3.1 ThermoMechanical Behaviour 249
5.3.2 Fracture Surface Analysis 253
5.3.3 Impact of Intermetallic Phase on the Hot Tearing Properties 255
Chapter 6 Conclusions and Suggestions for Future Studies 262
6.1.1 Consistent α-Al Grain Size 262
6.1.2 Intermetallic Phase Identity, Quantity & Morphology Verification 263
6.1.3 ThermoMechanical Analysis 265
Chapter 7 Further Investigation 267
Chapter 8 Bibliography 269

Chapter 1 Introduction

6xxx Al alloys (AlMgSi) are extensively used for their medium-strength combined with better weldability, extrudability and corrosion resistance compared to other aluminium alloys [1]. Amongst the AlMgSi alloys, 6063 in particular is the most widely used due to its mechanical properties [1]. During solidification, various AlFeSi-based secondary intermetallic phases form which can have significant impact on the downstream processing of the alloy. It is believed that the chemical composition and solidification conditions of the alloy determine the chemical stability, identity, morphology, amount and distribution of the AlFeSi-based intermetallic phases.

Of the various defects that occur during casting, hot tearing: when an irreversible crack forms during the semisolid state, is one of the most severe and unrecoverable defects [2]. It is being considered whether the AlFeSi-based phases can affect hot tearing susceptibility of a 6xxx Al alloy, for example by possible bridging of propagating cracks and decohesion. Thus, the main aim of this investigation is to understand the influence of these phases on the hot tearing and mechanical properties of 6063 alloy in the semisolid state.

1.1 Objectives

1.1.1 Consistent α-Al Grain Size

To study the role of secondary intermetallic phases in isolation, it is essential to maintain a consistent α-Al/cell size between samples. α-Al grain size can be altered by varying the alloy chemical composition or through casting conditions.

Chemical compositions of the aluminium alloys affect the intermetallic phase identity, for example additions of Zr has been reported to discourage the formation of β-AlFeSi, while AlTiB-type grain refiner are found to encourage the formation of β-AlFeSi phase [3]. Chemical composition, however, also has a significant impact on the grain size.

Investigations carried out by Park [4] indicated that a 7xxx Al alloy processed via the new rheocasting (NRC) process had a consistent α-Al microstructure, regardless of whether the alloy contained grain refiners or not. Thus, the different alloys were processed using NRC to obtain similar grain sizes, while chemical composition was altered to control intermetallic phase identity.

1.1.2 Intermetallic Phase Identity, Quantity & Morphology Verification

Once the α-Al grain size has been established to be comparable between the sample, it will be vital to determine the intermetallic phase identity, approximate quantity and morphology.

1.1.3 ThermoMechanical Analysis

According to Haaften [5] tensile experiments corresponding to the semisolid temperature range can be used to simulate hot tears present in industrial ingots, due to the significant similarities found between both fracture surfaces. Thus, the hot tear susceptibility of the intermetallic phases can be established at the semisolid temperature range of the alloy.

1.2 Outline of Thesis

– Chapter 2 provides a review of the literature on 6xxx Al alloys, semisolid alloy processing techniques, solidification, the secondary intermetallic phases most commonly observed in 6xxx alloys and the thermomechanical behaviour.

– Chapter 3 presents the experimental details of the processing technique used to simulate NRC in small scale alloy production. The parameters used for chemical, microstructural and thermomechanical analyses are also provided in the chapter.

– Chapter 4 presents chemical compositions of the samples, which were carried out using OES. The α-Al grain and cell size calculations were carried out using optical and secondary electron microscopy (SEM), while x-ray diffraction (XRD) was used to establish intermetallic phase identity and approximate quantity. Differential scanning calorimetry (DSC) analysis and phase calculations using the Scheil model on MTDATA was used to establish the phase transformation temperatures of the alloys, while a ThermoMechanical analyser (TMA) was used to understand the thermomechanical behaviour of the alloys.

– Chapter 5 analyses the impact of NRC processing technique on the α-Al grain and cell size. The influence of chemical composition on the intermetallic phase identity and approximate quantity are also discussed. And finally, an evaluation of the impact of intermetallic phase identity and morphology on the hot tear susceptibility is presented.

– Chapter 6 summarises and concludes the findings of this investigation.

– Chapter 7 makes suggestions for future work to take the study forward.

Chapter 2 Literature Review

2.1 6xxx Aluminium Alloys

The 6xxx Al alloys are categorised by the additions of magnesium (Mg) and silicon (Si) as the main alloying elements [6,7,8].

Iron (Fe) is generally present in all commercial Al alloys as an unavoidable impurity [9], and sometimes added to increase the toughness and strength of the Al [10]. A small amount of Al-5Ti-1B grain refiner may also be added to achieve a more equiaxed and consistent microstructure [9], which improves castability during direct chill (DC) casting.

Aside from the main alloying elements, various trace elements may also be present in the alloy with or without intention. All the alloying and trace elements have an individual, as well as combined effect on the nucleation, growth and solid-state transformation of the α-Al and intermetallic phases of the alloy, which in turn affects the overall mechanical and microstructural properties of the alloy.

2.1.1 Effects of Mg and Si Additions

Mg has a relatively high solid solubility in Al (14.9wt% at 450ºC) while Si has a comparatively low solid solubility (1.65wt% at 580ºC) [11]. The alloying elements Mg and Si therefore partly remain in solid-solution in the α-Al matrix, while they can also exist as Mg_2Si phases [12].

During heat treatment of 6xxx Al alloys, particles of magnesium silicide (Mg_2Si) precipitate from the Al solid solution, and then act as the main strengthening mechanism in the alloy [6]. The exact proportions required for Mg_2Si formation is a Mg:Si weight ratio close to 1.73:1, which makes the relative proportions of Mg and Si introduced to alloys very important [9]. Hence, the 6xxx Al alloys can be divided into three main categories based on the proportions of Mg and Si added [6]. The 'balanced' group is where Mg and Si are added close to the required 1.73:1 ratio to a super-pure Al base, and thus, no excess Mg or Si is left after the formation of Mg_2Si [9]. The two other groups depart from the 'balanced' ratio either with 'excess Mg' or 'excess Si' [6]. One example of a balanced 6xxx Al alloy is the commercial AA6063, which is used more extensively due to its combination of high strength, ductility and formability [6].

Liu and Kang [13] investigated 6xxx Al alloys with varying amounts of Mg, which was observed to have a significant effect on the as-cast microstructure. Increasing Mg content increased the amount of Mg_2Si particles in the solid state, and the Fe present segregated during solidification forming ternary AlFeSi phases. These Fe-based phases contain a substantial amount of Si, and form near the solidus temperatures of the Al alloys. The Mg_2Si particles, however, precipitate at a significantly lower temperature (approximately 600ºC) [14]. The Fe-based phases therefore are able to consume some of the Si during solidification, leaving inadequate amounts of Si for the formation of Mg_2Si particles. Thus, Si is added in excess to compensate for this reaction.

2.1.2 Effect of Fe Additions

The presence of Fe has a significant effect on the final properties of Al alloys due to the very low solid solubility of Fe in Al (a maximum of 0.05wt% at 655ºC [11]). Thus during solidification, almost all the Fe present segregates to the liquid and forms various Al-Fe and Al-Fe-Si based insoluble secondary intermetallic particles of various morphologies [15], that can be either equilibrium or metastable phases. One option would be to use Al alloys with reduced amounts of Fe. However, this can only be achieved at increased production costs, and therefore commercial alloys tend to have a certain amount of Fe present [16]. The Fe-rich phases will be discussed in further detail section 2.4.1.

2.1.3 Effects of Ti and B Additions

In commercial casting processes, grain refiners are frequently added to achieve a fine equiaxed as-cast microstructure, which results in improved castability and mechanical strength [17]. Al-Ti-B type grain refiners are used extensively around the world for Al alloys, and the proportions of Ti:B are usually 5:1 [18]. The refined microstructure is known to reduce hot tear susceptibility of Al alloys, as well as providing isotropic properties [19]. Previous studies carried out at University of Oxford report that TiB_2 phase promotes the formation of β-AlFeSi particles [3], and indicate that Ti:B proportions of 2.21:1 produced effects on the microstructure similar to that of the ratio 5:1 [20].

2.1.4 Effect of Zr Additions

Jones and Pearson [21] established that a small amount of Zr can cause 'Zr poisoning', whereby the efficiency of Al-Ti-B type grain refiners is drastically reduced. Bunn et al. [22] explained that the Zr poisoning effect is the substitution of Zr in place of Ti in the TiB_2 phase. Lui [20] reported that the presence of Zr promotes cubic α-AlFeSi phase formation, suppressing the formation of β-AlFeSi phase. However, the presence of Ti (i.e. not bonded to B) delays the Zr 'poisoning effect' forming β-AlFeSi phase. He therefore concluded that the secondary intermetallic phase selection can be altered by varying the amounts of Ti, TiB_2 and Zr.

2.2 Semisolid Alloy Processing

In semisolid metal (SSM) processing techniques, the starting materials are neither solid (as is the case for solid state processing) nor liquid (as it is for casting). The feedstock remains in between the metal's solidus and liquidus temperatures, i.e. in a semisolid slurry state whereby the solid particles are non-dendritic and dispersed in the liquid metal matrix, resulting in a characteristic thixotropic behaviour [23]. An example of such behaviour is shown in Figure 2.1. The semisolid processing techniques available at present exploit these rheological behaviours to attain the desired mechanical properties.

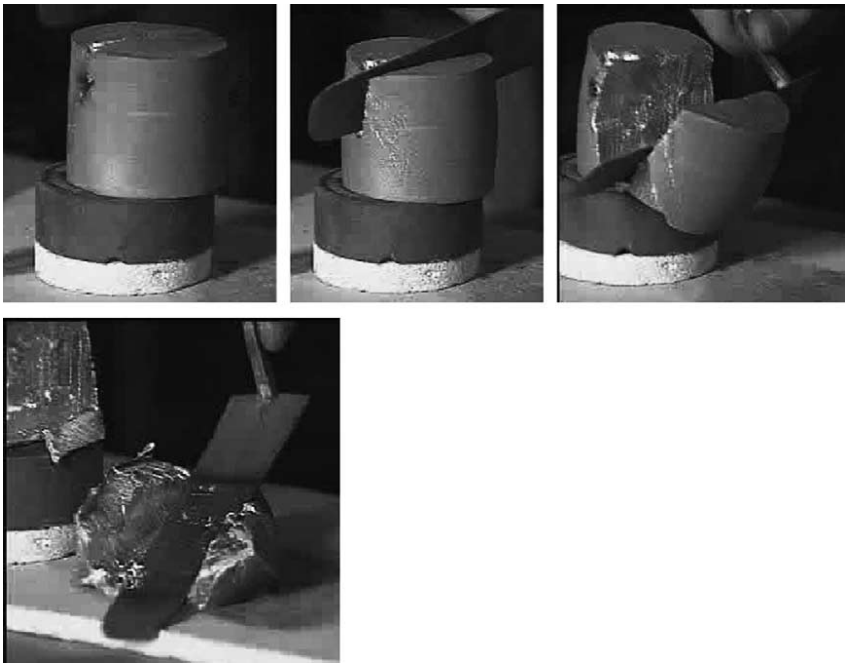


Figure 2.1: Sequence of photographs displaying the thixotropic behaviour of semisolid alloys [24]

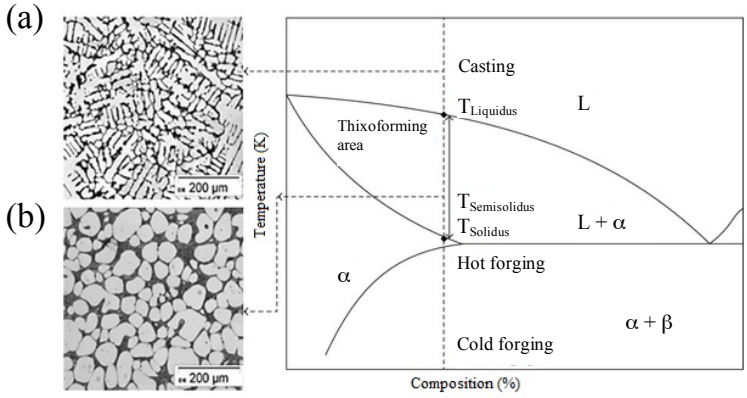


Figure 2.2: Micrographs showing the microstructures of (a) a dendritic as-cast sample, and (b) an equiaxed alloy sample cast using semisolid processing techniques [24]

Figure 2.2 shows a comparison between a typical microstructure obtained from DC cast, and an example of the microstructure generally obtained from semisolid processed

alloys [24]. In has been established that (a) columnar grains reduce formability, yield strength, and tensile elongation to failure [25]; (b) a variety of surface defects can develop in coarse grained alloys that are rolled or extruded [26]; and (c) it is generally believed that the defects related to hot-tearing that develop in the shell zone of a DC casting are more severe in alloys with grains that are not equiaxed [26]. On the contrary, the benefits of consistent, fine equiaxed grain structure are [19] (a) improved mechanical properties that are uniform throughout the alloy; (b) uniform distribution of secondary intermetallic phases and microporosity, resulting in a better formability; (c) reduced shrinkage porosity; and (d) overall improvement in strength and fatigue life. Thus, the consistent, fine equiaxed microstructure is preferred in the commercial context.

Since the inception of thixotropic alloy behaviour, a large range of processing technologies have been developed and applied to produce fine equiaxed microstructures. However, semisolid processing techniques can be mainly divided in to two main routes: rheocasting, where the feedstock material preparation generally involves shearing the molten alloy during solidification; and thixoforming, where thixotropic feedstock materials are prepared and then reheated to semisolid temperatures for component shaping [27]. Figure 2.3 shows a schematic of the different semisolid processing routes [28]. The thixotropic feedstock material can be prepared either by ‘agitation’ or ‘non-agitation’ processes. The process being used in this investigation is based on ‘non-agitation’, and therefore processes that involve ‘agitation’ will not be discussed.

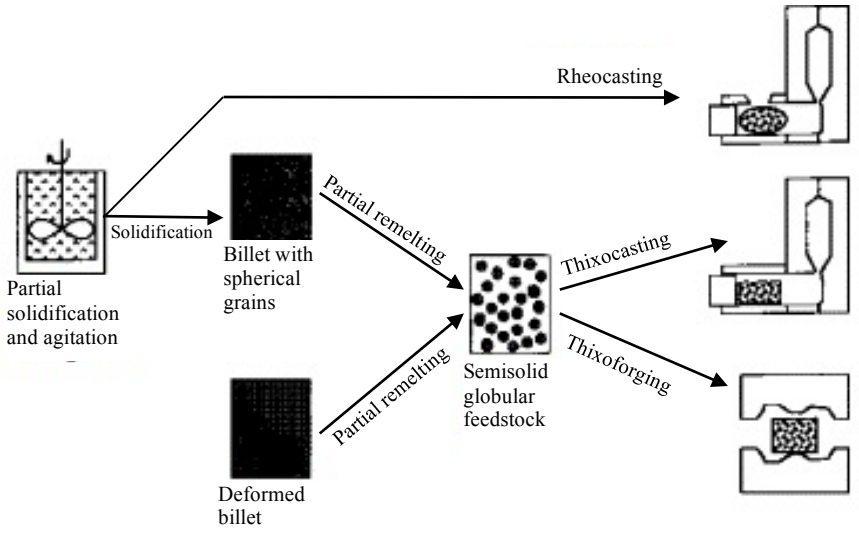


Figure 2.3: Schematic showing the different semisolid processing techniques [28]

2.2.1 Non-Agitation Process

(a) Liquidus Casting/New Rheocasting (NRC)

Casting metal with a uniform temperature just above the liquidus can also produce small globular grain sizes; a process known as liquidus casting or NRC [29], and a schematic of the process shown in Figure 2.4. This technique has been successfully tested on both cast [30] and wrought [31] Al alloys, and has the significant advantages of being simple and cost effective. There are two main limitations of this process: difficulty in (i) controlling the temperature to ensure accuracy and homogeneity across the melt, and (ii) achieving the resultant grain structure repeatedly and uniformly, especially in large-scale production.

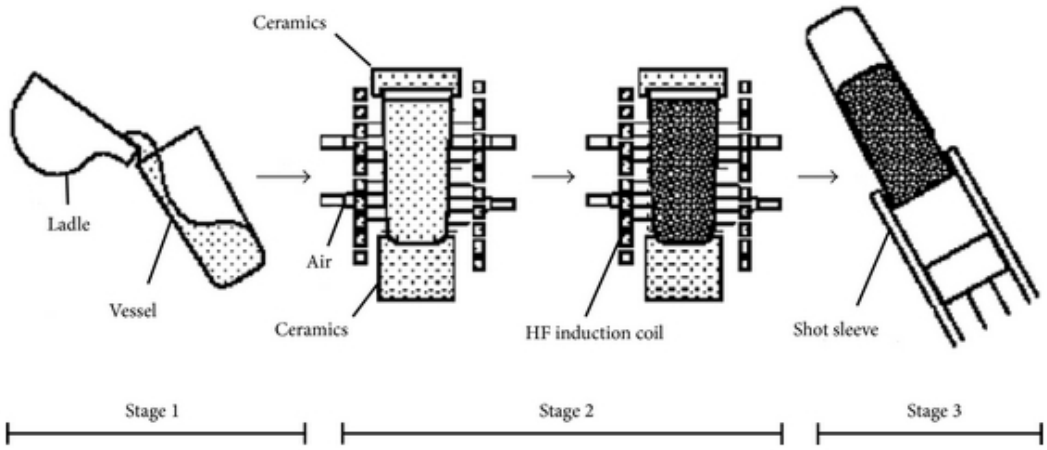


Figure 2.4: Schematic illustration of the stages of New Rheocasting (NRC) [30]

(b) Chemical Grain Refinement

Adding chemicals, such as Al-Ti-B and Al-Ti-C type grain refiners that suppress columnar growth in Al alloys, is one of the common industrial practices for achieving fine and equiaxed grains [32]. Chemical additions have been considered for the production of non-dendritic microstructures due to the advantage of significantly low production costs. It was also noted that adding grain refiners in higher than standard amounts can achieve grain sizes of around 100μm in Al alloys [33]. To further reduce the grain sizes of the alloy, chemical grain refinement is usually used in combination with other grain refinement processes, such as liquidus casting and magnetohydronamic (MHD) agitation [23]. MHD is where molten alloy is sheared using rotating electromagnetic fields.

Some of the disadvantages of chemical grain refinement include (i) the chemical additions being effective to certain alloys systems only, as well as (ii) some of the additives being present in the final product, affecting the alloy's mechanical properties

and recyclability [34].

2.2.2 Component Shaping Technologies

(a) Thixoforming – Requires Feedstock Reheating

Thixoforming techniques involve using feedstock with a spherical microstructure, which is reheated to its semisolid temperature range, followed by final shaping [35]. The microstructure of the precursor material is very important to obtain the thixotropic alloy properties, which is necessary for the technique. A thixotropic alloy is one that flows on shearing and thickens when allowed to stand [36]. The required feedstock with spherical microstructure is commonly achieved by continually casting the alloy while using electromagnetic stirrers [36].

Thixoforming can be further divided into two categories: i) thixoforging, where the semisolid alloy is deformed by open dies [37, 35]; and ii) thixocasting, where the semisolid alloy is deformed by injecting it into closed dies [36, 41]. Schematics of both processes are shown in Figure 2.5.

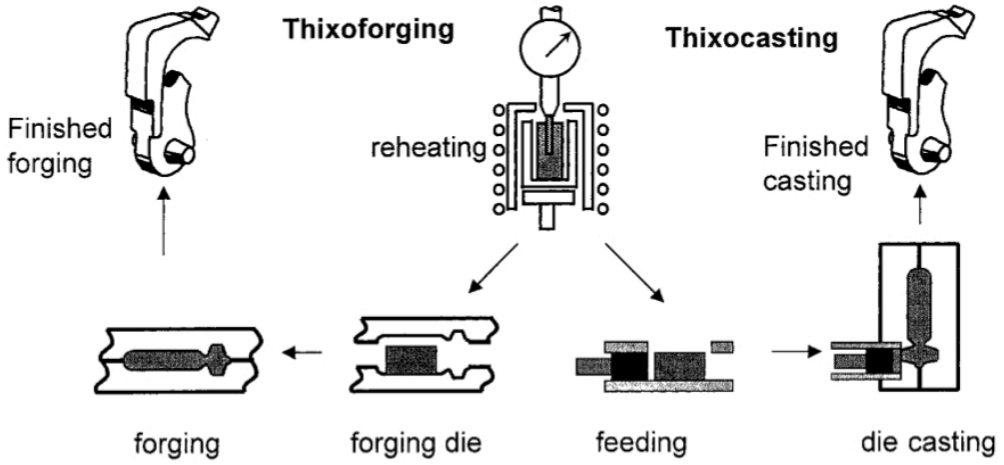


Figure 2.5: Schematic of the processing steps of thixoforging and thixocasting [23]

The various advantages of using thixoforming processes include comparable costs to conventional die casting [36], energy efficiency, and lower processing temperature requirements resulting in increased die life of 20% [35]. There are disadvantages however of using these processes, which include the higher cost of precursor materials (which are 20% more expensive compared to raw materials for conventional die casting) [35], along with a smaller number of precursor material suppliers [36]. The low recyclability of scrap is another disadvantage [37, 33].

(b) Ube NRC – Requires no Feedstock Reheating

The Ube NRC process [38] does not require any precursor material, and therefore the running costs for this process are 20% lower than that of conventional thixoforming [39]. This is because this technique has the ability to produce semisolid slurries with globular microstructure by subjecting the melt to controlled cooling. Additionally, the Ube NRC process is able to produce a more homogeneous and less segregated microstructure in comparison to thixoforming [39]. The disadvantage of using this

process is the requirement of accurate temperature measurement and control, since the microstructure is very dependent on the solid fraction during processing. Figure 2.6 shows the processes that take place during NRC.

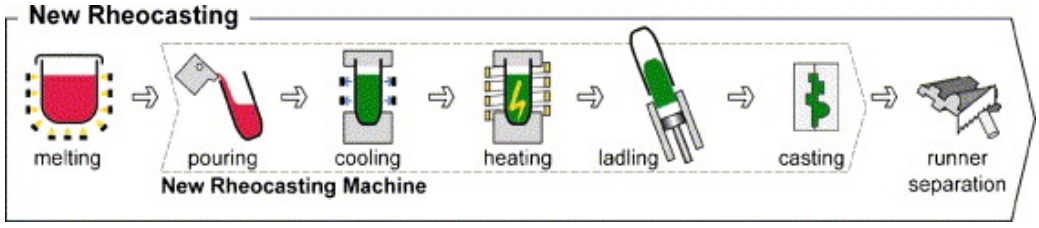


Figure 2.6: The process concept of NRC system [39]

As Figure 2.6 shows, the Ube NRC processes consist of 5 main steps [4]:

(i) Preparation of the surfaces that will be in contact with the molten alloy is the initial step, where the cup (that will hold the sample during processing) is cleaned and coated, followed by preheating.

(ii) Ladling of the alloy into the preheated cup is done very gradually to reduce turbulence, and the cup is positioned at a specified angle to reduce air entrapment.

(iii) Cooling the cup in a slurry making station is the next step, where insulation is provided on both top and bottom of the cup to reduce thermal gradients. The cooling continues until a specified temperature is achieved, that is, the optimum solid fraction to encourage a spherical microstructure to develop. Cooling rate can be increased by using a high-pressured air nozzle.

(iv) Heating the cup using induction heating is then carried out to reduce the temperature difference between the cup and the slurry, as well as slow down the cooling rate.

(v) Forming is the final step, where the slurry is removed from the slurry making station,

and then inverted to avoid oxide incorporation into the final product. Microstructural examinations can be carried out at this stage by quenching the slurry after removal.

Ube NRC is still a comparatively new manufacturing technique, and is currently being studied to better understand its characteristics. Recent studies indicate that reducing the temperature during pouring can produce a significantly finer and more spherical microstructure [40]. The mechanism behind this behaviour, however, is still under examination. Park [4] investigated the influence of Ube NRC processing parameters on a solidified AA7032 alloy microstructure. Parameters such as the melt temperature, temperature of the cup, as well as cooling and heating rates were all varied systematically. Figure 2.7 shows the influence of melt temperature on the alloy's microstructure.

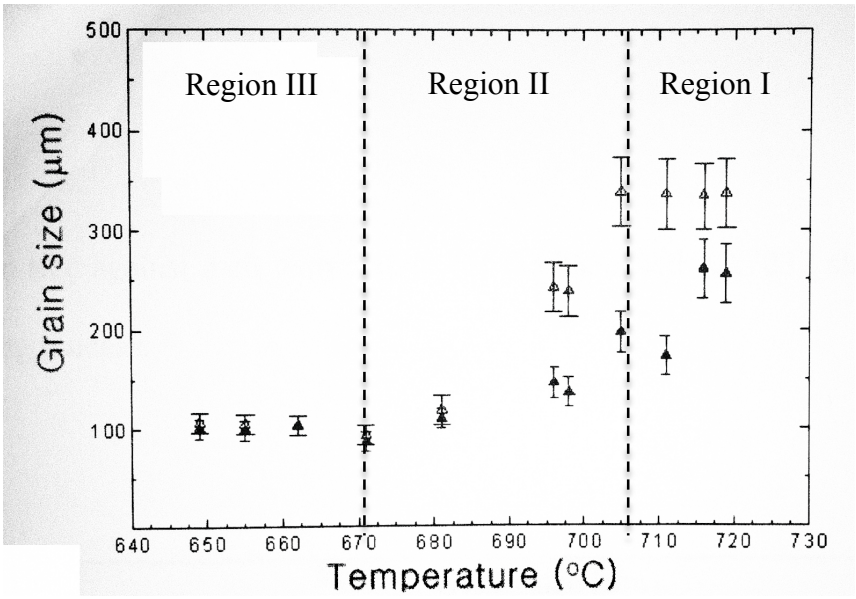


Figure 2.7: Plot shows grain size against melt temperature for a AA7032 alloy, manufactured using the UBE NRC process followed by rapid quenching [4]. Open triangles represent the grain sizes near the sample edge, and black triangles represent the grain sizes near the sample centre

The solidus and liquidus temperatures of the sample AA7032 alloy were calculated to be 508ºC and 663ºC respectively, using MTDATA. On Figure 2.7, the plot can be divided into three main regions:

– Region I, revealing that the grain sizes near the edge are significantly larger near the liquidus than the ones near the centre, and they continue to increase with decreasing melt temperature. The considerably larger grains in region I were attributed to growth during ladling [4].

– Region II, exhibiting a reduction in grain size as melt temperature reduces, and display very little difference in grain sizes between the microstructure near the edge and the centre.

– Region III, exhibiting a slight increase in grain size as melt temperature reduces, and like region II, displaying very little difference in grain sizes between the microstructure near the edge and the centre.

Varying the temperatures of the preheated enthalpy cans between 200 to 240ºC exhibited little difference in grain sizes. However, at around an enthalpy can temperature of 510ºC, the grain sizes were large and very dendritic due to the very high cup temperatures reducing heat extraction rates, causing the nuclei to re-melt [4]. The impacts of heating and cooling rates on the α-Al grain sizes were also investigated, but no significant effect was observed on the microstructure.

2.2.3 Semisolid Processing Technique vs Conventional Casting

The processing parameters of any Al alloy have significant effects on the microstructure of the material, which in turn determines the mechanical properties of the final product [4]. The viscosity of semisolid alloys is higher than that of liquid alloys, and therefore during semisolid processing the turbulence while filling the mould is significantly reduced [41]. This in turn reduces air entrapment during processing, resulting in fewer material defects and therefore enhanced material properties [37, 41]. It was also reported that in comparison with dendritic microstructures, alloys with a spherical microstructure develop improved mechanical properties on solidification [41]. Other advantages of semisolid processing techniques include reduced volume shrinkage [29], the potential to produce near net-shaped high-integrity components [29, 41], shorter time for process completion and improved die life due to lower processing temperatures [33, 29].

2.3 Solidification

Solidification is the term used to describe the nucleation and growth processes of a material, and can be summarised as follows:

(a) Nucleation: With reducing temperature of a melt the system loses thermal energy, causing particles in the bulk material to nucleate tiny clusters known as nuclei. This mechanism is known as homogeneous nucleation [44]. Homogeneous nucleation only takes place in very pure melts, and therefore does not generally occur in foundry practices. Due to the inclusions present in Al alloys, it has been recognised that Al

alloys generally experience heterogeneous nucleation, whereby an impurity particle catalyses the nucleation process [25].

(b) Growth: Depending on the size of impurity and solute particles and rate of undercooling, the nucleus can either freely grow into grains by consuming the surrounding melt, or re-dissolve into the melt.

(c) Growth into Final Microstructure: The growth in grain sizes continue until they impinge on each other, forming the final grain structure [42].

(d) Intermetallic Phase Formation: Since only a small proportion of the impurities and solutes actively nucleate the α-Al grains, the larger proportion of redundant solute assemble in the liquid remaining in between the grains.

The solidification mechanisms vary depending on the solidification parameters, such as the melt temperature, alloy composition, potency of the inoculants, cooling rate, size of cast, and so on. The mechanisms of nucleation and growth have been further discussed in the following sections, and intermetallic phase formation has been discussed later section 2.4.

2.3.1 Nucleation

The mechanism of nucleation can be categorised into two main groups, homogeneous nucleation and heterogeneous nucleation [43].

(a) Homogeneous Nucleation

With reducing temperature of melt, the system loses thermal energy causing particles in the bulk material to nucleate tiny clusters known as nuclei. This mechanism is known as homogeneous nucleation. The nucleated nuclei are generally assumed to be spherical for the sake of modelling. With the introduction of these solid phase embryos an interface energy barrier is created (see **Figure 2.8** a), and these embryos are only stable if the volume free-energy has reduced adequately so that the energy barrier due to interfacial energy can be overcome (see **Figure 2.8** b).

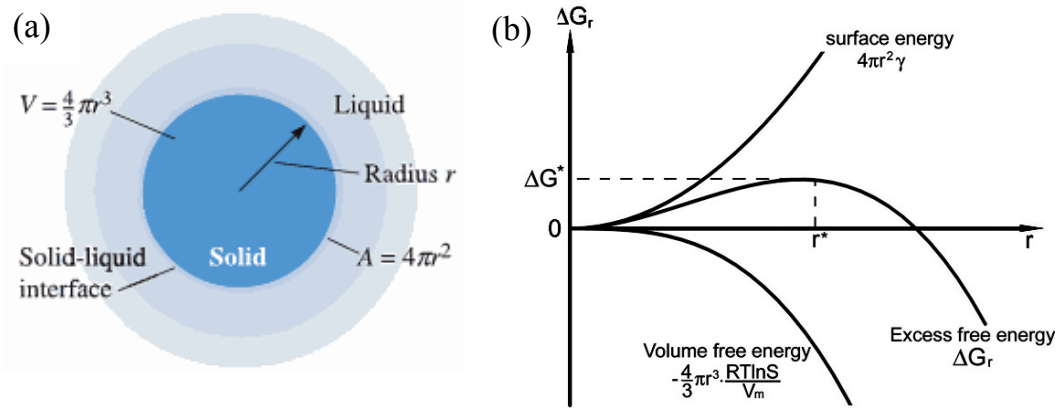


Figure 2.8: (a) Solid-liquid interface created on the introduction of solid in the melt [44], and (b) the relationship between total free-energy and the size of the solid [45]

The relationship of the embryo radius (r) and free energy in the system (ΔG_r) can be described as equation 2.1.

$$\Delta G_r = -\frac{4}{3}\pi r^3 \Delta G_V + 4\pi r^2 \sigma_{SL} \qquad (2.1)$$

where ΔG_V is the volume free-energy change on solidification and σ_{SL} is the interfacial energy between the solid and liquid. For homogeneous nucleation, the critical radius r_{ho}^* and the energy barrier ΔG_{ho}^* are given by equation 2.2 and 2.3 [43].

$$r_{ho}^* = \frac{2\sigma_{SL}}{\Delta G_V} \quad \text{and} \tag{2.2}$$

$$\Delta G_{ho}^* = \frac{16\pi\sigma_{SL}^3}{3\Delta G_V^2}. \tag{2.3}$$

Homogeneous nucleation only takes place in very pure materials, and therefore does not generally occur in metal alloys due to the inclusions that are present. Thus, it has been recognised that Al alloys generally experience heterogeneous nucleation.

(b) Heterogeneous Nucleation

Heterogeneous nucleation is when the nucleus formation is catalysed by the presence of foreign nucleants (such as inclusions, container wall, etc.). The nucleus is described as forming in the shape of a spherical cap on the nucleant surface (see Figure 2.9 a), and as a result reduces the energy barrier of the system (see Figure 2.9 b). This mechanism is known as the spherical cap model.

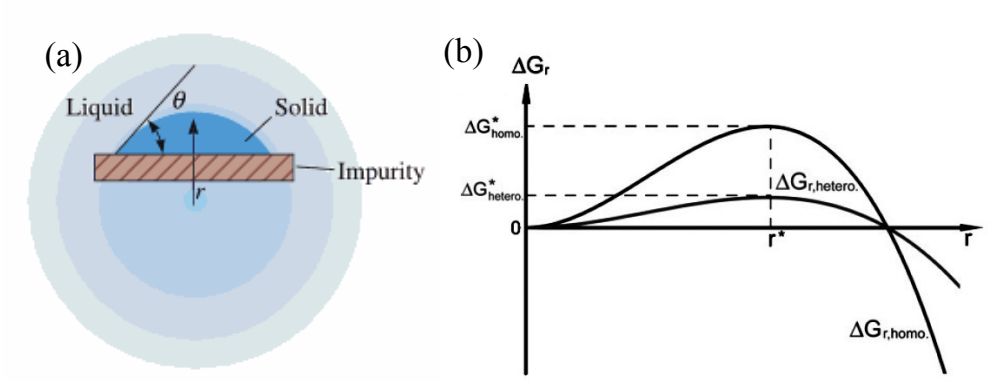


Figure 2.9: (a) The critical radius can be achieved with a smaller increase in energy when solid forms on a foreign substrate [44] and (b) comparison of the total free-energies of homogeneous and heterogeneous nucleation [45]

Thus, for heterogeneous nucleation, the critical radius r_{he}^{*} and the energy barrier ΔG_{he}^{*} are given by equations 2.4 and 2.5 [43].

$$r_{ho}^{*} = \frac{2\sigma_{SL}}{\Delta G_V} = r_{he}^{*} \quad \text{and} \tag{2.4}$$

$$\Delta G_{he}^{*} = \frac{16\pi\sigma_{SL}^{3}}{3\Delta G_V^{2}} f(\theta) = \Delta G_{ho}^{*} f(\theta) \tag{2.5}$$

where f(θ) is the nucleant efficiency and θ is the contact angle at the solid-liquid-nucleant triple point. f(θ) and θ can be expressed as equation 2.6 and 2.7.

$$f(\theta) = \frac{(2+\cos\theta)(1-\cos\theta)^{2}}{4} \quad \text{and} \tag{2.6}$$

$$\cos\theta = \frac{\sigma_{LN} - \sigma_{SN}}{\sigma_{SL}} \tag{2.7}$$

where σ_{LN} and σ_{SN} are the interfacial energies between the liquid-nucleant and solid-nucleant interfaces respectively. It is also worth noting that with decreasing value of θ, the energy barrier (ΔG_{he}^{*}) reduces and the nucleant therefore is more potent. However, when the value of θ is too small, such as ~10 to ~20°, according to the spherical cap model the nucleus is below a single layer to a few atoms thick. It is thus assumed that the spherical cap model is ineffective when θ is very small [46].

(c) Adsorption Theory

Cantor [47] suggested that heterogeneous nucleation takes place through adsorption, whereby atom-by-atom adsorption occurs on the nucleant and liquid interface instead of forming a spherical cap nucleus. The model at present functions for an immiscible two-part system; part A, the catalyst, and part B, the solidifying liquid. The surface energy of A adsorbing atoms from B, γ_{ad}, can be expressed as equation 2.8 [48].

$$\gamma_{ad} \approx -\phi R_g \Delta T + R_g T\left(\phi \ln\phi + (1-\phi)\ln(1-\phi)\right) + \frac{3}{2}\phi(1-\phi)R_g T_m$$
$$+\frac{1}{4}\left(\phi(\omega_S + 3R_g T_m) + (1-\phi)(\omega_L + 3R_g T_{mA})\right) \tag{2.8}$$

where ϕ is the monolayer fraction that is adsorbed on the surface, R_g is the gas constant, T_m is the melting point of B, ω_S and ω_L are the A/B interaction parameters in the solid and liquid respectively, and T_{mA} is the melting point of A. The degree of surface adsorption is controlled by the first and fourth terms in equation 2.8, which are also

linear in ϕ. The adsorption undercooling, ΔT_{ad}, can be expressed as shown below in equation 2.9 [47].

$$\Delta T_{ad} \approx \frac{1}{4}\frac{(\omega_S - \omega_L)}{R_g} - \frac{3}{4}(T_{mA} - T_m) \tag{2.9}$$

Thus, the efficiency of A (catalyst) for heterogeneously nucleating B (solidifying liquid) is dependent on the difference in their immiscibilities and their melting points [46, 47].

According to Cantor [46, 48], high efficiencies would result for heterogeneous nucleation if the difference between the nucleant and alloy immiscibilities is small, and the difference between their melting temperatures is large. Results from experimental observations were in agreement with Cantor's model [47].

2.3.2 Growth

(a) Free Growth of Nucleus

Al-Ti-B type grain refiner is commercially used as a nucleant to nucleate α-Al grains, and it is regularly reported that only about 1% of the grain refiner particles added to the melt nucleate α-Al grains [49]. Maxwell and Hellawell [50] explained this phenomenon by suggesting that the initial nuclei production produces latent heat and therefore the local melt temperature increases, which in turn results in a decline in nucleation rate. Greer [51] however suggested that the energy barrier formed during the nucleation phase remains active during the growth of the nuclei that have already formed, as outlined in Figure 2.10.

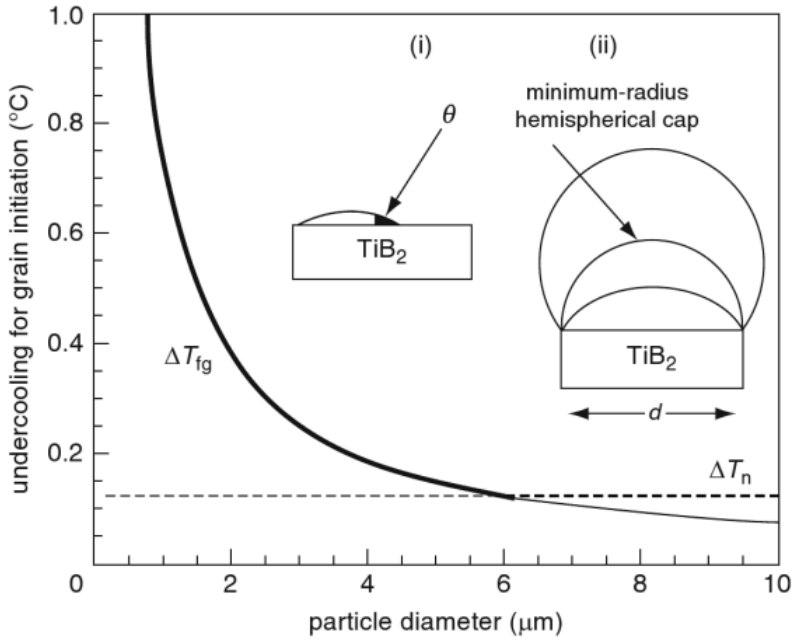


Figure 2.10: Grain size distribution of TiB_2 nucleant particles in a commercial Al-5Ti-B refiner, while the insets show (i) the conventional spherical cap model and (ii) α-Al grain growing on the (0001) plane of a hexagonal nucleant through free growth [52]

Greer [51] indicated that the diameter of the nucleant and the amount of undercooling required for nucleus growth (also known as 'free growth') are inversely proportional, and can be expressed as equation 2.10.

$$\Delta T_{fg} = \frac{2\sigma_{SL}}{\Delta S_V d} \tag{2.10}$$

where ΔT_{fg} is the amount of undercooling required for free growth, σ_{SL} is the interfacial energy between the solid and liquid, ΔS_V is the entropy of fusion, and d is the diameter of the nucleant.

Greer [52] carried out further work to model the free growth criterion, taking into account the free growth criterion, distribution of inoculant size, controlled undercooling

through constant heat loss from the system, and the effect of recalescence. Figure 2.11 region (a) shows the predictions of the numbers of grains made using the model proposed by Maxwell and Hellawell [50], and Figure 2.11 region (b) shows the predictions made using the free growth criterion.

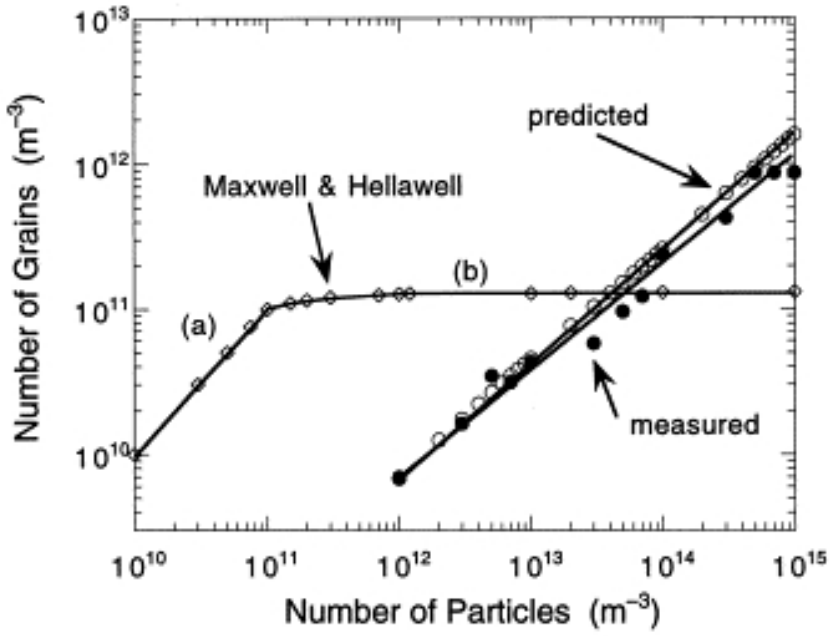


Figure 2.11: The number of grains per unit volume as a function of nucleant particles per unit volume, where the diamonds represent the calculations carried out according to Maxwell and Hellawell's suggestions, open circles represent the calculations carried out according to Greer's suggestions, and the black circles represent the measured grain diameters obtained from TP-1 tests. Calculations according to Maxwell and Hellawell's suggestions reveal (a) a section 100% efficiency, and (b) a point after which the number of grains saturate [52]

The first prediction takes into account a combination of heterogeneous nucleation control and recalescence, according to Maxwell and Hellawell's [50] suggestions. The model predicts that at lower concentrations of inoculants, the inoculants have sufficient time to act as nucleants. However, as the concentration of inoculants increase beyond a

certain point, the effect of recalescence causes the number of grains to plateau. The results from the second model, which takes into account the free growth criterion and the distribution of inoculant size, corresponds to experimental findings. The reported phenomenon of only ~1% of inoculants being active is best explained when the free growth criterion, which suggests just a fraction of the inoculants are active, is combined with the recalescence effect [51, 52]. This leaves almost 99% of the inoculants disused and dispersed throughout the cell and grain boundaries, which may cause the local chemistry to change and as a result, affect the intermetallic phase selection [53, 54]. Sha [55] supports this theory and reports observing low index zone axes when investigating the orientation relationship of TiB_2 particles connected to β-AlFeSi phase. The impact of inoculants on intermetallic phase selection will be discussed section 2.4.

(b) Growth into Final Microstructure

Although both the removal of thermal energy and solute diffusion control the growth rate of grains, the solute diffusivity in the liquid is commonly significantly smaller than thermal diffusivity, and therefore the growth rate is mainly determined by the solute diffusivity [56]. Thus, if solutes are chosen with lower diffusivity in a given alloy, the grain growth would be restricted allowing time for further new grains to nucleate, producing a finer grained microstructure [52]. The growth restriction ability of solutes is measured with the parameter Q, known as the growth restriction factor [52, 57]. Q is directly proportional to the solute content (C_0) in a binary system where the liquidus and solidus are assumed to be straight lines, and can be expressed as shown in equation 2.11 [57].

$$Q = m_L(k-1)C_0 \tag{2.11}$$

where m_L is the liquidus slope gradient and k is the equilibrium partition coefficient, and expressed as equation 2.12.

$$k = C_S^*/C_L^* \tag{2.12}$$

where C_S^* and C_L^* are the equilibrium solute content of the solid and liquid at the interface. Various investigations have been carried out to understand the relationship between Q of various solutes in Al alloys and the resultant grain diameters [22, 58]. Some Q values per unit concentration of solutes commonly found in Al alloys are given in Table 2.1, and it can be seen that Ti had a significantly high Q value compared to the rest [57, 59].

Table 2.1: Growth restriction factors of various solutes in Al alloys [60]

Solute Element	Ti	Si	Zr	Mg	Fe	Cu	Cr	Mn
Q/C_0	154	5.2	4.6	3.7	2.8	2.2	2	0.46

For multicomponent systems, Q values were initially calculated using the combined contributions of the individual solutes in binary systems (i), as shown in equation 2.13 [61].

$$Q_{\Sigma binary} = \sum Q_{binary,i} = \Sigma m_{binary,i}(k_{binary,i} - 1) \cdot c_{0,i} \tag{2.13}$$

This calculation however disregards any multicomponent interactions and the effect of low level primary intermetallic phase formation, the combined effect of which can cause negative contributions to the Q value which is impossible in binary alloys [62].

A realistic calculation of Q value would require a thermodynamic software and a reliable database of the alloy system.

To understand the nucleant potency further, Easton and StJohn investigated the relationship between grain size and 1/Q with additions of varying amounts of TiB_2 using Al-3Ti-1B master alloy and pre-solidification cooling rate of $1Ks^{-1}$ into graphite enthalpy cups [63]. The graph displaying the relationship between grain size and 1/Q values is given in Figure 2.12. Although a significant grain size reduction can be seen on addition of AlTiB-type grain refiner, the amount of grain refiner did not seem to make a major difference in the grain sizes.

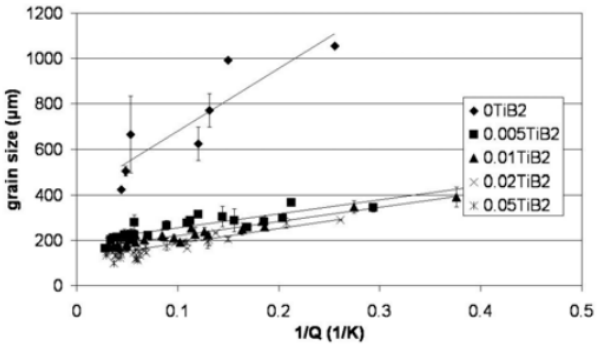


Figure 2.12: A graph of grain size as a function of 1/Q for Al alloys 1050, 2014, 3003, 5083, 6060, 6061 and 6082 at varying TiB_2 contents up to 0.05wt.% [63]

2.3.3 Development of the Equiaxed Microstructure

Various mechanisms have been suggested to explain the transformation of dendritic grains found in direct chill (DC) cast alloys to the relatively uniformly fine equiaxed microstructures found in alloys cast using semisolid processing techniques. It has been suggested that the increased number of grains obtained using semisolid processing

techniques is a result of (a) dendrite arm fragmentation, (b) dendrite arm root remelting, and (c) growth control mechanisms [41].

(a) Dendrite Arm Root Fragmentation

It has been suggested that the dendrite arms may get fragmented at their roots due to the shear forces present during agitation, giving rise to grain multiplication and a more equiaxed microstructure. According to this suggestion, the dendrite arms plastically bend under the shear forces, introducing 'geometrically necessary dislocations' in the form of significant grain misorientations [64]. At elevated temperatures, recrystallisation causes the dislocations to reorganise and coalesce to form high angle grain boundaries, which contain high levels of energy. If the angle of the bent grain boundary exceeds 20^{o}, the energy at the grain boundary is more than double the energy of the liquid-solid interface, which results in liquid metal wetting the grain boundary and detaching the dendrite arm. This mechanism is schematically shown in Figure 2.13. However, according to this suggestion, these shear forces would need to originate from velocity gradients between the arms of a freely floating dendrite and the melt [65], it is worth noting that these dendrites grow as near perfect crystals and can therefore be very difficult to simply fragment [37]. Furthermore, due to high ductility of Al alloys at semisolid temperatures, the dendrite arms are more likely to bend rather than break apart.

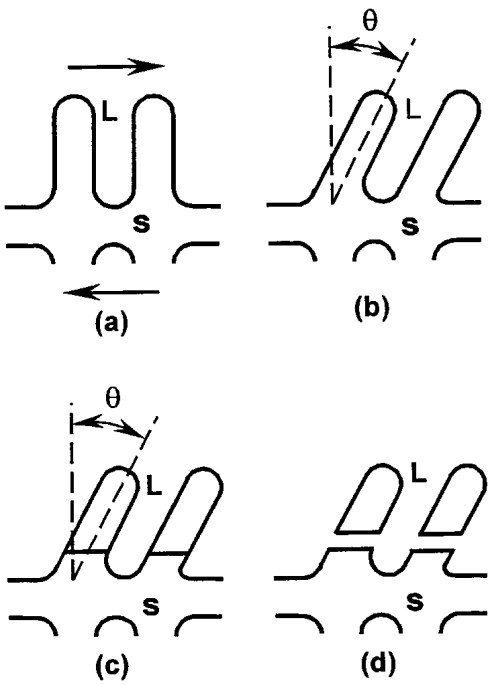


Figure 2.13: Schematic diagram of dendrite arm fragmentation mechanisms: (a) undeformed dendrite arms, (b) after bending due to shear forces, (c) recrystallisation forms high angle grain boundaries, and (d) fragmentation on wetting of grain boundary by melt [66]

(b) Dendrite Arm Root Remelting

It has also been suggested that the dendrite arms may melt away at their roots causing grain multiplication due to solute enrichment lowering the local melting point, and thermosolutal convection causing accelerated solute diffusion, thermal fluctuation and generating stress at the dendrite arm roots [37]. This mechanism has been further supported by recent work carried out by Liotti et al. [67].

The correct mechanism of dendrite fragmentation has not yet been identified, however, it is possible that different mechanisms might be active under different solidification conditions.

Although detached dendrite arms continue growing dendritically given the right conditions [37], laminar flow modifies the dendritic growth morphology to rosette form, while turbulent flow modifies the rosette growth morphology to spherical form (see Figure 2.14) [23]. Agitation also improves solute transportation and therefore accelerates heterogeneous nucleation.

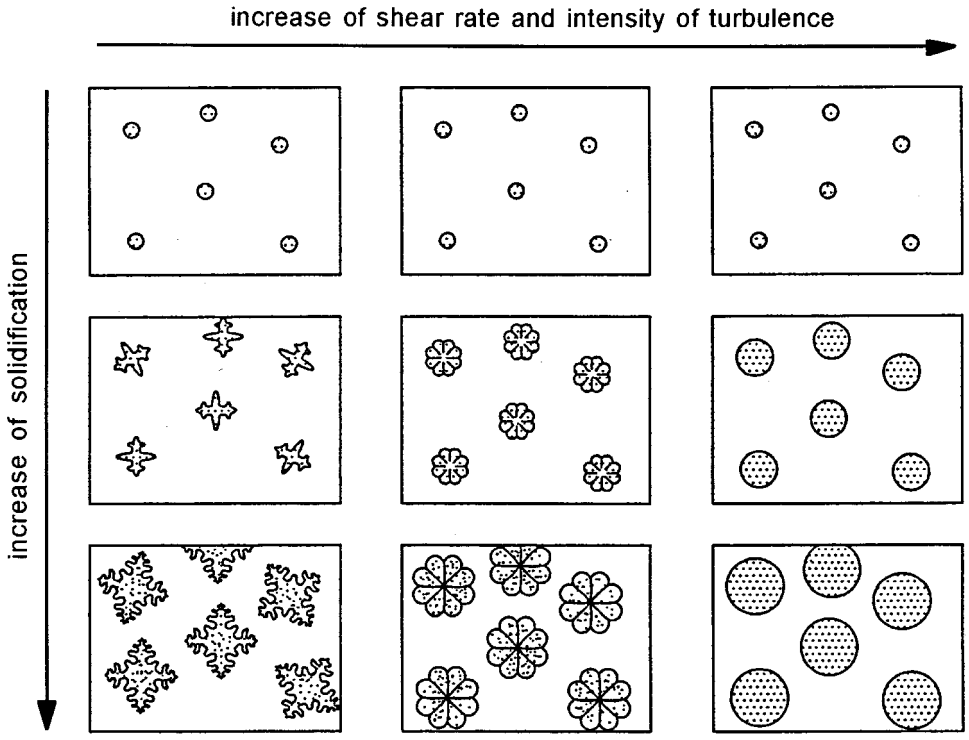


Figure 2.14: Schematic diagram of the impact of increasing shear rate and agitation intensity, transforming the α-Al microstructure from dendritic to rosette, then globular [68]

2.4 Secondary Intermetallic Phases

2.4.1 Fe-rich Phases in 6xxx Al Alloys

The chemical stability, identity, morphology, amount and distribution of the AlFeSi based phases are determined by the alloy composition and solidification conditions. Each of these aspects of the AlFeSi based phases have an effect on the mechanical properties of a 6xxx Al alloy, which in turn significantly affects the mechanical properties of the alloy, which in turn influences its down-stream processing [69].

2.4.1.1 Ternary Phases: Al-Fe-Si based Phases

The phases that form in the presence of Si are generally the AlFeSi based ternary phases [70]. The most commonly observed secondary intermetallic phases in 6xxx Al alloys are α-Al_8Fe_2Si and β-Al_5FeSi phases [71].

(a) α-Al_8Fe_2Si Intermetallic Phase

α-Al_8Fe_2Si phases can be metastable, and are observed with various crystal structures. Although under equilibrium conditions, α-Al_8Fe_2Si adopts the hexagonal structure expressed as α_h-Al_8Fe_2Si [72], commercial cooling conditions are generally non-equilibrium [69], and therefore α_h-Al_8Fe_2Si is not frequently observed. Non-equilibrium cooling conditions combined with certain elements such as V, Cr, Mn, Cu, Mo and Ti promote the formation of the metastable body-centred cubic structure α_c-Al_8Fe_2Si, also known as α-AlFeSi. Thus, the α-Al_8Fe_2Si phase is observed more frequently in its metastable body-centred cubic form [70].

Physical appearances of α-AlFeSi include blocky, plate-like and rosette-like

morphologies, although the lamellar/dendritic morphology (also known as 'Chinese script') is most commonly observed [69, 70]. Figure 2.15 shows an example of the dendritic and rosette morphologies in 2D, while Figure 2.16 shows those morphologies in 3D (after extraction from the α-Al). Various other crystal structures and compositions of α-AlFeSi phase have been observed in previous studies. Dons [73] identified the monoclinic phase α_v-AlFeSi in a DC cast alloy with Al-0.2 wt% Fe-0.2 wt% Si, and claimed that the α_v-AlFeSi phase was associated with the Al-Al_9Fe_2 binary phase. Dons [73] also observed a variant of the α-Al_8Fe_2Si phase in the same material, denoted α_T-AlFeSi phase. Although the crystal structure of α_T-AlFeSi phase was unidentified, it was related to the cubic α-AlFeSi structure. Westengen [74] identified another variant of the cubic α-AlFeSi phase but with lower Si content, denoted as α″-AlFeSi phase.

(b) β-Al_5FeSi Phase

The β-Al_5FeSi phases, also denoted as β-AlFeSi, are promoted in the presence of excess Si and exhibit a monoclinic crystal structure [75]. Like α-Al_8Fe_2Si, β-AlFeSi phase can be metastable and able to exist in a range of morphologies: needle-like, plate-like, etc. [70]. The β-AlFeSi phases are most commonly observed in the plate-like morphology, whereby the phases branch out both from the base as well as the branches [16, 76]. An example of the plate-like morphology can be seen in 2D and 3D in Figure 2.15 and Figure 2.16 respectively. Westengen [74] identified a lower Si content variant of the β-AlFeSi phase, denoted as β′-AlFeSi phase.

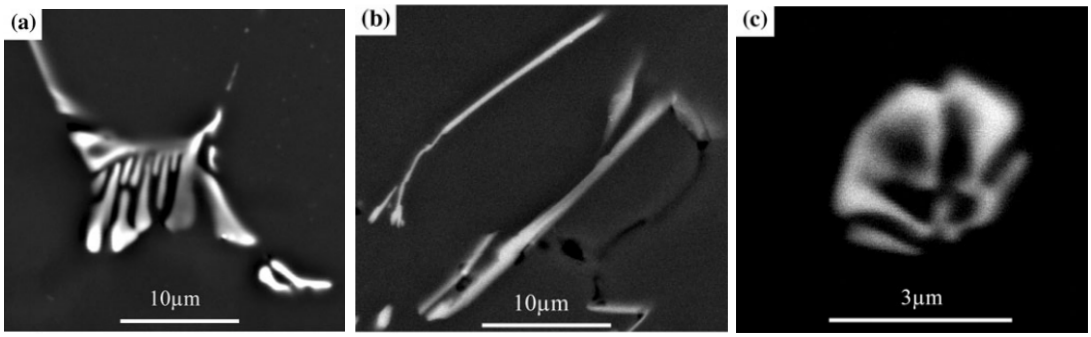


Figure 2.15: BSE-SEM images showing the (a) 'Chinese script'-like, (b) plate-like and (c) rosette-like phase morphologies in 2D [77]

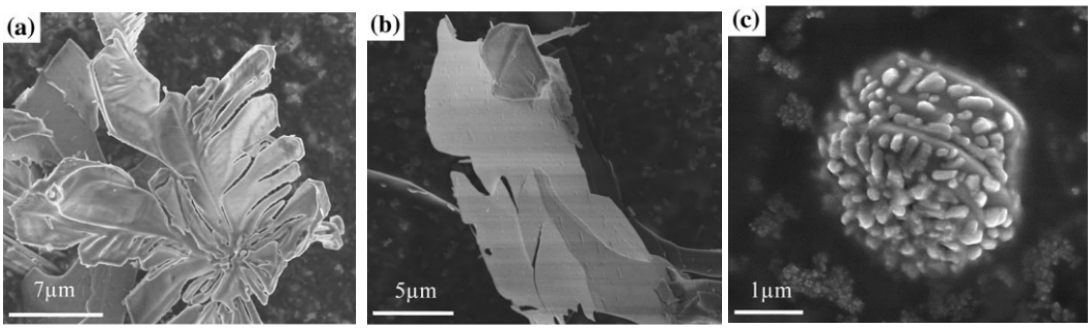


Figure 2.16: FEG-SEM images showing the (a) dendritic α_c-AlFeSi, (b) plate-like β-AlFeSi and (c) rosette-like α_c-AlFeSi phase morphologies in 3D [77]

A characterisation study carried out by Davidson [3] reported that additions of the Al-Ti-B type grain refiners affected the phase selection in the α-Al. The Al-Ti-B type grain refiner was observed to encourage the formation of β-AlFeSi over α_c-AlFeSi phase. It was therefore suggested that the active particles of Al-Ti-B type grain refiner, i.e. TiB_2, might either be causing the local chemistry to change resulting in favourable conditions for β-AlFeSi phase formation, or are acting as nucleants for the phase.

2.4.2 Impact of Intermetallic Phases on Al Alloys

As mentioned section [2.4.1], it has been established that the phase selection, their size and distribution contribute to the final mechanical properties of an alloy [69, 78]. For example, large and brittle phases distributed non-uniformly can produce an alloy with defects and non-uniform mechanical behaviour across the cast [78].

The β-AlFeSi phase is less desirable in the commercial context because it is detrimental during extrusion, its brittle behaviour causes significant reduction in ductility, and can act as crack initiators by decohesion at the bulk material and phase interface [79]. However, unlike the β-AlFeSi phase, it is generally believed that smaller particles of α-AlFeSi phases do not deteriorate the mechanical properties and formability of 6xxx Al alloys as badly [55].

2.4.3 Stability of β-AlFeSi in 6xxx Al Alloys

The β-AlFeSi phase can be metastable in 6xxx Al alloys, and it is possible to transform the plate-like metastable β-AlFeSi phase into smaller and more rounded α-AlFeSi phase during a homogeneousation heat treatment [80]. Figure 2.17 shows the difference in morphology of the two phases when extracted from the α-Al matrix. Furthermore, as β-AlFeSi has a higher Si content compared to α-AlFeSi, homogenisation releases the excess Si promoting Mg_2Si precipitation at later stages. Thus, homogenising the β-AlFeSi phase also enhances the alloy strength [81]. However, despite the improvement in mechanical properties, the introduction of alloy homogenisation significantly increases the manufacturing costs [82], and it is therefore preferable to be able to control

the phase selection, their size and distribution during the solidification processes to keep the production costs down.

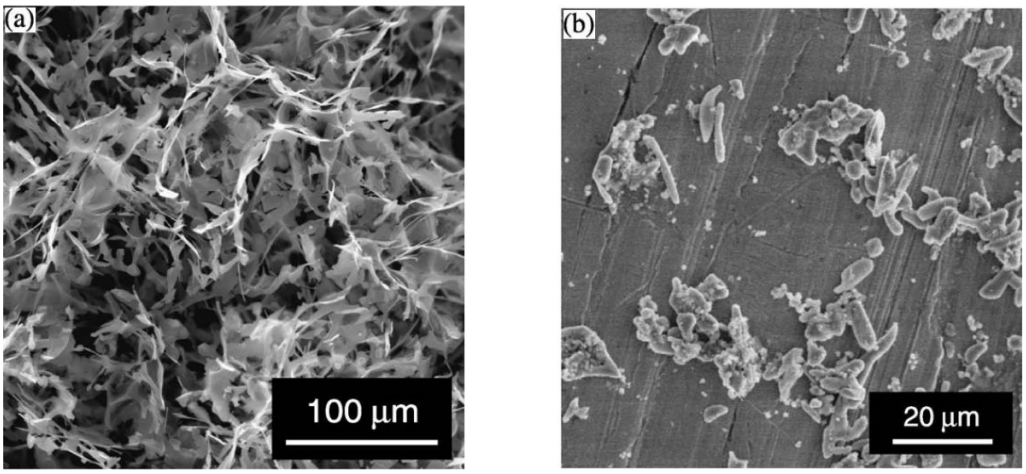


Figure 2.17: SEM Images of (a) β-AlFeSi Particles in Plate-Like Morphology Extracted from a AA6005 Alloy, and (b) Extracted α-Al(FeMn)Si Particles after Homogenisation [83]

2.4.4 Solidification Reactions

During solidification of alloys, the various reactions that take place can usually be divided into three main categories; eutectic, peritectic and quasi-peritectic reactions. Eutectic solidification reactions define the formation of two or more solid phases from a liquid phase (L → S1 + S2), while peritectic solidification reactions define the formation of a solid phase from a liquid and one or more solid phases (L + S1 → S2) [55]. Quasi-peritectic solidification reactions define the formation of two solid phases from a liquid and a solid phase (L + S1 → S2 + S3), and ternary-peritectic solidification reactions define the formation of a solid phase from a liquid and two solid phases (L + S1 + S2 → S3). Due to the different mechanisms involved in these reactions, the microstructures produced from each may vary widely. Some of these solidification

reactions may result in the formation of intermetallic phases.

2.4.5 The Al-Mg-Fe-Si Alloy Systems

Equilibrium phase diagrams for the Al-Mg-Fe-Si alloy system are given below in Figure 2.18. The combination of Mg, Si and Fe content produces a quanternary phase, $Al_8FeMg_3Si_6$ (π-AlFeMgSi), alongside the binary and ternary phases (Al_3Fe, Al_8Mg_5, Mg_2Si, α-AlFeSi, β-AlFeSi and Si) from the subsidiary ternary systems Al-Mg-Si, Al-Mg-Fe and Al-Fe-Si [15, 28]. The π-AlFeMgSi phase has a hexagonal crystal structure, and contains 10.9 wt% Fe, 14.1 wt% Mg, and 32.9 wt% Si [24]. The five-phase invariant reactions associated with this system are given in Table 2.2.

Table 2.2: The Five-Phase Solidification Reactions of the Al-Mg-Fe-Si Alloy Systems [84]

Point	Reactions	Composition of Phase Components (left to right)			Temp. °C
		Liquid	1	2	
		Fe wt.% Si	Fe wt.% Si	Fe wt.% Si	
e_6	L → α-Al + Al_3Fe + Mg_2Si	~1.00	~10.00	~7.00	>587
E_1	L → α-Al + Al_3Fe + Al_8Mg_5 + Mg_2Si	0.11	33.30	0.35	448
E_2	L → α-Al + Si +Mg2Si + π-AlFeMgSi	0.15	4.90	12.90	554
P_1	L + β-AlFeSi → α-Al + Si + π-AlFeMgSi	0.52	2.90	12.15	567
P_2	L + β-AlFeSi + Mg_2Si → α-Al + π-AlFeMgSi	0.55	6.00	11.40	568
P_3	L + α-AlFeSi → α-Al + Mg_2Si + β-AlFeSi	0.82	6.45	9.50	576
P_4	L + Al_3Fe → α-Al + Mg_2Si + α-AlFeSi	1.35	7.25	7.05	586

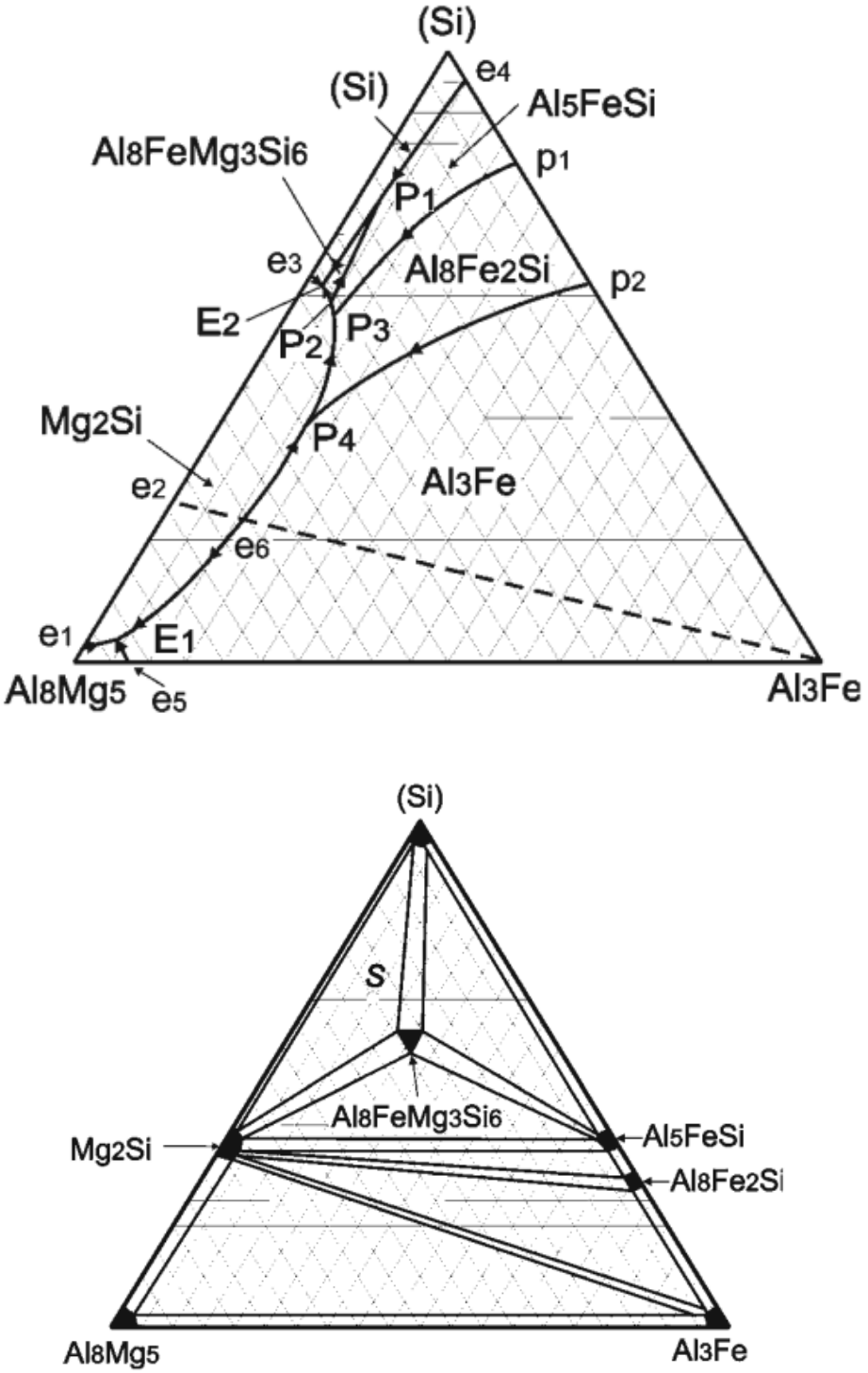


Figure 2.18: Al-Mg-Fe-Si equilibrium phase diagram: (a) polythermal projection of the liquidus and (b) solidus with phase information [85]

Al-Mg-Fe-Si Alloy System under Non-Equilibrium Conditions

The phases formed in alloys manufactured under equilibrium conditions can be established from equilibrium phase diagrams [55]. However, commercial casting techniques are generally carried out under non-equilibrium conditions [69], where some of the solidification reactions, especially peritectic and quasi-peritectic reactions which require long range diffusion of solutes through a solid phase, may not go to completion [55,86]. Thus several studies have been carried out to better understand the characteristic phases of Al alloys manufactured under non-equilibrium conditions [55,69,81,86,87,88]. Various findings indicated that some of the solidification reactions that take place under equilibrium conditions might get suppressed under non-equilibrium conditions. There were also indications that the alloy composition and growth velocity during solidification can determine the solidification reactions that will occur, resulting in a varied solidified final microstructure [55].

Under non-equilibrium conditions, Mulazimoglu [86] confirmed that the following solidification reactions all took place in an AA6201 alloy modified with Sr:

$L \rightarrow \alpha\text{-Al}$	dendritic network	(2.14)
$L \rightarrow \alpha\text{-Al} + Al_{13}Fe_4$	binary eutectic	(2.15)
$L + Al_{13}Fe_4 \rightarrow \alpha\text{-Al} + \alpha\text{-AlFeSi}$	quasi-peritectic	(2.16)
$L \rightarrow \alpha\text{-Al} + \alpha\text{-AlFeSi}$	binary eutectic	(2.17)
$L + \alpha\text{-AlFeSi} \rightarrow \alpha\text{-Al} + \beta\text{-AlFeSi}$	quasi-peritectic	(2.18)

He also denoted reaction (2.18) to be most important. On the contrary, Kosuge [86] suggested that at high cooling rates the equilibrium phase $Al_{13}Fe_4$ (produced from

reaction 2.15) was hard to nucleate. Thus, he claimed solidification reactions such as reaction 2.16 might not occur due to the possibility of $Al_{13}Fe_4$ phase being substituted by other phases. Sha [55] did observe the presence of equilibrium phase $Al_{13}Fe_4$ in alloys grown at low growth velocity, and he reported that the prevalent solidification reactions forming Fe-based phases were 2.14, 2.15, 2.17, 2.19 and 2.20.

$L \rightarrow \alpha\text{-Al} + \beta\text{-AlFeSi}$ binary eutectic (2.19)

$L \rightarrow \alpha\text{-Al} + Mg_2Si$ binary eutectic (2.20)

The alloy examined for his investigation was a 6xxx series model alloy, Bridgman solidified along with grain refiner TiB_2 additions. He also observed that the equilibrium quasi-peritectic reaction 2.16 was replaced by a non-equilibrium quasi-peritectic reaction 2.21.

$L + Al_{13}Fe_4 \rightarrow \alpha\text{-Al} + \beta\text{-AlFeSi}$ quasi-peritectic (2.21)

Composite particles $Al_{13}Fe_4$ / β-AlFeSi had formed during this solidification reaction, where β-AlFeSi encapsulated the $Al_{13}Fe_4$ phase. The quasi-pertitectic reaction 2.18 was also observed, where β-AlFeSi encapsulated the α-AlFeSi.

2.4.6 Observation of TiB_2 in Alloys

To better understand the impact of Al-Ti-B type grain refiners on the phases, various investigations have examined the Ti-containing particles in relation to its proximate

microstructure. Some of the observations from various processing techniques are summarised below:

– Davies et al. [89] carried out a characterisation study of DC cast 6xxx Al alloys, and reported that Al_3Ti particles were present at the centre of the α-Al grains, displaying preferred epitaxial orientations. Ti and B containing particles, however, were observed at the interdendritic regions and displayed no preferred orientation (shown in Figure 2.19).

– Another characterisation study carried out by Jin et al. [90], observed black regions which were reported to be either TiB_2 or Al_3Ti particles, and boride clusters at the centre of the α-Al grains (shown in Figure 2.20).

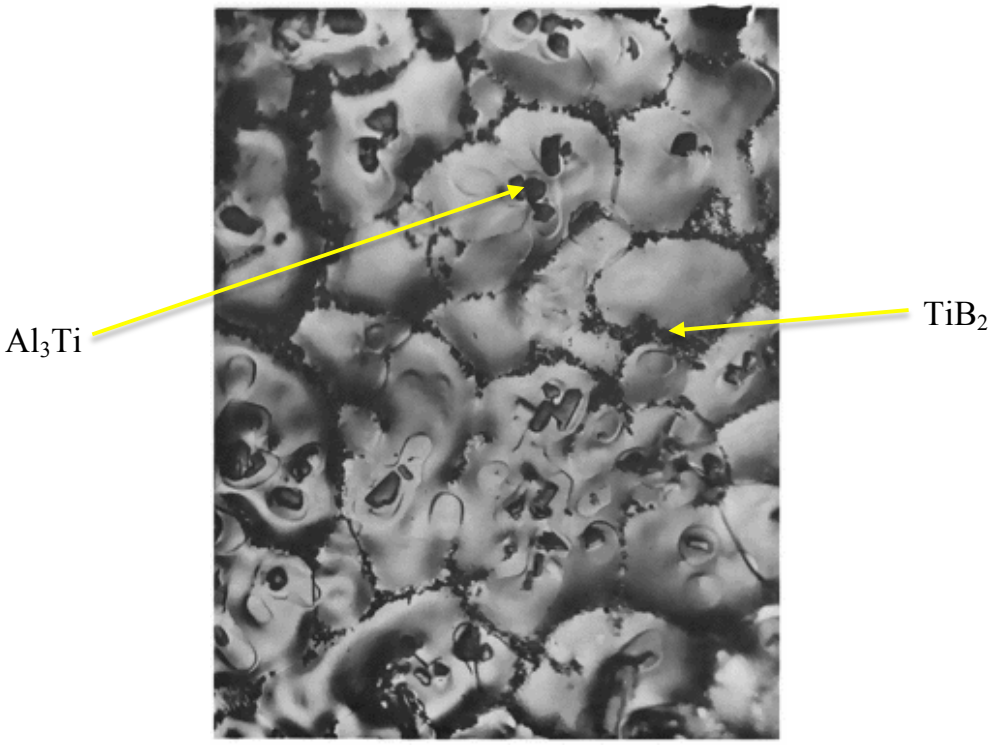


Figure 2.19: Optical micrograph showing the α-Al grain structure and particle distribution of a commercial Al alloy with 5:1 Ti-B grain refiner additions (x340 magnification) [89]

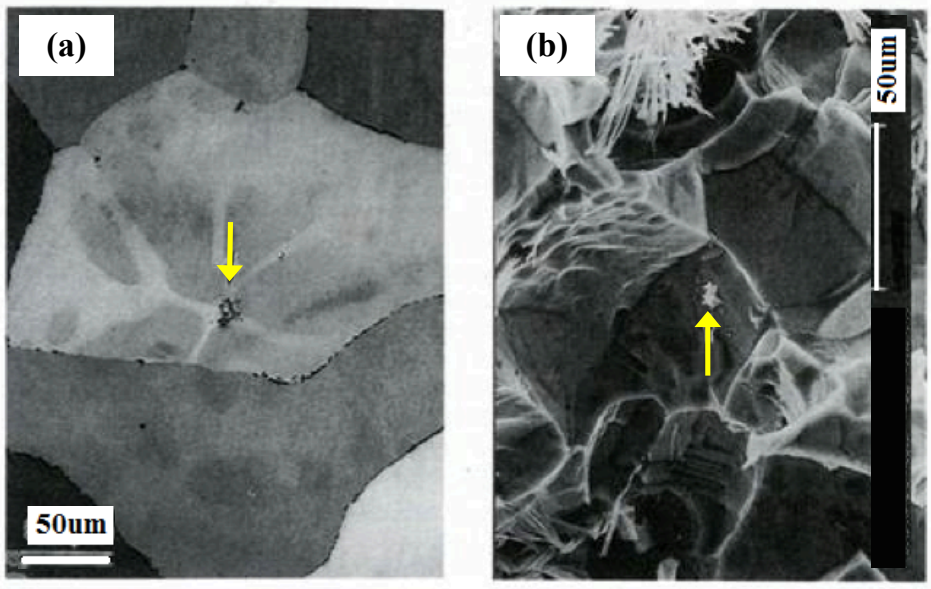


Figure 2.20: (a) Optical and (b) SEM micrographs showing α-Al grains with boride clusters at the centre [90]

– Davidson [3] also carried out a characterisation study, and reported that several Ti rich regions were related to AlFeSi-based phases in both metallographic samples and extracted particles. Ti-rich regions in extracted particles are shown in Figure 2.21. Boron, however, once again had not been located and therefore it could not be concluded whether it was TiB_2 particles or other Ti-based phases that may have initiated the AlFeSi-based phases.

– A characterisation study carried out by Lui [76] indicated that Ti-B particle clusters were observed infrequently, and were found to be unevenly distributed in both the metallography samples and extracted particles. Particles were located within the α-Al grains, as well as at grain and cell boundaries (shown in Figure 2.22).

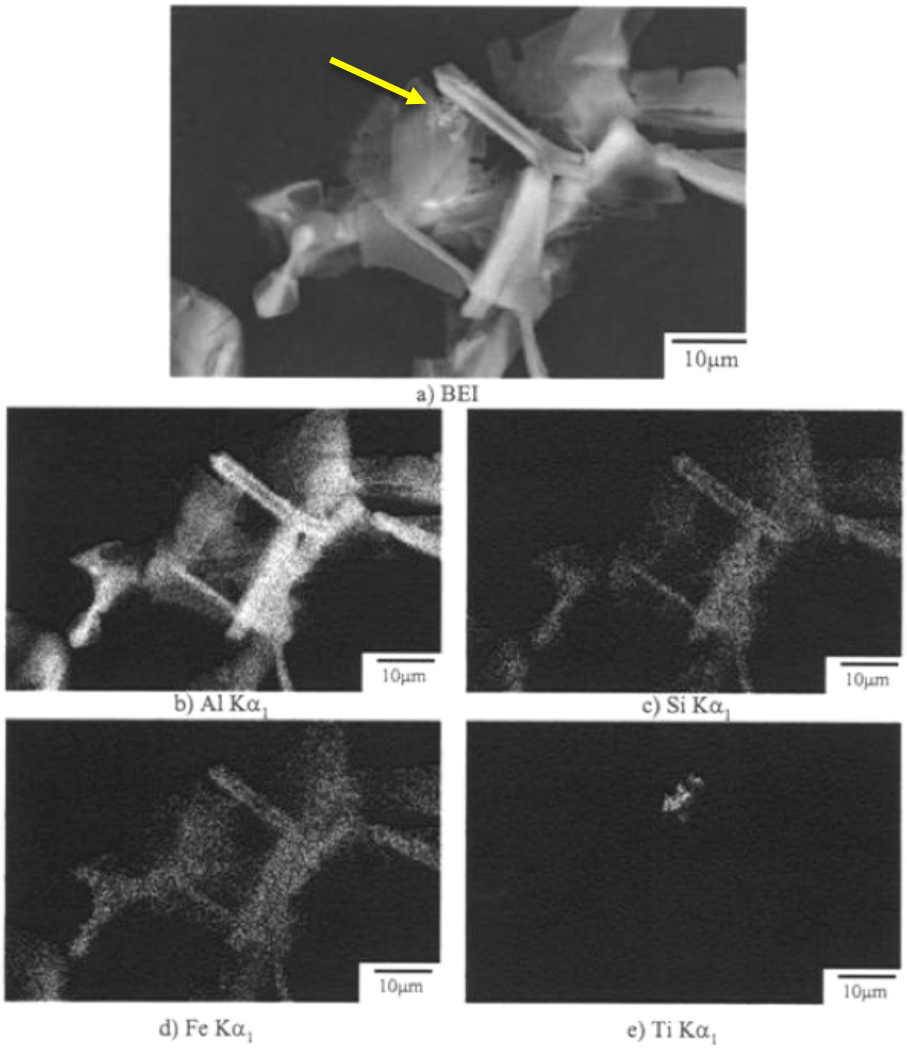


Figure 2.21: (a) Backscattered SEM micrograph of an extracted phases with a Ti-rich region (yellow arrow), and EDX element maps showing the element distributions [3]

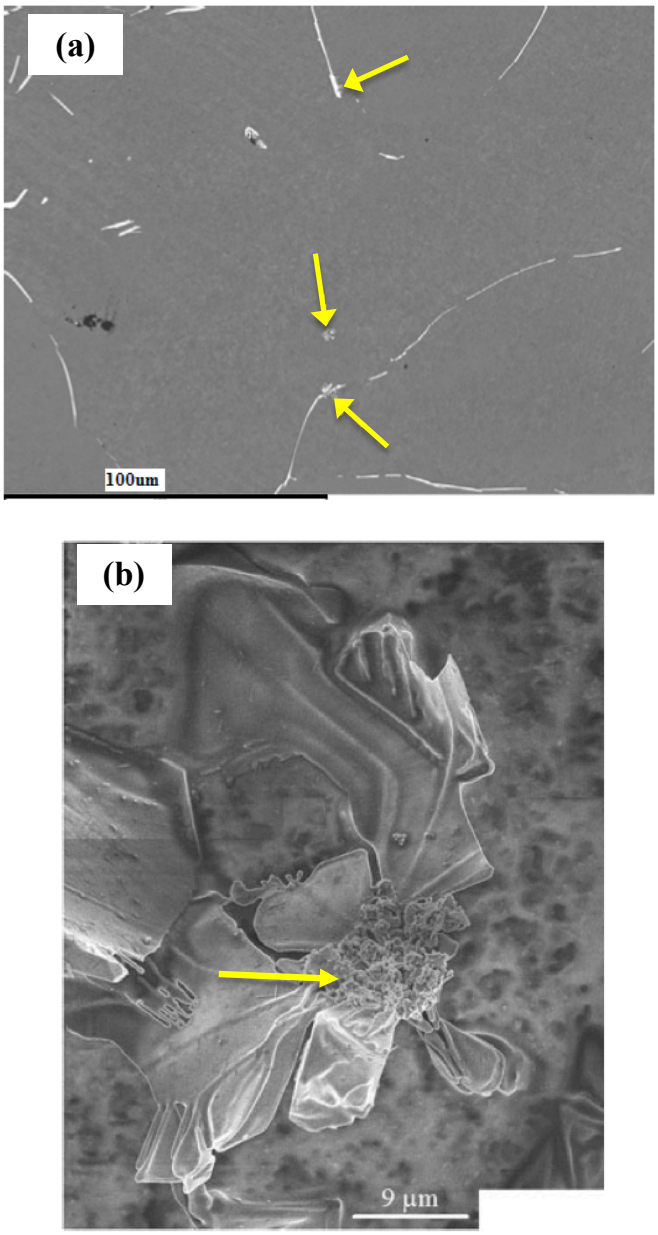


Figure 2.22: (a) Backscattered SEM micrograph showing three Ti-rich regions (yellow arrows); two of which are associated with the AlFeSi-phases while the third is located within the α-Al grain, and (b) SEM micrograph of an extracted phase with a Ti-rich cluster (identified with a yellow arrow) [76]

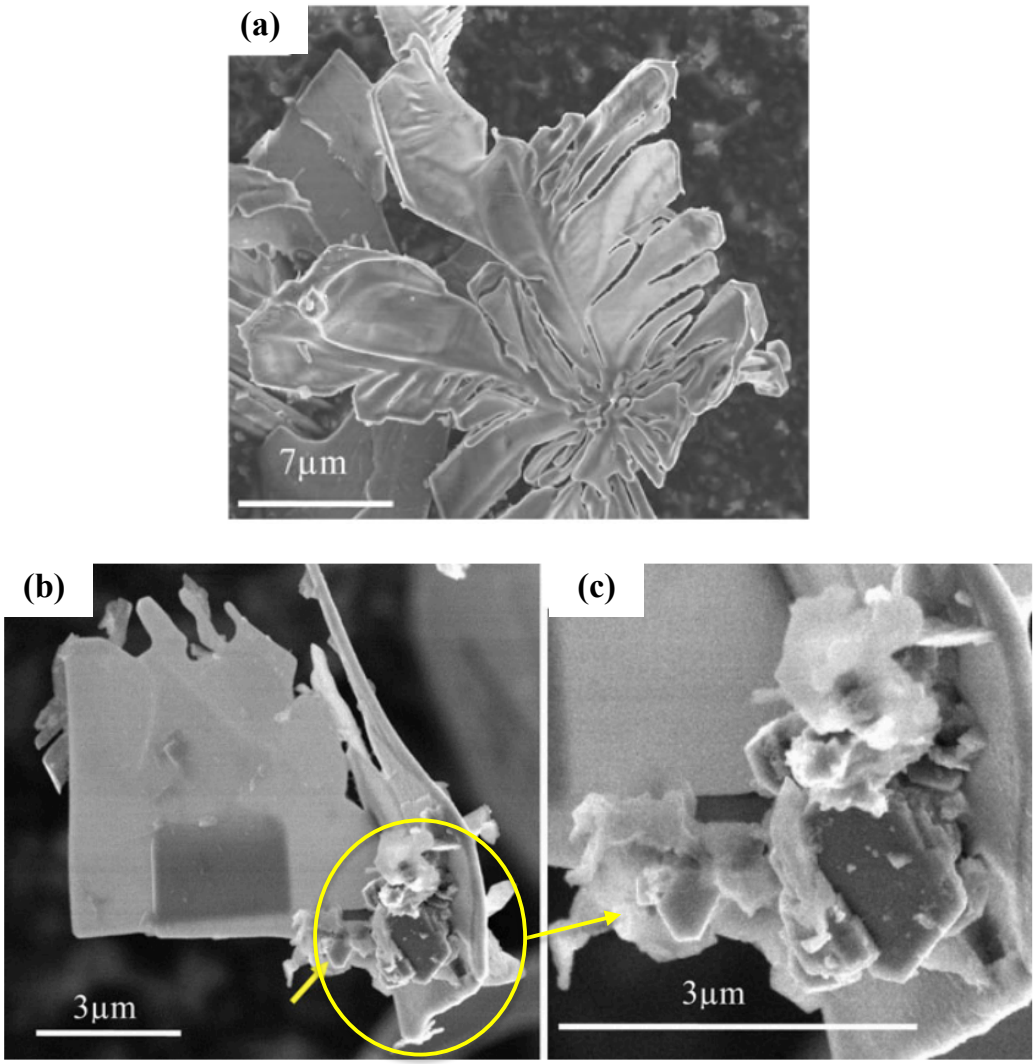


Figure 2.23: FEG-SEM micrographs of (a) dendritic α_c-AlFeSi phase, (b) plate-like β-AlFeSi phase containing Ti-B particle cluster, and (c) displays the hexagonal morphology of the Ti-B particle cluster at higher magnification [77]

– Allen et al. [91] investigated partially re-melted melt-spun ribbons, and reported that there was no relationship between Ti-rich regions and regions rich in Fe and Si. As they expected Al_3Ti to have dissolved during casting, no attempts had been made to identify boron and it was assumed that the Ti-rich regions were most likely displaying TiB_2 particles.

– A characterisation study carried out by Kumar et al. [77] reported that several Ti-rich particle clusters were related to α_c-AlFeSi and β-AlFeSi phases:

(a) EDS analysis carried out on the multi-faceted α_c-AlFeSi particle growing outwards from the centre point, shown in Figure 2.23 (a), displayed the presence of Ti-rich particles at the centre, indicating possible nucleation site;

(b) A plate-like β-AlFeSi particle displayed the presence of a Ti-rich particle cluster, shown in Figure 2.23 (b-c), indicating possible nucleation event.

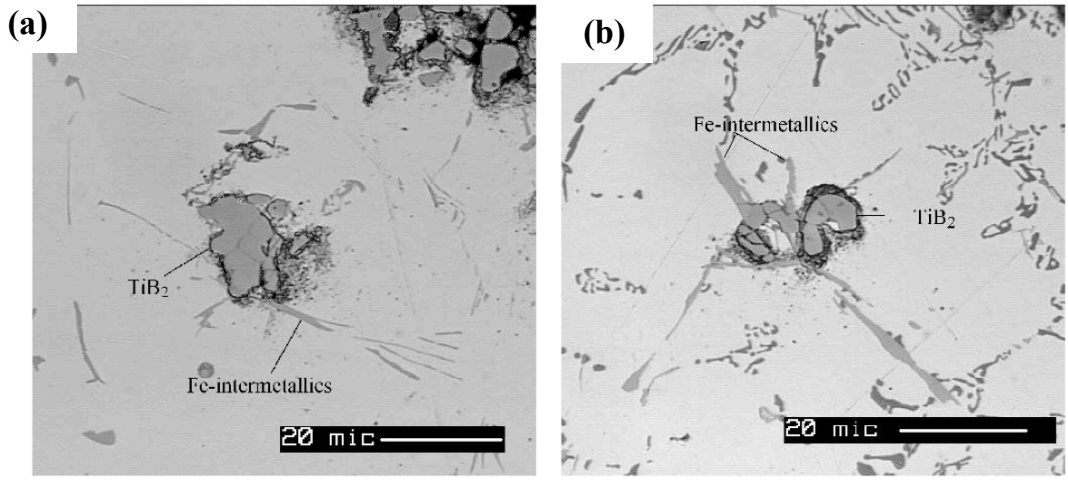


Figure 2.24: Optical micrographs displaying Fe-phases in association with TiB_2 particles (a) at the interdendritic regions and (b) inside an α-Al grain [92]

– Khalifa et al. [92] gas injected TiB_2 particles into the melt, and reported observing those particles both in α-Al grains and in the interdendritic regions (examples shown in Figure 2.24). Based on the assumption that physical contact between the particles and the Fe-bearing phases displayed an indication of nucleation initiated by the particle, it was concluded that TiB_2 did not have a significant impact on the nucleation of either α-AlFeSi and β-AlFeSi phases. Furthermore, possible oxide films can be seen to be

associated with the TiB_2 particles in Figure 2.24, which has been reported to nucleate Fe-bearing phases [76].

– Carroll [54] investigated surface re-melted alloys, and reported TiB_2 observations without any obvious characteristic behaviour. TiB_2 clusters were detected (a) at the edge of α-Al grains (Figure 2.25 a), (b) at locations not related to any obvious microstructural feature (Figure 2.25 b), and (c) physically connected to intermetallic particles of α-AlFeMnS (Figure 2.25 c).

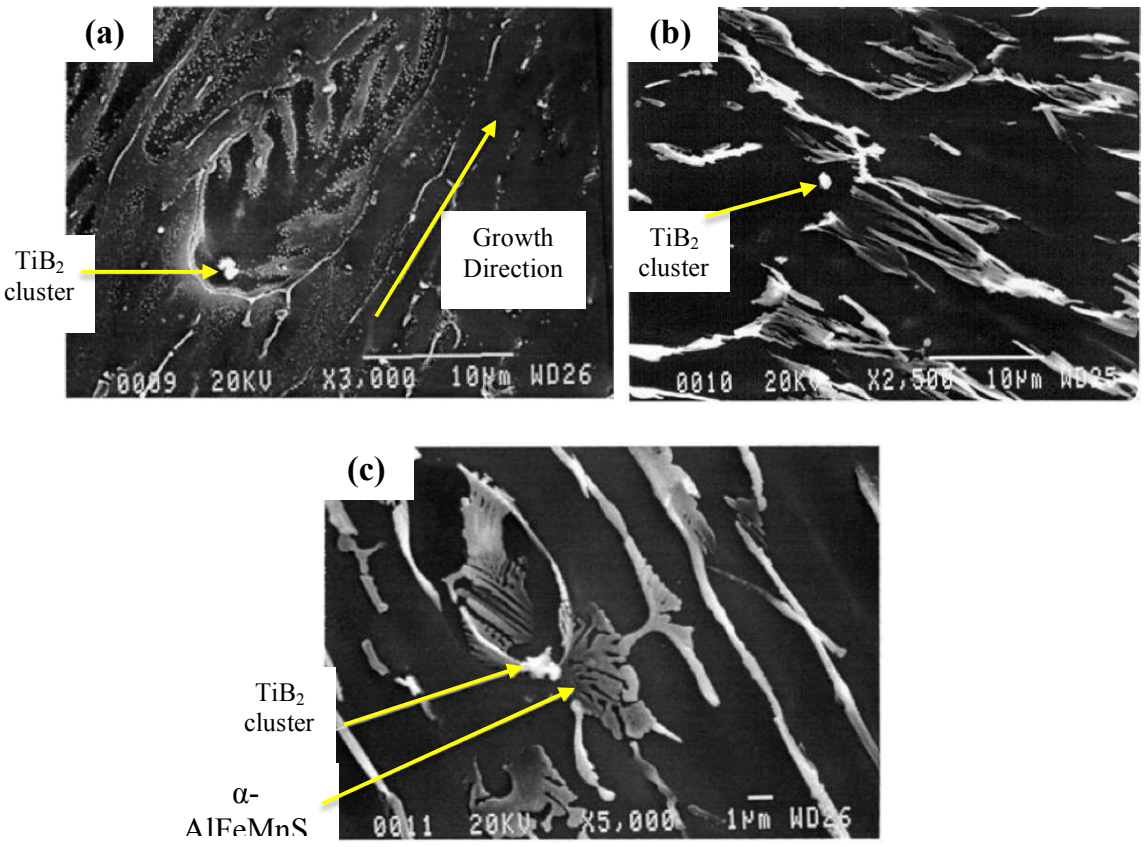


Figure 2.25: TiB_2 particle clusters observed (a) at the edge of primary Al grains, indicating a possible nucleation event, (b) at a location not associated with any microstructural feature, and (c) Physically connect to α-AlFeMnS intermetallic particles [54]

2.4.7 Intermetallic Phase Selection Mechanisms

Although several factors affect the phase selection in a 6xxx Al alloys, the factors that have been recognised to be most important are competitive nucleation, competitive growth, suppression of equilibrium solidification reactions and microsegregation [70]. The competitive nucleation and growth mechanisms discussed in section 2.3 correspond to the α-Al matrix, while the influence of competitive nucleation and competitive growth of secondary intermetallic particles are discussed here.

(a) Competitive Nucleation

It has been proposed that in the absence of impurities, one phase (such as phase A) can kinetically displace another phase (such as phase B), provided the nucleation temperature (T_n) fulfils the condition $T_{n,A} > T_{n,B}$ and they can both form under the given solidification conditions [93]. It can be summarised that competitive nucleation encourages the formation of phases with higher nucleation temperatures.

(b) Competitive Growth

It has been proposed that one phase (such as phase A) can kinetically displace another phase (such as phase B), provided the growth temperature (T_g) fulfils the condition $T_{g,A} > T_{g,B}$ and they can both form under the given solidification conditions [93]. If this displacement takes place during a critical growth velocity of U_{crit} or at a critical cooling rate of $(dT/dt)_{crit}$, then at a given temperature gradient of G across the solid/liquid interface, the one dimensional steady-state growth condition (equation 2.22) can define the relationship between the cooling rate dT/dt and the growth velocity U.

$$\frac{dT}{dt} = \frac{dT}{dx} \cdot \frac{dx}{dt} = G \cdot U \tag{2.22}$$

Thus, the relationship between the critical cooling rate and solidification velocity for the displacement of phase A by phase B can be expressed as follows:

$$\frac{dT}{dt_{crit}} = G \cdot U_{crit} \tag{2.23}$$

It can be summarised that competitive growth encourages the formation of phases with higher growth temperatures and / or growth rate.

(c) Suppression of Equilibrium Solidification Reactions

Although DC cast microstructures commonly display Si rich phases, such as eutectic Si and the α-AlFeSi and β-AlFeSi phases, the phases could not have been formed through equilibrium peritectic or ternary eutectic reactions. This is because in a peritectic reaction, the reaction will be taking place at the α-AlFeSi and liquid interface, forming the β-AlFeSi phase and Al (which can be expressed as Liquid + α-AlFeSi → β-AlFeSi + Al). The layer of β-AlFeSi and Al will act as a diffusion barrier between α-AlFeSi and liquid, causing the reaction rate to slow down as the layer thickens. In DC casting, which experiences non-equilibrium solidification conditions, the lack of time for this reaction to reach completion would result in the β-AlFeSi having a core of α-AlFeSi phase.

α-AlFeSi and β-AlFeSi are generally not observed as cored phases in DC casts, and it was therefore assumed that the phases do not form through equilibrium reactions [70]. One of the possible mechanisms, suggested by Langsrud [94], is that the phases α-

AlFeSi and β-AlFeSi precipitate directly from the interdendritic liquid, which has very high solute content. The solidification reactions causing the phases to form metastably are assumed to be pseudoeutectic, and to take place at undercoolings lower than their respective equilibrium peritectic temperatures.

(d) Microsegregation

Solidification conditions are crucial in determining the extent of alloying elements and nucleant segregation into the solute-rich liquid. Some of these parameters include the alloy chemical composition, cooling rate, growth velocity, and the temperature gradient both in the liquid and across the solid/liquid interface. Thus, different solidification conditions give rise to specific combination of intermetallic phases, due to the varied element segregation caused by individual solidification paths and their resultant solidification reactions. Since reliable experimental techniques to monitor element segregation are not yet available, the concept is mainly researched using theoretical modelling.

2.5 ThermoMechanical Behaviour of Al Alloys

2.5.1 Hot Tearing

Hot tears occur at temperatures above the solidus where the solid fraction (f_s) is very high [95, 96, 97, 98]. As an alloy solidifies over a range of temperature, it consists of a mixture of both solid and liquid phases for a considerable amount of time. With increasing solid-fraction, a coherent network is produced by the interlocking dendrite growth [99]. The temperature between the coherent temperature and solidus

temperature was defined by Pumphrey [100] as the brittle temperature range (BTR), and the duration of BTR was correlated to hot tear susceptibility of Al alloys. Hot tear susceptibility was also suggested to be dependent on the percentage shrinkage during BTR, which in turn is dependent on the alloy composition.

Pellini's theory [101] for hot tear formation was strain dependent, where strain accumulation in the liquid film between the networked dendrites causes the tearing of dendrites on volume shrinkage. Rappaz et al. [99] further suggested that on increasing solid fraction, liquid flow gets restricted due to increased viscosity and surface tension, and thus insufficient liquid flow between solidifying dendritic regions may cause pore formation and/or hot tearing [99]. Thus hot tearing is promoted where the solidification time is longer, as the alloy remains in the vulnerable state for a prolonged period [102]. It was also proposed that hot tears form under tensile loading [99]. Further studies have indicated that hot tear susceptibility of Al can be affected by the interdendritic liquid morphology, grain size and impurity content, along with the strength development during solidification and semisolid mechanical properties [78,102,103]. Figure 2.26 shows a micrograph of a typical hot tear fracture surface.

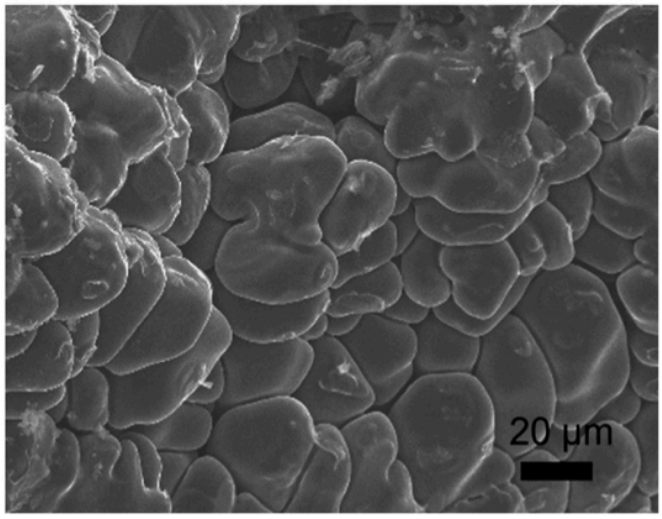


Figure 2.26: SEM micrograph of a typical hot tear, observed in an AA6056 displaced at the speed of 0.4mm s^{-1} [104]

2.5.2 Criteria for Predicting Hot Tear Formation

Over the last 35 years, various criteria have been formulated to explain the mechanisms involved in hot tearing, and predict its formation. The criteria to predict hot tearing can be divided into three main categories; mechanical criteria, non- mechanical criteria, and combined mechanical and non-mechanical criteria.

(a) Mechanical Criteria

In 1962, Prokhorov [105] proposed that hot tears form if the equation 2.24 condition is met. His assumption included low ductility of alloys during BTR.

$$\dot{\varepsilon}_{\min} \leq \dot{\varepsilon}_{free} + \dot{\varepsilon}_{app} \tag{2.24}$$

Where $\dot{\varepsilon}_{\min}$, $\dot{\varepsilon}_{free}$ and $\dot{\varepsilon}_{app}$ represent fracture strains of the mushy zone, free shrinkage and apparent strain rate respectively. Novikov [106] suggested that hot tear

susceptibility is dependent on shrinkage strains within the mushy zone and fracture strain of the mushy zone.

(b) Non-Mechanical Criteria

Feurer [107], in 1976, proposed that hot tearing forms at pores formed due to insufficient liquid flow into interdendritic openings, which in turn is caused by solidification shrinkage. His criterion however ignored possible influences from both thermal shrinkage and external forces.

In 1981, Clyne and Davies [96] put forward an alternative criterion for hot tearing, where it was assumed that hot tears are caused by uniaxial tension developed during the final stage of freezing. Campbell [97] and C. Davidson [108] both agree with this criterion. Solid fraction, f_s, was a crucial parameter for Clyne and Davies' [96] analysis. They suggested that when strain developed in the earlier stage of liquid and mass feeding, where solid fractions are low ($0.10<f_s<0.90$), the casting is able to fully accommodate the strain. However, during the freezing stage where solid fractions are higher ($0.90<f_s<0.99$), the dendrites formed interlock with each other obstructing grain movement, and therefore strain accumulates. The cracking susceptibility coefficient (CSC, equation 2.25) was developed based on these assumptions.

$$CSC = t_V / t_R \tag{2.25}$$

Where t_R represents the length of time where the process of stress accommodation (also known as stress-relaxation) is dominant, and t_V represents the length of time where the

material is vulnerable to cracks. However, the criterion cannot provide a quantitative assessment of hot tear susceptibility, and is therefore limiting.

(c) Combined Mechanical and Non-Mechanical

Soon after, Katgerman [98] combined the criteria proposed by both Feurer [107] and Clyne and Davies [96], along with a model of heat flow that characterises the DC casting technique. Modifications, however, were made to Clyne and Davies's criterion [96], where a variable 'critical solid fraction' (f_{cr}) was introduced to account for the boundary between the two processes of strain-relaxation and strain accumulation. So ($0.10<f_s<0.90$) was modified to ($0.40<f_s<f_{cr}$), and ($0.90<f_s<0.99$) to ($f_{cr}<f_s<0.99$). The new model could be used to calculate solid fractions at the centre of a DC cast billet along the axial direction at every increment of time, while equation 2.26 was developed to calculate the hot cracking index (HCI).

$$HCI = \frac{(z_{0.99} - z_{cr})}{(z_{cr} - z_{0.40})} \tag{2.26}$$

Where z represents the distance along the axial direction, from the billet bottom up to length of specified solid fraction, and $z_{0.40}$, $z_{0.99}$ and z_{cr} represents solid fractions of 0.40, 0.99 and critical solid fraction (f_{cr}) respectively. Katgerman et al. [98] observed the HCI to be sensitive to alterations in alloy composition, processing parameters (for example casting speed) and microstructure. The model however was not comprehensive as it only provided a qualitative measure of hot tear susceptibility.

Rappaz et al. [99] developed a two-phase model for hot tear formation, namely Rappaz-

Drezet-Gremaud (RDG) criterion, where they assumed strain rate to be consistent along the perpendicular direction of the primary dendrite arms. The RDG criterion accounts for the combined effect of both fluid flow and the solid network deformation. The critical pressure drop in the mushy zone is used to characterise hot tear nucleation. M'Hamdi [109] modified the RDG criterion to accommodate the mushy zone rheology, allowing more accurate measurements of strain development to be taken during solidification.

Campbell [97] has brought forward quite a different perspective on the mechanisms involved in hot tearing. Al oxidises instantaneously on exposure to oxygen, and this results in continual formation of an oxidised film while processing temperatures are above the solidus. On experiencing turbulence (such as stirring, etc.), the melt is liable to fold in on itself through waves breaking or splashed out droplets merging back into the bulk. Since oxide films are present on most surfaces of molten Al, folding on itself creates a 'bifilm'. Bifilm describes the entrained film suspended in the melt as double oxide films, where the dry surfaces of the films are facing each other. Due to Al oxide being almost inert, the dry surfaces of the bifilm fail to bond sufficiently, resulting as a crack in the bulk liquid. The number of entrained bifilms increase rapidly with each disturbance in the melt and/or melt pouring. Additionally, Al oxides are very stable and therefore the bifilms introduced remain suspended within the melt for significant amounts of time, causing various defects in the final material. According to Campbell, the presence of bifilms cause most of the normal metallurgical defects in Al alloys [97].

Campbell [97] describes hot tear formation as the opening of entrained bifilms, and that hot tears therefore grow along the bifilm. He further suggests that bifilms are pushed

and flattened into intergranular spaces during columnar grain growth, and hot tears therefore should be expected along these regions. He also claimed that dendrites never grow across a bifilm as they are not able to grow through air, and therefore the hot tear fracture surface should only contain a layer of Al oxide.

Contradicting Campbell's theory, Lin et al. [78] observed second phase particles on hot tear fracture surfaces of AA1050, AA3104 and AA5182. Figure 2.27 (a) and (b) shows two of the SEM images. Haaften et al. [5] had also observed secondary intermetallic phases on the hot tear fracture surface of AA5182 alloy.

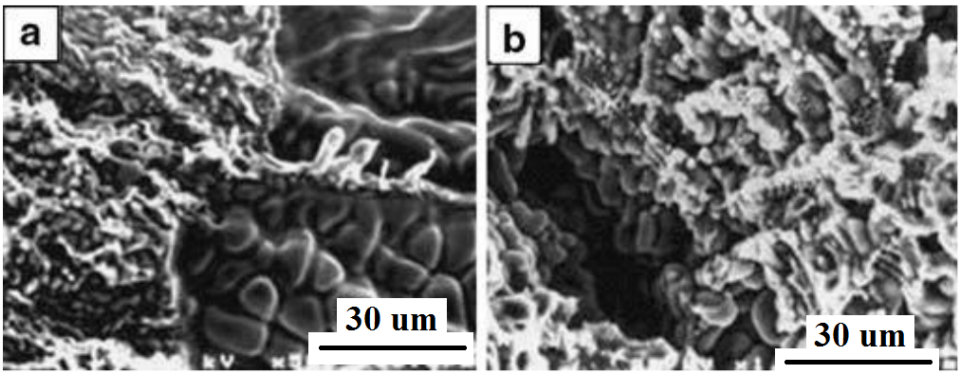


Figure 2.27: SEM micrograph of (a) AA1050 hot tear fracture surface partially covered with intermetallic phases, and (b) hot tear fracture surface of AA5182 covered with intermetallic phases [78]

The presence of intermetallic phase was observed to be dense around the hot tear regions compared to other dendrite boundaries [78]. Two possibilities were attributed to this observation: (i) liquid present in the final stages of solidification may have provided intergranular feeding or caused hot tear healing, and (ii) local concentration

of intermetallic phases may have caused hot tear initiation. Thus further investigations are required to understand the absolute mechanisms of hot tearing.

2.5.3 Semisolid Tensile Tests

The semisolid tensile test methods can be divided into two main groups; solidification and remelting [102]. 'Solidification' is when the molten test alloy is subjected to freezing to a temperature below the liquidus, and 'remelting' is when the test alloy is subjected to heating to a temperature above the solidus. Solidification test methods can be further categorised into two groups; one group where cooling continues along with the test, while the other group is where the conditions are isothermal, that is, the sample is cooled to a certain temperature before tests are carried out [102]. Thus, the structure attained varies depending on test methods, and the results vary accordingly.

(a) Solidification

Ackermann and Kurz [110] developed a novel instrument that allowed in situ observation of the solidifying alloy during tensile testing. The instrument design consisted of two copper cylinders, each with a separate water circuit maintaining the temperature. The cylinders were then immersed into molten alloy, allowing the alloy to solidify on the cylinder surface creating a shell. These water-cooled copper cylinders initially remained in contact, acting as one structure. Once the solidifying shell acquired the desired thickness, the cylinders were separated from each other at a constant displacement rate ranging from 3.5×10^{-3} to $2.17\times10^{-1}s^{-1}$, subjecting the shell to tensile strain. There were, however, large temperature gradients in the test alloy and therefore the results cannot be correlated to an absolute temperature and solid fraction.

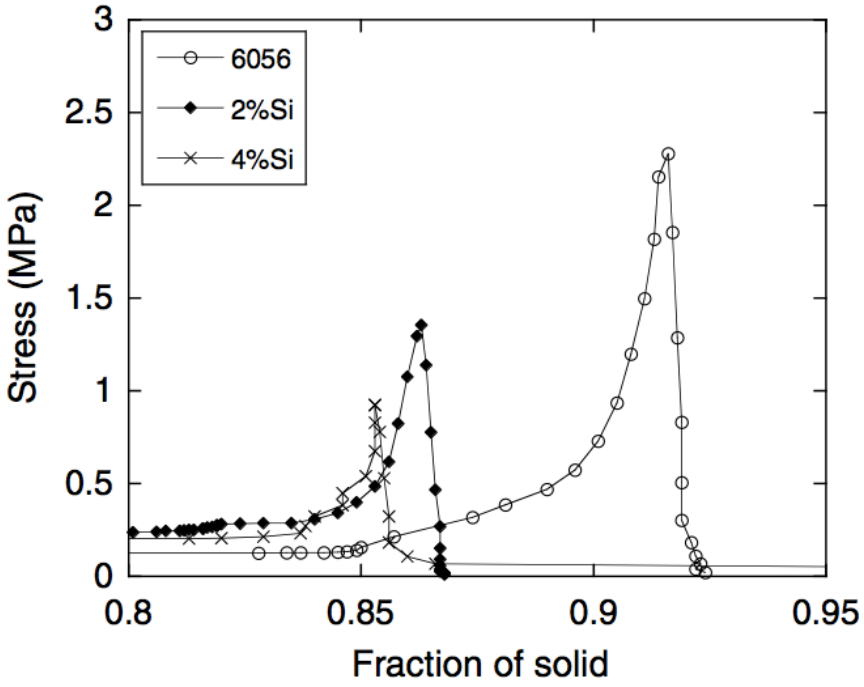


Figure 2.28: Stress against temperature during non-isothermal tensile test with varying Si content, sample prepared with cooling rate of 70 Ks^{-1} [104]

Fabrègue [104] used a novel apparatus to examine the mechanical properties of AA6056 based alloys during solidification, in non-isothermal tensile conditions. The tests were carried out with varying cooling rates and alloy compositions, and it was observed that these parameters determine the critical speed for rupture to occur in the semisolid state. Figure 2.28 shows that with increase in Si content, a more brittle failure was observed, and the alloy exhibited a decrease in the maximum stress at which it fractured. The occurrence of two possible mechanisms were attributed to this behaviour; (a) additional energy may be required to build intergranular bridges between the primary aluminium phase (α-Al) and eutectic liquid, and (b) Si rich eutectic intermetallic phases may be rather brittle. Neither theory was confirmed so further studies are required.

(b) Remelting

Tensile thermomechanical simulators, such as GleebleTM 1500 and 3500, have been used in recent years to examine the strength and ductility of remelted semisolid Al alloys [111]. The GleebleTM has several advantages, one being able to melt the test alloy using direct resistance heating [112]. It was found that slow heating of the test alloy, which is usually the case for conventional furnaces, can cause solute to diffuse back and disperse from the eutectic phases in the as-cast structure [113]. However, the test alloy can be heated as rapidly as $10{,}000^{o}Ks^{-1}$ using the Joule heat from the GleebleTM [112]. Additionally, it has the capability to retain the desired shape of the molten test alloy as well as providing more control over the stress and strain that is applied [102]. Some of the drawbacks of GleebleTM, however, are that the equipment is very bulky and expensive.

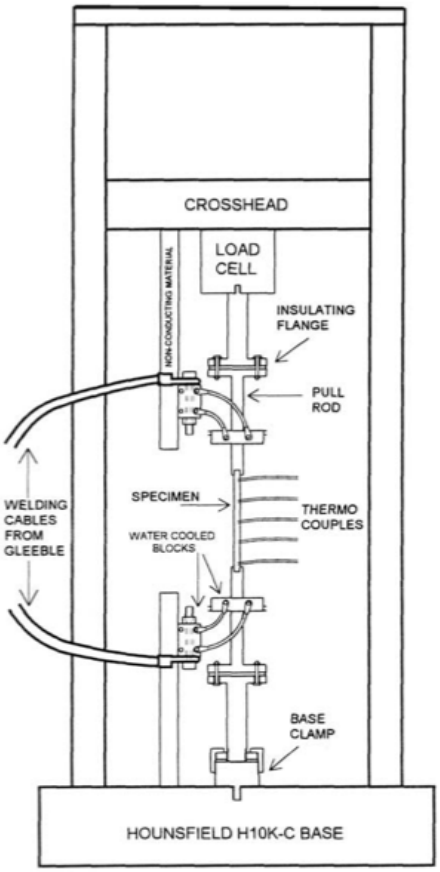


Figure 2.29: Schematic of test rig developed by Spittle et al. [113]

Spittle et al. [113] used the GleebleTM 1500 for their investigation into the tensile properties of AA2024 alloy. Figure 2.29 shows a schematic of their apparatus. The electrical current from GleebleTM was transferred through to the test rig via the welding cables, which in turn were connected to the water-cooled copper blocks. These series of connections were made to avoid connecting the welding cables directly to the load train, as the weight of the welding cable may have affected the load measurements. Spittle et al. [113] observed that the mechanical properties of casting and wrought alloys varied significantly, as shown in Figure 2.30.

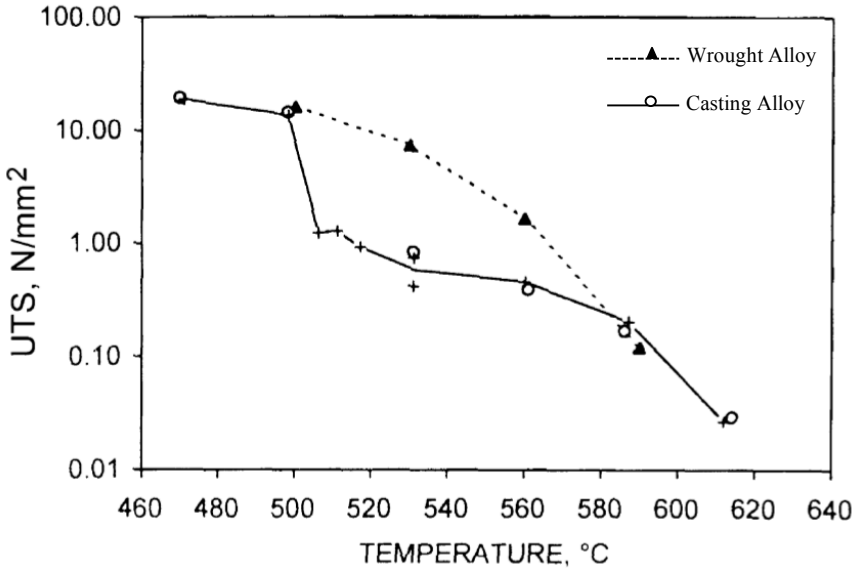


Figure 2.30: Variation in tensile strength of casting and wrought alloys during solidification [113]

They found that the tensile strength of the wrought alloy decreased more gradually in comparison to that of the casting alloy, which displayed a rapid reduction after about 500ºC. The temperature corresponding to the tensile strength drop in the casting alloy displayed a rapid rise in liquid fraction, while a more gradual increase in liquid fraction was observed for the wrought alloy. Thus it was suggested that the amount of liquid fraction has a significant effect on the mechanical properties of a semisolid alloy. The investigation carried out by Haaften et al. [114] agreed with this theory, as he also noticed a reduction in tensile strength with increasing liquid fraction. Haaften et al. [114] used the GleebleTM 3500 for their tests, examining AA3104 and AA5182 with strain rates ranging from 3×10^{-5} to $1\times10^{-3}s^{-1}$.

A novel tensile apparatus using a GleebleTM 3500 was developed by Colley et al. [115] based on Spittle's instrument design [113]. The effect of varying temperature and strain rate was investigated in a 5182 aluminium alloy, and the results are shown in Figure

2.31. Colley's results [115] are in agreement with Spittle [113] and Haaften's [114], where an increase in temperature exhibited a decrease in the tensile properties of the alloy, which can be attributed to the decrease in solid fraction.

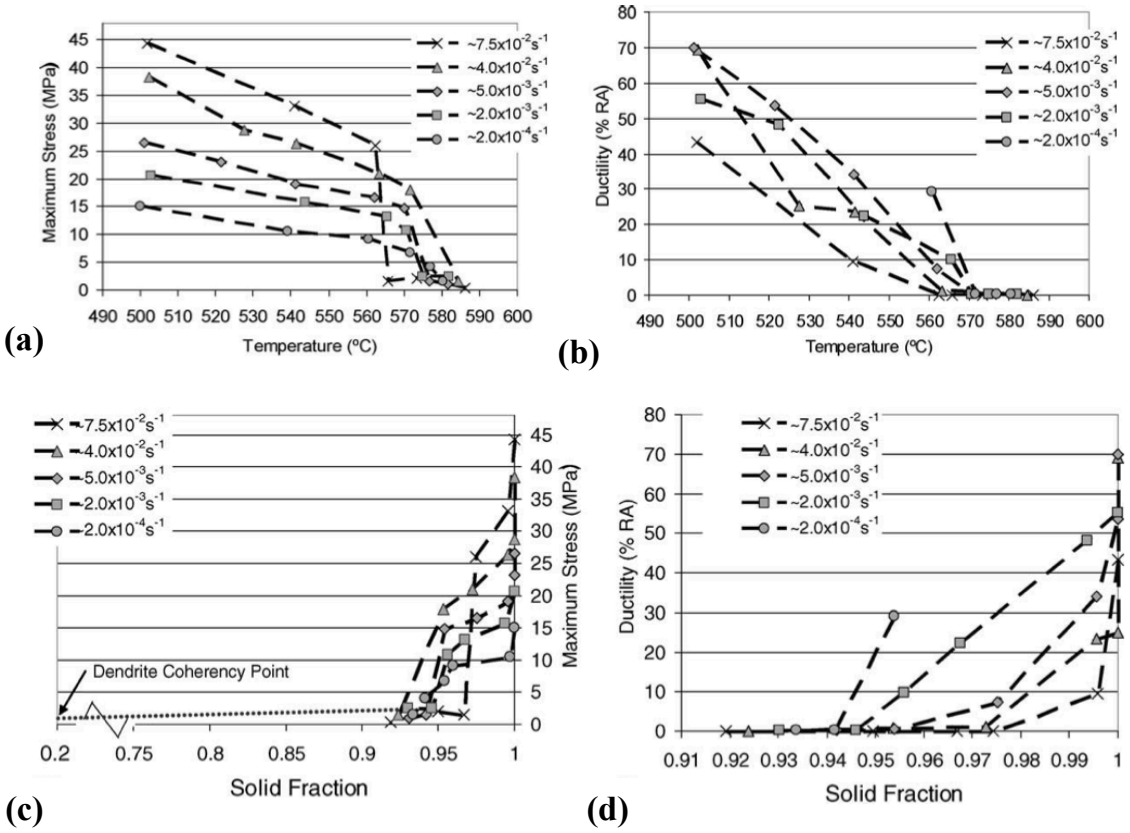


Figure 2.31: Variation in (a) tensile strength with temperature, (b) ductility with temperature, (c) maximum stress with solid fraction, and (d) ductility with solid fraction of 5182 alloy [115]

2.5.4 Development of Tensile Strength at Elevated Temperatures

Pure metals in the solid phase transform to liquid at a specific temperature, whereas alloys transform over a range of temperatures consisting of both solid and liquid phases for a considerable amount of time. Thus, while the mechanical strength of pure metals drop to zero beyond melting temperatures, alloys heated above their solidus

temperatures exhibit significant amounts of strength up to a certain temperature [116]. The lowest temperature at which the tensile strength is still zero is defined as the 'zero strength temperature' (ZST), and the lowest temperature at which the ductility is still zero is defined as the 'zero ductility temperature' (ZDT) [117]. The ZST for some aluminium alloys have been observed to be 5-30ºC above the solidus temperature [116].

While investigating into the tensile properties of semisolid aluminium alloys, James et al. [118] also examined the ZSTs on remelting samples. The observed ZST for AA6061 alloy corresponded to a solid fraction of approximately 0.85, and for AA2024 and AA5083 to about 0.70. Nagaumi and Umeda [119] subjected a solidifying AA6061 alloy to tensile stresses at elevated temperatures, and observed the ZST corresponding to a solid fraction of about 0.70, which is significantly lower than James's observation [118]. Nagaumi and Umeda [119] measured the ZDT as corresponding to a solid fraction of about 0.77.

Fabrègue et al. [104] measured the ZST and ZDT of a 6056 aluminium alloy under solidifying conditions (the details of the procedure has been discussed section 2.5.3a). The ZST was observed as corresponding to a solid fraction of 0.90 to 0.95, and the ZDT was observed as corresponding to about 0.95 to 0.98. Both ZST and ZDT values are high in relation to James [118], and Nagaumi and Umeda's observation [119]. Phillion et al. [120] observed the ZDT of a 6111 aluminium alloy to correspond to a solid fraction of 0.99, which agrees very well with Fabrègue's findings [104]. Phillion [120] also suggested that there is a possibility that the difference in alloy composition might have an effect on the solid grain morphology, which in turn will affect the tensile properties of the semisolid alloy.

2.5.5 Alloy Composition

The effects of excess Si was investigated by Fabrègue [104], and has already been discussed section 2.5.3(a) Knuutinen [103] investigated into the effects of altering alloy composition on the porosity formation. An A356.0 alloy was modified with barium (Ba), calcium (Ca), yttrium (Y) and ytterbium (Yb) systematically. It was found that an increasing amount of Ba produced more refined pores, that were better distributed throughout the casting. Ca and Y additions exhibited a more dispersed and reduced amount of hot tearing, while an increase in porosity was observed with increasing amount of Y. The effect of adding Yb was very similar to that of Ba, except that pores were observed to be relatively smaller and fewer in number.

There is a possibility that additions of alloying elements may change the hydrogen solubility, amount of hydrogen and inclusions in the casting, surface tension, and solid and liquid densities [103]. However, further investigations are required in these fields as present data are very limited.

2.5.6 Post Hot Tear Fracture Surface Examinations

Haaften et al. [5] investigated an AA5182 alloy in tension, testing the alloy at temperatures ranging from 500-580ºC. The test alloy was rapidly reheated at a rate of $50ºKs^{-1}$ using a Gleeble^{TM} 3500. A low strain rate of $3\times10^{-3}s^{-1}$ was applied. The results from these tests were compared with an industrial AA5182 ingot, and significant similarities were observed between both fracture surfaces, including intergranular

fracture, secondary cracks on the side of the main fracture, liquid films, solid bridges, as well as grain size. It was suggested by Haaften [5] that hot tears initiate at weak areas such as at cavities or partially liquid grain boundaries, and then propagate by separation of fluid film around the interdendritic regions. Investigations carried out in the past [107,121] also agree with these suggestions.

2.6 Summary

From the studies discussed in this section, it can be concluded that chemical composition of 6xxx Al alloys has a significant effect on both the grain size and intermetallic phase of the alloy. It is evident that additions of Zr encourage the formation of α-AlFeSi, while additions of AlTiB-type grain refiners encourage the formation of β-AlFeSi. AlTiB-type grain refiners also have high growth restriction abilities, which causes significant reduction of the α-Al grain size.

The various semisolid processing techniques display smaller and more equiaxed grains, while no effect on the intermetallic phases have been documented. Park reported that NRC process produce fine, equiaxed grain size regardless of grain refiner additions [4].

It is generally proposed that the AlFeSi-based intermetallic phases form directly from the liquid phase during solidification, and that the most commonly observed phases are cubic α-AlFeSi and monoclinic β-AlFeSi.

Analyses on hot tearing have mainly been carried out in relation to liquid fraction and mechanical strength. However, no direct comparison between the effect of α-AlFeSi and β-AlFeSi on the hot tearing properties of a 6xxx Al alloy has yet been presented.

Chapter 3 Experimental Procedures

3.1 Alloy preparation

Three alloys were chosen for this project, all based around the 6063 aluminium alloys. One alloy was considered as the model alloy or base alloy (BA), and the other two alloys were modifications made to the base alloy with additions of AlTiB-type grain refiner (GR) and AlZr (ZR) to control the intermetallic phase formation. BA was designed to have the nominal chemical composition of Al-0.30Fe-0.50Si-0.40Mg, all in wt.%.

To reduce contamination from equipment, all surfaces expected to come in contact with the molten aluminium, such as crucibles, ladles, stirrers, etc., were coated with Vernacoat 1600 mould wash and dried in a furnace.

3.1.1 Solid Fraction Estimations

MTDATA software was used to estimate the thermodynamic relationship between solid fraction and temperature of the base alloy with the desired nominal chemical composition (Al-0.30Fe-0.50Si-0.40Mg, all in wt.%). The weight fraction of each phase present in the alloy system in the temperature range of 500ºC to 700ºC is shown in Figure 3.1.

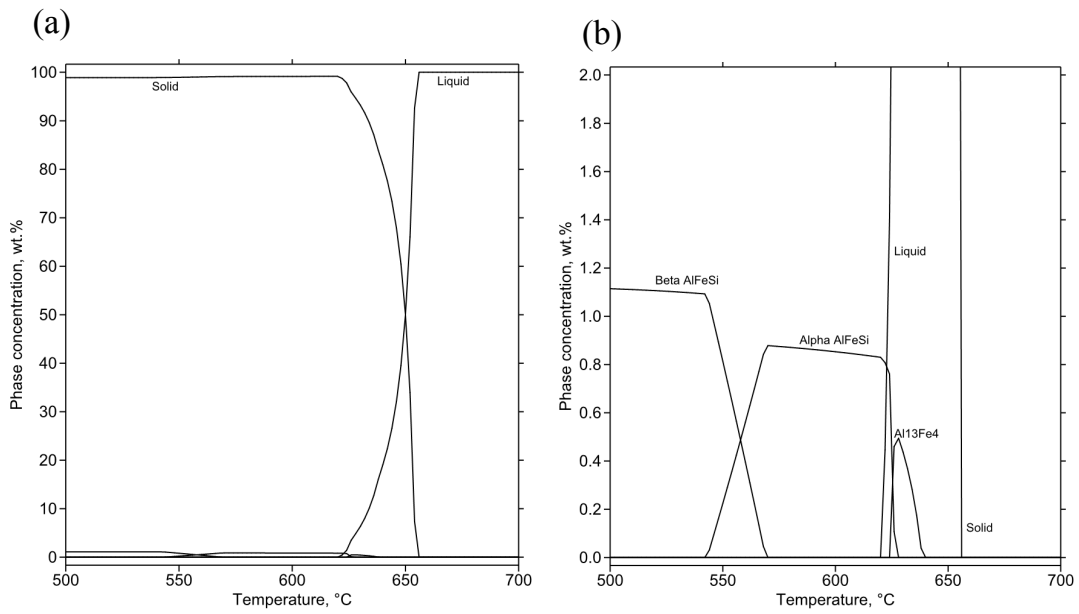
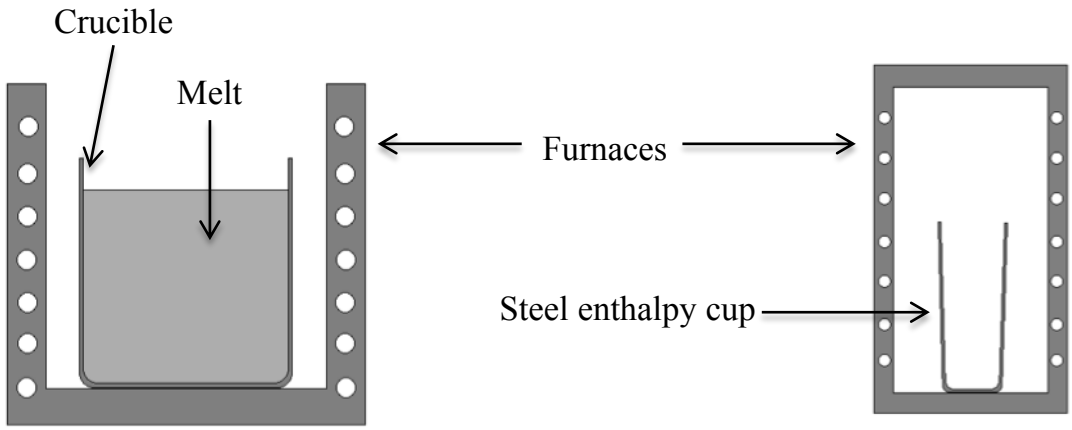


Figure 3.1: Thermodynamic phase diagrams of phase concentration up to (a) 100wt.% as well as (b) 2wt.%, plotted by MTDATA using lever rule calculations, of the base alloy, with the nominal chemical composition of Al-0.30Fe-0.50Si-0.40Mg, all in wt%

3.1.2 Base Alloy (BA)

The processing technique employed for this investigation was developed in-house to replicate the alloy properties of NRC-processed 6xxx Al alloys (details of process can be found in Section 2.2.2 b), but on a smaller scale. A schematic of the procedure used is shown in Figure 3.2.

(a) Melting and preheating the enthalpy cup



(b) Adding alloying element

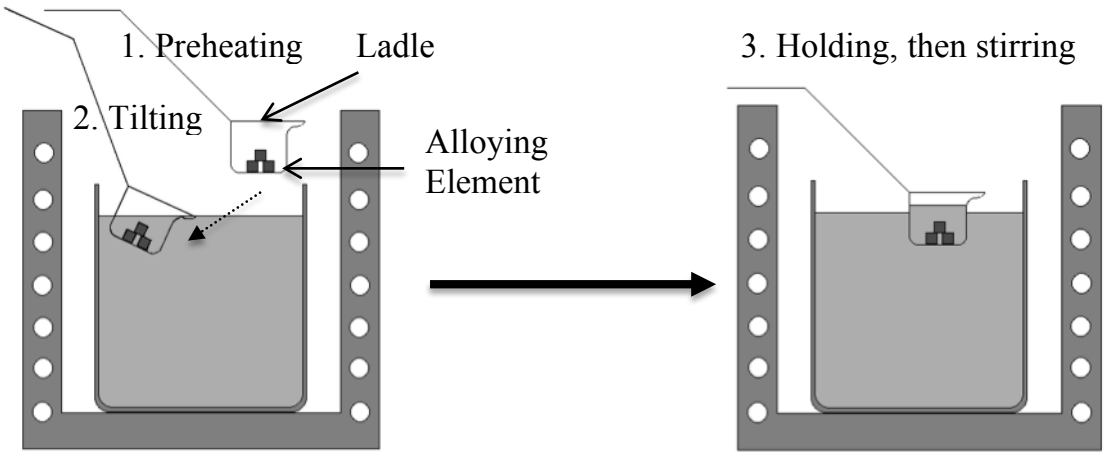


Figure 3.2: (a)-(c) Shows the schematic diagrams of the slurry making process (not to scale).

(c) Processing the Alloy

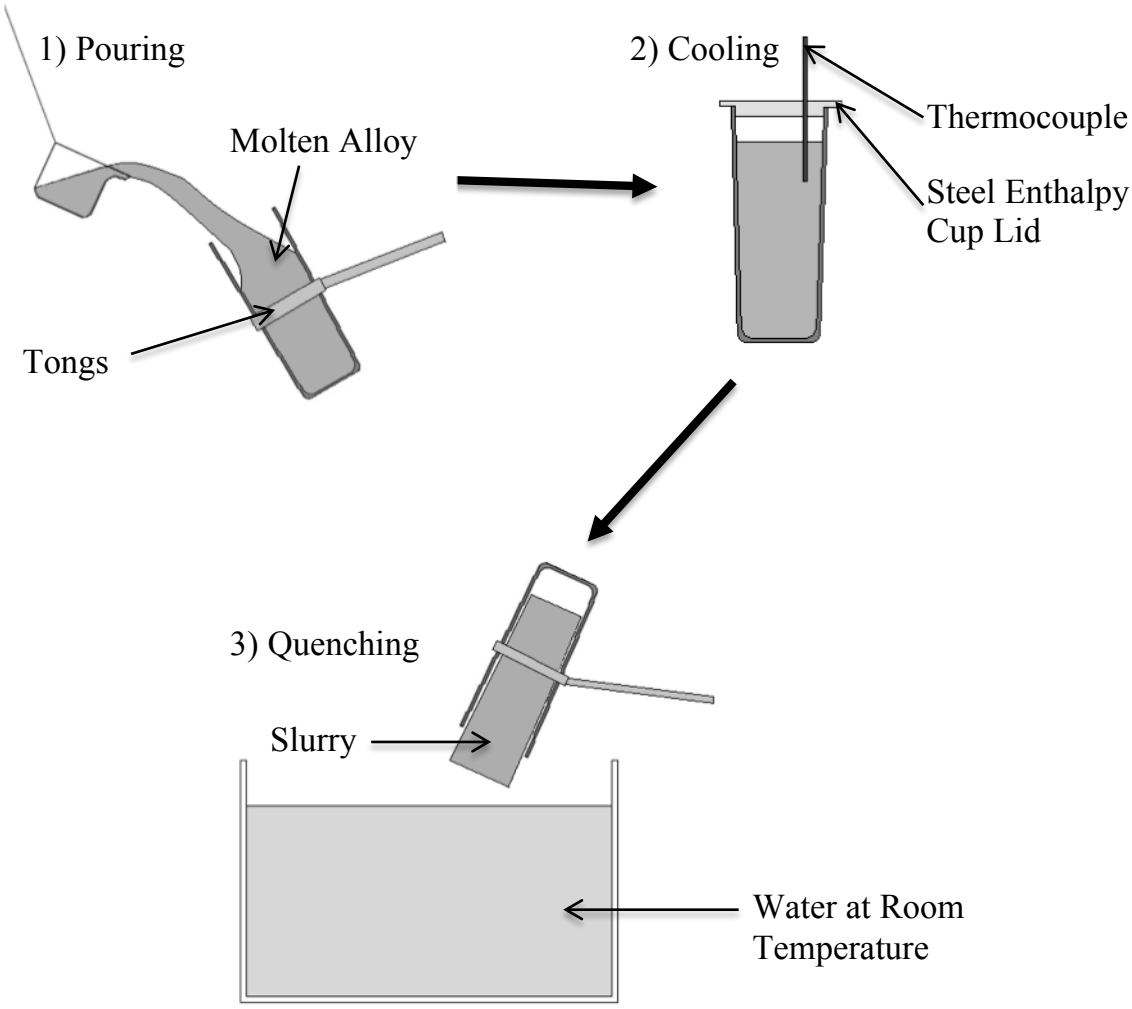


Figure 3.2**: Continued**

All the master alloys and grain refiners used in this investigation were supplied by London and Scandinavian Metallurgical Co. Ltd. (LSM). Commercially pure aluminium (99.97wt.%), and master alloys 20wt%Al-80wt%Fe and 50wt%Al-50wt%Si (produced on a super-purity aluminium base) were heated in an electric resistance furnace using a boron-nitride coated clay graphite crucible. The temperature was held at 400±10ºC overnight, before raising and maintaining it at 750±10ºC to melt the metals. The temperature was carefully monitored with an external K-type

thermocouple inserted 75 to 100mm into the melt. Once the metals had melted, additions of 99.9wt%Mg were made to add Mg to the mix, stirring the melt at regular intervals to improve the dissolution and uniformity of element distribution.

The melt was then cooled to 730ºC, and once the temperature was consistent, molten alloy was ladled into a pre-heated (at 200ºC) steel enthalpy can and sealed with a steel lid pre-heated to the same temperature to reduce variations in temperature gradient through the mould wall. The steel enthalpy can was 185mm high with a wall thickness of about 2.5mm, and an internal radii of 35mm at the top and 30mm at the bottom. The temperature of the liquid inside the steel enthalpy can was monitored using a K-type thermocouple inserted through a hole in the can lid, located at a distance of about 7.5mm from the can centre. To reduce error margins caused by variations in temperature gradients, the tip of the thermocouple was maintained at a height of approximately 150mm from the base of the steel enthalpy can. By the time the melt was transferred from the crucible to the steel enthalpy can, the temperature of the melt had dropped from ~730ºC to ~650ºC. The temperature of the melt inside the steel enthalpy can was allowed to cool down to various temperatures before quenching it in cold water. It was observed that the samples quenched at temperatures greater than 635ºC deformed significantly on hitting the water-tank floor. Based on MTDATA analysis, the alloy is expected to be 90vol.% solid at 635ºC.

Thus, the melt inside the steel enthalpy can was allowed to cool down to 635ºC before quenching it in water at room temperature. This loss in heat took place rather rapidly, and therefore the time taken for the temperature to drop from ~650ºC (solid volume fraction of 50%) to ~635ºC (solid volume fraction of 90%) could not be recorded

accurately. To better understand the impact of mould temperature on phase selection, an additional slurry was produced using steel moulds pre-heated to 400ºC.

3.1.3 Grain Refined Alloy (GR)

Grain refiner additions containing Ti and B were made using Al-5wt%Ti-1wt%B master alloy, which were supplied as rods. Since TiB_2 has a weight ratio of Ti:B of 2.21:1, the 5:1 ratio of the master alloy contains more than double the amount of Ti required for all the B present to form TiB_2.

Davidson indicated that additions of Al-5Ti-B type grain refiner can discourage the formation of α-AlFeSi phase while encouraging formation of β-AlFeSi [3]. The relationship between weight percentage of α-AlFeSi and the amount of Al-5Ti-1B type grain refiner is shown in Figure 3.3.

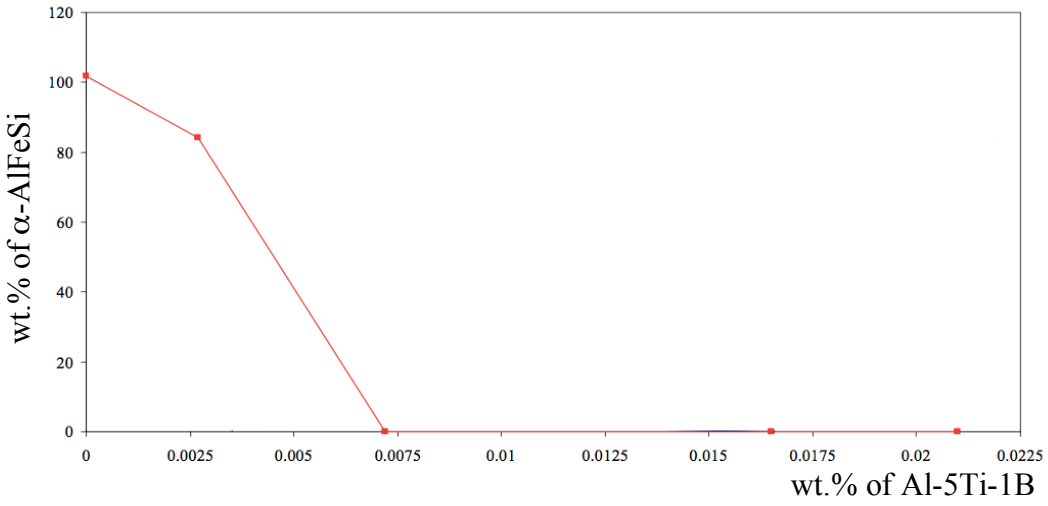


Figure 3.3: Relationship between wt.% of α-AlFeSi and 5:1 AlTiB-type grain refiner [3]

Based on

Figure 3.3 and common industrial practice, the amount of Al-5Ti-1B type grain refiner to add was chosen to be 0.02wt.% for the grain refined alloy (GR).

3.1.4 Zr Containing Alloy (ZR)

For the alloy with Zr additions, Al-15wt%Zr waffle master alloy was used to add 0.1wt.% of Zr into the base alloy. The master alloy was added into the liquid metal, and allowed to mix for several hours before being solidified.

The BA, GR and ZR alloys processed using semisolid technique with steel enthalpy can preheated to 200°C will be identified as BA200, GR200 and ZR200 respectively. The set of alloys processed with enthalpy cans preheated to 400°C will be identified as BA400, GR400 and ZR400 respectively.

3.1.5 Alloy Addition Calculations

The amount of master alloying elements and grain refiner required were calculated based on the final weight percentage desired in the alloy. Since the nominal chemical composition of BA was desired to be Al-0.30Fe-0.50Si-0.40Mg in weight percentage, equations were rearranged and solved to calculate the correct masses of master alloying elements and grain refiners required.

As mentioned in section 3.1.2, commercially pure aluminium (99.97wt.%) was used as the base and master alloying elements Fe, Si and Mg were introduced through 20wt%Al-80wt%Fe, 50wt%Al-50wt%Si and 99.9wt%Mg. 0.02wt.% of AlTiB-type

grain refiner and 0.1wt.% of Zr were added through Al-5Ti-1B grain refiner rods and Al-15wt%Zr waffles. Although only Fe and Si were produced on a super-purity aluminium base, it was assumed that all the aluminium additions made through master alloying elements and grain refiners were of the same composition as the commercially pure aluminium grade used for this project. This assumption should have negligible effect on the overall alloy composition as the total mass of master alloys and grain refiners added equal to 1.3% of the final melt.

36 kg of alloy was prepared, so the required alloying elements were:

– 00.30 wt.% was Fe, so 36 x 0.003 = 0.108kg of Fe;

– 00.40 wt.% was Mg, so 36 x 0.004 = 0.144kg of Mg;

– 00.50 wt.% was Si, so 36 x 0.005 = 0.180kg of Si; and

– 98.80 wt.% was Al, so 36 x 0.988 = 35.568kg of Al.

Thus, the masses of master alloying elements required are:

– Fe (80wt% in master alloy), thus 0.135kg is required, where 0.027kg is Al;

– Mg (99.9wt% in master alloy), thus 0.144kg is required, where 0.000kg is Al;

– Si (50wt% in master alloy), thus 0.360kg is required, where 0.180kg is Al; and

– Al (100wt% purity), thus (35.568 – 0.027 – 0.180) kg = 35.361kg is required.

Given TiB_2 has a weight ratio of 2.21:1 for Ti:B, a significant amount of excess Ti was expected to be present in the resultant GR alloy. Assuming the Al-5Ti-1B grain refiner rods predominantly contain TiB_2, calculating the amount of grain refiner required based on B additions would ensure approximately 0.02 wt.% of TiB_2 additions to GR.

Al-5Ti-1B type grain refiner and Zr were added to 12kg of base alloy, so the required alloying elements were:

– 0.02 wt.% of TiB_2 (which is assumed to be predominant in the grain refiner rod), so 12 x 0.0002 = 0.0024kg of TiB_2. Since the atomic number of Ti is 22 and B is 5, the wt% of B is 31.25 wt% in TiB_2, and the mass of B required is 0.00075kg.

– 0.10 wt.% was Zr, so 12 x 0.0010 = 0.012kg of Zr.

The masses of grain refiner and Zr required are as follows, and the Al additions are considered to be insignificant compared to the total amount of Al in the alloy.

– B (3.91wt% in master alloy), thus 0.01918kg is required to get 0.00075kg of B;

– Zr (15wt% in master alloy), thus 0.080kg is required to get 0.012kg of Zr.

3.1.6 TP-1 sample casts

The standardised industrial test for assessing grain refiner performance in aluminium alloys [122], the TP-1 grain refiner test, was used to compare the microstructure of all three alloys against each other, and against the semisolid cast slurries. The setup, a schematic of which is shown in Figure 3.4, includes:

(a) a mild steel ladle in a truncated cone shape, with a slit on the side to only allow the exact amount of melt to remain (specifications shown in Figure 3.5);

(b) a quench tank with a continuous flow of fresh cold water, where the water flow is being monitored by a flow meter (specifications shown in Figure 3.6).

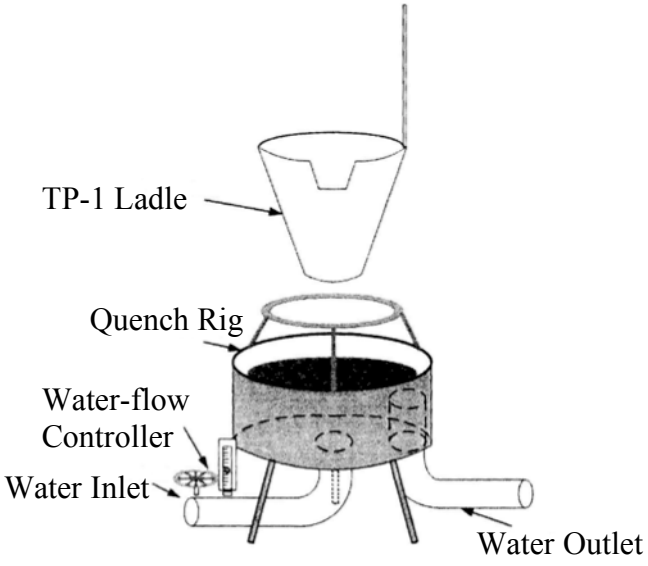


Figure 3.4: Schematic diagram of the TP-1 cooling rig and ladle [122]

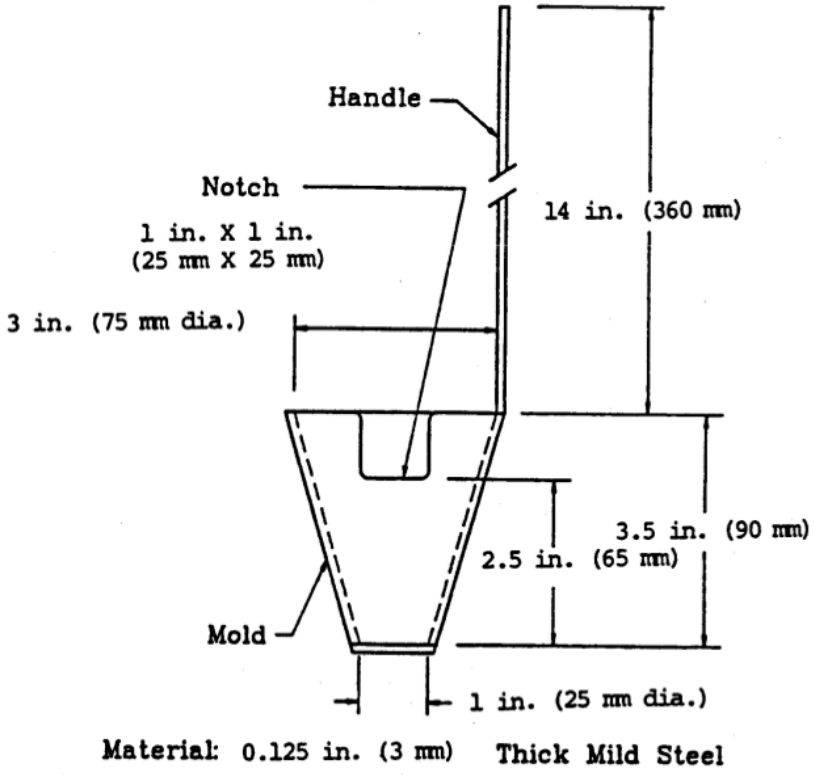


Figure 3.5: Schematic diagram showing the specifications for the TP-1 ladle [122]

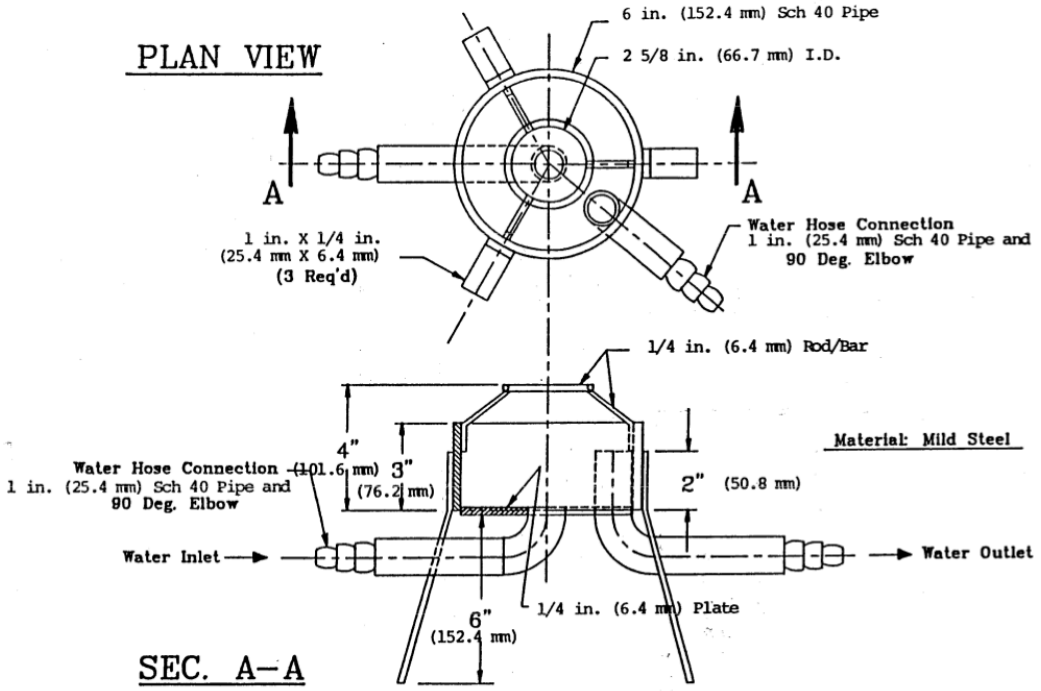


Figure 3.6 Schematic diagram showing the specifications of the TP-1 quench rig [122]

The parameters and procedure specified in the TP-1 standard are described below [122]:

- The mild steel ladle is coated with boron-nitride spray to avoid any interaction with the melt, and preheated to 315ºC;
- The preheated ladle is submerged underneath the aluminium melt, held there for 30 seconds, and then elevated vertically. This ensures the ladle is filled from its base to the bottom of the slit.
- The ladle is then placed on the ring holder of the quench tank, where the melt is cooled at a controlled rate to reflect the experiences of materials from the centre of a direct-chill (DC) cast ingot.
- During cooling, just the base of the ladle gets immersed under the set water flow of 3.78 litres per minute.

– The final samples are generally around 280g in weight (specifications shown in Figure 3.7).

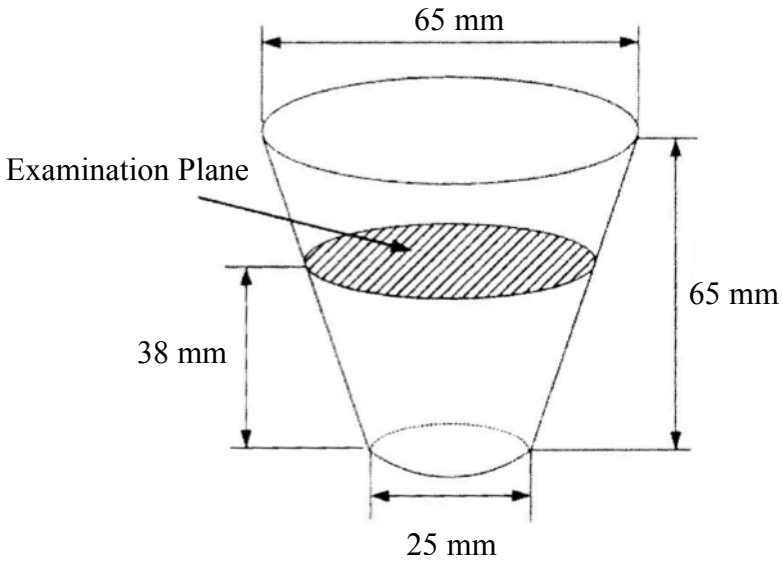


Figure 3.7: Schematic diagram of a TP-1 sample [122]

Some of the parameters however were changed when casting the TP-1 samples for this investigation to ensure they were more comparable with casts produced in earlier projects within the group. The changes that were made are as follows:

– After stirring the melt thoroughly, the TP-1 ladle was heated to a red-hot state by letting its base just touch the melt.
– In the quench tank, the water flow was set at 4 litres/minute, and the samples were quenched in the tank for 90 seconds each.

TP-1 samples of BA, GR and ZR alloys will be identified as BATP-1, GRTP-1 and ZRTP-1 respectively.

3.2 Optical Emission Spectroscopy (OES)

To ensure the desired chemical composition was achieved, each aluminium alloy was examined before preparing the slurries and TP-1 samples. During the alloy preparation stage, a small amount of melt was cooled down to solid state in a chill cast disk mould for non-ferrous alloys, and SiC abrasive paper was used to grind the sample surface to a P800 grit finish. Since the microstructure was not important at this stage, the cooling conditions experienced by the sample was not important.

All measurements were carried out using a Spectrolab LAVFA05A spark analyser, which functions by vaporising a small volume of the sample, resulting in the emission of characteristic radiation from the elements present. The radiation gets converted to intensity counts before it reached the Spectro Analyzer software, which in turn converts it into the element concentrations of the given material.

Ambient conditions, such as the humidity and temperature of the room, affected the spectrometer's performance and results obtained. Thus, the spectrometer was standardised before every session using the standardisation samples provided, and the results were compared with the installation calibration values, which were certified. In case of significant deviations from the original calibration, the Spectro Analyzer software was used to calculate correction factors and apply it to succeeding measurements. To ensure reliability, the chemical composition of each alloy was measured five times, taking the average as the accurate result.

3.3 Slurry and TP-1 Sample Segmenting

To be able to examine and compare the grain structure across the whole sample, each solidified slurry was segmented in half vertically (see Figure 3.8). One half (Part A) was used for phase extraction and X-ray diffraction (XRD). The second half (Part B) was retained for grain structure observations after macro-etching. Once macro-etching analysis was complete, sections (as shown in Figure 3.8) were taken out for micro-etching, scanning electron microscopy (SEM) and thermomechanical analysis (TMA). A few TMA samples were further cut up for DSC analysis. For each solidified slurry, only the height of 165 mm from the bottom was used for microstructure analyses.

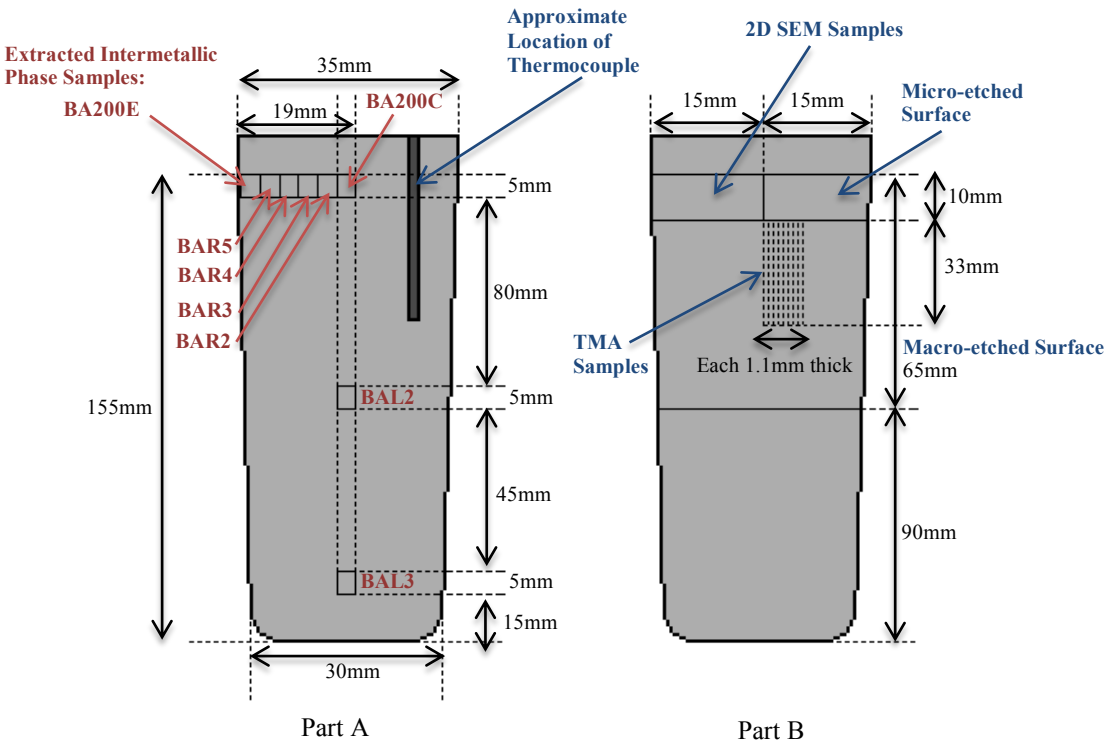


Figure 3.8: Schematic diagram of the solidified slurry segmentation plan (not to scale)

The TP-1 sample examinations were based on previous work carried out by Lui [76]. For TP-1 samples, the generally accepted plane for examinations is the 38 mm horizontal plane from the sample base [122]. However, Lui indicated that cooling rates are almost equal between the horizontal planes 30 to 45mm from the sample base, and therefore the differences in the material's microstructure would be insignificant. Thus, samples from TP-1 casts were taken from within this given range. Each TP-1 cast was segmented into 2 sections (see Figure 3.9); Part A was used for micro-etching, phase extraction, XRD and SEM examinations, while Part B was used macro-etching.

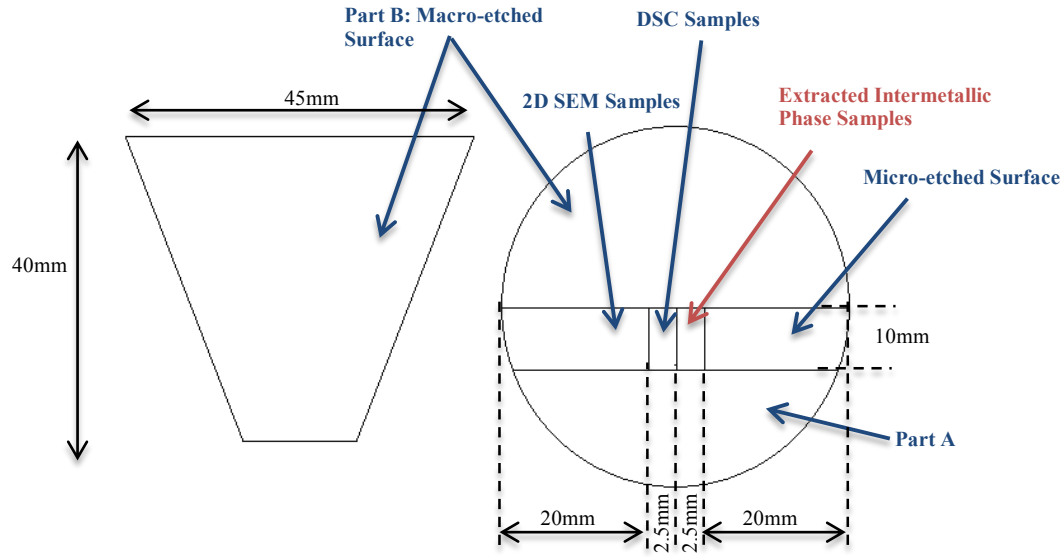


Figure 3.9: Schematic diagram of the TP-1 sample segmentation plan (not to scale)

3.4 Macro-etching

Parts B for each alloy (including slurries and TP-1 casts) were ground to a P1200 grit finish using SiC abrasive paper and macro etched with Tucker's reagent (45% HCl, 15% HF, 15% HNO_3 and 25% H_2O) for 3-4 min, until the grain structure was revealed. The etching process involved soaking a piece of cotton wool in the reagent, and then

wiping the surface continually until the grain structure began to appear. For microstructure observations, a flat-bed scanner was used to scan the macro-etched surfaces immediately after the etching process to minimise oxide formation on the etched surface.

The grain sizes were measured on the cross-sections at approximately 10mm from the top surface of each slurry, using the line-intercept method [123]. Three horizontal lines were drawn at random, going from the centre towards the edge, and the change in grain size was measured in units of 2.5mm, diving the length by the number of grain boundaries intercepting it. The software ImageJ was used for the grain measurements, where the lines drawn for each image were calibrated using the scale provided in the micrograph. Due to the difficulty in accurately measuring the grain boundaries from the macro-etched surface, the averages of 3 readings were plotted in the graphs. The average of two measurements from a point of reference, i.e. either edge or centre, was calculated as an indication of the grain diameter in that area.

The standard plane for examination of TP-1 samples is the horizontal plane measured at 38mm from the base. However, to better understand the grain structures of the sample, the vertical cross-sections of the TP-1 casts were also macro-etched for visual examination and comparison. Thus all the TP-1 casts were vertically sectioned, and then horizontally sectioned at 38-40mm from the base. Both surfaces were macro-etched, and scanned immediately after the etching process to avoid oxide formation on the etched surface. The grain size measurements were only carried out on the 38mm horizontal plane, at every 2.5mm going from centre towards the edge (radially). The averages of 20 readings were plotted in the graphs.

The microstructures were compared to understand the effects of NRC and conventional DC-casting; NRC casting with steel enthalpy cup temperatures of 200ºC and 400ºC; and the additions of Al-Ti-B type grain refiners and Zr to a 6063 aluminium alloy.

3.5 Micro-etching

To compare the grain diameters with the cell diameters of the slurry samples, the cross-section was cut out (shown in Figure 3.8 and Figure 3.9) and mounted in non-conductive Bakelite (phenolic mounting resin). The P1200 grit finish was further polished with diamond suspension in water followed by colloidal silica suspension for 20 minutes. The 5μm and 1μm diamond suspensions were used on Struers 'PA-W' cloth, while the colloidal silica suspension was used with Metprep 'multi' cloth.

A schematic of the set up used to anodise the samples is shown in Figure 3.10. Part of the sample surface was coated with silver dag, and connected to a crocodile clip to act as the anode. The sample was then immersed into Barker's reagent (5ml of Fluoroboric acid in 200ml of water), alongside a cathode (stainless steel) and held for 60 seconds with a voltage of 20V and current of 0.01A.

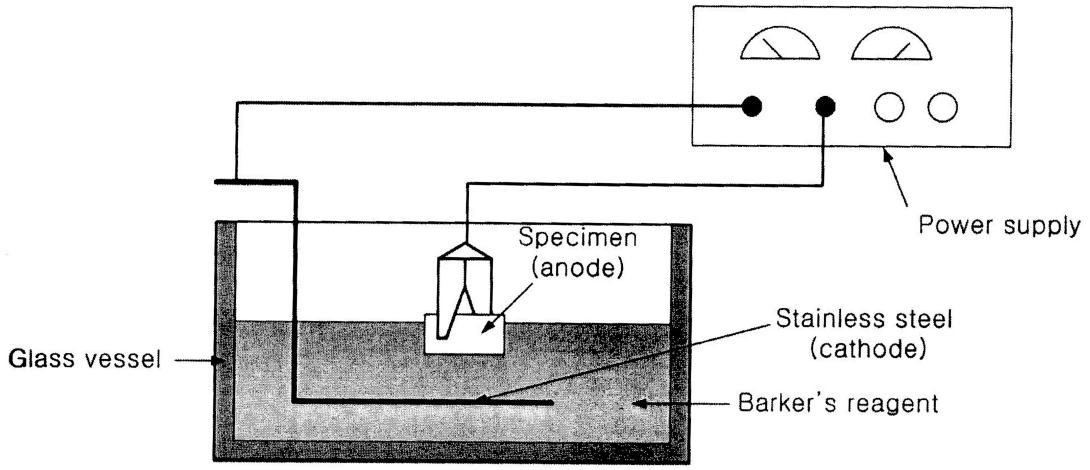


Figure 3.10: Schematic diagram of the sample anodisation set-up (not to scale)

The surfaces were then photographed using Zeiss Axiophot2 optical microscope with polarised light, and the cell sizes were measured using line-intercept method [123]. Several micrographs were taken to cover the surface, and 2 straight lines were drawn horizontally to measure the change in grain size in units of 2.5mm.

3.6 Intermetallic Phase Extraction

Intermetallic particles make up only a few volume percent (less than 7%) of the 6xxx Al alloys, and therefore it is difficult to analyse them *in situ* using XRD. However, XRD is essential in determining the phase identity, and thus, the phases were extracted from the aluminium matrix and studied separately.

The extraction procedure used is based on Simensen et al. technology, which uses anhydrous butan-1-ol in an argon atmosphere to dissolves the α-Al matrix, leaving behind the intermetallic particles of interest unaffected [124].

To attain anhydrous butan-1-ol for the extraction process, a small amount of 99.999% pure Al filings was introduced to the butan-1-ol and refluxed for 3 hours in the distillation apparatus shown in Figure 3.11 to ensure any water present within the solvent would react with the pure Al to form Al hydroxide. This step was carried out to speed up the drying process, as well as make sure that there were no OH^- ions left to react in the same way with the alloy during the extraction process.

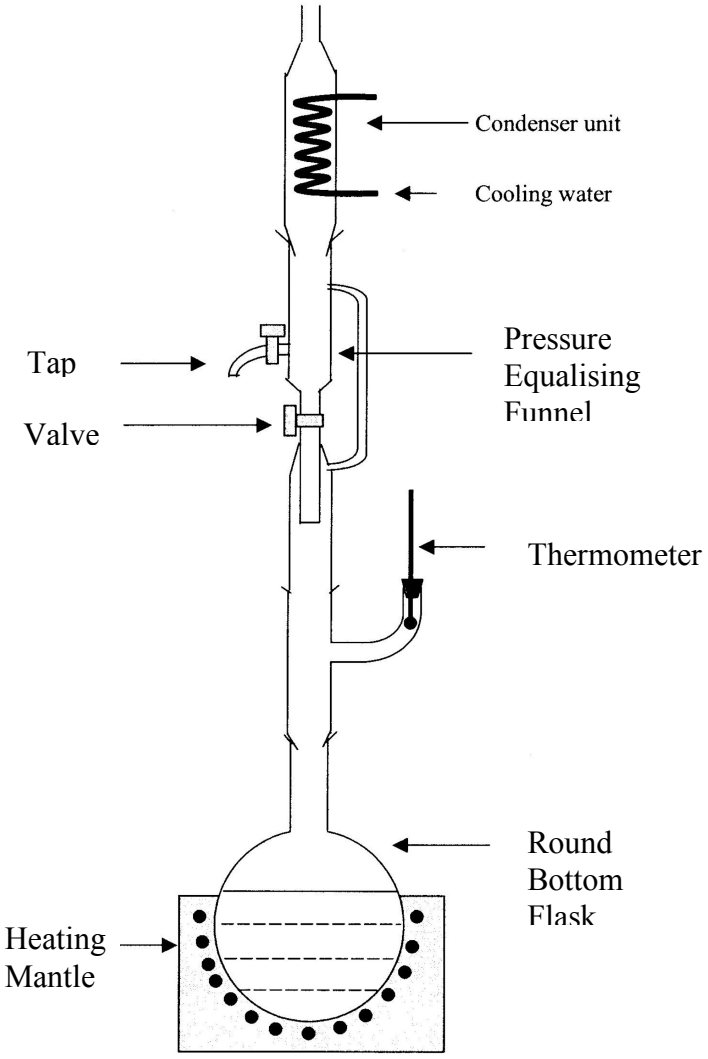


Figure 3.11: Schematic of the distillation apparatus

The entire extraction process was carried out in autoclaves (shown in Figure 3.12) to speed up the reaction. Each autoclave was prepared by cleaning the base part, screens, O-ring and the lid in an ultrasonic bath filled with de-ionised water, while ethanol was used to wipe the autoclave barrel. Once cleaned, the dismantled parts were left in an oven to dry for an hour at 150ºC. The autoclave was then assembled with its lid and base part; the base part fitted with both screens (underdrain screen and then screen support), a PTFE filter disc of 47mm diameter and 0.2μm pore size (from Sartorius Ltd.) and then the O-ring. The autoclave was dried in the oven at the same temperature for another hour.

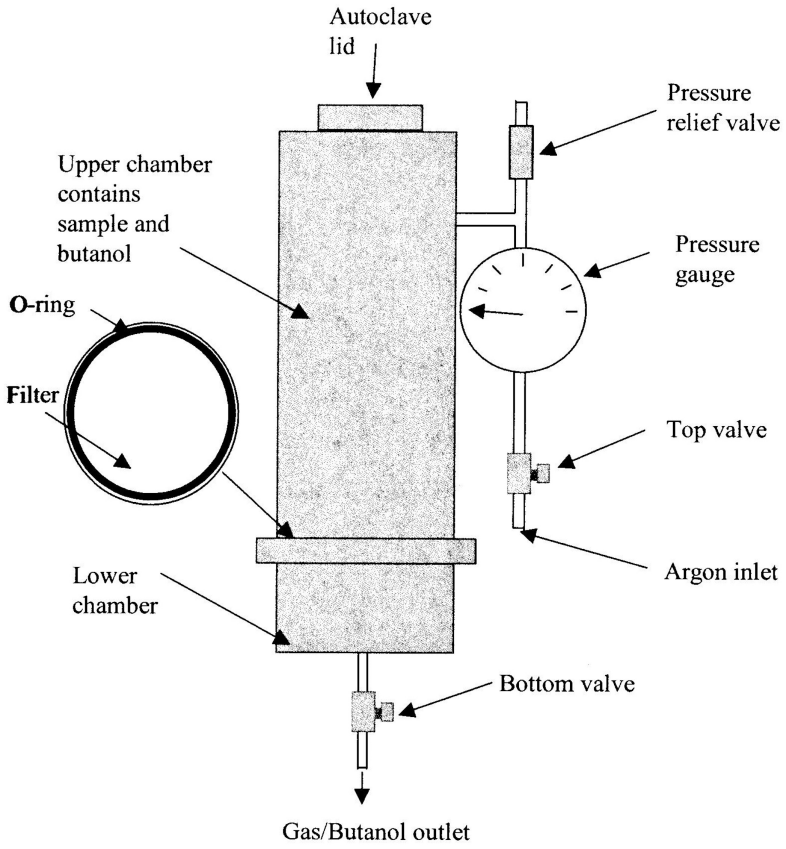


Figure 3.12: Schematic of the autoclave used for the extraction process

The samples for extraction were approximately 0.42g, and cut out from the bulk material of each sample. For the butan-1-ol to successfully attack the aluminium and dissolve it, the surface of the samples needed to be free of any oxide layer or grease. The samples were thus chemically cleaned with an etchant containing 2.5vol% HNO_3, 40vol% HPO_3, and 5vol% H_2SO_4 in water, for approximately 1.5 minutes at 60ºC, and then dried in Schlenk tubes under vacuum. The Schlenk tubes were then filled with argon, and the samples were kept there until further use.

Once the butan-1-ol had been refluxed for 3 hours, the autoclave was connected to a manifold and evacuated, leak tested and then filled with argon and 80ml of dried butan-1-ol. To ensure the sample surface remain free of oxide layers, the sample was inserted into the autoclave while both the Schlenk tube and the autoclave were pumped with argon to avoid contact with air. Once the autoclave was sealed, it was returned to the pre-heated oven (at 150ºC) for approximately 3 to 4 hours.

The reaction that takes place during this process is:

$$2Al_{(S)} + 6C_4H_9OH_{(L)} \rightarrow 2Al(C_4H_9O)_{3(L)} + 3H_{2(G)} \qquad (3.1)$$

The reaction could be monitored via a pressure gauge fitted on each autoclave, and once the pressure increase caused by H_2 stabilised, the process was assumed to be complete. The autoclave was then removed from the oven, and with the help of the increase in internal pressure, the remainder of the butanol was ejected through the filter from the

bottom valve of the autoclave. The contents inside the autoclave were then rinsed with ethanol, followed by dismantling of the apparatus. The extracted intermetallic particles (typical example of appearance shown in Figure 3.13 a) which remained on the filter paper were very carefully removed, still on the filter, with tweezers and placed in a polystyrene petri dish for transport and storage purposes. The phases extracted from the TP-1 samples, however, revealed a powder like appearance (shown in Figure 3.13 b), which had to be immersed in methanol and scraped off the filter paper using a stainless steel spatula.

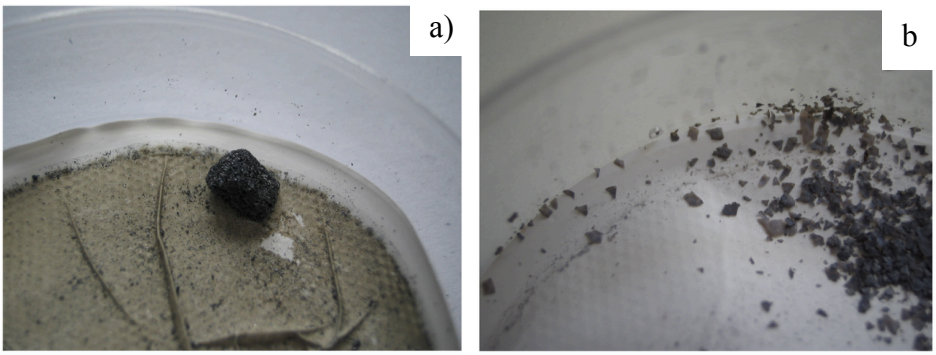


Figure 3.13: Example of the (a) 3D structure typically obtained on extracting the phases from the alloys manufactured using semisolid processing technique, and (b) powder-like intermetallic phase extracted from TP-1 casts

3.7 X-ray Diffraction (XRD) Identification

All the XRD measurements were carried out using a Philips 1700 series X-ray diffractometer, which has a radiation source of Cu-K_α with 1.54Å wavelength. The acceleration voltage used was 35kV while the current was maintained at 50mA. The

range of every scan taken (at 2θ values) was 15^{o} to 65^{o}, increasing by 0.05^{o} and exposing for 12.5 seconds on each step.

To establish trends in phase selection throughout the slurry, 3 samples were examined over the height of the BA slurry at about 150-155mm (BA200C), 65-70mm (BAL2) and 15-20mm (BAL3) from the base of the alloy (schematic shown in Figure 3.8). 6 samples were also examined across the radius at approximately 150-155mm from the base (schematic shown in Figure 3.8), referred to as BA200C, BAR2, BAR3, BAR4, BAR5 and BA200E, horizontally going from centre towards the edge respectively.

To verify the phase selection trend observed in BA, the phase identity of GR and ZR were also examined at the centre (GR200C and ZR200C, respectively) and near the edge (GR200E and ZR200E, respectively). The samples from GR and ZR were taken from the same location as BA200C and BA200E (Figure 3.8).

3.7.1 Sample preparation

Examining the intermetallic particles as-extracted would provide XRD spectra of the sample's preferred orientation of the crystallographic planes, known as texturing. Lui indicated that texturing effect could be reduced significantly by grinding the intermetallic particles into fine powder with an agate pestle and mortar [76]. He also observed that using a glass slide as the substrate introduced a broad hump around 2θ values of 15^{o} to 45^{o}, and that Si-grease contributed least to the pre-existing glass-slide hump.

Thus, the extracted intermetallic particles were ground to powder with an agate pestle and mortar, and then carefully spread across a glass slide with a fine silicone-grease layer. An XRD spectrum was obtained for a glass-slide with a fine silicon-grease layer, and the resultant broad hump was subtracted from the spectra of the samples.

To better understand how the phase selection is affected throughout the solidified BA200 slurries, the phase selection was examined for samples taken from various points within the BA200 alloy. 6 samples were examined along the diameter of BA200 at 150-155 mm from the base, and 3 samples were examined along the length vertically going downwards from the centre at heights of 150-155 mm, 65-70 mm and 15-20 mm from the base.

3.7.2 Identification of phases

The phases present in each sample were identified by comparing them with the spectra obtained with the JCPDS reference patterns for β-AlFeSi from International Centre for Diffraction Data, and a theoretical plot for metastable α_c-AlFeSi (since no pattern for reference was provided in the database). This theoretical plot was calculated according to Cooper's suggestion of the α_c-AlFeSi crystal structure [125], using the crystallographic software Powdercell 2.0. The JCPDS reference patterns for β-AlFeSi and theoretical plot for α_c-AlFeSi are shown in Figure 3.14.

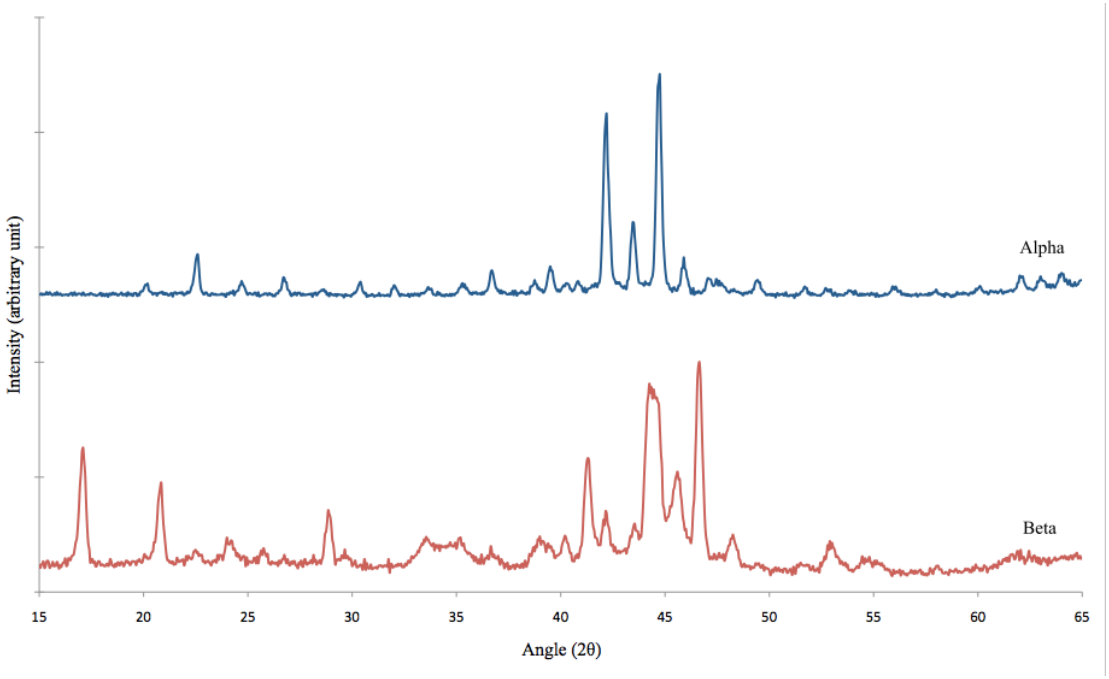


Figure 3.14: JCPDS reference patterns for β-AlFeSi and theoretical plot for α_c-AlFeSi

3.7.3 Phase content quantification

Along with phase identification, the relative weight fractions of α_c-AlFeSi phases were also worked out from the XRD spectra. Previous studies conducted at Oxford [55] have generated a curve based on pure phases of α_c-AlFeSi and β-AlFeSi mixed in known proportions of 10-90%. Due to the proportions of α_c-AlFeSi and β-AlFeSi phases used, the accuracy of the calculations was assumed to be accurate to the nearest 10%.

Three characteristic peaks were selected for both α_c-AlFeSi and β-AlFeSi phases, which were then used to work out the average peak intensities of the nine intermetallic phase β-AlFeSi : α_c-AlFeSi ratios, R.

$$R = \frac{1}{9}\left[\sum_{i,j=1-3}\left(\frac{I_{\beta i}}{I_{\alpha j}}\right)\right] \tag{3.2}$$

where I_β = selected characteristic peaks for β-AlFeSi phase, which are at 17.03º, 20.81º and 28.96º 2θ, and I_α = selected characteristic peaks for α_c-AlFeSi phase, which are at 22.37º, 26.53º and 36.44º 2θ. Thus the regression curve, Figure 3.15, is calculated from equation 3.3.

$$wt\%\alpha = 73.438e^{(-0.8864R)} + 34.1839e^{(-0.8864R)} \tag{3.3}$$

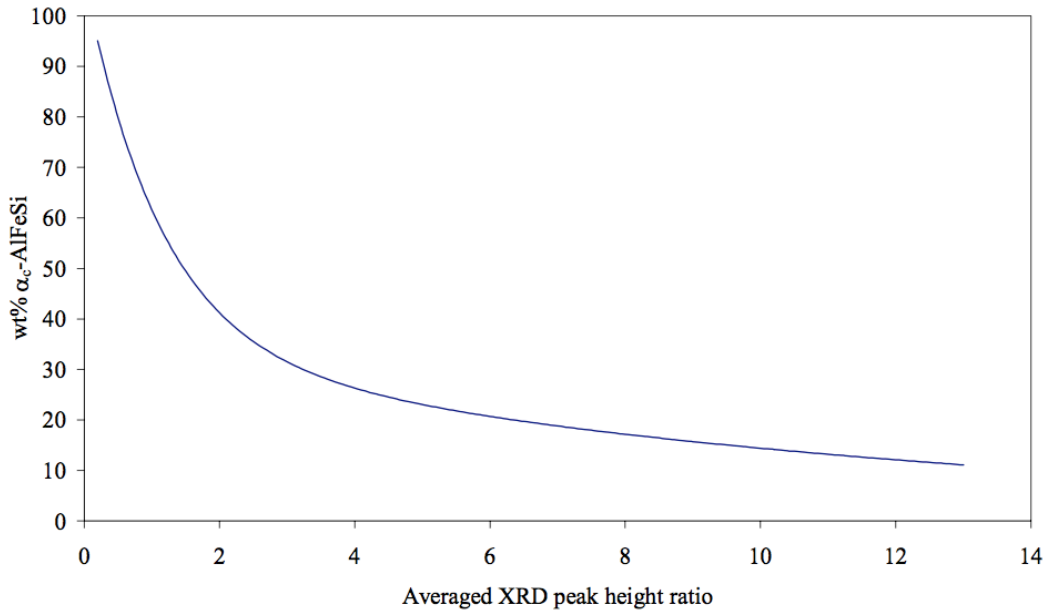


Figure 3.15: Regression curve to calculate α_c-AlFeSi weight fraction from averaged XRD peak height ratio [55]

Previous investigations have indicated that the phase content quantification using XRD analysis is not absolutely accurate, and can be affected by how the extracted phase samples were prepared [76]. It was suggested that the selected peaks, such as 17^{o} 2θ which is a characteristic peak displaying the presence of β-AlFeSi phase, can be sensitive to the orientation of the extracted intermetallic particles and may display discrepancies in peak intensity between samples [76]. Thus, the phase content quantification calculations obtained from XRD analysis were considered to be only a close approximation of the true value, and all the calculations have been rounded to the nearest 10%.

3.8 MTDATA Analysis

Lever rule (equilibrium) and the Scheil-Gulliver equation (non-equilibrium) both assume complete solute distribution in the liquid phase due to the large atomic mobility and convection present in the liquid. For solid phase, lever rule assumes complete diffusion while Scheil rule assumes diffusion is negligible (neither of which is always true for binary systems). Thus, both rules were employed by the MTDATA software to estimate the thermodynamic relationship between solid fractions and temperatures of all three alloys, using the chemical compositions measured from OES for each alloy.

3.9 Differential Scanning Calorimetry (DSC)

Differential scanning calorimetry (DSC) was used to ascertain the temperatures at which possible phase transformations were taking place for each alloy. All

measurements were carried out using a TA Instrument DSC 2010, and all samples were cleaned with acetone to remove any grease.

Since the samples were examined at temperatures close to the melting point of Al (660ºC), Copper (Cu) pans (melting point of 1083ºC [126]) were used to hold the samples. However, as Figure 3.16 (a) shows there would be significant reactions taking place at the Al sample / Cu pan interface at high temperature ranges. Molybdenum (Mo) on the other will not react with the Al sample around the temperatures being examined (660ºC / 933K), shown Figure 3.16 (b).

Thus, a Mo disc was placed on the Cu pan before placing a 5-8g cleaned sample on top of the Mo disc. The sample was then covered with a second Mo disc on top to act as a lid. The Cu pan was then crimped, sealing the sample encapsulated between the Mo discs. An empty pan, i.e. a Cu pan crimped with 2 Mo discs was used as the reference. The entire chamber was purged with argon to restrict reactions taking place between the Al sample and air molecules.

Samples were analysed with a heating rate of 10K/min to observe the phase transformation temperatures of each alloy. As it is believed that both α-AlFeSi and β-AlFeSi phases can be metastable, a slow heating rate might cause the phases to transform before the onset temperature of the phase have been reached. Since, faster heating and cooling rates translate into higher sensitivity and throughput, a faster heating rate of 40K/min was also analysed for BA200.

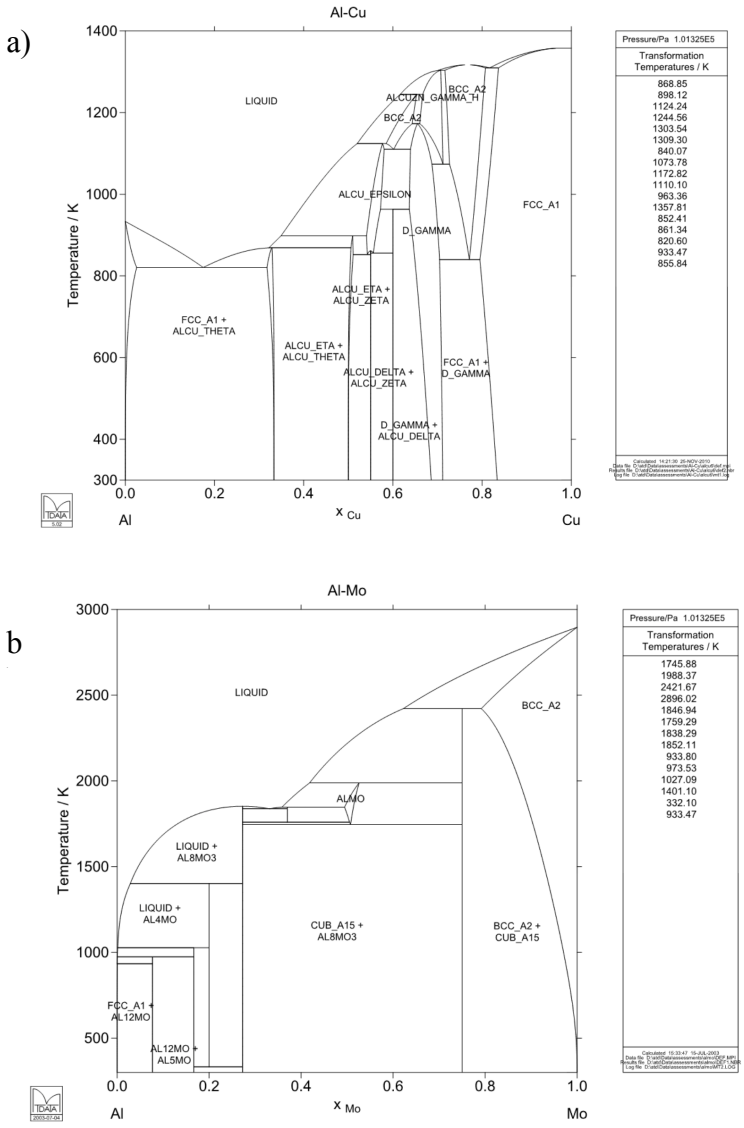


Figure 3.16: Calculated binary phase diagrams of (a) Al-Cu and (b) Al-Mo [127]

Thus, the equipment was calibrated by melting pure indium (156.60º), zinc (419.53º) and super pure aluminium (660.37º) using this Cu pan / Mo disc set up [10,128]. Each set of calibration metal was heated at the rates of 10K/min and 40K/min to match the tests being carried out. The melting onset of the samples were manually calculated from the point at which the arbitrary heat flow starts to reduce (shown in Figure 3.17). Pre-tests displayed that each phase transformation absorbed large amounts of energy, and therefore a super-pure aluminium baseline was not necessary to be subtracted from the

DSC curves to reveal the phase transformations. The onset calculations were carried out directly on the curves obtained from DSC. The tests were run three times for each type of alloy, and the curves obtained were comparable. One curve from each set has been presented in the results section.

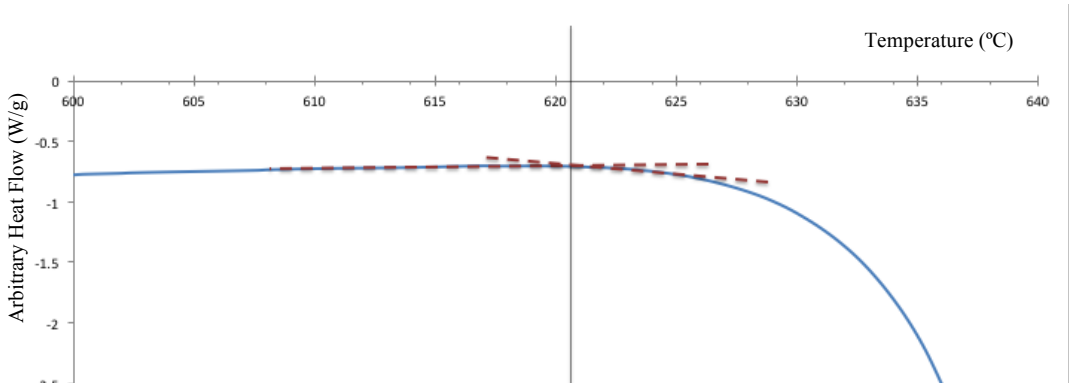


Figure 3.17: Onset calculations from DSC curves

To determine the identity of phases transforming at specific temperatures, the DSC curves were compared with the phase diagrams calculated from MTDATA.

3.10 Scanning Electron Microscopy (SEM)

Based on a previous investigation carried out by Lui [76], it was established that TEM is not the most suitable technique for the examination of AlFeSi-based intermetallic particles. This was due to difficulty and inefficiency in getting a clear diffraction pattern from the intermetallic particles, establishing their identity and structural connectivity, measuring their true dimensions, as well as locating TiB_2 particles. Furthermore, examinations are limited to two-dimensions, in extremely restricted areas due to the appropriate sample thickness. In addition, particles can fall out during sample

preparation, rendering the results inaccurate. Thus SEM was used for all microscopic analysis.

SEM was employed in this investigation had the following main aims; to observe the topographical formation of intermetallic particles, to examine the extracted phase morphologies, and to establish the location of TiB_2 particles for both polished metallographic samples and extracted intermetallic particles.

3.10.1 Sample Preparation for SEM

(a) Metallographic Microstructure:

The metallographic samples were prepared using a similar technique to the micro-etched samples section 3.5. Samples were cut out from near the top, shown in Figure 3.8 section 3.5 and mounted in conductive Bakelite this time. The sample surfaces were treated in the same procedure as micro-etched samples:

- polished with 5 and 1 μm diamond suspensions in water, using Struers 'PA-W' cloth;
- polished with colloidal silica suspension for 20 minutes, using Metprep 'multi' cloth.

The metallographic samples were used to examine the surface structure, so the formation of various types of intermetallic particles could be compared, and the location of TiB_2 particles could be established.

Backscattered electron (BSE) images were captured using a Jeol 840A scanning electron microscope. The acceleration voltage used was 10kV, because at this voltage an increase in the atomic number raises the backscattering coefficient [129]. Thus, the intermetallic particles with higher concentrations of Fe, Si and Ti offer a compositional contrast against the primary aluminium, whereby the phases appear a lighter shade than the dark grey primary aluminium background.

(b) Extracted Microstructure:

The intermetallic particles extracted from all of the alloys were mostly rigid enough to maintain their structural integrity during careful handling. This enabled examination of intermetallic particles in their natural 3D environment. However, for samples that crumbled, the smaller 3D structures were used for SEM examinations. Thus, for each material, sections were cut off the main body of extracted intermetallic particle structure and placed on a sticky carbon tab. The carbon sticky tabs were then stuck on aluminium stubs for examination. To ensure all loose particles were removed from the carbon tab, an aerosol duster was used to blow them away.

Samples from BA200, GR200 and ZR200 were extracted from the centre (BA200C, GR200C and ZR200C respectively), near the edge (BA200E, GR200E and ZR200E respectively) and near the base (BAL3, GR200B and ZR200B respectively) of each alloy for phase morphology comparisons. The samples from near the edge base were taken around 5mm past the edge to avoid regions of columnar grain.

(i) Semisolid Processed Alloys

On extraction of phases from the semisolid processed alloys, the phases displayed an interconnected three-dimensional (3D) sponge-like structure. The extracted phases were dark grey to black in colour, structurally very unstable and crumbled on contact. Although all the extracted phases were delicate, the phases from GR samples were sturdiest when handled. The phases from ZR on the other hand were the weakest, and just crumbled at the lightest touch.

The average pore diameter of each sample was examined for comparison with the measurements from the anodised samples. Examples of well-defined pore structures are identified in Figure 3.18 using green and orange markers. Since the line-intercept method could not be used on this occasion as not all the pores are in the same plane, the pores were measured across their longest and shortest lengths, denoted 'A' and 'B' in Figure 3.18. The intermetallic pore diameter was calculated using the average of both A and B lengths of 10 to 20 pores, while the aspect ratio of each pore was calculated using A/B.

Pores with an aspect ratio of ~1 would indicate that its length and width are equal, and therefore can be considered equiaxed. Pores with one length significantly longer than the other will have a smaller aspect ratio, and can be considered columnar.

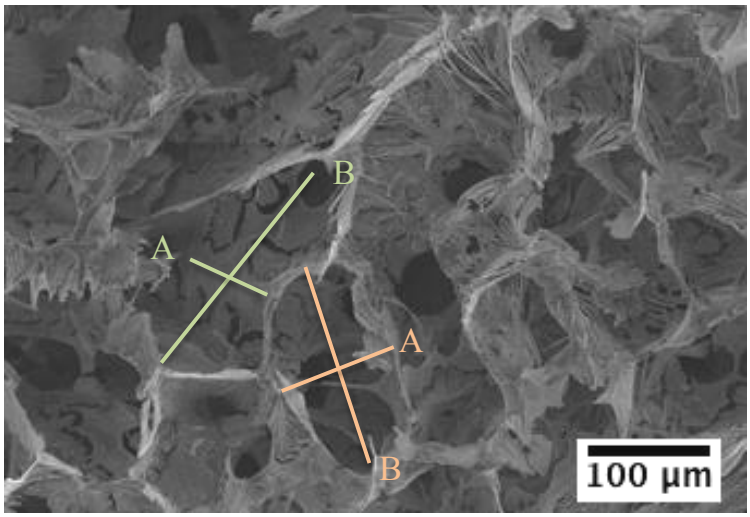


Figure 3.18: SE micrographs of extracted intermetallic particles of BA200C

(ii) TP-1 Cast Alloys

It was interesting to note that the phases extracted from TP-1 casts displayed a powder-like form; the macroscopic 3D structure was not displayed by phases from any of the TP-1 samples.

The extracted intermetallic particles from the TP-1 samples were solely used for obtaining their XRD spectra, and were not analysed through SEM due to the large amount of work that has already been carried out on TP-1 intermetallic phases [20, 76].

3.10.2 Topographical Examination

For surface formation examinations, all the SEM measurements were carried out using a Jeol JSM-840A scanning electron microscope, equipped with energy dispersive X-ray spectroscopy (EDX). The acceleration voltage used was 15kV to obtain better contrast in the micrographs, current was set at 6.0nA, working distance at 10mm, and the largest aperture.

Micrographs were taken of the sample surfaces at various magnifications, starting from x100 to x7500. The x100 micrographs were taken to be able to observe the overall structure of the sample surface. The micrographs magnified at x200 were intended for measurements of the average distance between intermetallic particles (in metallographic samples) and the average diameter of pore structures (in the extracted intermetallic particles).

Higher magnifications were used for extracted particle surface examinations. Micrographs were taken every 200μm, in a grid-like fashion to ensure the trends in particle structures could be quantified across the sample surface. Specific features of interest were identified by sight, and then analysed for chemical composition using element mapping/EDX. The software used to obtain the EDX spectra was INCA version 4.05 – Microanalysis Suite 15+SP3. A deadtime of about 10 to 15% and process time of 5 seconds could generally be obtained using 1 x 10^{-8}A.

3.10.3 TiB_2 Particle Location

To establish the location of TiB_2 particles, chemical analysis using energy dispersive X-ray spectroscopy (EDX) was necessary to analyse the TiB_2 particles. For chemical composition analysis through X-ray techniques, a beam of electrons from the probe hit the sample surface causing the excitation and 'drop down' of sample electrons from a certain volume, releasing characteristic X-rays that can be used to identify the elements present. The volume of material that is affected by the probe electrons is known as the

interaction volume [129, 130], and is an important parameter when establishing the accuracy of certain elements identified by the process.

Lui [76] investigated the interaction volume of EDX at different accelerating voltages of Al, AlFeSi and TiB_2. He indicated that estimations using Monte Carlo simulation and Kanaya-Okayama Range were in agreement, and concluded that the dimensions of interaction volume of AlFeSi and TiB_2 at various acceleration voltages were as follows: (a) depth and width of $\leq$0.5μm for 4kV, (b) ~1μm for 10kV and (c) $\geq$2.5μm for 15kV.

To detect the presence of Ti particles, an acceleration voltage of 10kV is necessary to excite the Ti electrons sufficiently. However, further examinations revealed that both, the extracted intermetallic particles and the TiB_2 particles were less than a micron in thickness and dimensions, respectively. Thus using an accelerating voltage of 10kV to detect the presence of Ti particles, a spectra analysing the interaction volume of ~1μm will be generated, which is larger than the area intended to be examined. Thus, to understand possible mechanisms involved in Ti-rich particles nucleating the phases, Ti-rich particles were identified using a combination of EDX and visual observation.

It was not possible to establish whether the Ti-rich particles were actually TiB_2 particles or simply Ti-containing phases, because of the difficulty in detecting signals from the small B content in the particles. This is due to X-rays being absorbed by the sample as well as the spectrometer efficiency dropping [130].

It can be concluded that chemical analysis to establish the presence of Ti particles on the sample surface will always include signal from the surrounding bulk material. Thus, EDX was used on the metallographic and extracted samples purely to identify the regions containing Ti containing particles. Other elements, such as Fe, Mg and Si were also mapped to differentiate between the different phases.

3.10.4 Element Mapping

To narrow down the Ti containing regions, the sample surfaces were first examined using element mapping, continually zooming into the regions to establish an exact location. However, once the magnification of approximately x1000 to x2500 was reached, a combination of image analysis, EDX and element mapping was used to establish whether the particle being examined contains high amounts of Ti.

The INCA Suite software requires the exact peak positions and the detector system resolution in order to identify the individual peaks accurately in an EDX spectrum. However, change in ambient temperatures can alter the detector system, while the microscope beam current varies with time. Thus, the peak positions were monitored before each microscopy session, by calibrating the peaks against the X-ray peaks of known energy. Pure Cu wire was either attached to a carbon sticky tab which in turn was attached to the bakelite regions of the metallographic sample, or the wire was attached to the sticky tab containing the extracted intermetallic particles directly.

3.11 ThermoMechanical Analysis (TMA)

The mechanical properties of the semisolid slurry samples, including tensile properties and strength development, were examined using a PerkinElmer Pyris Diamond TMA. This was made possible by kind arrangement with Paul Bastock from the Optoelectronics Research Centre at the University of Southampton. Figure 3.19 displays a schematic of the machine and its basic circuits, while Figure 3.20 shows the sample holder set specifically for tensile testing. Using this equipment correctly was one of the larger challenges of this investigation, as this technique has never been used to study the tensile properties of semisolid materials before.

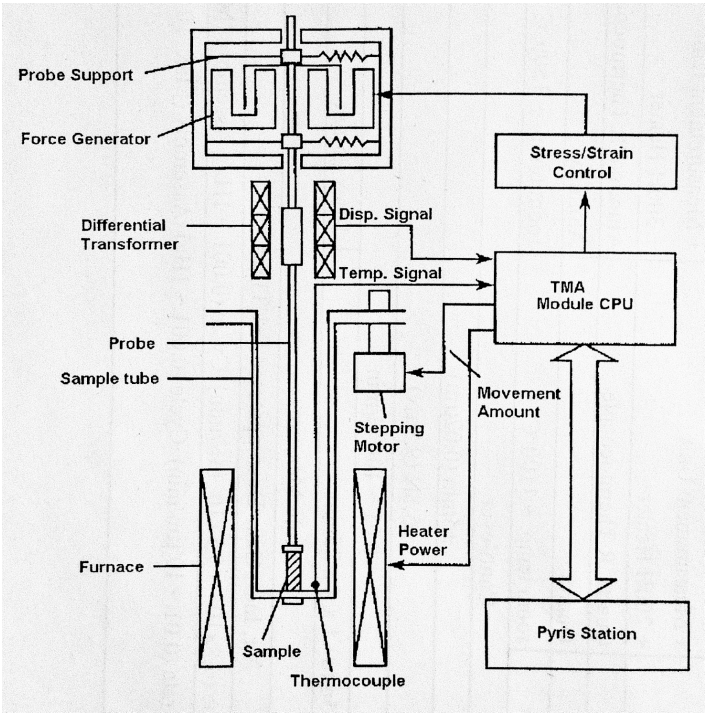


Figure 3.19: Schematic diagram of the TMA Measurement principle [131]

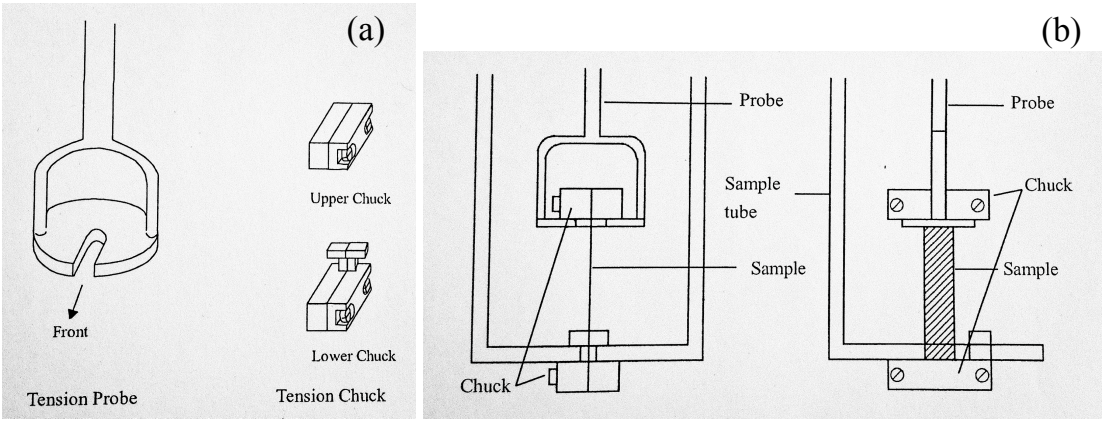


Figure 3.20: Schematic diagram showing the (a) tensile test accessories, and (b) a tension mounted sample [131]

3.11.1 Equipment Calibration

One of the key factors of this investigation is being able to control the sample's solid fraction, which in turn is critically dependent on the temperature. Load applied also plays a crucial role in determining the mechanical properties. Thorough investigations were therefore carried out into calibrating the machine, since the slightest fluctuations in temperature or load will have significant effects on the deformation behaviour. General calibration was carried out according to the manufacturer's guidance.

3.11.2 Sample Preparation

Sample dimensions for the tensile tests were dictated by the equipment dimensions, which were very restrictive. Rectangular samples of 33.0mm length, 4.3mm width and 1.1mm thickness were cut from Section B (see Figure 3.8) using an Isomet precision cutter. Once the samples were separated from the bulk material, each end was ground to achieve a uniform length of 30mm, using P800 grit SiC abrasive paper.

Due to the small sizes of the samples being examined, the presence of even slight scratches on the sample surface may act as fracture initiation sites during the tensile tests. Thus to reduce this effect, several tensile samples were attached on a flat surfaced holder using hard wax and ground for a few minutes on SiC abrasive paper of P800 finish, and another few minutes on a P1200 grit paper. This process was repeated on all surfaces, and the final sample dimensions achieved (measured just before loading sample into tensile tests) were ~3.3mm width and ~1.0mm thickness. However, there is a possibility that this grinding process may contribute to the samples' residual stresses.

3.11.3 Technique Development

Two key aspects of the technique development were the heating curve and load applied.

Heating Curve

The Diamond TMA records three different temperatures:

(a) Program Temperature – the temperature calculated according to the program set by the operator;

(b) Sample Temperature – measurements taken from a thermocouple that was located in the immediate vicinity of the sample; and

(c) Furnace Temperature – measurements taken from a thermocouple that was located within the furnace.

The accuracy of the thermocouple reading the sample temperature was established by raising the furnace temperature and monitoring the measurements using an external thermocouple. The readings from both the internal and external thermocouples were in agreement. The accuracy of the thermocouple measuring furnace temperature could not be established using an external thermocouple due to the location of the internal thermocouple, so consistency of the readings was checked during tests instead.

The heating curve was determined based on the phase transformation temperatures for both α-AlFeSi and β-AlFeSi phases, calculated from the MTDATA analysis and DSC curves. Based on the DSC analysis, the points of interest in terms of phase transformations are around 610ºC for β-AlFeSi phase, and around 640ºC for α-AlFeSi phase. Thus, tests were carried out starting with 610ºC. Three different types of tests were carried out to understand the different temperature measurements:

(a) Three tests without any sample;
(b) Three further tests with tensile samples, whereby the thermocouple measuring sample temperature was in contact with the samples; and
(c) Three final tests with tensile samples, whereby the thermocouple measuring sample temperature was located in the immediate vicinity of the samples, but not directly in contact.

With regards to heating rate, based on the DSC curves, it was concluded that the heating rate of 40K/min displayed a larger presence of β-AlFeSi phase. This may be because at a slow heating rate, there is a high possibility that the phase would have adequate time

to transform during the heating cycle. Thus, for TMA analysis, the samples were heated at a rate of 40K/min.

(a) Test Set 1: Tests without any sample

Three test runs were performed without any samples present so the variance between the program, sample and furnace temperature could be ascertained. The experiments were performed in compression mode, and the furnace was allowed to heat up to 400ºC before the run was started. Once the furnace temperature stabilised, the programmed run increased the temperature at the rate of 40K per minute, going up to a maximum of 610ºC, 620ºC and 630ºC. The temperature was held at the maximum for 5 minutes, after which the furnace was allowed to cool down to room temperature. The curves obtained are shown in Figure 3.21. The results displayed a relatively consistent temperature lag of around 20ºC between the measured and programmed temperatures, after holding the temperature for 5 minutes.

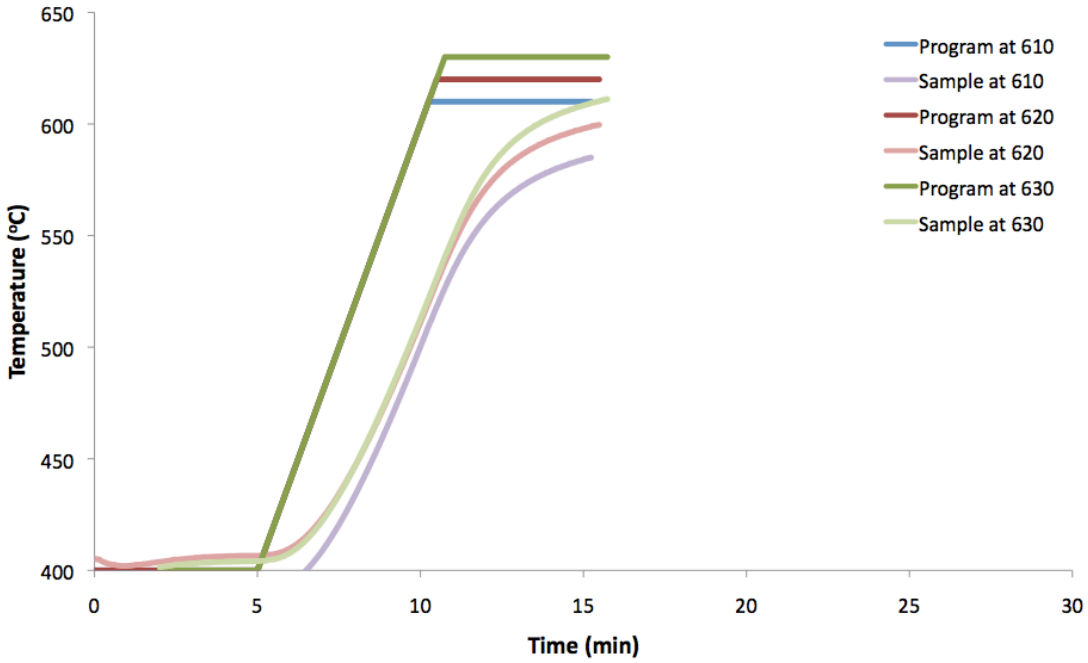


Figure 3.21: Difference in programmed and measured temperatures without any sample present

It can also be noted that the measured temperature was not yet stable after 5 minutes of holding the programmed temperature, and continued to increase. Thus, to establish the point at which the measured temperature stabilises, the three tests carried out with tensile sample in contact with the thermocouple were held at temperature for 15 minutes.

(b) Test Set 2: Tests with tensile samples in contact with the thermocouple

The methodology used for the tests carried out with samples in contact with the thermocouple were as follows:

(a) hold the programmed temperature at 400ºC for 5 minutes;

(b) increase the programmed temperature at 40K per minute to maximum temperature; and

(c) hold it at maximum temperature for 15 minutes.

The maximum temperatures tested were 610ºC and 625ºC, while 595ºC was tested retrospectively (see section 4.8.1 for more details). The curves obtained are displayed in Figure 3.22.

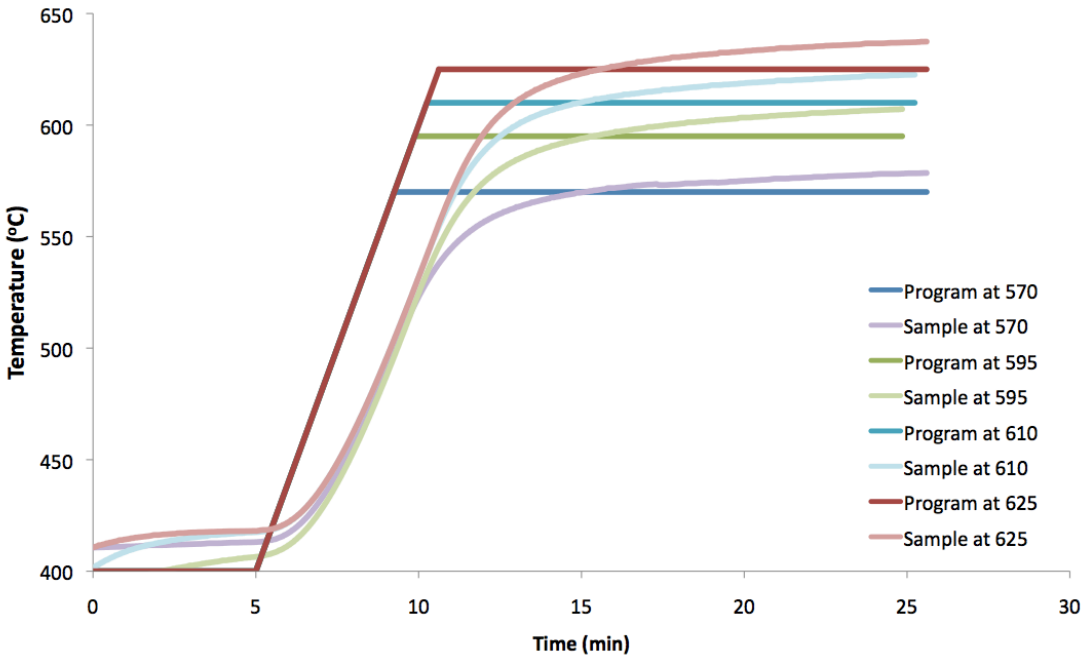


Figure 3.22: Difference in programmed and measured temperatures while samples are in contact with the thermocouple

All three samples displayed the same characteristics:

(a) a lag of 60ºC when the program temperature increased at the rate of 40K per minute;

(b) the programmed and measured sample temperatures were equal after holding the programmed temperature for 5 minutes (on average); and

(c) after holding the programmed temperatures for 15 minutes, the measured sample temperatures were on average 12K higher than the programmed temperature.

It was also noted, however, that the contact force of the thermocouple caused a downward force on the probe resulting in significant inaccuracies in the probe displacement measurements. Thus, it was decided that the TMA tests should be carried out with the thermocouple measuring the sample temperature not in direct contact with the sample.

To ensure a consistent temperature is obtained inside the furnace, the furnace temperature at program temperatures of 400ºC, 595ºC, 610ºC and 625ºC were noted down during these tests, and compared with the readings from Test Set 3 (where the thermocouple was not in direct contact with the samples). The furnace temperatures recorded at the given programmed temperatures were:

(a) Program temperature of 400ºC = Furnace temperature of 469ºC;

(b) Program temperature of 595ºC = Furnace temperature of 685ºC;

(c) Program temperature of 610ºC = Furnace temperature of 701ºC; and

(d) Program temperature of 625ºC = Furnace temperature of 717ºC.

(c) Test Set 3: Tests with tensile samples not in contact with the thermocouple

The methodology mentioned section (b) Test Set 2 was used again, but this time the thermocouple measuring the sample temperature was located in the immediate vicinity of the sample, and not in direct contact. The furnace temperature measured at the selected programmed temperatures were identical to those of Test Set 2, and it was

therefore assumed that the samples of Test Set 3 experienced the same thermal conditions as the samples from Test Set 2. The curves obtained from Test Set 3 are shown in Figure 3.23.

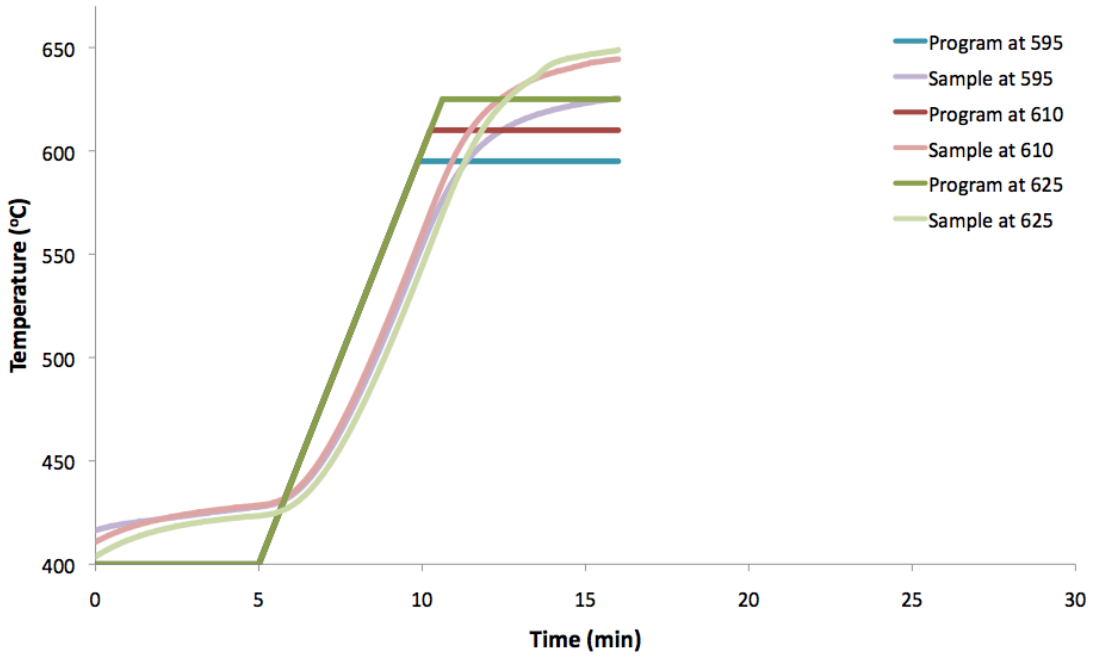


Figure 3.23: Difference in programmed and measured temperatures while samples are not in direct contact with the thermocouple

All three samples displayed a lag of 40ºC when the program temperature increased at the rate of 40K per minute, however, the discrepancies after holding the programmed temperature for 5 minutes varied slightly. The difference in programmed and measured sample temperatures at 595ºC, 610ºC and 625ºC were +30K, +35K and +25K respectively. The reduced difference in programmed and measured sample temperature at 625ºC could have been caused by the sample fracturing, and absorbing thermal energy in the process.

Load Applied

A few pre-test runs were carried out with a load of 0mN, which displayed unstable probe movements throughout the run. This was because no contact was maintained between the probe and the sample, and therefore the probe motion did not reflect any changes within the sample. Thus, a very small load of 200mN was applied throughout all tests to ensure that a constant contact was maintained between the sample and the probe, but not enough to deform the material. Once the sample reached the desired temperature, a maximum load of 981mN (100g) was applied at the rate of 150mN per minute, and maintained at the maximum for a further 10 minutes.

3.11.4 Test Conditions

Based on the preliminary tests, all the test samples were run using the following conditions:

(a) hold the programmed temperature at 400ºC for 5 minutes;

(b) increase the programmed temperature at 40K per minute to maximum temperature;

(c) hold it at maximum temperature for 5 minutes;

(d) increase the load from 200mN to 981mN (100g) at a rate of 150mN per min;

(e) hold the temperature and load at maximum for a further 10 minutes before ending the test.

The GR200 and ZR200 alloys were tested at maximum temperatures of 610°C (GR610 and ZR610) and 625°C (GR625 and ZR625). To better understand the thermodynamic behaviour of the fracture mechanism, another set of samples were tested at the

maximum temperature of 595°C (GR595 and ZR595). Due to time constraints only two samples from each alloy were tested at the same maximum temperature, and each sample will be identified with suffixes _01 and _02.

3.11.5 Test Data Analysis

Based on the Test Sets 2 and 3, it was concluded that:

(a) the furnace temperature remained consistent despite the discrepancies in sample temperature measurements; and

(b) maintaining the programmed temperature for 5 minutes allowed the sample temperature to equalise with the programmed temperature.

Given the sample temperature recorded by the equipment thermocouple was inconsistently higher than the actual temperature of the sample (measured by leaving the thermocouple in contact with the sample at the corresponding temperatures), an offset value was used to calculate the true temperature of the sample from the equipment measured sample temperature. This offset value was calculated individually for each set of data using equation 4.1 and 4.2.

$$\Delta T = ST_{5\,\min} - PT_{5\,\min} \tag{4.1}$$

and

$$T = ST - \Delta T \tag{4.2}$$

where:

(a) **ST** represents the sample temperature;

(b) **PT** represents the programmed temperature;

(c) **5min** represents that the PT has been maintain at the maximum temperature for a 5 minute period; and

(d) **T** represents the calculated temperature of the sample at any given time.

3.11.6 Fracture Surface Analysis

The fracture surfaces of the samples that had fractured were examined using a Jeol JSM-5510LV scanning electron microscope (SEM), equipped with EDX. The acceleration voltage used was 10kV to avoid charging the sample, and a working distance of 15-17mm. Once again, element mapping was used to identify regions containing Ti-rich particles, which were then analysed with EDX for confirmation.

The fracture surface analysis was carried out to obtain a better understanding of the possible mechanisms that may have caused the fracture, as well as to compare fracture surfaces of samples containing the different percentages of α_c-AlFeSi phase. If no phases are observed between the cracked surfaces, it will support John Campbell's bifilm theories [97].

Chapter 4 Results

4.1 Alloy Composition

Each alloy system was analysed using OES to establish their chemical composition. The average of 5 measurements, taken from the vertical cross-section of each slurry about 100mm above the base, is presented in the following sections. From the test results, all elements that displayed changes in readings were considered to be present in the alloy, and the ones that displayed amounts of less than detectable limits (such as <0.0005wt% for B) were considered to be either not present or present in insignificant amounts. The measurements obtained for the calibration standard 6063 sample provided by the manufacturer, and the alloys BA, GR and ZR alloys are given in Table 4.1.

Sample	Si	Fe	Mg	Ni	Cr	Ti	B	V	Zr
6063*	0.52	0.23	0.55	0.0293	0.0150	0.0334	<0.0005	0.0221	0.0034
BA	0.54	0.34	0.37	0.0019	<0.0010	0.0033	<0.0005	0.0076	0.0011
GR	0.51	0.34	0.36	0.0029	<0.0010	0.0176	0.0015	0.0085	0.0010
ZR	0.60	0.45	0.35	0.0080	0.0076	0.0030	<0.0005	0.0064	0.0946

Table 4.1: Average chemical compositions in weight percentages, based on 5 measurements (*denotes calibration standard material for the OES, provided by the manufacturer)

Chemical analysis of BA showed that the nominal chemical composition of 6063, 0.30wt%Fe, 0.50wt%Si and 0.40wt%Mg, was achieved for the batch of alloy examined in this project. BA had a chemical composition of 0.34wt%Fe, 0.54wt%Si and 0.37wt%Mg, with trace elements Ti, Ni, Pb, Ca, Ga, Na and V. With additions of Al-

Ti-B type grain refiner to BA, the main alloying element content (Fe, Si and Mg) remained consistent at 0.34wt%Fe, 0.51wt%Si, 0.36wt%Mg, with 0.0176wt%Ti and 0.0015wt%B. The trace elements observed in GR, Ni, Cr, Pb, Ca, Ga, Na and V, also remained relatively consistent between the two alloys.

A change in the amounts of Fe and Si was observed on additions of 0.1wt%Zr to BA; the chemical composition of the alloy was 0.45wt%Fe, 0.60wt%Si, 0.35wt%Mg and 0.0946wt%Zr, with trace elements Ti, Ni, Cr, Pb, Ca, Ga, Na and V. It was interesting to note that the amount of both Fe, Si, Ni and Cr are much higher compared to BA, indicating that there were Fe, Si, Ni and Cr impurities present in the Al-Zr master alloy that was used to add Zr into the base alloy. The altered chemical composition of ZR would affect the local solute diffusivity, which in turn would have an impact on the thermodynamics and kinetics during solidification. The overall Q factor (discussed in 2.3.2 b) would also be different in ZR compared to BA and GR due to the altered contributions from the individual solutes to the overall undercooling of the alloy. These differences in chemical compositions can have an impact on the α-Al microstructure, phase selection and morphology.

4.2 Macro-etch

(a) BA200

The macro-etched cross-sections of BA200 can be seen in Figure 4.1 and the average grain sizes are shown in Figure 4.2.

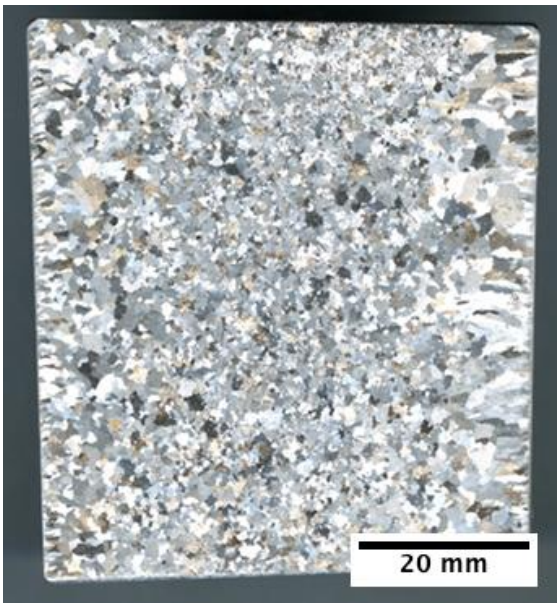


Figure 4.1: Macro-etched microstructure of BA200

There was porosity on the surface, which made grain size measurements less accurate. The grain sizes of BA200 display a gradual change; the section of columnar grains observed near the edge of BA200 expand to about 2mm in width, and then blend into a coarser equiaxed grain structure in the bulk material, steadily getting finer towards the centre. The average grain sizes measured for BA200 ranged from 160±40μm to 230±40μm. The grain size distribution observed in BA400 are shown in Figure 4.2, and will be discussed in the following section.

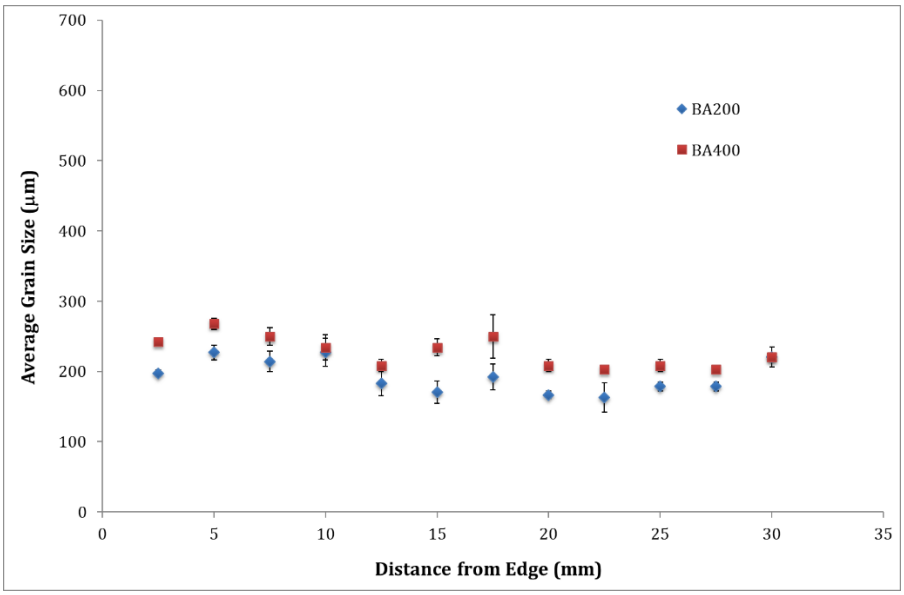


Figure 4.2: Average grain sizes of BA200 and BA400

(b) BA400

The macro-etched cross-sections of BA400 can be seen in Figure 4.3 and the average grain sizes are shown in Figure 4.2.

The grain sizes of BA400 are almost identical to those of BA200 in terms of the columnar grain section near the edges expanding to about 2mm, and then blending into a coarser equiaxed grain structure in the bulk material, which is finer towards the centre. Porosity was also observed on the surface. The average grain sizes measured for BA400 ranged from 200±15µm to 270±10µm.



Figure 4.3: Macro-etched microstructure of BA400

(c) BATP-1

The average grain size of BATP-1 is given in Figure 4.4, and the average grain sizes of GRTP-1 and ZRTP-1 will be discussed in the following sections. The macro-etched cross-sections of BATP-1 are shown in Figure 4.5.

The microstructure displayed by the vertical cross-section of BATP-1 has a very wide section of columnar grains all around the outer edges, starting from the base up to approximately the 30mm horizontal plane. The columnar grains on the sides appear to change angle with increasing height:

- The grains near the base have an angle of approximately 40^{o} when measured from the horizontal plane at ~5mm from the base;
- At about the 17mm horizontal plane, the angle decreases to about 34^{o};

– The angle of the grains then increases to around 65^{o} at the 30mm horizontal plane.

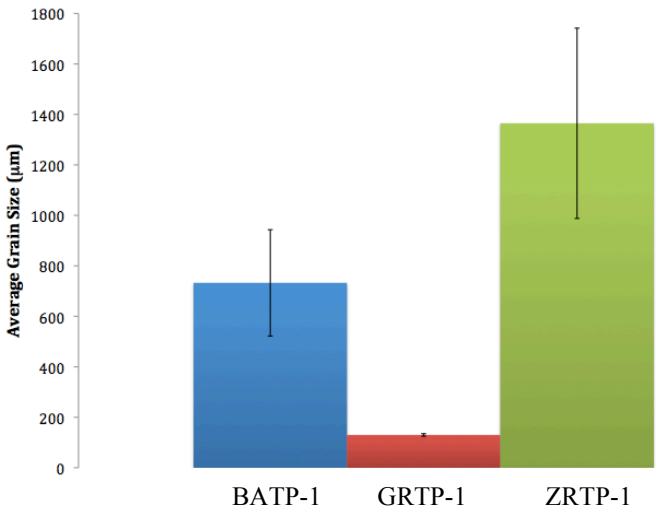


Figure 4.4: Average grain sizes of BATP-1, GRTP-1 and ZRTP-1

The grains near the top surface are mildly columnar and vertically orientated. It is difficult to establish whether these grains display an independent columnar grain section, or if they are an extension of the columnar grains observed on the sides. The columnar grains on the side extend almost all the way to the centre, leaving just ~2.5mm width at the centre, where the grains are globular and significantly smaller.

The horizontal cross-section of BATP-1 mostly displayed equiaxed-appearing grain structures of varying sizes, and did not exhibit any obvious columnar grains. The grain sizes near the centre were generally smaller and the grains more equiaxed. The grain sizes measured for the horizontal cross-section of BATP-1 ranged between 520±90µm and 960±380µm, with an overall average of 730±230µm. It can be seen from Figure 4.4 and the error values (which were calculated from the standard deviation of the

number of grains intercepted by the line-intercept method) that the grain size varied significantly on the BATP-1 surface, and therefore an average size is not representative of the surface microstructure.

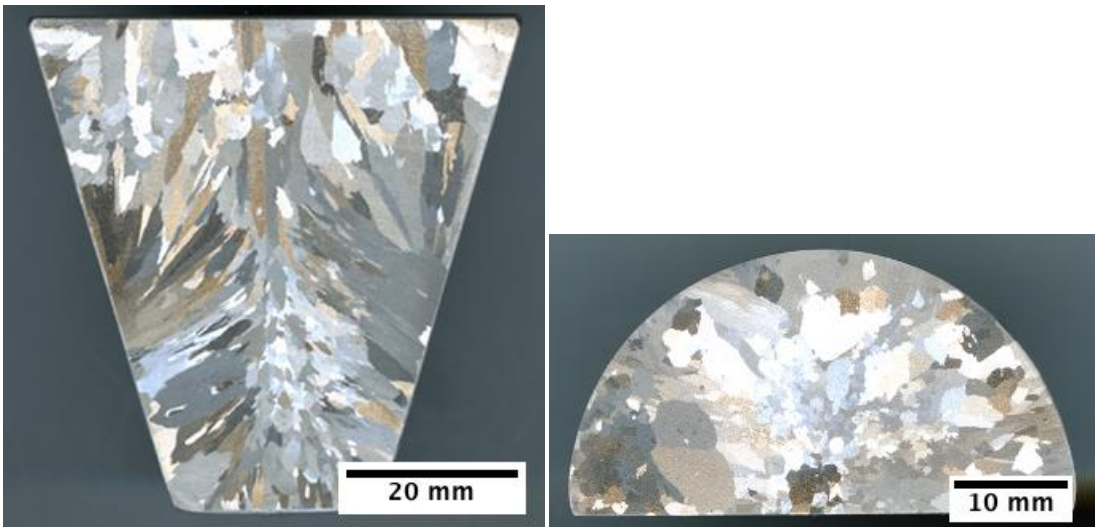


Figure 4.5: Macro-etched microstructure of BATP-1

(d) GR200

The macro-etched cross-sections of GR200 can be seen in Figure 4.6 and the average grain sizes are shown in Figure 4.7. The grain sizes of GR200 display consistent equiaxed globular grains throughout the cross-section; no columnar grains could be observed. The average grain sizes measured for GR200 ranged between 120±5μm and 140±10μm. The grain size distribution observed in GR400 are shown in Figure 4.7, and will be discussed in the following section.

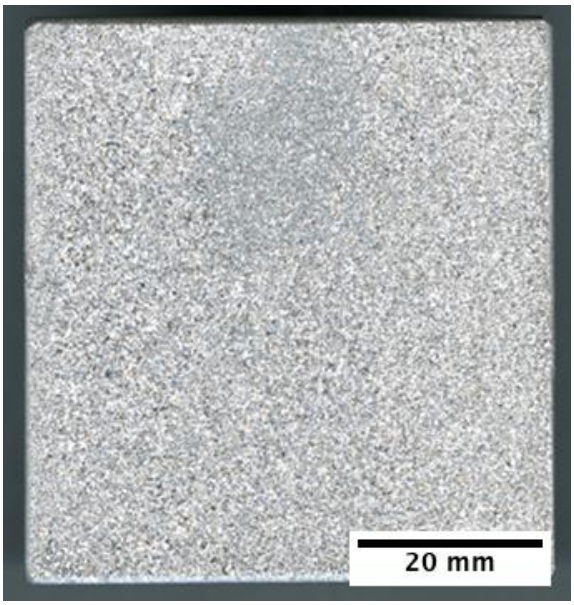


Figure 4.6: Macro-etched microstructure of GR200

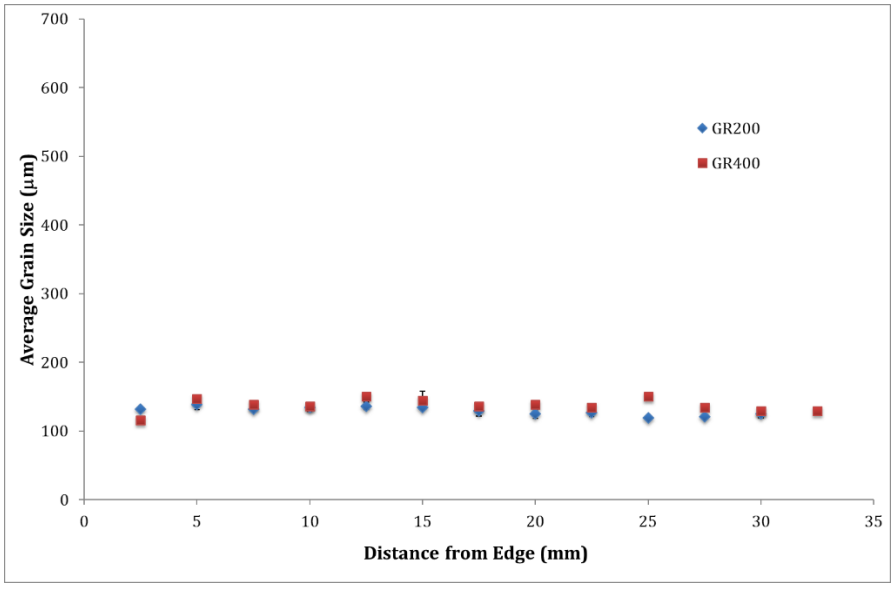


Figure 4.7: Average grain sizes of GR200 and GR400, maintaining the same scale as BA200 and BA400 to enable direct comparison

(e) GR400

The macro-etched cross-sections of GR400 can be seen in Figure 4.8 and the average grain sizes are shown in Figure 4.7. The grain sizes of GR400 are almost identical to those of GR400, displaying consistent equiaxed globular grains throughout the surface. The average grain sizes measured for GR400 ranged between 120±5μm and 150±5μm.



Figure 4.8: Macro-etched microstructure of GR400

(f) GRTP-1

The macro-etched cross-sections and average grain size of GRTP-1 are presented in Figure 4.9 and Figure 4.4 respectively. The microstructure displayed by the vertical cross section of GRTP-1 is identical to that of the horizontal cross-section. The grains observed are very fine, equiaxed and uniformly distributed throughout the cross-section. It was also interesting to note that neither cross-section exhibited sections of columnar grains near the edge. The grain sizes measured for the horizontal cross-section

of GRTP-1 ranged between 90±5μm and 150±5μm, with an overall average of 130±5μm.

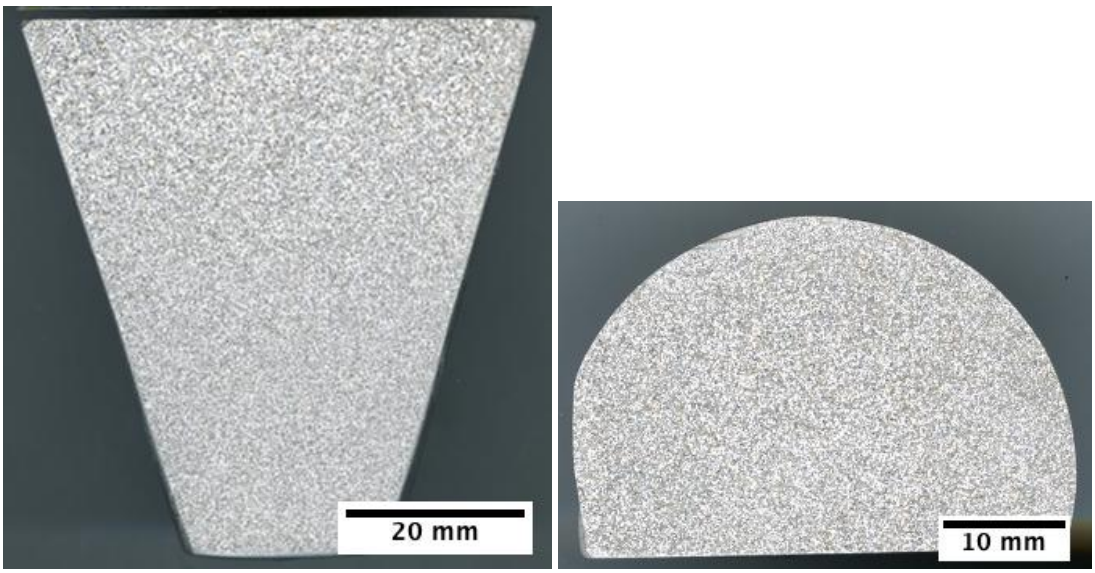


Figure 4.9: Macro-etched microstructure of GRTP-1

(g) ZR200

The macro-etched cross-sections of ZR200 can be seen in Figure 4.10 and the average grain sizes are shown in Figure 4.11. The grain size distribution observed in ZR400 are shown in Figure 4.11, and will be discussed in the following section.

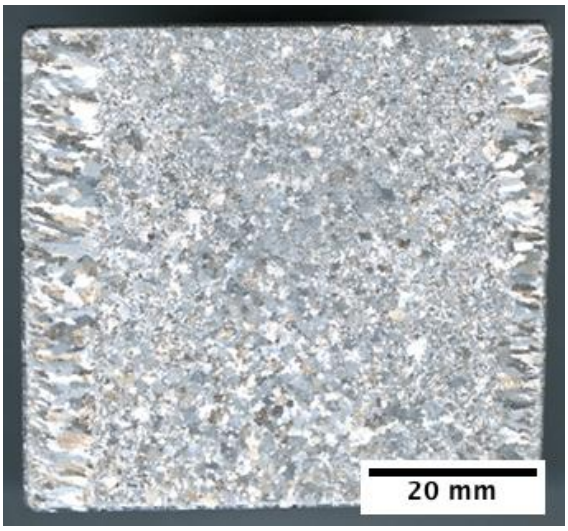


Figure 4.10: Macro-etched microstructure of ZR200

The grain sizes of ZR200 displayed a region of columnar grains near the edges, spanning to about 5mm in width. It can be seen from Figure 4.10 that the average grain sizes of ZR200 vary across the cross-section; just past the columnar sections, the sample displays an area of large grains, which gradually reduces to the finer grains towards the centre. The average grain sizes measured for ZR200 ranged between 130±5μm near the centre and 340±30μm just past the columnar section. There was, however, high level of porosity present on the macro-etched surface of ZR200, making it difficult to visually differentiate between the different grain boundaries, and therefore increasing the error margin significantly.

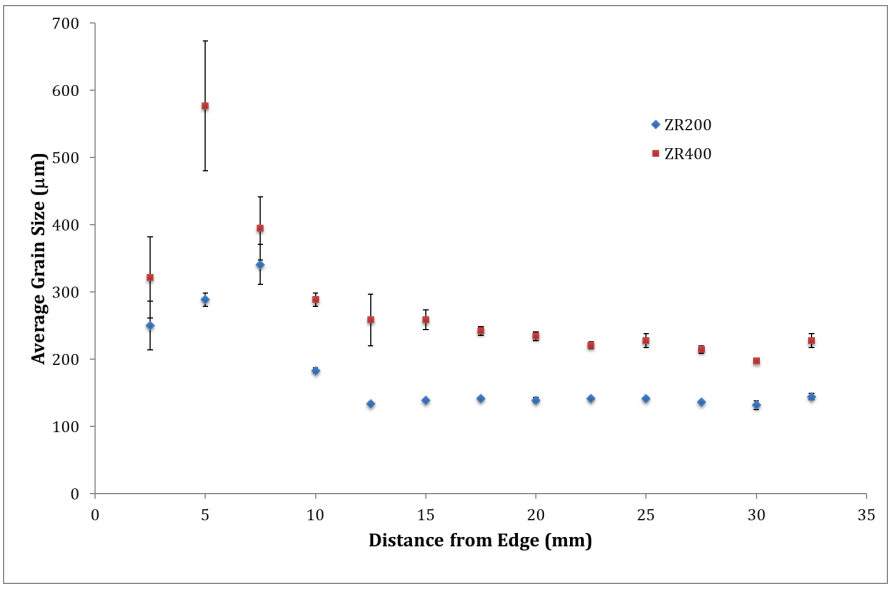


Figure 4.11: Average grain sizes of ZR200 and ZR400, maintaining the same scale as BA200 and BA400 to enable direct comparison

(h) ZR400

The macro-etched cross-sections of ZR400 can be seen in Figure 4.12 and the average grain sizes are shown in Figure 4.11.

The grain sizes of ZR400 are comparable to those of ZR200 in terms of the columnar grain section near the edges expanding to about 5mm, which then gradually get finer and more equiaxed towards the centre. The average grain sizes measured for ZR400 ranged from 260±5µm near the centre to 580±95µm just past the columnar section. The surface of ZR400 did not contain porosity and therefore grain size measurements were more accurate in comparison to ZR200.

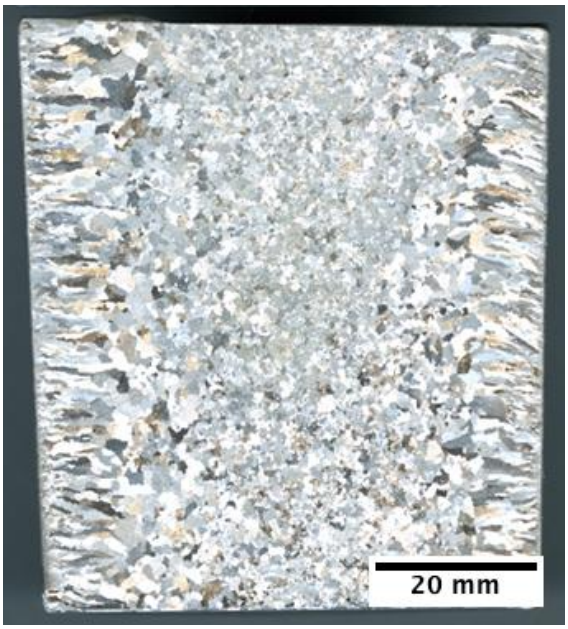


Figure 4.12: Macro-etched microstructure of ZR400

(i) ZRTP-1

The macro-etched cross-sections of ZRTP-1 are shown in Figure 4.13 and average grain sizes in Figure 4.4. The grains observed near the top half of the vertical cross-section of ZRTP-1 are rather large, where some measured up to several millimetres horizontally and up to about 20mm vertically.

There are some mildly columnar grains on the outer edges of the vertical cross-section, mainly obvious at the ~15mm horizontal plane where they appear to extend at an angle of 45^{o} to the horizontal plane. These columnar grains extend up to ~2.25mm from the centre, where the grains are smaller and more equiaxed. Some mildly columnar grains can also be observed at the top edge, which are vertically aligned. As in the case of BATP-1, it is not clear whether the vertically aligned columnar grains at the top

gradually changed angle to form the columnar section near the base, or whether the grains formed independently.

The horizontal cross-section of ZRTP-1 was very different to the vertical cross-section; large and small grains appeared to be interdispersed, and some very mildly columnar grains could be observed aligned along the radius. The grains varied significantly in size, whereby some large grains were over 10,000μm (over 1cm) in length and some smaller grains were around 150μm (0.15mm). The grain sizes measured for the horizontal cross-section of the ZRTP-1 sample ranged between 770±75μm and 2080±280μm, with an overall average of 1370±345μm. It is clear from Figure 4.13 and the magnitude of error that an average grain size for the horizontal cross-section of ZRTP-1 is not representative of the sample microstructure.

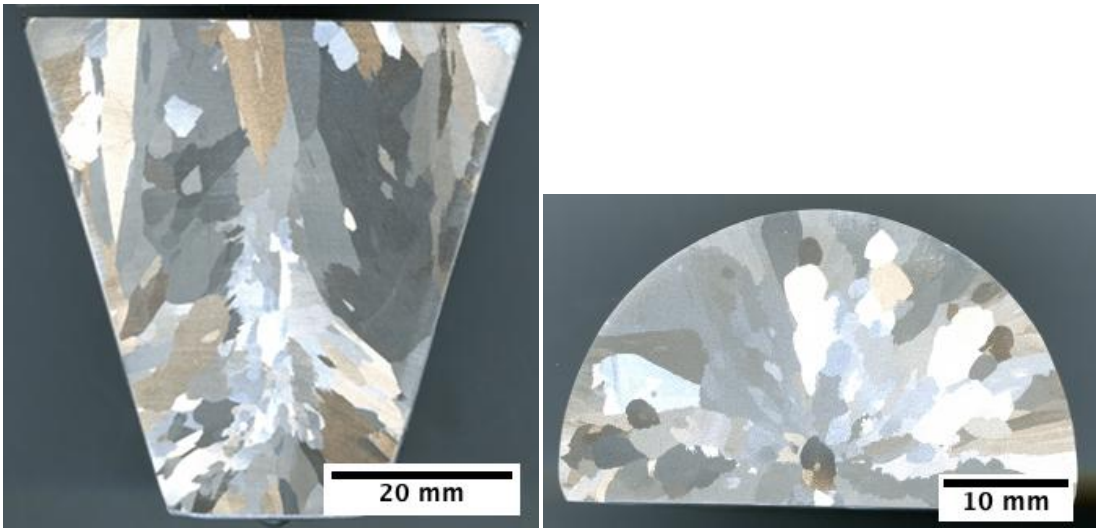


Figure 4.13: Macro-etched microstructure of ZRTP-1

(j) Summary

Based on macro-etched observations (summary provided in Table 4.2), it was established that the grain size differences between solidified slurries cast using steel enthalpy cans at 200ºC and 400ºC is around 20% for BA and negligible for GR. Although a grain size difference of 40-50% was observed for ZR, the measurements for ZR200 contained high error margins and therefore were not considered for further analysis. Only the solidified slurries cast with steel enthalpy cans at 200ºC and TP-1 samples from the 38mm horizontal planes were anodised to further establish their grain and cell sizes.

It was also noted that the objective to obtain consistent α-Al grain size between the sample with different chemical composition was achieved through the processing technique.

Table 4.2: Summary of grain sizes established from macro-etched samples

BA200 (μm)	BA400 (μm)	BATP-1 (μm)	GR200 (μm)	GR400 (μm)	GRTP-1 (μm)	ZR200 (μm)	ZR400 (μm)	ZRTP-1 (μm)
160-230	200-270	520-960	120-140	120-150	90-150	130-340*	260-580	770-2080

* The surface of ZR200 contained high level of porosity and therefore the measurements had high error margin.

4.3 Micro-etching (anodising)

The line-intercept method was employed to calculate the grain and cell sizes, going from the centre of the sample surface towards its edge. Two readings were taken from

each point, and their average was used to plot the graphs. The average of two measurements from a point of reference, i.e. either edge or centre, was calculated as an indication of the grain size in that area.

(a) Grain and cell sizes of BA200

The anodised micrographs of BA200 can be seen in Figure 4.14 and the average grain and cell sizes are shown in Figure 4.15.

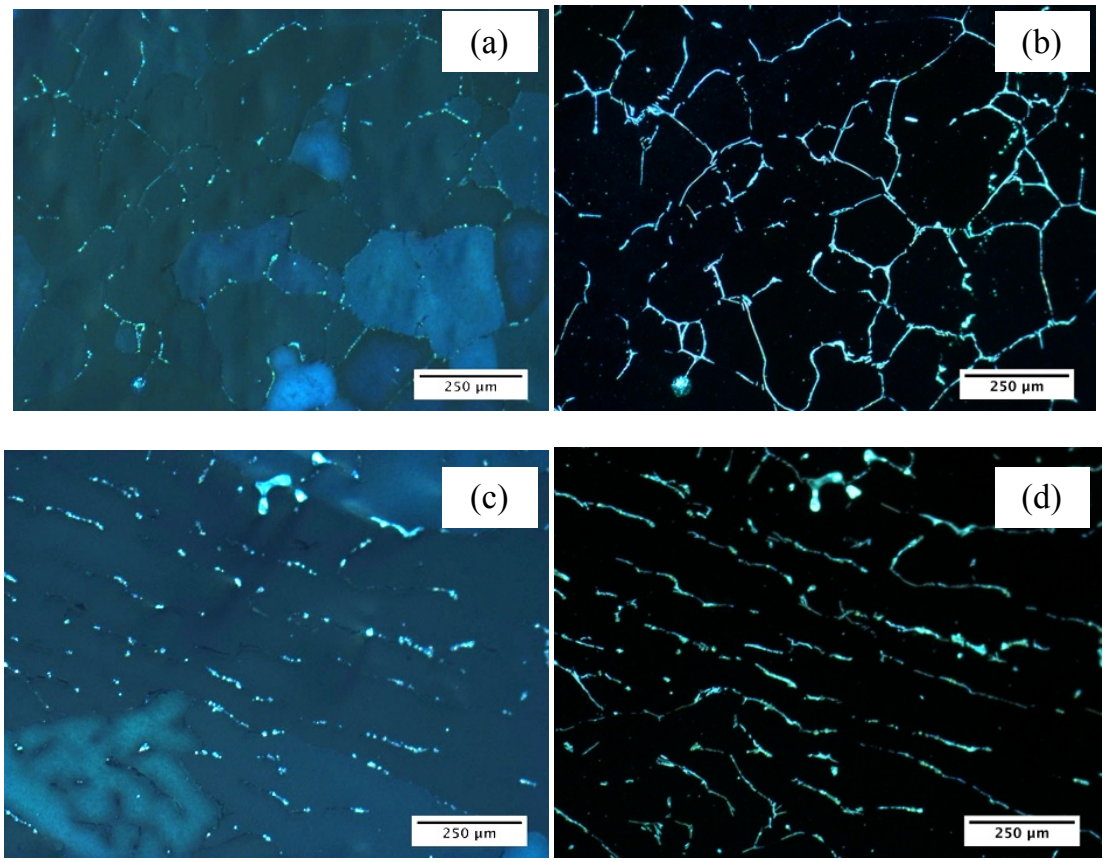


Figure 4.14: Optical micrographs of BA200 showing the grain and cell structures near (a, b) the centre and (c, d) the edge

The grain sizes of BA200 display significant variation in the average sizes, with an overall trend of getting finer towards the centre. The average grain sizes measured from the anodised samples are significantly larger than the measurements taken from macro-etched samples. The cell sizes however remain relatively consistent throughout the radius, gradually reducing in size. The average grain and cell sizes measured for BA200 near the centre were 290±25μm and 140±10μm, and near the edge were 610±150μm and 240±20μm respectively.

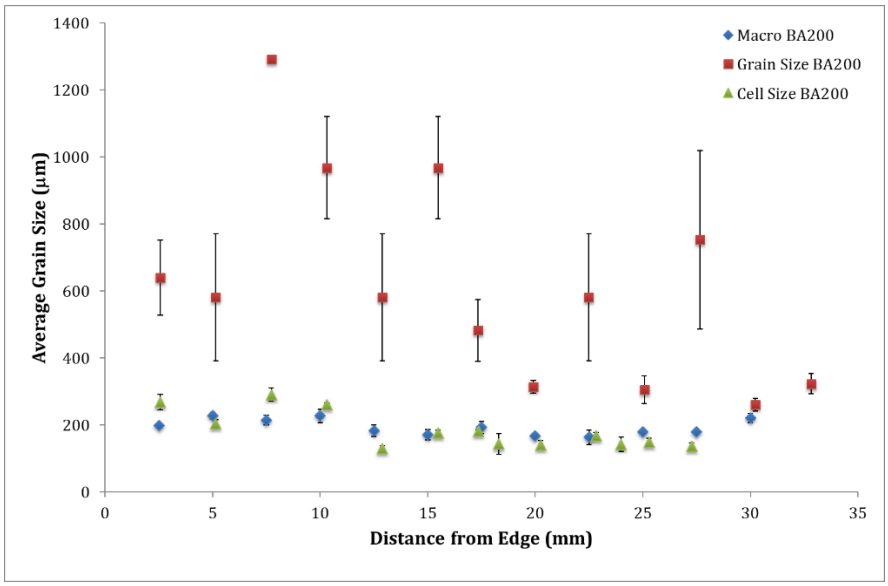


Figure 4.15: Average grain and cell sizes calculated from the macro-etched and anodised BA200 samples

(b) Grain sizes of BATP-1

The anodised micrographs of BATP-1 can be seen in Figure 4.16, while Figure 4.17 shows the difference in average grain size calculated from the macro-etched and anodised sample surfaces. The grain sizes of BATP-1 display a distinct trend of reducing in size towards the centre. The average grain sizes measured from the anodised

samples are once again significantly larger than the measurements taken from macro-etched samples. The cell sizes could not be calculated from the micrographs as they appear to be completely disconnected from each other, forming in what appears to be random structures. The average grain size measured for BATP-1 was 790±100µm.

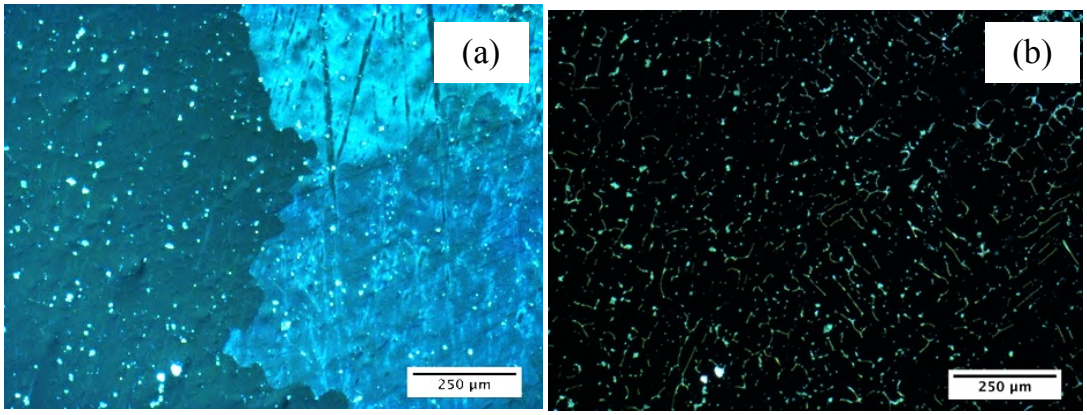


Figure 4.16: Optical micrographs of BATP-1 showing the (a) grain structures near the centre, and (b) the disconnected intermetallic particles

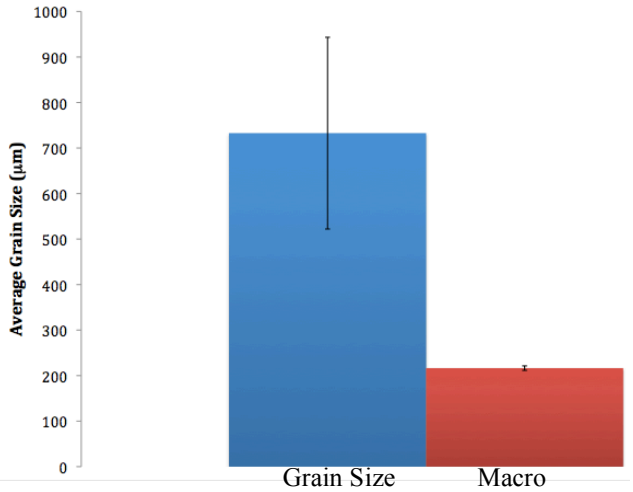


Figure 4.17: Average grain sizes calculated from the macro-etched and anodised BATP-1 samples

(c) Grain and cell sizes of GR200

The anodised micrographs of GR200 can be seen in Figure 4.18 and the average grain and cell sizes are shown in Figure 4.19.

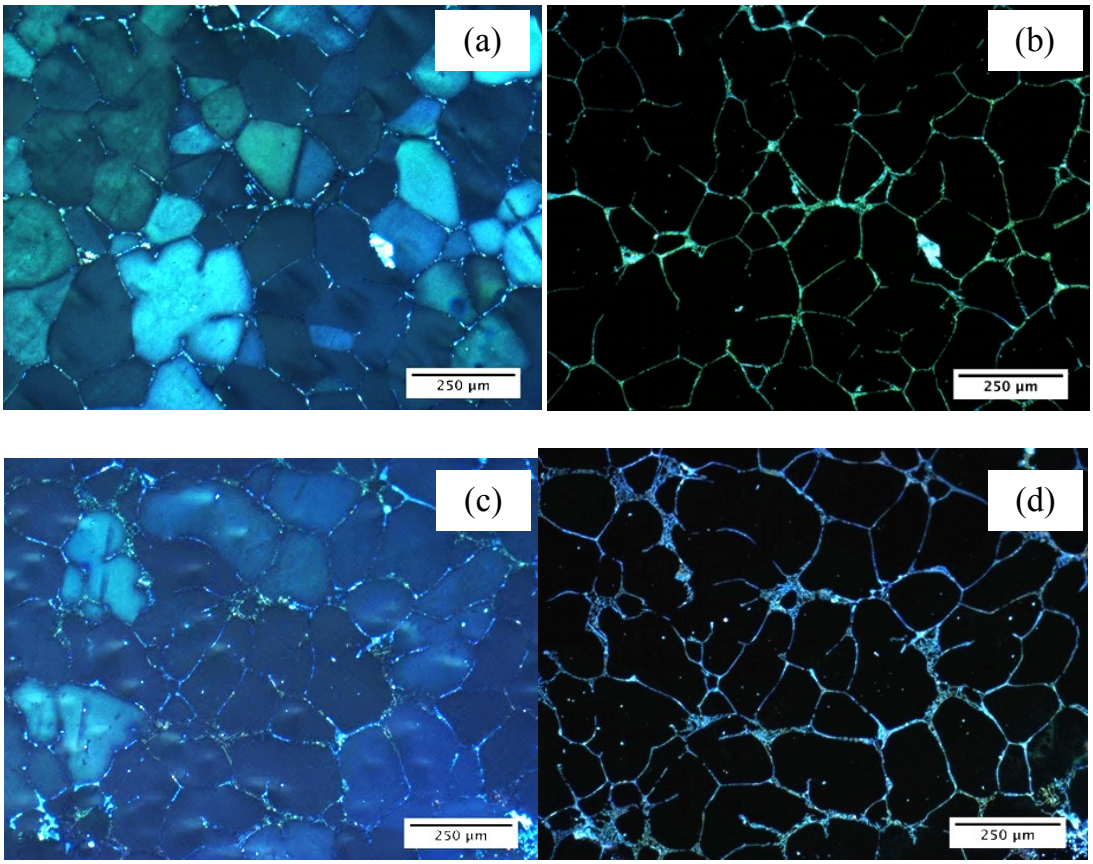


Figure 4.18: Optical micrographs of GR200 showing the grain and cell structures near (a, b) the centre and (c, d) the edge

GR200 display very similar grain and cell sizes, both of which display an overall trend of getting finer towards the centre. The average grain sizes measured from the anodised samples are comparable to the measurements taken from macro-etched samples. The average grain and cell sizes measured for GR200 near the centre were 170±20µm and 120±5µm, and near the edge were 260±20µm and 150±5µm respectively.

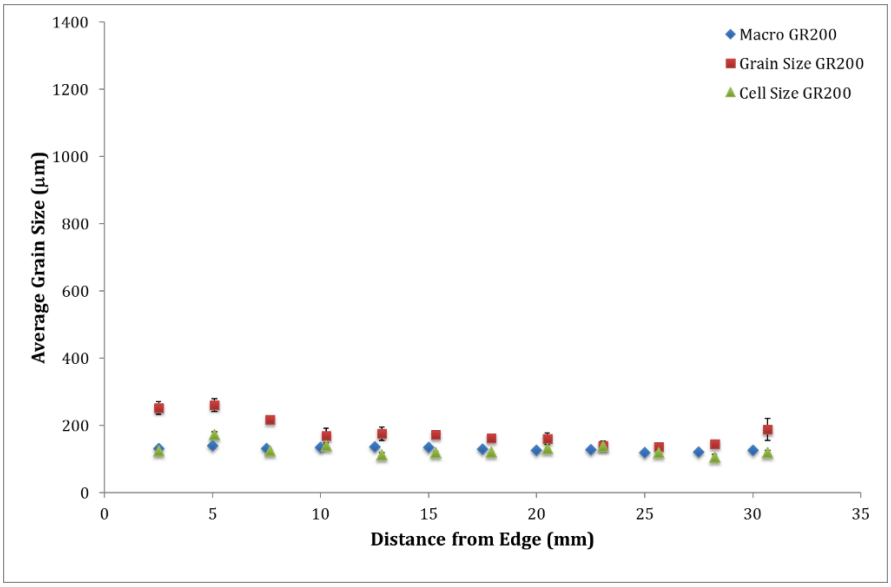


Figure 4.19: Average grain and cell sizes calculated from the macro-etched and anodised GR200 samples

(d) Grain and cell sizes of GRTP-1

The anodised micrographs of GRTP-1 can be seen in Figure 4.20 and the average grain and cell sizes are shown in Figure 4.21.

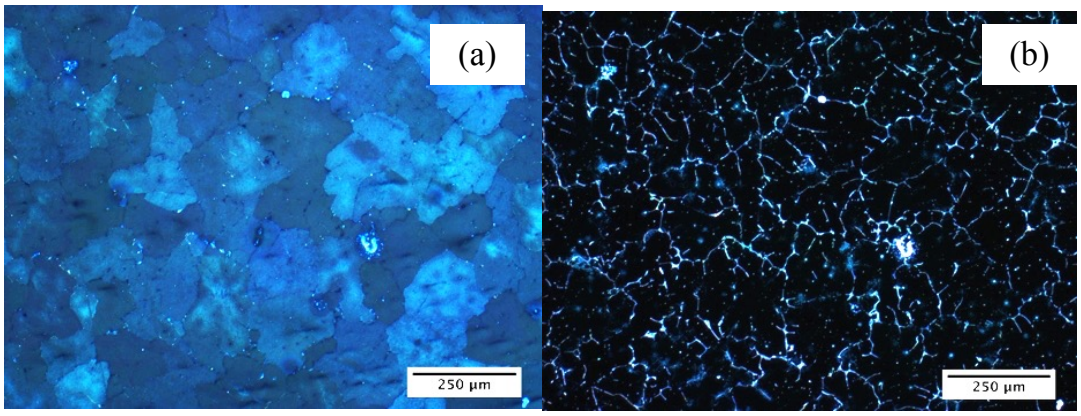


Figure 4.20: Optical micrographs of GRTP-1 showing the (a) grain and (b) cell structures near the centre

The grain sizes of GRTP-1 display very similar grain and cell sizes, which in turn is comparable in size to those of GR200. The average grain sizes measured from the anodised samples are comparable to the measurements taken from macro-etched samples. The average grain and cell sizes measured for GRTP-1 were 160±10μm and 110±5μm, respectively.

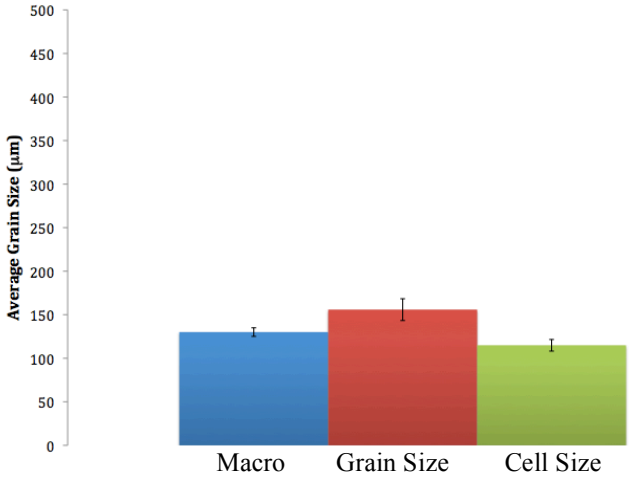


Figure 4.21: Average grain & cell sizes calculated from the macro-etched and anodised GRTP-1 samples

(e) Grain and cell sizes of ZR200

The anodised micrographs of ZR200 can be seen in Figure 4.22 and the average grain and cell sizes are shown in Figure 4.23.

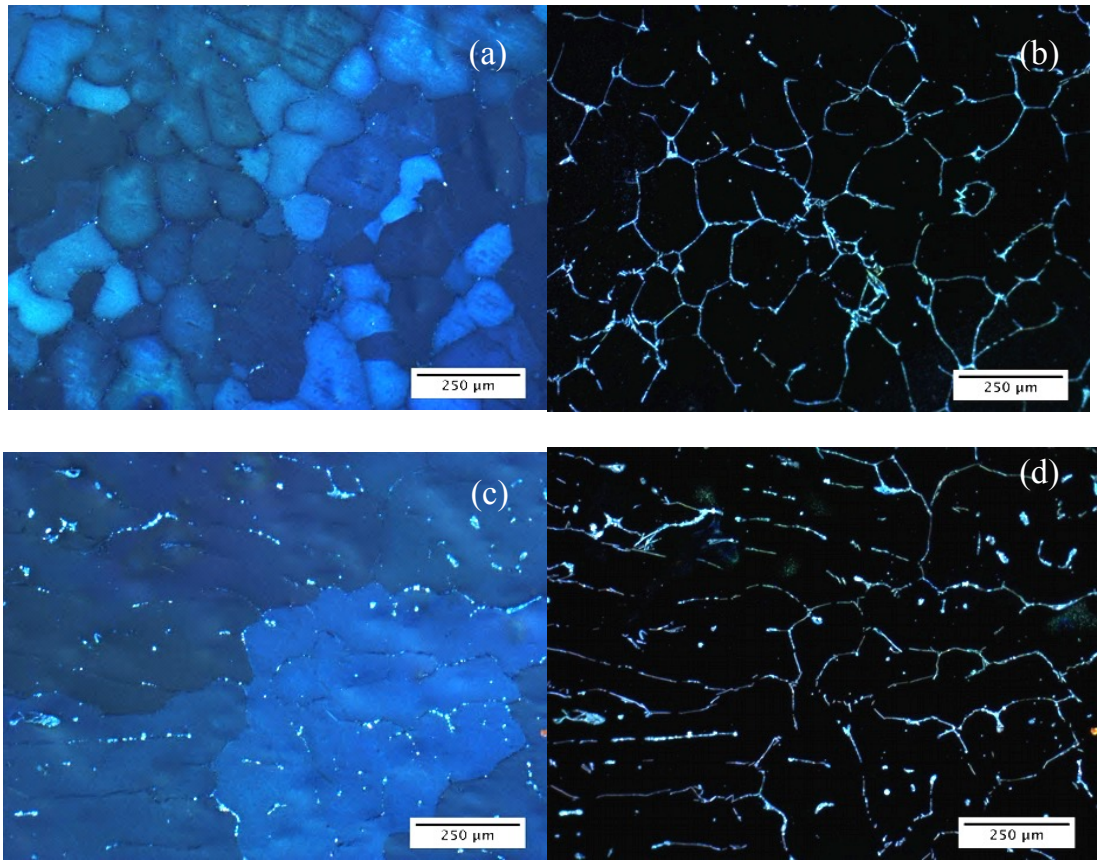


Figure 4.22: Optical micrographs of ZR200 showing the grain and cell structures near (a, b) the centre and (c, d) the edge

The grain sizes of ZR200 display significant variation in the average sizes, with an overall trend of getting finer towards the centre. The average grain sizes measured from the anodised samples are smaller than the measurements taken from macro-etched samples. The cell sizes however remain relatively consistent across the radius, gradually reducing in size. The average grain and cell sizes measured for ZR200 near the centre were 220±25µm and 150±15µm, and near the edge were 720±165µm and 330±25µm respectively.

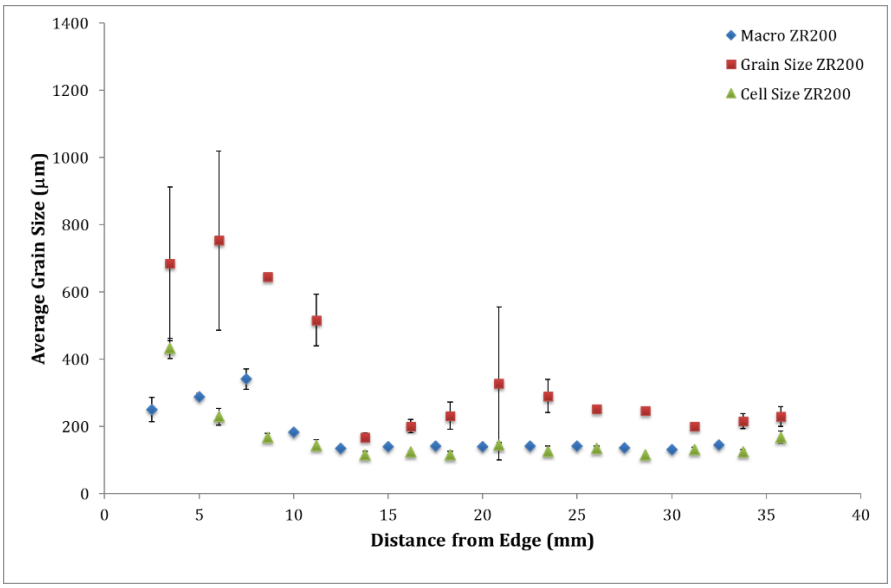


Figure 4.23: Average grain and cell sizes calculated from the macro-etched and anodised samples

(f) Summary

Once again, micro-etched observations (summary provided in Table 4.3) indicated that there are differences in grain and cell sizes between the alloys, as well as along the diameter of the sample surfaces. However, the grain and cell sizes of all three alloys are comparable near the centre, enabling direct comparison between the alloys.

Table 4.3: Summary of grain and cell sizes established from micro-etched samples

BA200 Grains (µm)	BA200 Cells (µm)	GR200 Grain (µm)	GR200 Cells (µm)	ZR200 Grains (µm)	ZR200 Cells (µm)
290-610	140-240	170-260	120-150	220-720	150-165

4.4 Thermodynamic Behaviour

(a) MTDATA Analysis and DSC Curves for BA

Figure 4.24 shows the MTDATA calculations of BA phases in the temperature range of 500ºC to 700ºC. MTDATA calculations of the equilibrium phases of BA calculated using the lever rule indicate that reactions involving the phases β-AlFeSi, α_c-AlFeSi and $Al_{13}Fe_4$ start melting around 580ºC, 630ºC and 640ºC respectively. According to the Scheil calculations however, Mg_2Si, β-AlFeSi, α_c-AlFeSi and $Al_{13}Fe_4$ start melting around 565ºC, 610ºC, 625ºC and 635ºC respectively (see Figure 4.25).

DSC analyses of BA200 carried out at heating rates of $10Kmin^{-1}$ and $40Kmin^{-1}$, and BATP-1 at a heating rate of $10Kmin^{-1}$ are shown in Figure 4.26. The phase transformation temperatures were calculated from their onset, and the summary of phase transformations temperatures observed in the DSC spectra correspond to the phases shown in Table 4.5. The phase transformation temperatures of GR and ZR will be discussed later in this section.

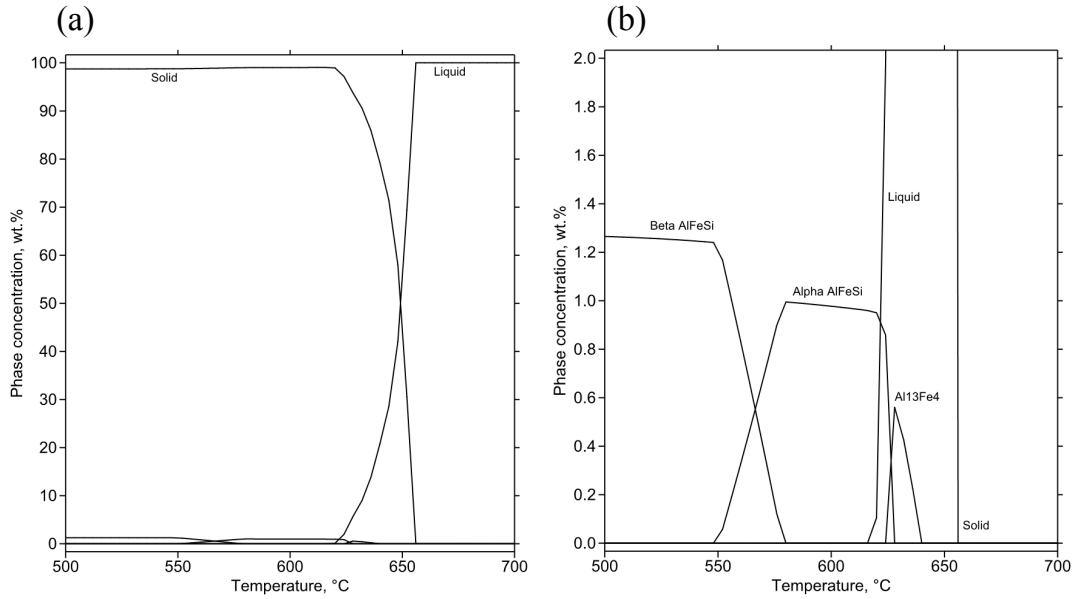


Figure 4.24: MTDATA calculations of the thermodynamic phase diagram of BA assuming Lever conditions, showing (a) the main phases and (b) the magnified view for the minor phases

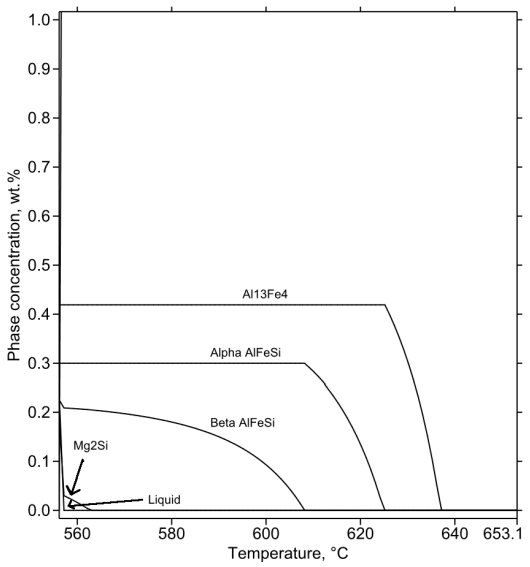


Figure 4.25: MTDATA calculations of the thermodynamic phase diagram of BA assuming Scheil conditions.

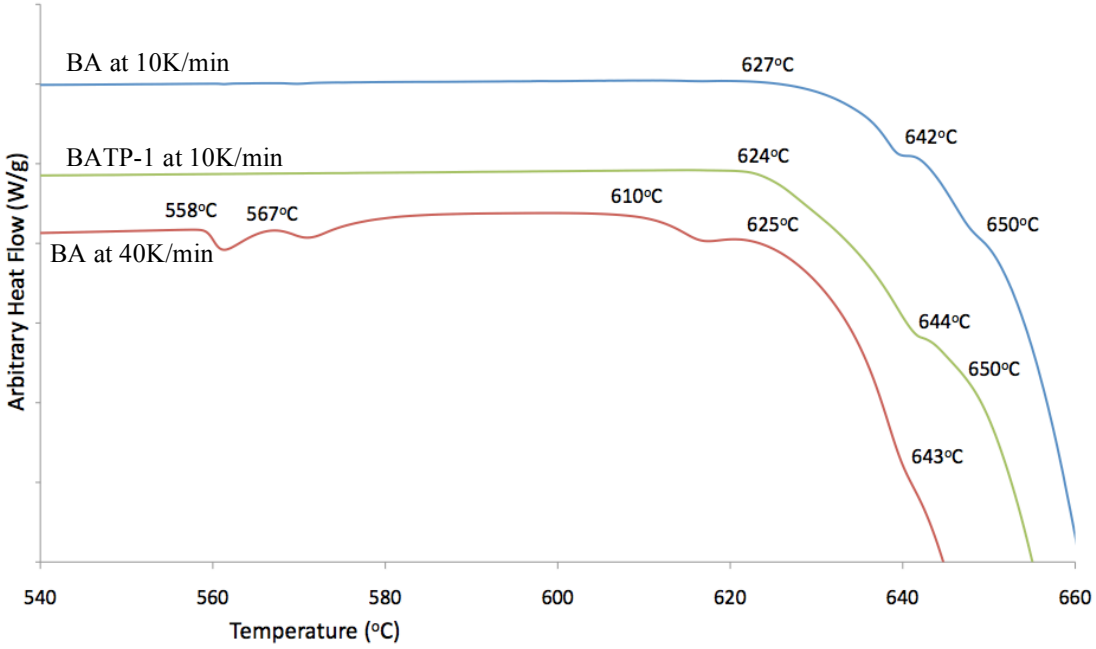


Figure 4.26: DSC Spectra of BA200 heated at 10 and 40K/min, and BATP-1 heated at 10K/min.

(b) MTDATA Analysis and DSC Curves for GR

Figure 4.27 shows the MTDATA calculations of GR phases in the temperature range of 500ºC to 700ºC. MTDATA calculations of the equilibrium phases of GR calculated using the lever rule and Scheil calculations both indicate the temperatures corresponding to reactions involving the phases β-AlFeSi, α_c-AlFeSi and $Al_{13}Fe_4$ remain the same: around 570ºC, 630ºC and 640ºC according to lever rule calculations, and around 610ºC, 625ºC and 635ºC according to Scheil calculations (Figure 4.28). Scheil calculation also indicate that Mg_2Si starts melting around 565ºC.

DSC analyses of GR200 carried out at heating rates of 10Kmin^{-1} and 40Kmin^{-1}, and GRTP-1 at heating rate of 10Kmin^{-1} are shown in Figure 4.29, and the summaries of phase transformation temperatures are given in Table 4.5.

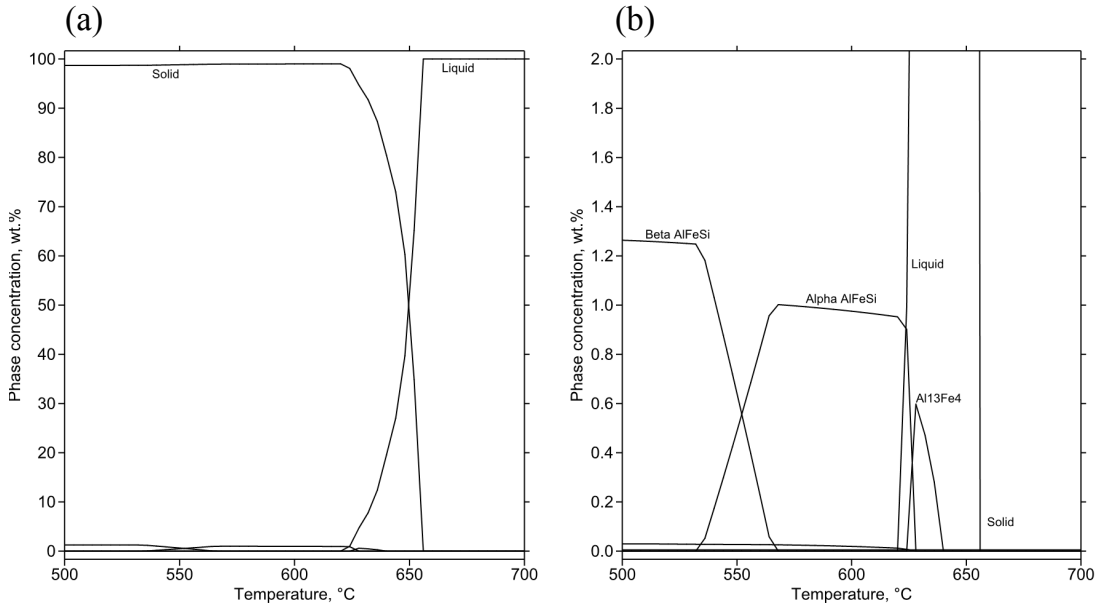


Figure 4.27: MTDATA calculations of the thermodynamic phase diagram of GR assuming Lever conditions, showing (a) the main phases and (b) the magnified view for the minor phases

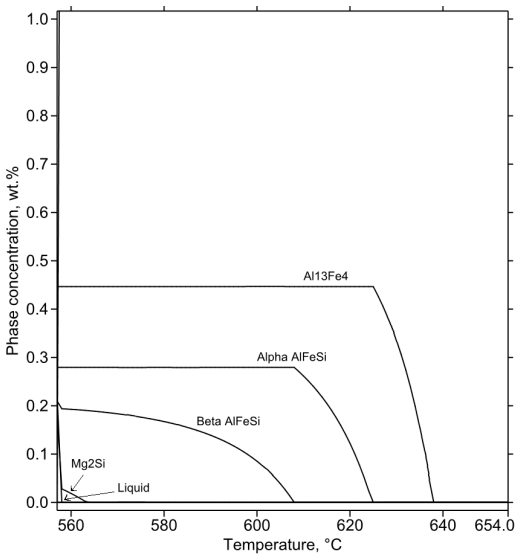


Figure 4.28: MTDATA calculations of the thermodynamic phase diagram of GR assuming Scheil conditions

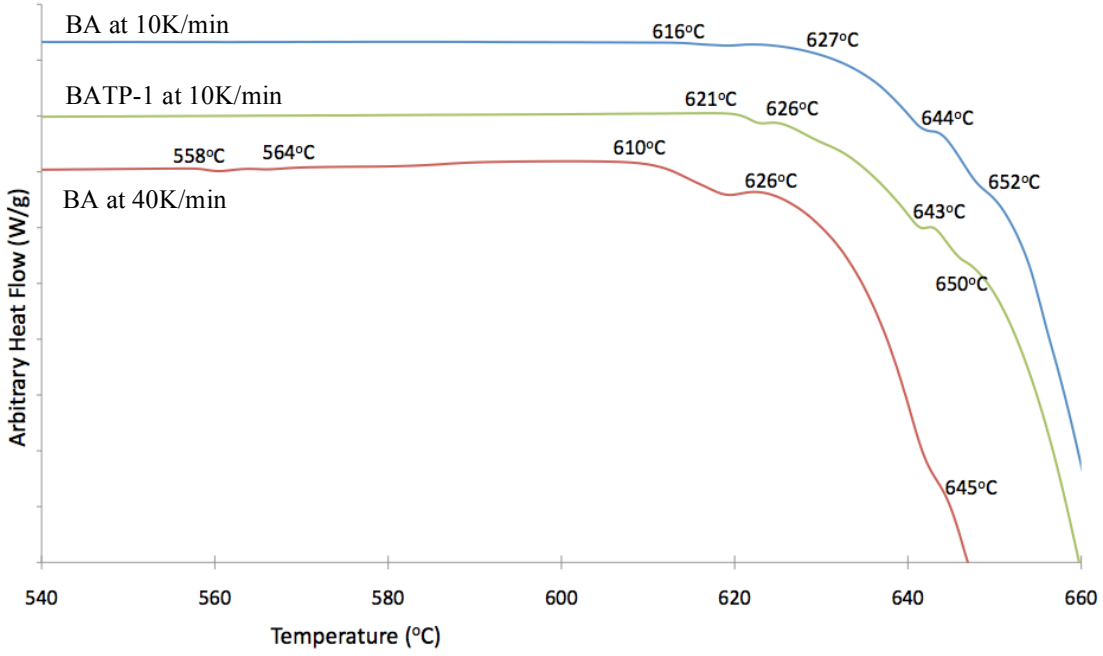


Figure 4.29: DSC Spectra of GR200 heated at 10 and 40K/min, and GRTP-1 heated at 10K/min.

(c) MTDATA Analysis and DSC Curves for ZR

The MTDATA software available for this project did not include Zr interactions in its database, and therefore the phase diagrams for this alloy system could not be calculated using MTDATA. However, due to the higher levels of Fe and Si in ZR compared to BA and GR, a thermodynamic phase diagram was calculated using the Al, Fe, Si and Mg content of the ZR alloy. Figure 4.30 shows the calculations in the temperature range of 500ºC to 700ºC. Once again, the MTDATA calculations of the equilibrium phases of ZR calculated using the lever rule indicate that the phases β-AlFeSi, α_c-AlFeSi and $Al_{13}Fe_4$ start melting around 590ºC, 630ºC and 645ºC, while the Scheil calculations indicate around 610ºC, 625ºC and 640ºC respectively. The Scheil calculations do not indicate any presence of Mg_2Si in this alloy.

DSC analyses of ZR200 carried out at heating rates of 10Kmin^{-1} and 40Kmin^{-1}, and ZRTP-1 at a heating rate of 10Kmin^{-1} are shown in Figure 4.32, and the summaries of phase transformation temperatures are given in Table 4.5.

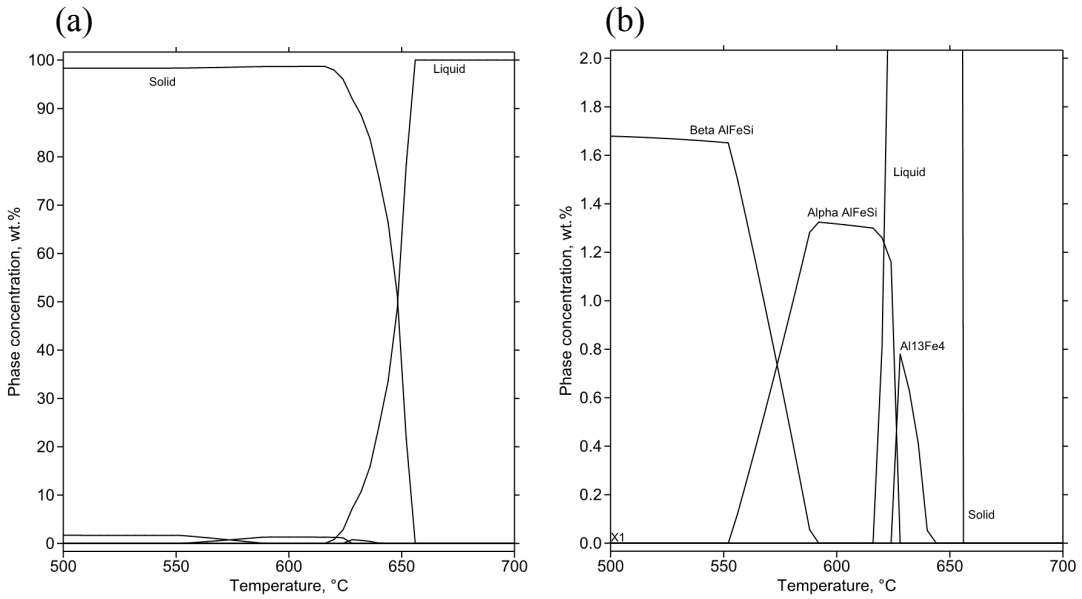


Figure 4.30: MTDATA calculations of the thermodynamic phase diagram of the Al-Fe-Si-Mg components of the ZR alloy assuming Lever conditions, showing (a) the main phases and (b) the magnified view for the minor phases

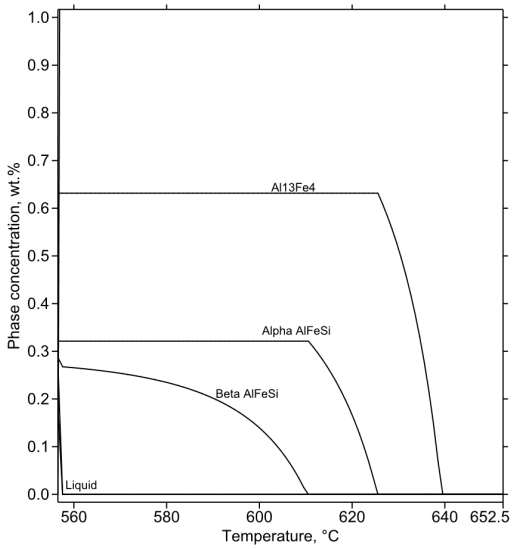


Figure 4.31: MTDATA calculations of the thermodynamic phase diagram of the Al-Fe-Si-Mg components of the ZR alloy assuming Scheil conditions

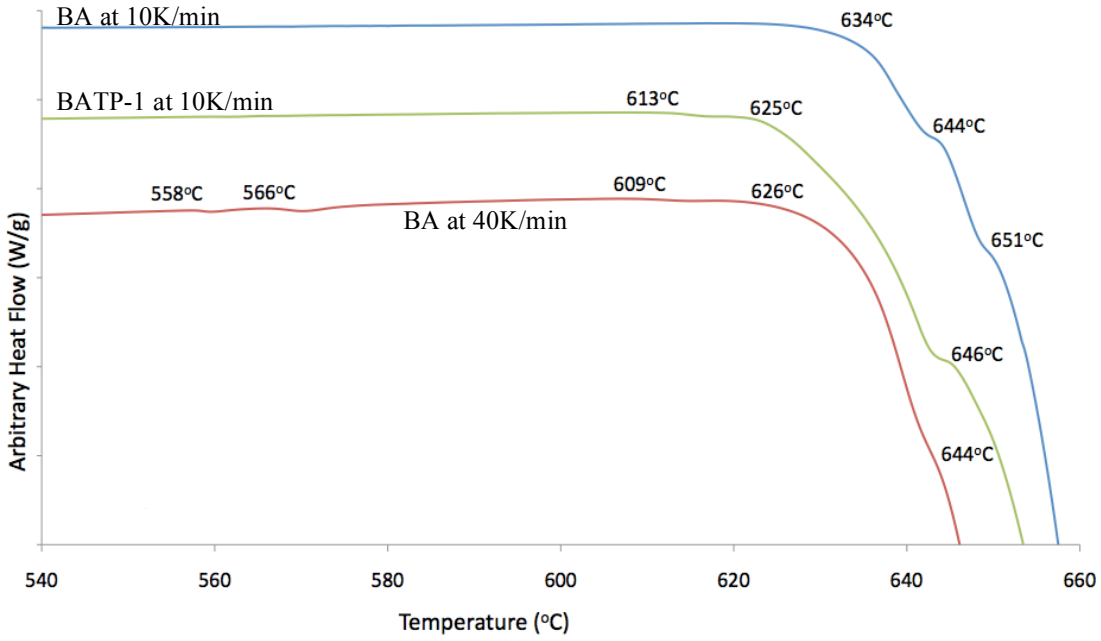


Figure 4.32: DSC Spectra of ZR200 heated at 10 and 40K/min, and ZRTP-1 heated at 10K/min.

(d) Summary

The summary of phase transformation temperatures, i.e. the starting temperature on cooling, predicted using the MTDATA lever rule and Scheil calculations are given in Table 4.4. Based on these MTDATA calculations, it can be assumed that the phase transformation temperatures observed in the DSC traces correspond to the phases shown in Table 4.5.

It is clear from Table 4.5 that α_c-AlFeSi is present in all the alloys, while β-AlFeSi was mainly observed in GRTP-1, GR200 and BA200. The DSC traces (see Figure 4.29 section 0) also indicate that the heating rate of 40K/min had the greatest effect on the β-AlFeSi phase transformations. Thus, it can be assumed that some of the β-AlFeSi phase was metastable in the α-Al matrix.

Thus, the DSC peaks observed at 616ºC, 621ºC and 613ºC for GR200, GRTP-1 and ZRTP-1 at 10K/min may be attributed to the metastable nature of β-AlFeSi phase. Since the DSC traces obtained from 40K/min reflect the phase transformation temperatures predicted by Scheil calculations, it can be assumed that the slower heating rate of 10K/min provides sufficient time for the metastable β-AlFeSi phase to transform to either a different phase or crystal structure, causing a shifted peak on the traces.

The predicted phases and their fractions according to Scheil calculations are presented in Table 4.6 to Table 4.8.

Table 4.4: Summary of phase transformation temperatures calculated on MDATA for level rule and Scheil conditions

	Lever Rule			Scheil Rule		
Phase*	**BA**	**GR**	**ZR**	**BA**	**GR**	**ZR**
Liquid	620°C	620°C	620°C	557°C	558°C	557°C
Mg_2Si	-	-	-	562°C	563°C	-
β-AlFeSi	580°C	570°C	590°C	607°C	607°C	610°C
α_c-AlFeSi	630°C	630°C	630°C	624°C	624°C	625°C
$Al_{13}Fe_4$	640°C	640°C	645°C	636°C	637°C	639°C
α-Al	655°C	655°C	655°C	653°C	654°C	653°C

*** the phases given are MTDATA predictions of whether certain phases are present, but not what the phase transformation might be.**

Table 4.5: Phase transformation temperatures observed in DSC spectra analysed

Phase	Heating Rate								
	10K/min						40K/min		
	BA	**GR**	**ZR**	**BA TP-1**	**GR TP-1**	**ZR TP-1**	**BA**	**GR**	**ZR**
Liquid	-	-	-	-	-	-	558°C	558°C *	558°C *
Mg_2Si	-	-	-	-	-	-	567°C	564°C *	566°C *
β-AlFeSi	-	616°C *	-	-	621°C	613°C *	610°C	610°C	609°C *
α-AlFeSi	627°C	627°C	634°C	624°C	626°C	625°C	625°C	626°C	626°C
$Al_{13}Fe_4$	642°C	644°C	644°C	644°C	643°C	646°C	643°C	645°C	644°C *
α-Al	650°C	652°C	651°C	650°C	650°C *	-	-	-	-

*** denotes peaks that were hardly visible on the DSC traces.**

Table 4.6: Phases and their fractions predicted by Scheil calculations for BA200

BA200	Temperature	653°C	636°C	624°C	607°C	562°C	557°C
Percentage of Phase Present	Liquid	85.58%	20.10%	10.93%	6.08%	2.64%	2.38%
	Mg_2Si	0.00%	0.00%	0.00%	0.00%	$3.78x10^{-3}$%	$4.73x10^{-3}$%
	β-AlFeSi	0.00%	0.00%	0.00%	$1.49x10^{-2}$%	$8.38x10^{-4}$%	$6.03x10^{-4}$%
	α_c-AlFeSi	0.00%	0.00%	0.03%	0.00%	0.00%	0.00%
	$Al_{13}Fe_4$	0.00%	0.05%	0.00%	0.00%	0.00%	0.00%
	α-Al	16.42%	1.30%	0.46%	0.18%	0.04%	0.04%

Table 4.7: Phases and their fractions predicted by Scheil calculations for GR200

GR200	Temperature	654°C	637°C	624°C	607°C	563°C	558°C
Percentage of Phase Present	Liquid	87.86%	20.06%	10.23%	5.70%	2.52%	2.26%
	Mg_2Si	0.00%	0.00%	0.00%	0.00%	$2.39x10^{-3}$%	$4.61x10^{-3}$%
	β-AlFeSi	0.00%	0.00%	0.00%	$1.38x10^{-2}$%	$8.43x10^{-4}$%	$5.90x10^{-4}$%
	α_c-AlFeSi	0.00%	0.00%	0.02%	0.00%	0.00%	0.00%
	$Al_{13}Fe_4$	0.00%	0.05%	0.00%	0.00%	0.00%	0.00%
	α-Al	12.14%	1.34%	0.46%	0.18%	0.04%	0.04%

Table 4.8: Phases and their fractions predicted by Scheil calculations for ZR200

ZR200	Temperature	653°C	639°C	625°C	610°C	557°C
Percentage of Phase Present	Liquid	87.86%	25.77%	12.49%	7.08%	2.75%
	β-AlFeSi	0.00%	0.00%	0.00%	$1.45x10^{-2}$%	$8.34\ x10^{-4}$%
	α_c-AlFeSi	0.00%	0.00%	0.03%	0.00%	0.00%
	$Al_{13}Fe_4$	0.00%	0.07%	0.00%	0.00%	0.00%
	α-Al	12.14%	1.86%	0.53%	0.20%	0.03%

4.5 Intermetallic Phase Identification

To establish the calibration accuracy of the x-ray diffraction (XRD) equipment, the XRD spectrum of pure Si powder was obtained and compared with the data provided by JCPDS [132]. The XRD spectrum can be seen in Figure 4.33. According to JCPDS, pure Si should display a peak at 28.44º 2θ corresponding to crystallographic plane (111), another at 47.30º 2θ for the (220) plane, and at 56.12º 2θ for (311) plane, between 15º and 65º 2θ. The remaining peaks are outside the range of interest. The spectrum obtained from this observation displayed peaks at 28.45º, 47.30º and 56.10º 2θ, thus indicating that the equipment calibration was accurate. The relative heights of the peaks were also in the correct proportions.

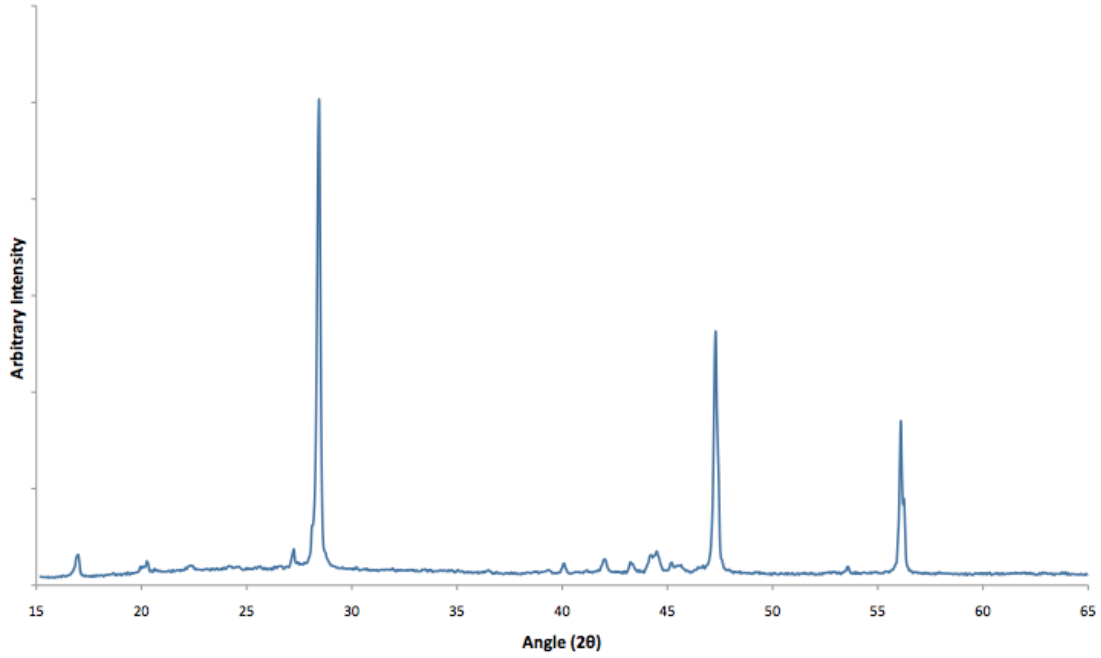


Figure 4.33: XRD Spectrum of pure Si, used for calibration

Lever rule and Scheil calculations both indicate the presence of $Al_{13}Fe_4$ phase, while Scheil calculations indicate the presence of Mg_2Si. Thus, all XRD spectra obtained

from samples were cross-referenced against the theoretical calculations for metastable α_c-AlFeSi phase, the reference spectra for β-AlFeSi phase, Mg_2Si and Al-5Fe (where $Al_{13}Fe_4$ is predominant phase) obtained using JCPDS reference patterns provided by the International Centre for Diffraction Data (shown in Figure 4.34).

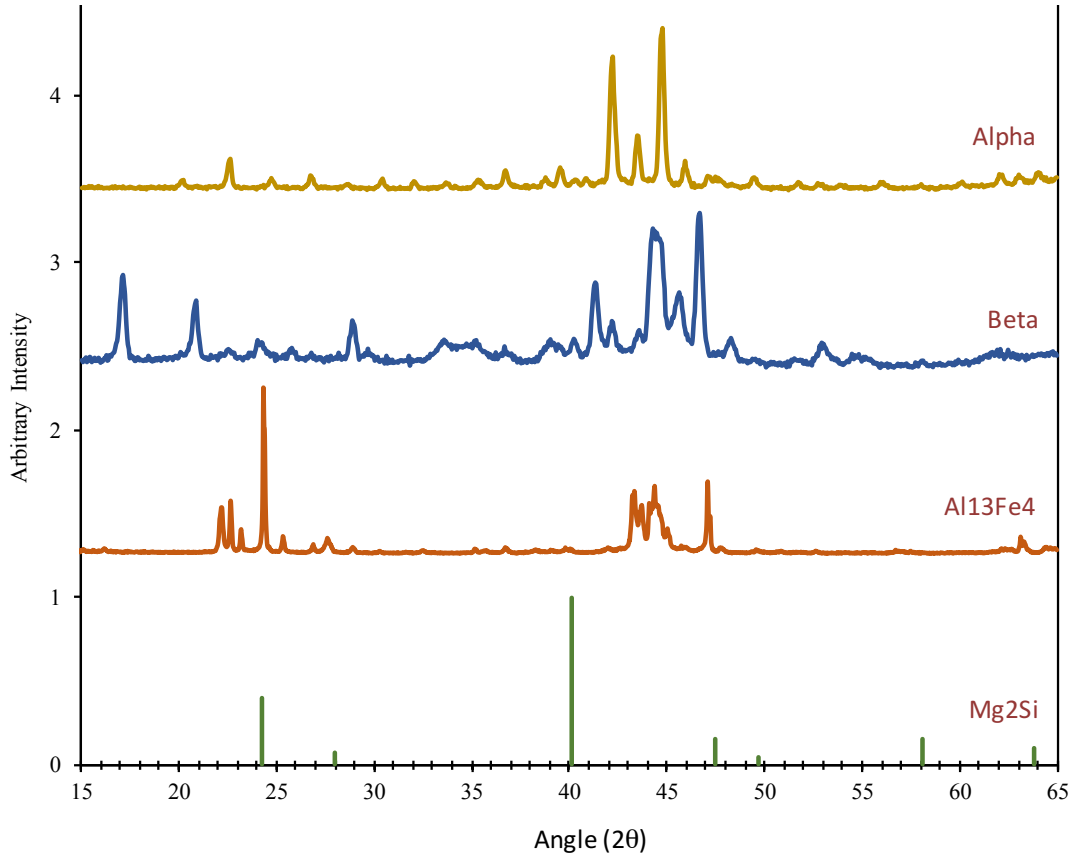


Figure 4.34: XRD Spectra showing theoretical calculations for α_c-AlFeSi phase, and reference spectra obtained using JCPDS reference patterns for β-AlFeSi, Mg_2Si and $Al_{13}Fe_4$ phases.

4.5.1 Intermetallic Phase Selection along the Radius and Length of BA200

The XRD spectra obtained from extracted phases of BA200 along the radius and length (BA200C at a height of 150-155mm from base, BAL2 at a height of 65-70mm from

base, and BAL3 at a height of 15-20mm from base) are all plotted in the same figure for direct comparison, and shown in Figure 4.35.

It can be seen that the phase selection remained consistent along the sample radius and length, and almost all of the peaks corresponded to either α_c-AlFeSi or β-AlFeSi phases. All the XRD spectra displayed α_c-AlFeSi as the predominant phase.

The characteristic β-AlFeSi peaks at 17.0º and 20.8º 2θ were exhibited with varying intensities. This variation between peak intensities is possibly due to preferred orientation caused by the sample preparation technique (texturing effect – see section 3.7.1). The characteristic β-AlFeSi peak at 29.0º 2θ, exhibited by all the samples, appeared to be shifted to 28.6º 2θ. The shift in those peaks could be either due to α_c-AlFeSi and β-AlFeSi peaks overlapping each other, or due to a different phase being present. α_c-AlFeSi and β-AlFeSi phases both exhibit peaks at 35.4º, 36.7º, 38.8º and 48.25º 2θ, and therefore it was not possible to conclusively determine which phase was causing the peaks at those angles on the spectra.

Very small amounts of Mg_2Si and $Al_{13}F_4$ phases were also observed, alongside a peak at 37.25º which did not correspond to any of the 4 phases referenced.

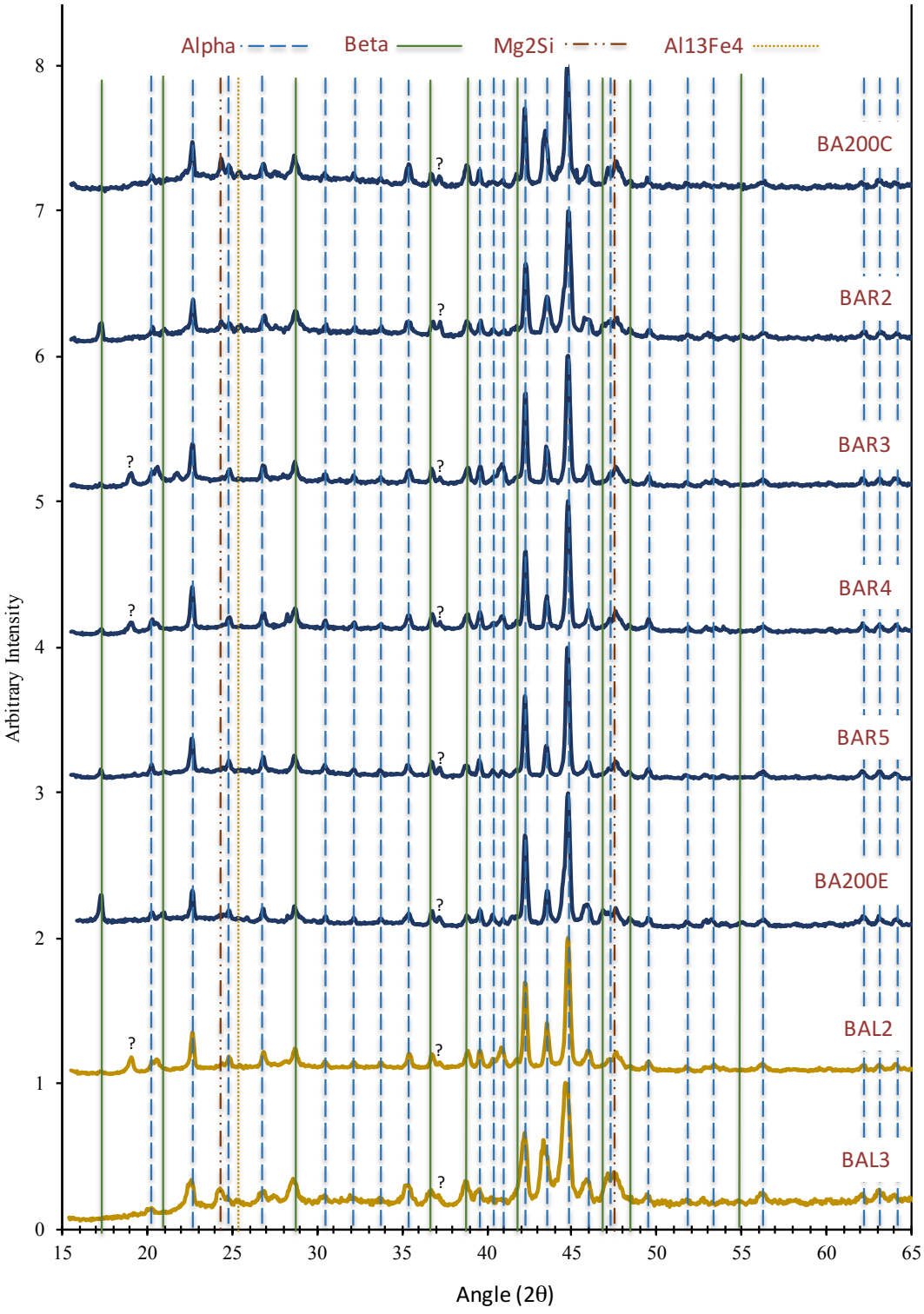


Figure 4.35: XRD Spectra showing phases present along the radius and length of BA200

4.5.2 Intermetallic Phase Selection in BA Alloys

The XRD spectra obtained from extracted phases of BA200C, BA200E, BA400 and BATP-1 are shown in Figure 4.36.

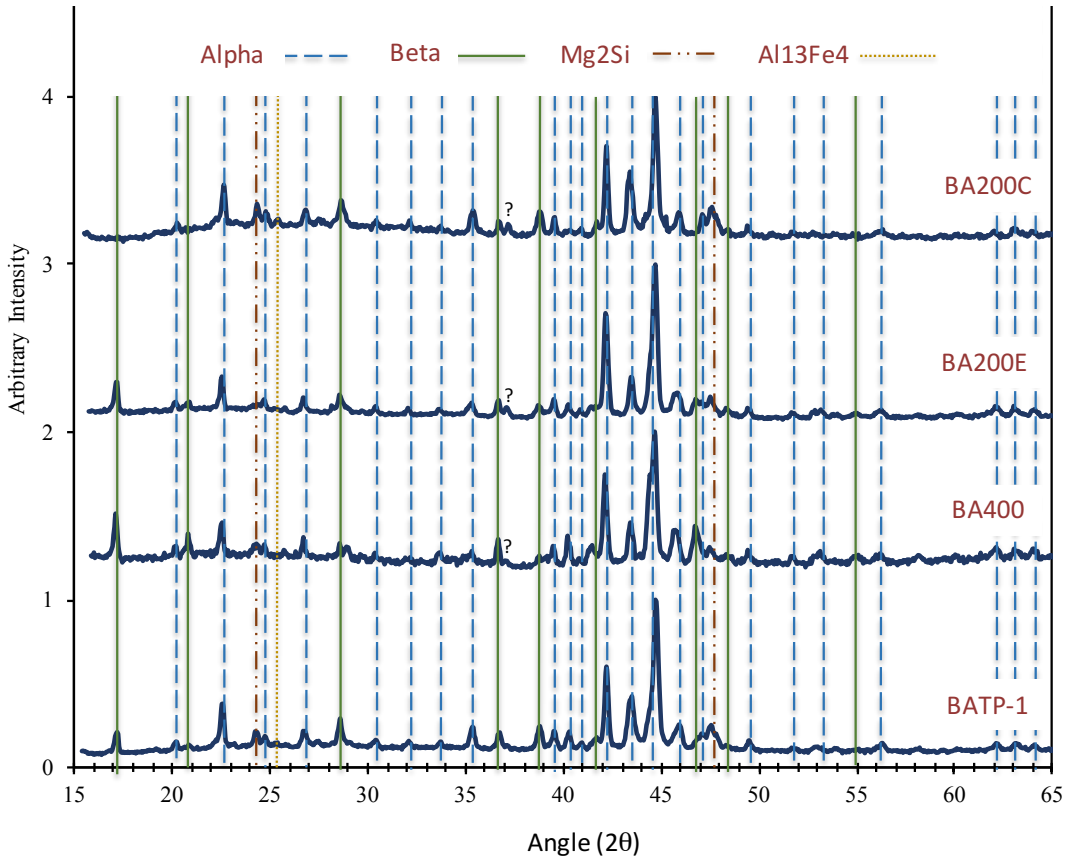


Figure 4.36: XRD Spectra showing phases present in BA alloys, manufactured using different processing techniques

Once again most of the BA400 and BATP-1 peaks corresponded to either α_c-AlFeSi or β-AlFeSi phase, with α_c-AlFeSi being the predominant phase. A similar set of characteristic β-AlFeSi peaks were exhibited by both BA400 and BATP-1, and the shifted β-AlFeSi peak (28.6º 2θ instead of 29.0º 2θ) and small amounts of Mg_2Si and $Al_{13}Fe_4$ were also observed.

4.5.3 Intermetallic Phase Selection in GR Alloys

On establishing that the phase selection did not change across the radius of BA200, GR200C and GR200E were selected for analysing the phase selection along the radius.

The XRD spectra of extracted intermetallic particles from GR200C, GR200E, GR400 and GRTP-1 are shown in Figure 4.37.

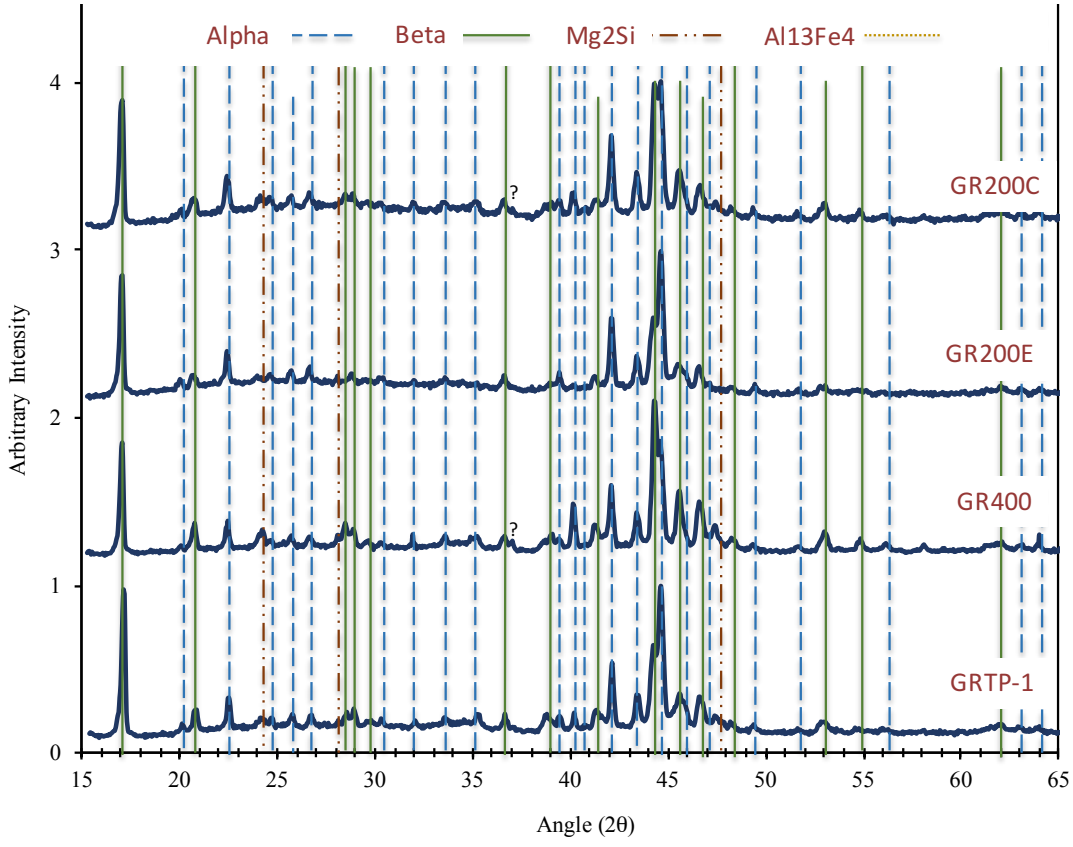


Figure 4.37: XRD Spectra showing phases present in GR alloys, manufactured using different processing techniques

Once again, the spectra closely resembled each other and almost all peaks corresponded to either α_c-AlFeSi or β-AlFeSi phases, while a few could be attributed to Mg_2Si and $Al_{13}Fe_4$ phases. Neither phase appeared to be predominant in this alloy. The characteristic β-AlFeSi peaks at 17.0º and 20.8º 2θ were exhibited by both samples with relatively high intensities. Unlike BA alloys, no shift was observed for the β-AlFeSi peak at 29.0º 2θ (exhibited by all samples); they were displayed at 28.9º 2θ. Also, several additional β-AlFeSi peaks were observed across the spectra at 20.6º, 24.0º, 25.7º, 41.3º, 44.3º, 45.6º, 46.6º, 52.8º, 54.5º and 62.0º 2θ.

4.5.4 Intermetallic Phase Selection in ZR Alloys

ZR200C, ZR200E, ZR400 and ZRTP-1 were examined for phase selection, and the XRD spectra from the extracted phases are shown in Figure 4.38. The phase selection was consistent between all the samples, and almost all peaks corresponded to α_c-AlFeSi and β-AlFeSi phases, with a few corresponding to Mg_2Si. No peaks corresponding to $Al_{13}Fe_4$ were observed. The samples appeared to predominantly exhibit characteristic α_c-AlFeSi peaks, indicating that α_c-AlFeSi is the prevalent phase in the ZR alloy. The characteristic β-AlFeSi peaks at 17.0º and 20.8º 2θ were not visible, and the β-AlFeSi peak at 29.0º 2θ appeared to be shifted to about 28.6º 2θ (as in the case of BA alloys).

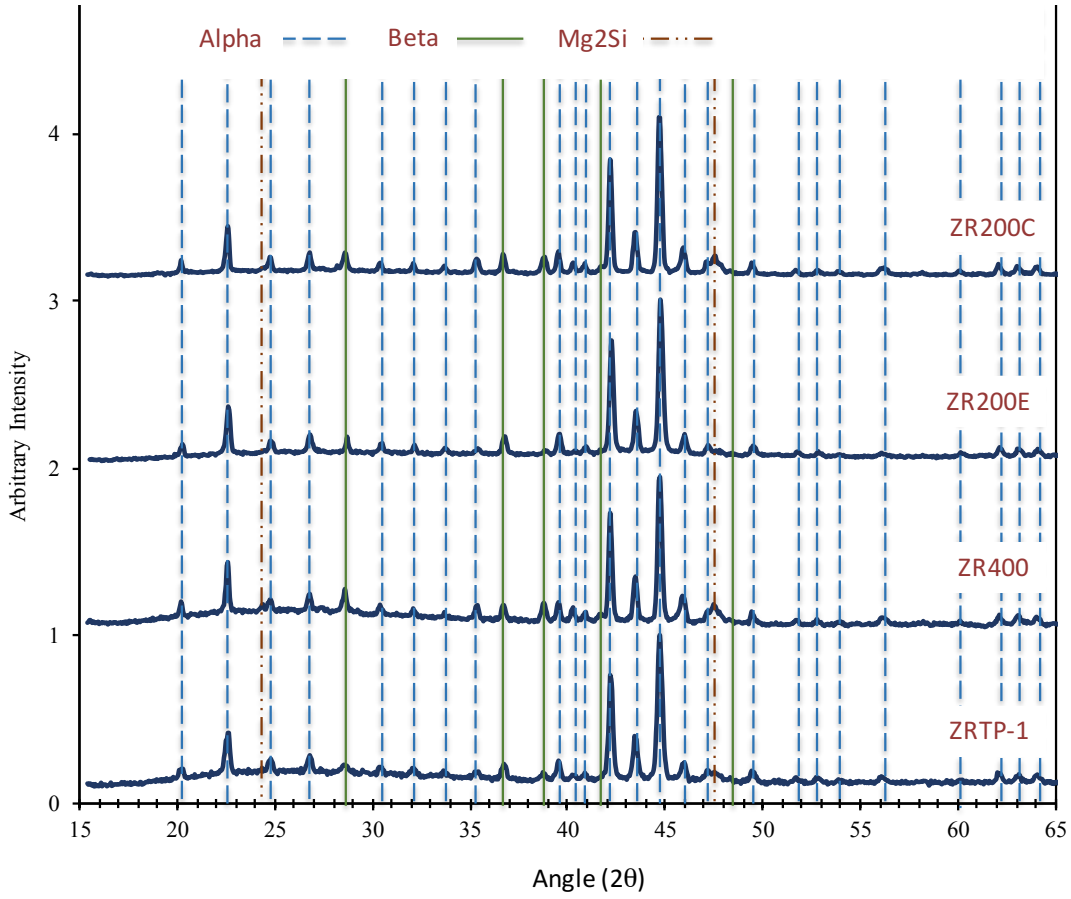


Figure 4.38: XRD Spectra showing phases present in ZR alloys, manufactured using different processing techniques

4.5.5 Summary

The approximate α-AlFeSi phase content calculated for the various alloys are given in Table 4.9. It was also observed, particularly in GR samples, that although the β-AlFeSi peaks of low intensity were observed in their expected positions, some of the characteristic high intensity β-AlFeSi peaks were missing. Furthermore, the intensity of the β-AlFeSi peaks were not in proportion to the reference spectra obtained using JCPDS reference. This may indicate that the high aspect ratio β-AlFeSi plates systematically display preferred orientation in relation to the incoming x-ray beam. This

effect could have been caused by sample preparation, whereby the β-AlFeSi platelets may not have broke down sufficiently, causing a texturing effect when examined.

Table 4.9: α-AlFeSi phase content found in the alloys

Sample	α-AlFeSi wt.%
BA200C	70
BAR2	70
BAR3	70
BAR4	70
BAR5	70
BA200E	60
BAL2	70
BAL3	70
BA400	60
BATP-1	70

Sample	α-AlFeSi wt.%
GR200C	50
GR200E	50
GR400	40
GRTP-1	40
ZR200C	80
ZR200E	80
ZR400	80
ZRTP-1	80

4.6 Intermetallic Phase Morphology (2D)

4.6.1 Base Alloy (BA200)

The backscattered (BSE) SEM micrographs of BA200C (sample taken from the centre at a height of 155-165mm from the base of BA200) and BA200E (sample taken from the edge at the same height of BA200) are shown in Figure 4.39.

BA200C and BA200E both displayed a combination of both 'needle'-like and 'Chinese script'-like intermetallic particle morphologies. Figure 4.40 and Figure 4.41 show some examples of the 'needle' and 'Chinese script'-like morphologies that were observed in both BA200C and BA200E.

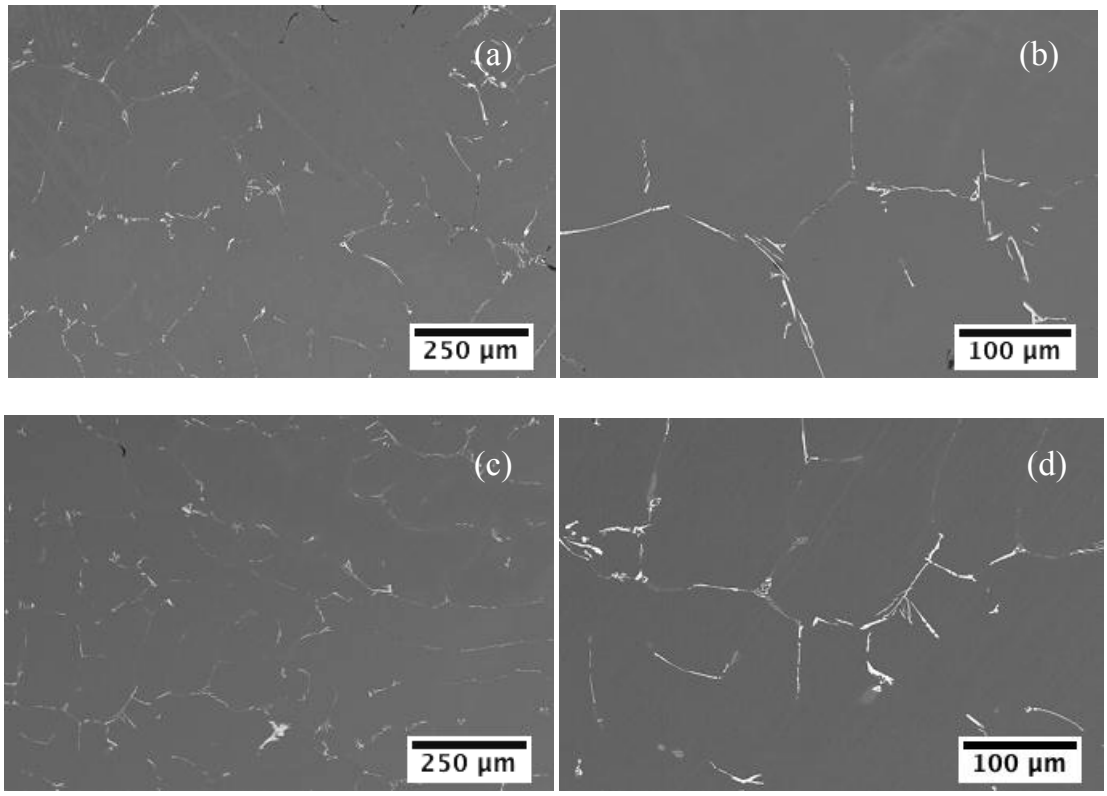


Figure 4.39: BSE micrographs of the overall intermetallic particle morphology of (a, b) BA200C and (c, d) BA200E

Figure 4.40 and Figure 4.41 demonstrate that the intermetallic morphologies observed in both samples are almost identical. The average thickness of the intermetallic particles was calculated by taking the average of 10-20 readings from various points of each micrograph. The average thicknesses of intermetallic particles with the 'Chinese-script'-like morphologies from BA200C (Figure 4.40 a, b, c) were 0.5 to 1.0µm, and

BA200E (Figure 4.41 a, b, c) were 0.7 to 1.0μm. The average thicknesses of the intermetallic particles with the 'needle'-like morphologies were comparable; BA200C (Figure 4.40 e, f) were 0.7 to 1.0μm, and BA200E (Figure 4.41 e, f) were 0.9 to 1.4μm.

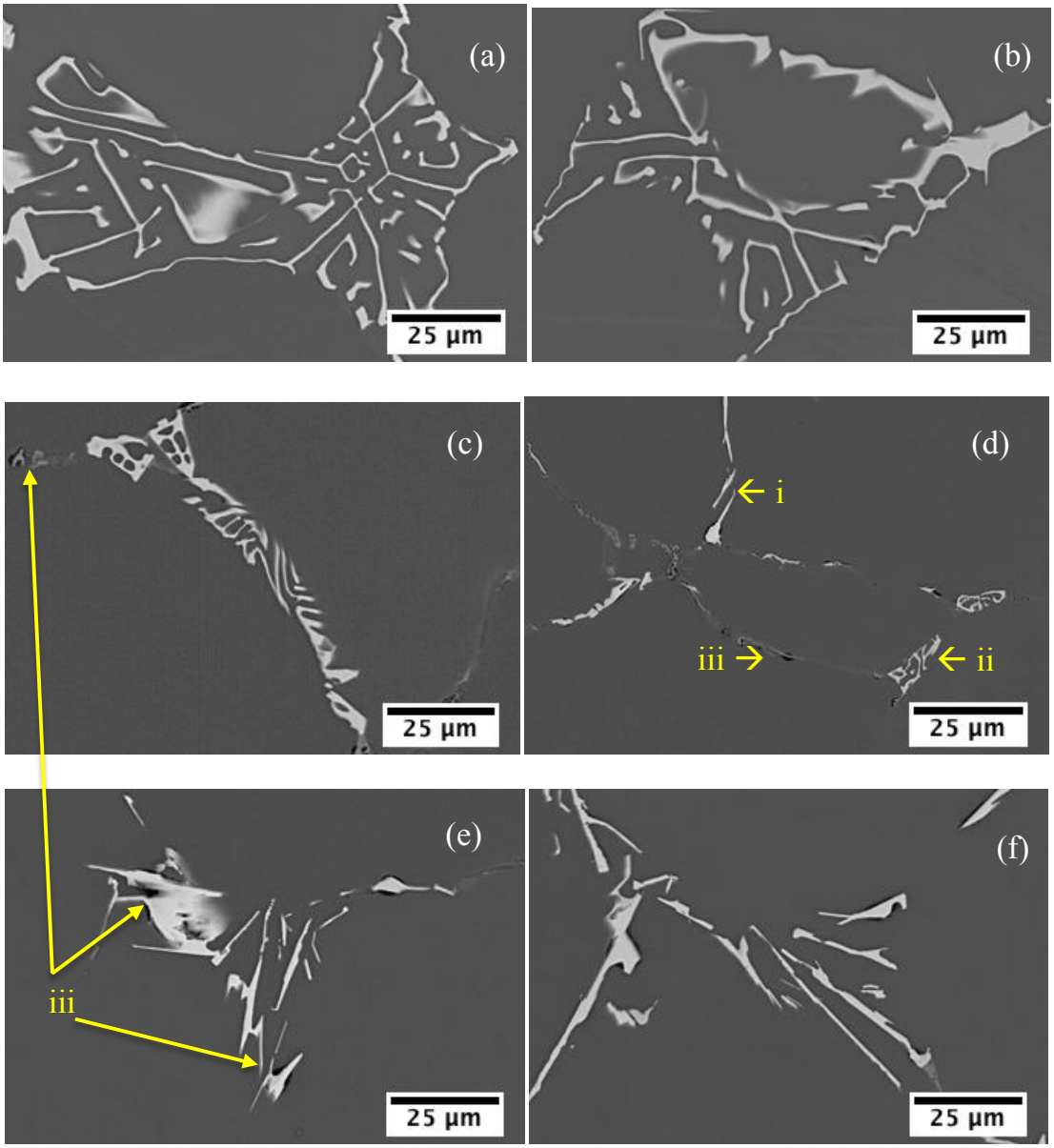


Figure 4.40: BSE micrographs of various intermetallic morphologies of BA200C: (a, b, c) shows various examples of 'Chinese script'-like intermetallic morphology, (d) shows an example where both i) 'needle' and ii) 'Chinese script'-like structures are connected, while (e, f) shows examples of 'needle'-like intermetallic morphologies. iii) Shows the potential presence of Mg_2Si phase

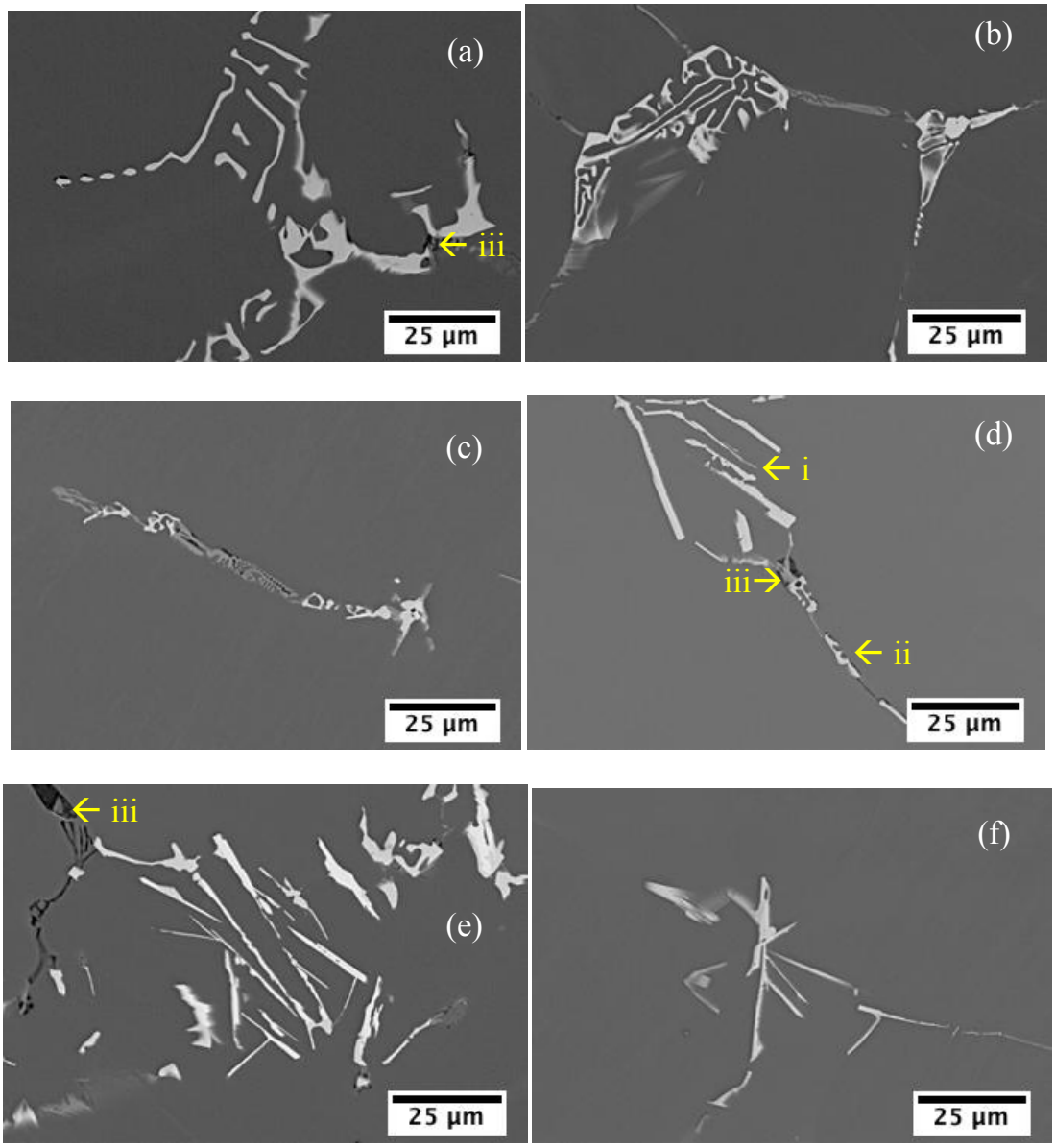


Figure 4.41: BSE micrographs of various intermetallic morphologies of BA200E: (a, b, c) shows various examples of 'Chinese script'-like intermetallic morphology, (d) shows an example where both i) 'needle' and ii) 'Chinese script'-like structures are connected, while (e, f) shows examples of 'needle'-like intermetallic morphologies. iii) Shows the potential presence of Mg_2Si phase

A third very dark phase was also observed in Figure 4.40 and Figure 4.41. Based on work carried out by Kumar et al. [133], it can be assumed to be that this very dark phase

is Mg_2Si. This is in agreement with the MTDATA (Scheil) calculations, DSC curves and XRD spectra obtained for this alloy.

4.6.2 Grain Refined Alloy (GR200)

The BSE SEM micrographs of GR200C (centre of grain refined alloy) and GR200E (edge of grain refined alloy) are shown in Figure 4.42. Once again they showed a combination of both 'needle'-like and 'Chinese script'-like phase morphologies. In contrast to BA200 samples, the 'Chinese script'-like morphology was more prevalent in the GR200 samples. The average thicknesses of intermetallic particles in both the 'Chinese-script' and 'needle'-like morphologies from GR200C and GR200E were 0.4 to 0.6μm, which is approximately 40% finer than that of BA200.

To understand the role of Ti particles in the GR alloy, X-ray spectroscopy was used to locate Ti-rich particles in both GR200 samples. Figure 4.43 shows some of the Ti-rich particles that were located, as well as the EDX spectrum from each particle. It is worth noting that the Ti-rich particles were observed near both 'Chinese script' and 'needle'-like structures, and always found at a distance from the intermetallic particles. In Figure 4.43 (g), the Ti-rich particle appears to be in amongst the primary aluminium. There is a possibility, however, that the Ti-rich particles are in fact connected to intermetallic particles below the surface of the primary aluminium, or had been connected to phases in the portion of the sample which has been removed during sample preparation, but no conclusive tests could be carried out to determine this.

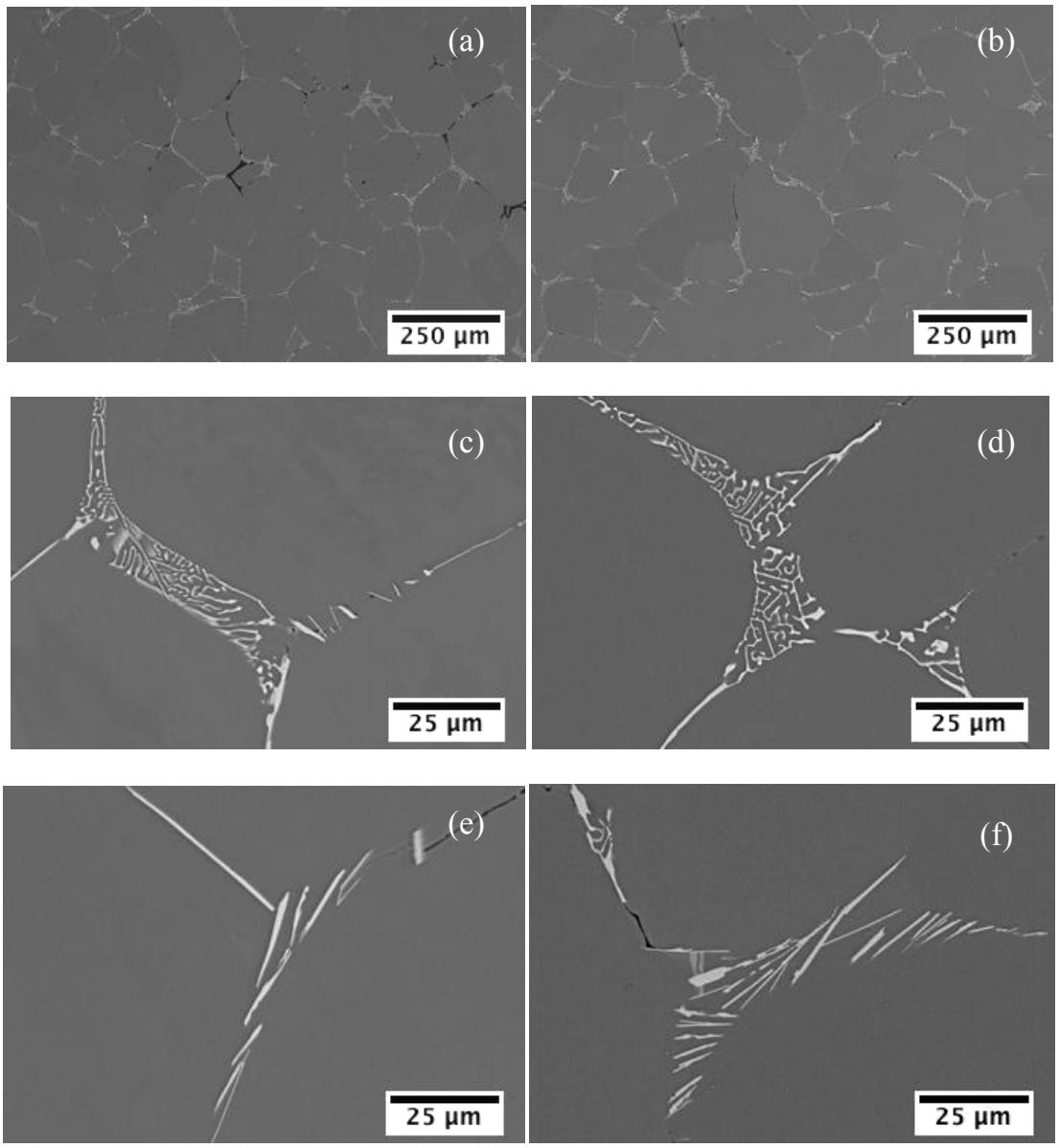


Figure 4.42: BSE micrographs of the overall intermetallic particle morphology of (a) GR200C and (b) GR200E, the 'Chinese script'-like morphology in (c) GR200C and (d) GR200E, and the 'needle'-like morphology in (e) GR200C and (f) GR200E

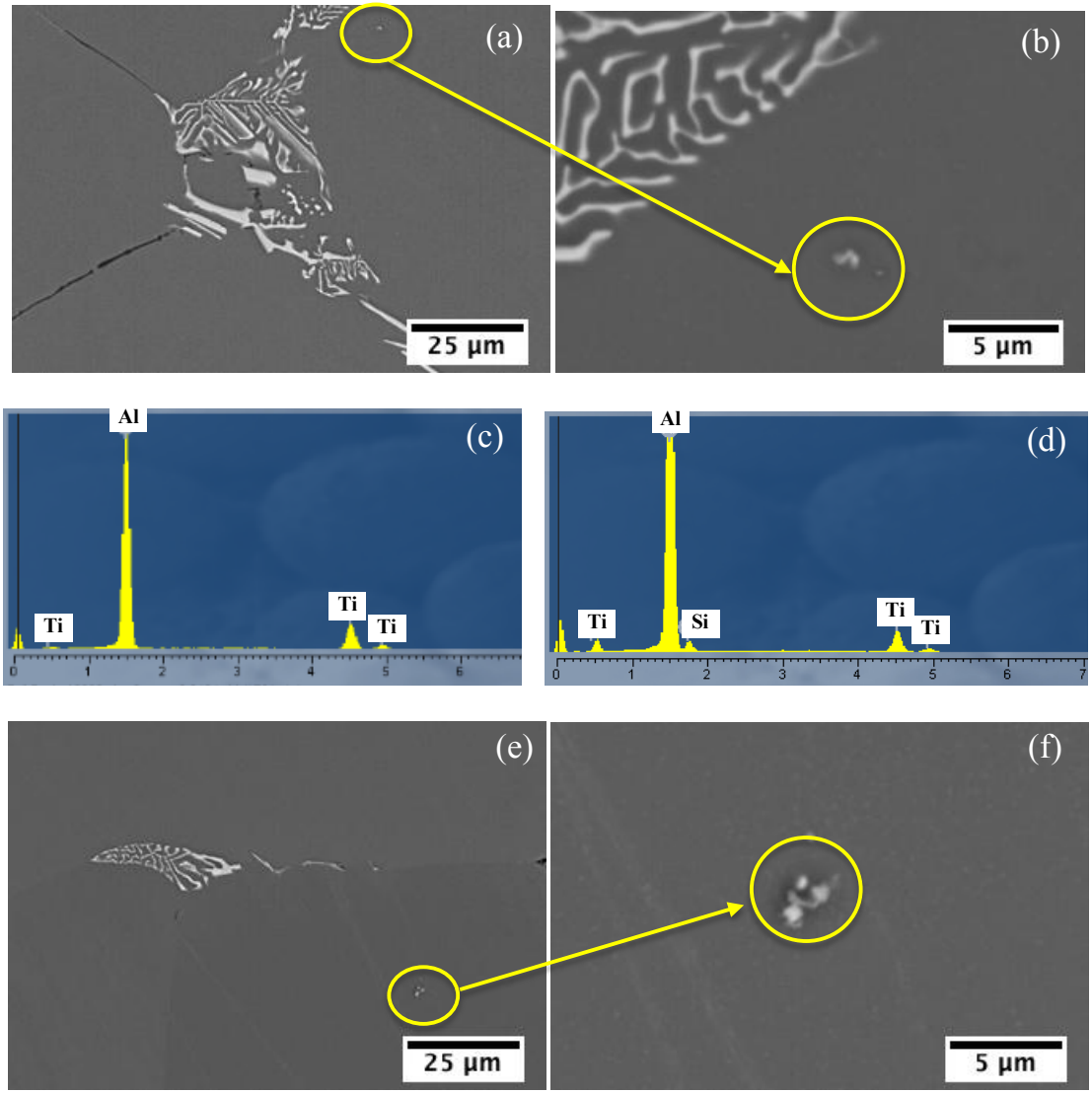


Figure 4.43: BSE micrographs show examples of Ti-rich particles (circled) found in (a) GR200C and (e) GR200E, the Ti-rich particles from (b) GR200C and (f) GR200E in higher magnification, and EDX spectra from the particles found in (c) GR200C and (d) GR200E displaying presence of Ti

4.6.3 Zr Added Alloy (ZR200)

The BSE SEM micrographs of ZR200C (centre of Zr added alloy) and ZR200E (edge of Zr added alloy) are shown in Figure 4.44. Like the BA200 and GR200 samples, both ZR200 samples display a combination of 'needle'-like and 'Chinese script'-like phase

morphologies. Similar to BA200, the 'needle'-like phase morphology was predominant in both ZR200 samples.

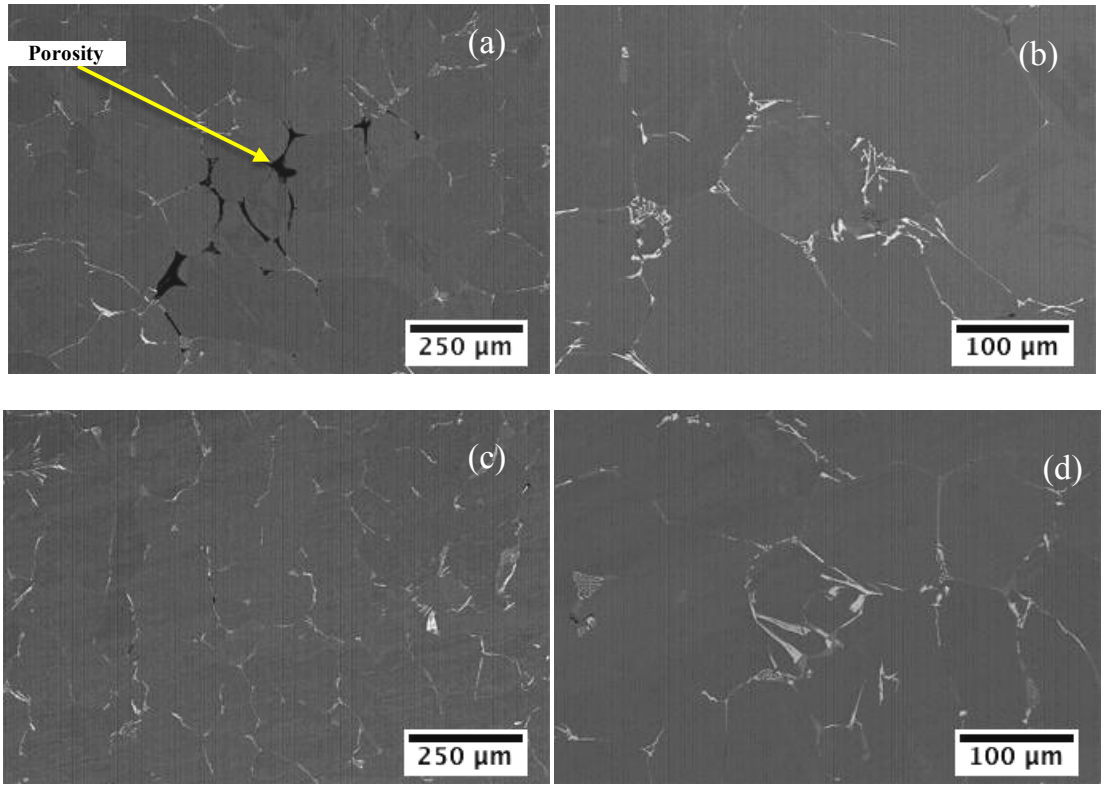


Figure 4.44: BSE micrographs of the overall intermetallic particle morphology of (a, b) ZR200C and (c, d) ZR200E

Some examples of the 'needle'-like and 'Chinese script'-like phase morphologies are shown in Figure 4.45. The average thicknesses of intermetallic particles in the 'Chinese script'-like morphologies from ZR200C were between 0.7 to 1.8µm, and from ZR200E were 0.4 to 1.0µm. The average thicknesses of intermetallic particles in the 'needle'-like morphologies were comparable; ZR200C were 0.7 to 1.2µm, and ZR200E were 0.5 to 1.0µm.

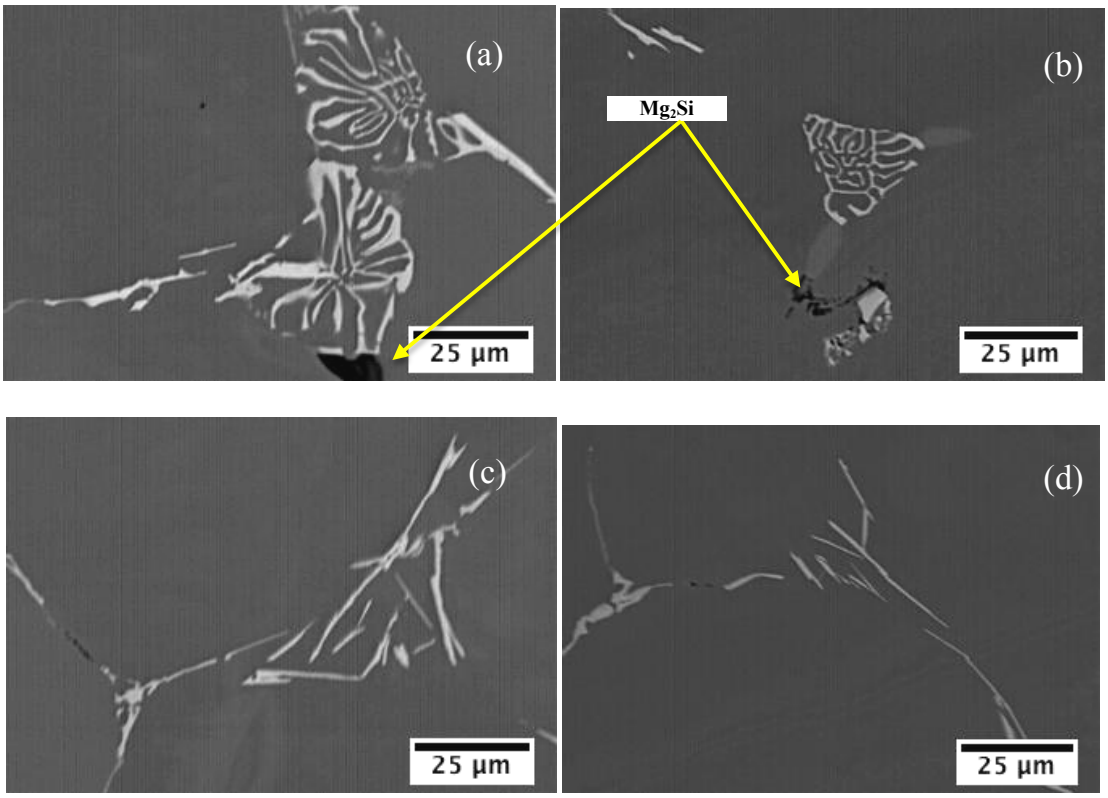


Figure 4.45: BSE micrographs of the 'Chinese script'-like morphology in (a) ZR200C and (b) ZR200E, and the 'needle'-like morphology in (c) ZR200C and (d) ZR200E

4.6.4 Summary

Based on the 2D intermetallic phase morphology analysis, it can be summarised that:

- All samples displayed a combination of the 'needle' and 'Chinese script'-like intermetallic morphologies;
- The 'needle'-like morphology was more prevalent in BA200 and ZR200, while the 'Chinese script'-like morphology was observed more frequently in GR200;
- The average thicknesses of intermetallic phases were 40% smaller in GR200 compared those in BA200 and ZR200; and
- Mg2Si phase was observed in both BA200 and ZR200.

4.7 Extracted Intermetallic Phase Morphology (3D)

4.7.1 Base Alloy (BA200)

Intermetallic particles were extracted from BA200C (top centre of BA slurry) and BA200E (top edge of BA slurry), as well as BAL3 (bottom centre of BA slurry) for a thorough comparison. The extracted samples are shown in Figure 4.46; a well-defined pore structure was evident in all intermetallic samples, corresponding to the primary aluminium matrix.

The average diameters of the intermetallic pores from BA200C, BA200E and BAL3 were all 150±15μm. The pores in BA200C were relatively equiaxed with an average aspect ratio of 0.75. The average aspect ratio of pores observed in BA200E was 0.63, indicating that the pore structures are more columnar in comparison. The BAL pores were once again more equiaxed, with an average pore aspect ratio of 0.72. The intermetallic particle thickness was also measured from various micrographs, and it was found to be less than 1μm for all three samples.

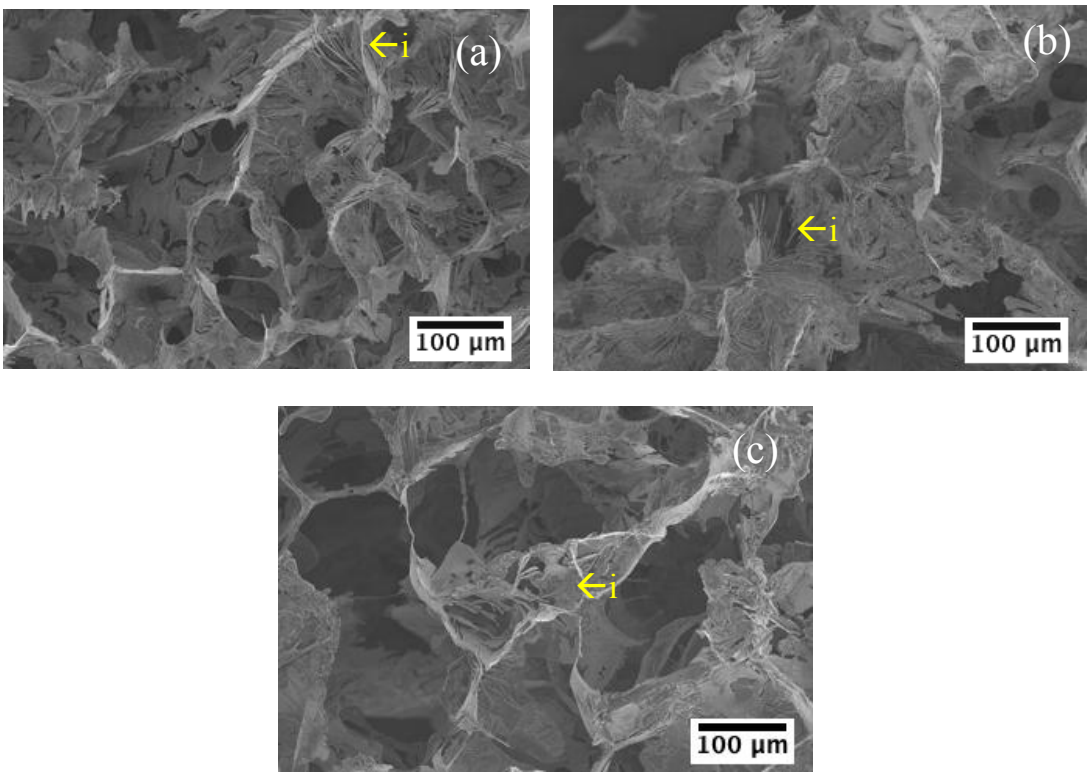


Figure 4.46: SE micrographs of extracted intermetallic particles of (a) BA200C, (b) BA200E and (c) BAL3. The features identified in yellow will be discussed later in this section

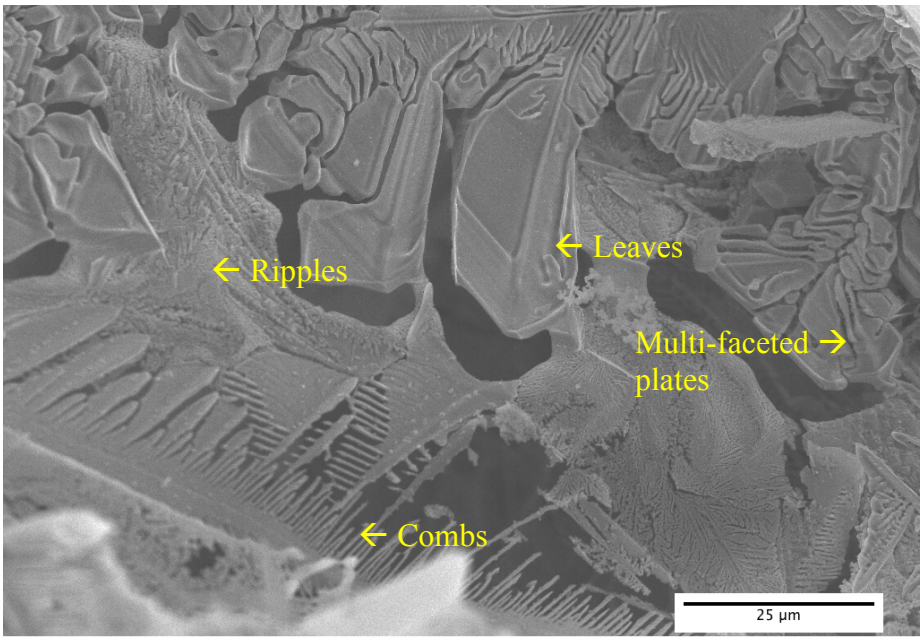


Figure 4.47: SE micrographs of extracted intermetallic particle from BA200C, displaying various topographical patterns

As shown in Figure 4.47, the 3D structure surface of the samples exhibited various topographical patterns, some of which resembled leaves, comb-like dendrites, multifaceted plates, and sometimes ripples, all curving around to create interconnected pores revealing the primary aluminium matrix. These intricate phases were assumed to be α-AlFeSi phase. Some phases were also observed that were flat, planar and contained angular edges, which were assumed to be β-AlFeSi phase. Some examples of the typical intricate and multifaceted surface structure are shown in Figure 4.48.

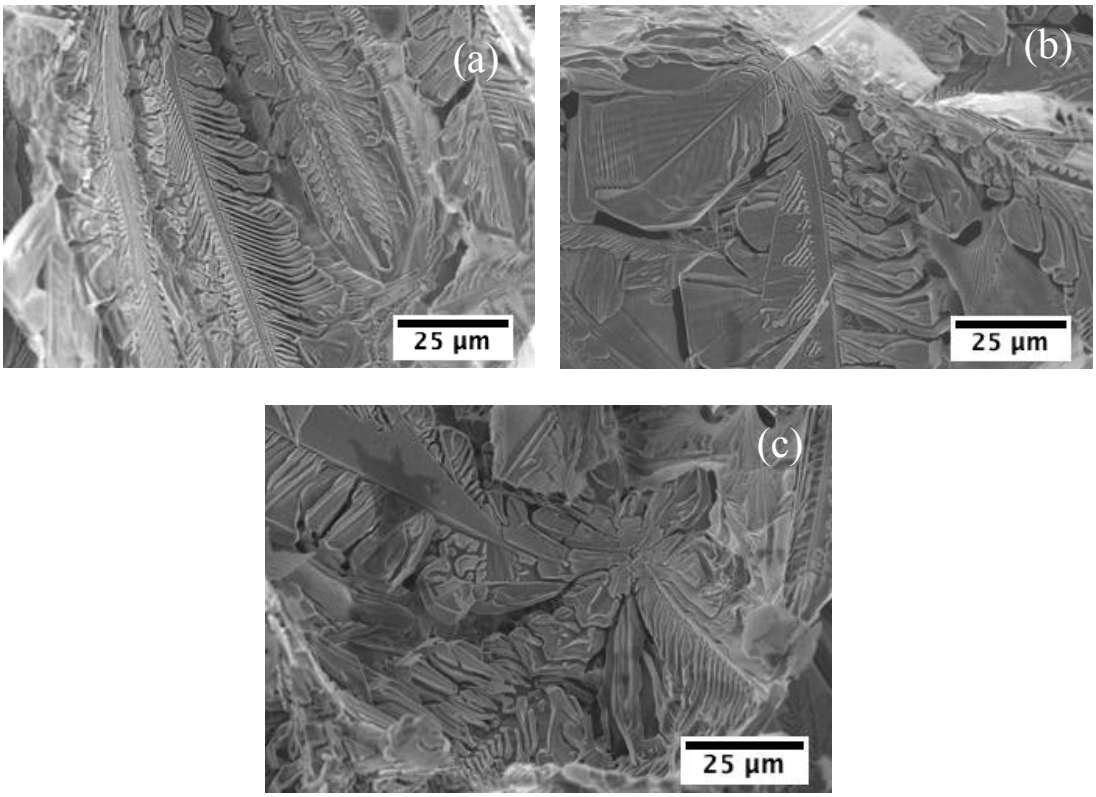


Figure 4.48: SE micrographs showing examples of extracted intermetallic particles with an intricate morphology from (a) BA200C, (b) BA200E and (c) BAL3

Amongst the intricate intermetallic particles, patches were observed (identified in Figure 4.46 with a yellow i) where the intermetallic morphology was plate-like; smooth

on the surface and angular at the edges. Some examples of these plate-like phases are shown in Figure 4.49, which indicate that most of these plate-like intermetallic particles form in multiple layers that are not parallel.

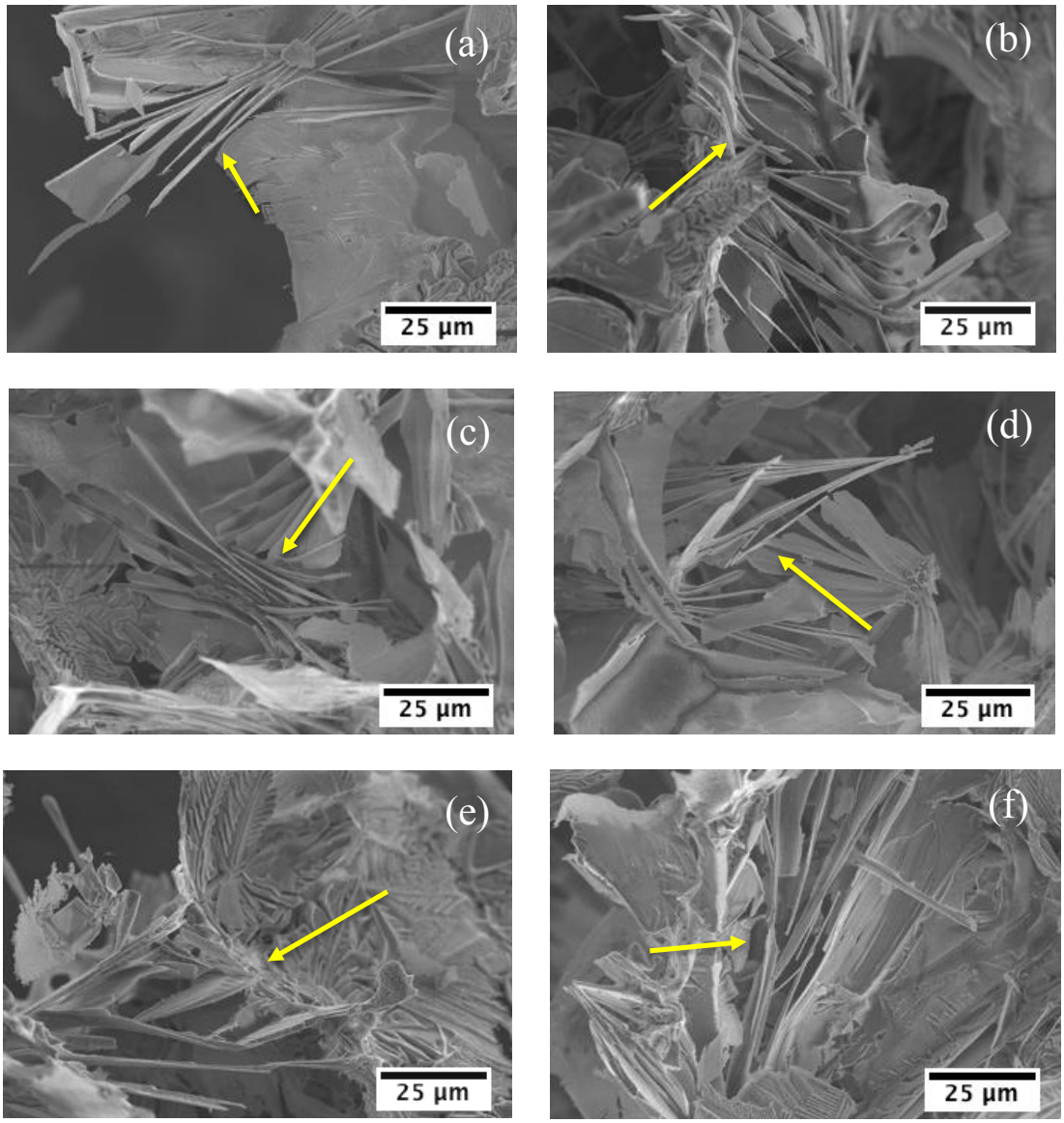


Figure 4.49: SE micrographs showing examples of extracted intermetallic particles with a planar surface and a plate-like morphology from (a, b) BA200C, (c, d) BA200E, and (e, f) BAL3. Each yellow arrow points towards intermetallic particles formed in multiple layers that are not parallel.

Another interesting feature that was occasionally observed in all three samples of BA200 are ‘flower’-like structures, whereby 6 ‘petals’ appear to extend from a central point, creating an intricate and multi-faceted ‘flower’-like structure. Some examples of this morphology can be seen in Figure 4.50.

The centre point of several of these ‘flower’-like structures were observed at higher magnification in order to identify what initiated this specific phase morphology, but nothing conclusive could be established. Attempts to identify phases using EDX were also not successful possibly due to the large interaction volume of the EDX beam against the very small phase thickness.

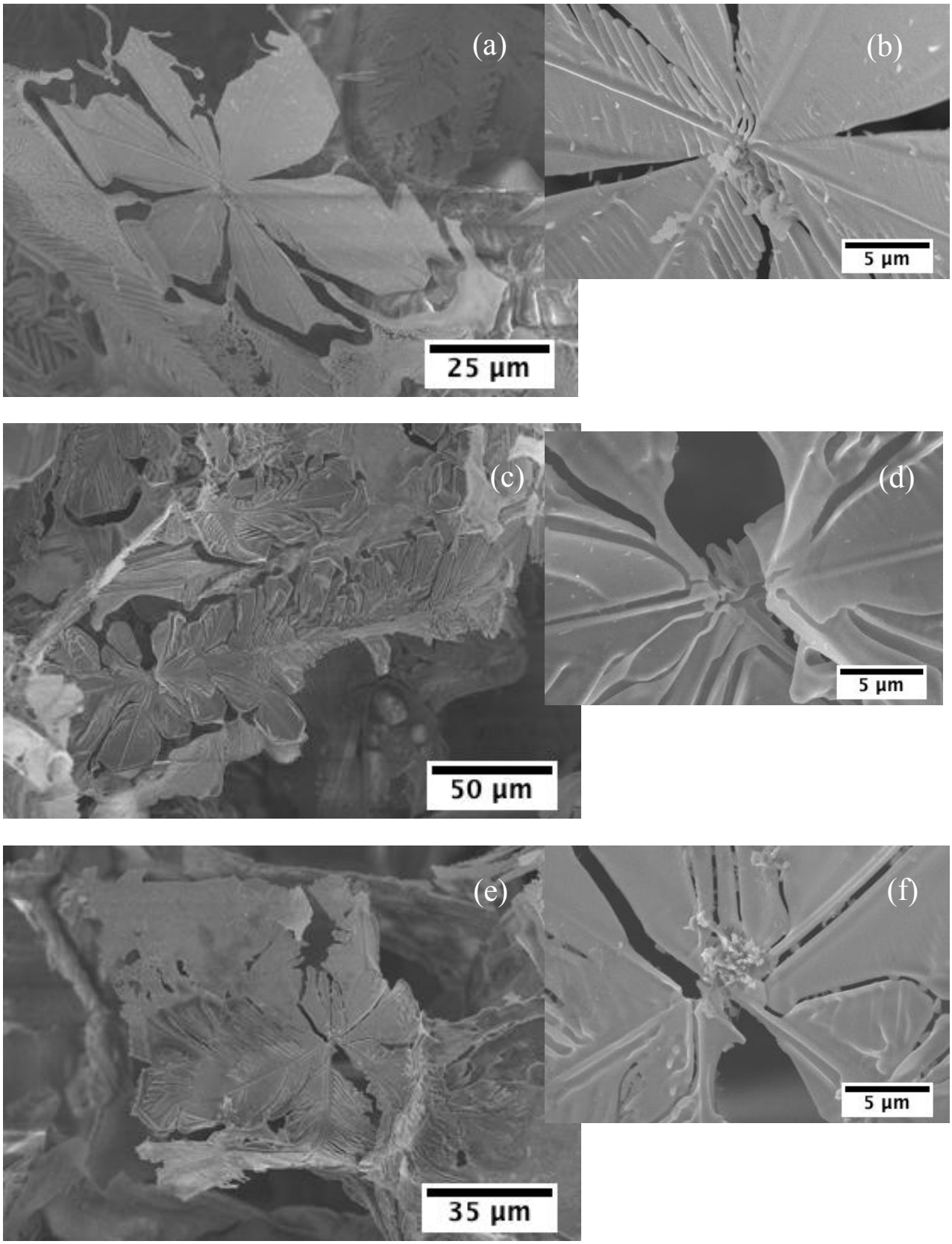


Figure 4.50: SE micrographs showing examples of the 'flower'-like morphology from (a) BA200C, (c) BA200E and (e) BAL3, while (b, d, f) shows their respective centres

4.7.2 Extracted Intermetallic Phase Examination: Grain Refined Alloy

Figure 4.51 shows the extracted phases from GR200C, GR200E and GR200B. All samples displayed a well-defined pore structure corresponding to the primary aluminium matrix, and the approximate diameters of the pores were 120±10μm, 130±5μm and 130±10μm for GR200C, GR200E and GR200B, respectively.

The pores in GR200C, GR200E and GR200B were all relatively equiaxed with average aspect ratios of 0.72, 0.75 and 0.79 respectively. Each average, once again, was calculated from 10 pore aspect ratio measurements. The thickness of the phases was less than 1μm.

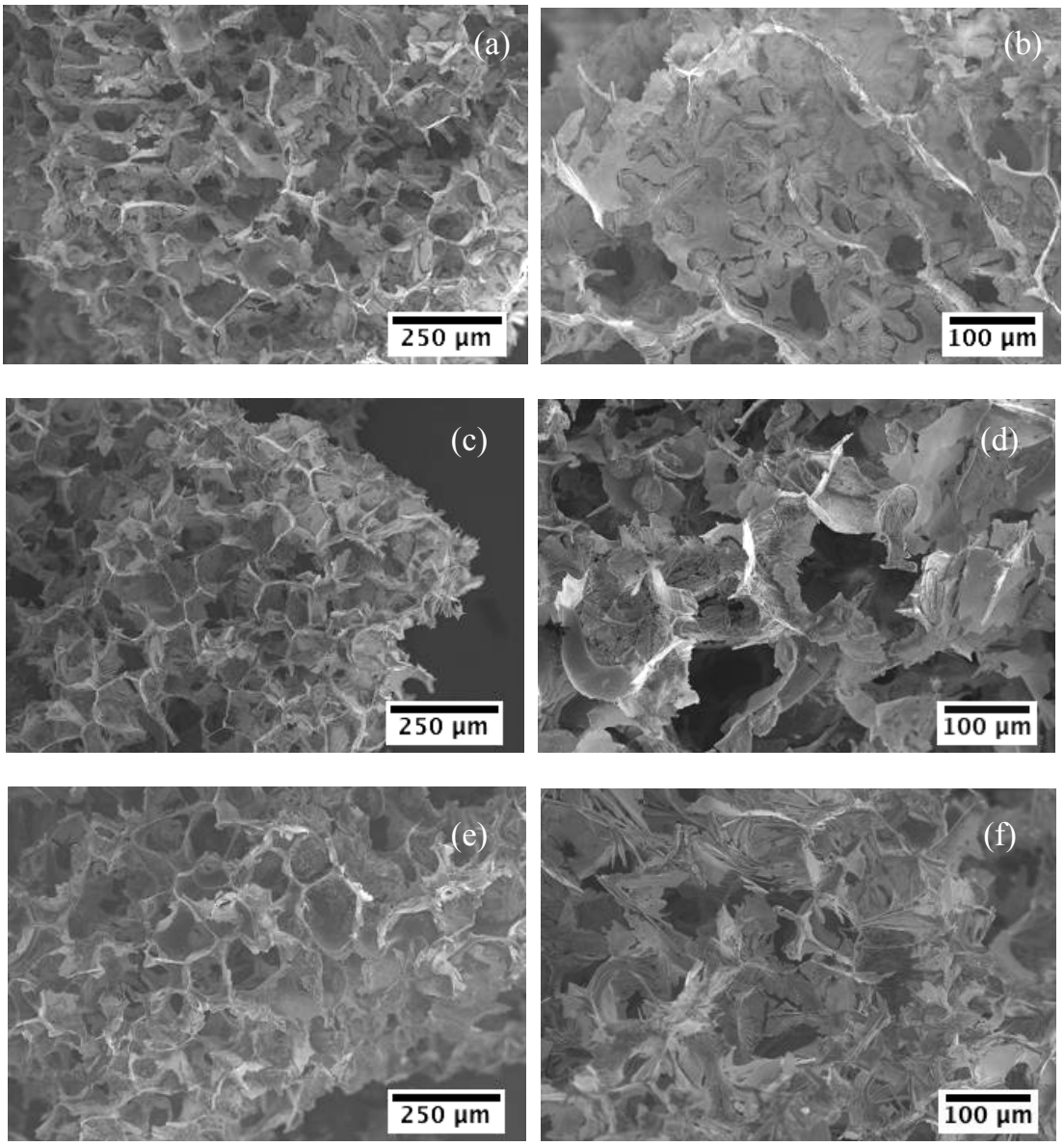


Figure 4.51: SE micrographs showing extracted intermetallic particles of (a, b) GR200C, (c, d) GR200E and (e, f) GR200B

The phase particles from all three GR200 samples displayed a similar structure to those of BA200 intermetallic particles, including the intricate patterns in the form of leaves, combs, multifaceted plates, ripples and flowers. The plate-like phases with angular edges were also observed. Some examples of the phases with intricate morphologies are shown in Figure 4.52, and the plate-like morphologies are shown in Figure 4.53.

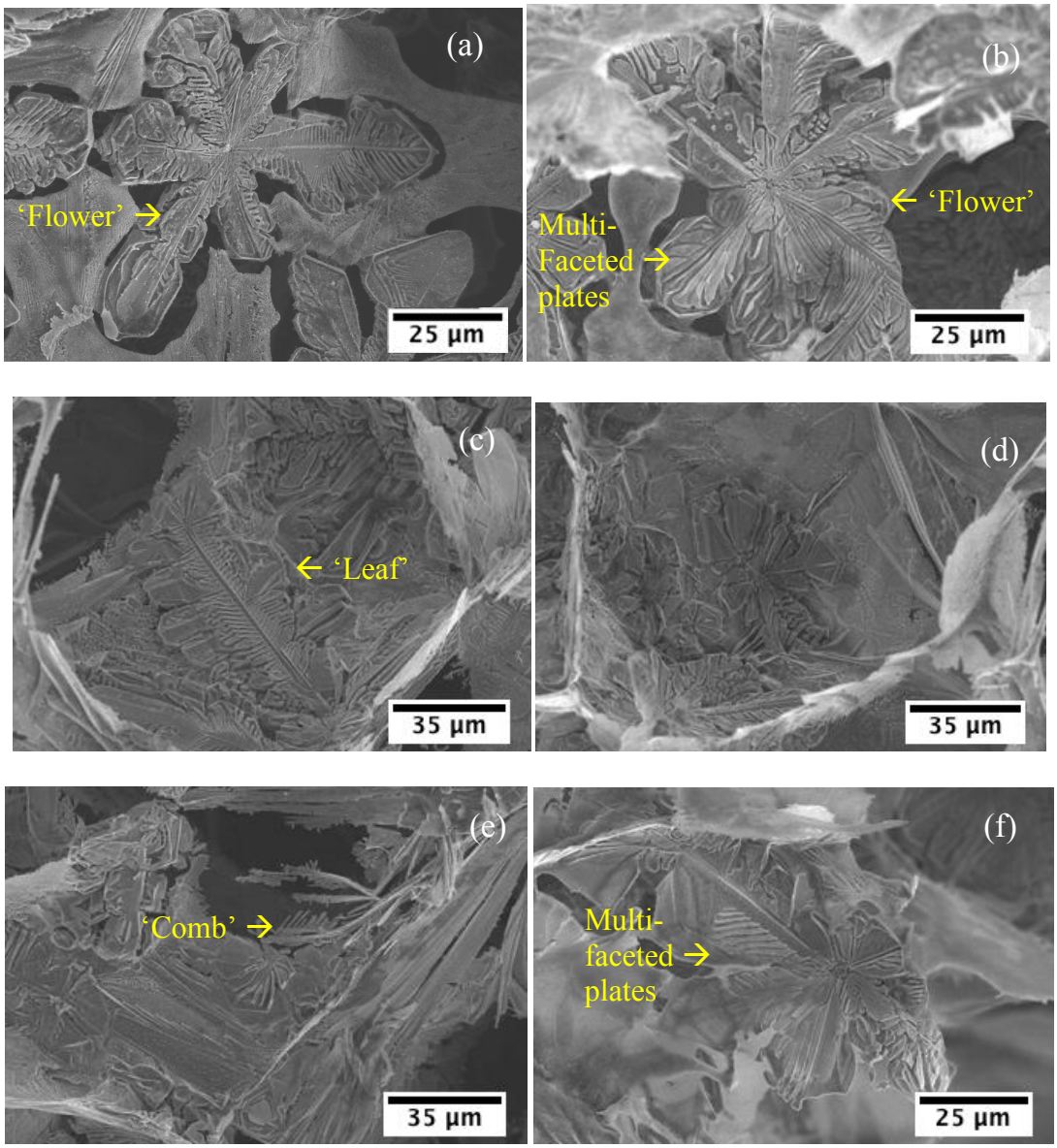


Figure 4.52: SE micrographs showing examples of extracted intermetallic particles with an intricate morphology from (a, b) GR200C, (c, d) GR200E and (e, f) GR200B

Patches of plate-like morphology similar to those observed in BA200 samples were also observed in GR200 samples, but with much higher frequency. Similar to BA200's plate-like phases, these phases also display intricate patterns developing over some of the plate-like surfaces (identified with an x on Figure 4.53 b and c).

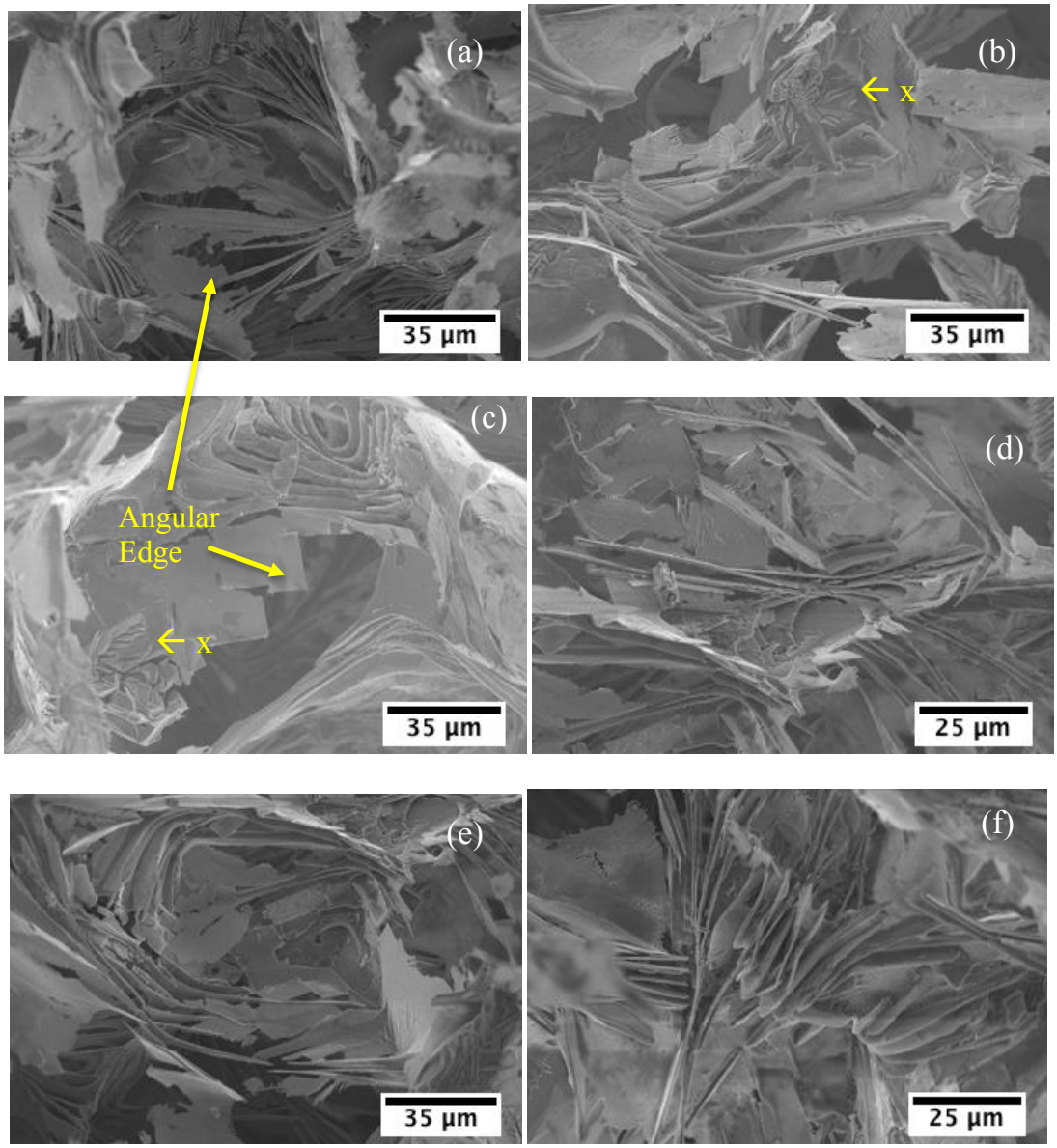


Figure 4.53: SE micrographs showing examples of extracted intermetallic particles with a plate-like morphology from (a, b) GR200C, (c, d) GR200E and (e, f) GR200B

Some examples of the 'flower'-like phases observed in GR200 are shown in Figure 4.54, where (a), (c), (e), (g) and (i) display the complete 'flower' structure, and (b), (d), (f), (h) and (j) display their corresponding centres at higher magnification. Some petals

were also observed to have additional petals branching off from the petals connected to the base (marked with an y in Figure 4.54 e, g).

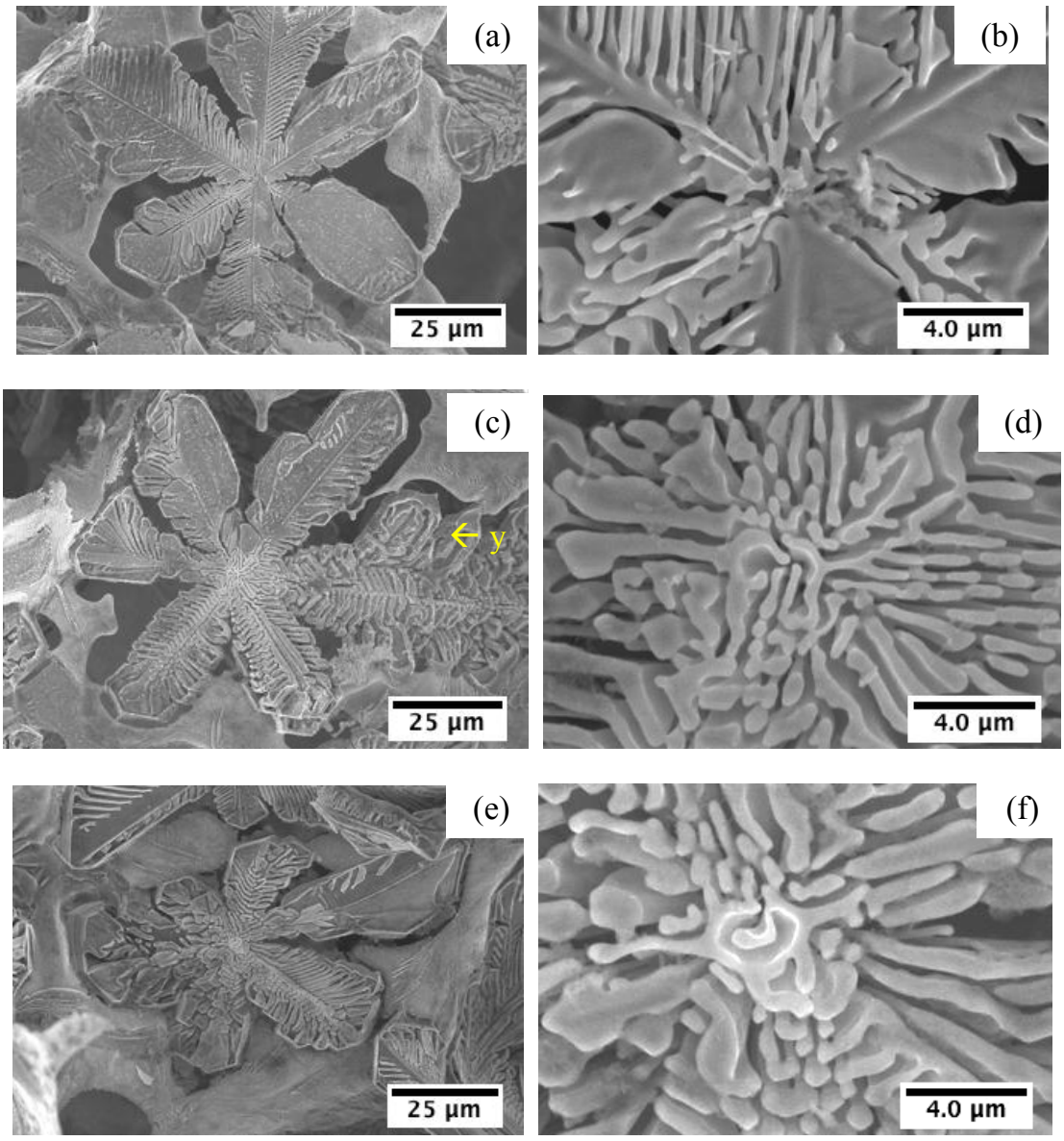


Figure 4.54: SE micrographs showing examples of extracted intermetallic particles with a 'flower'-like morphology from GR200C, where y marks the additional petals branching out of the base petals

The second SEM sample of broken intermetallic particles from GR200C had fewer layers of phases behind the observed particles, and so it was used to locate the Al-Ti-B phases. A few Ti-rich clusters were observed scattered amongst the intermetallic particles, but the distribution appeared to be random. Figure 4.55 to Figure 4.59 show the Ti-rich clusters that were located using element mapping, followed by EDX scans on GR200C and GR200E respectively. Attempts to locate Ti-rich clusters in GR200B were unsuccessful.

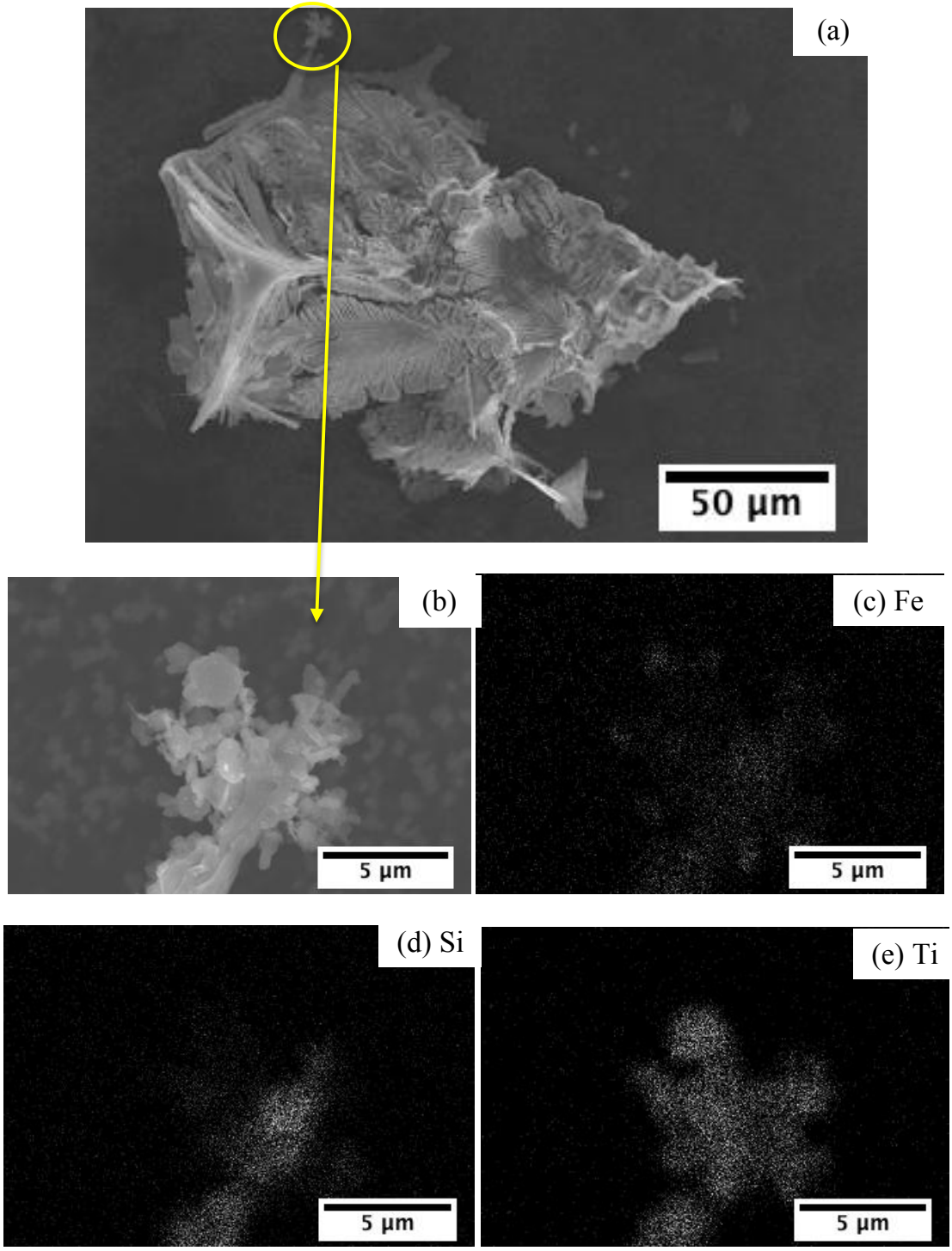


Figure 4.55: Example of Ti-rich clusters found in extracted intermetallic particles in GR200C, where (a) shows SE micrograph of the overall intermetallic particle; (b) shows SE micrograph of the Ti-rich region at a higher magnification; (c, d, e) shows the element maps of the area. The Ti-rich cluster appears to be isolated on an extended growth of a plate-like intermetallic particle

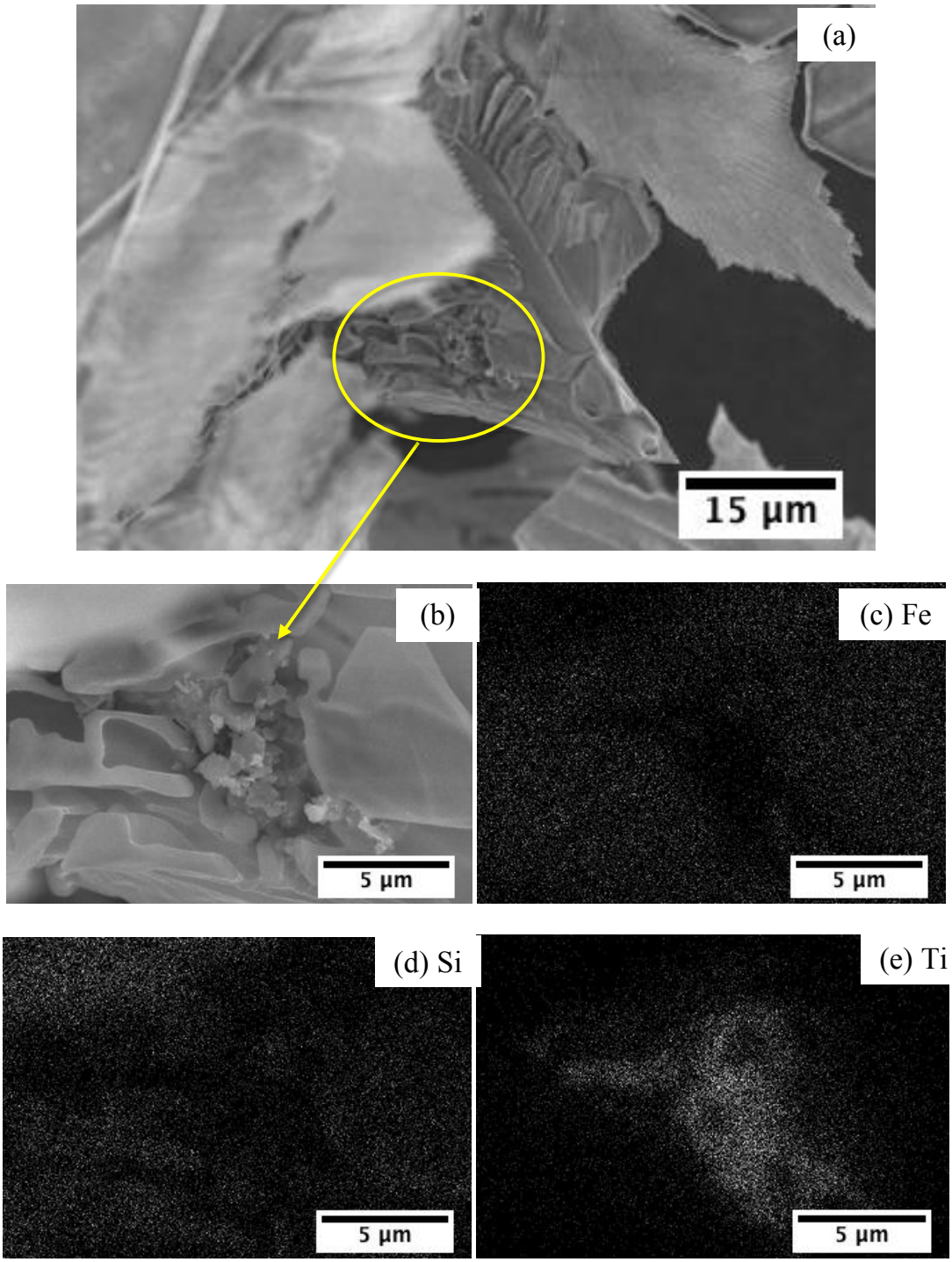


Figure 4.56: Another example of Ti-rich clusters found in extracted intermetallic particles in GR200C, where (a) shows SE micrograph of the overall intermetallic particle; (b) shows SE micrograph of the Ti-rich region at a higher magnification; and (c, d, e) shows the element maps of the area. The Ti-rich cluster appears to be integrated into the intricate intermetallic particle surface

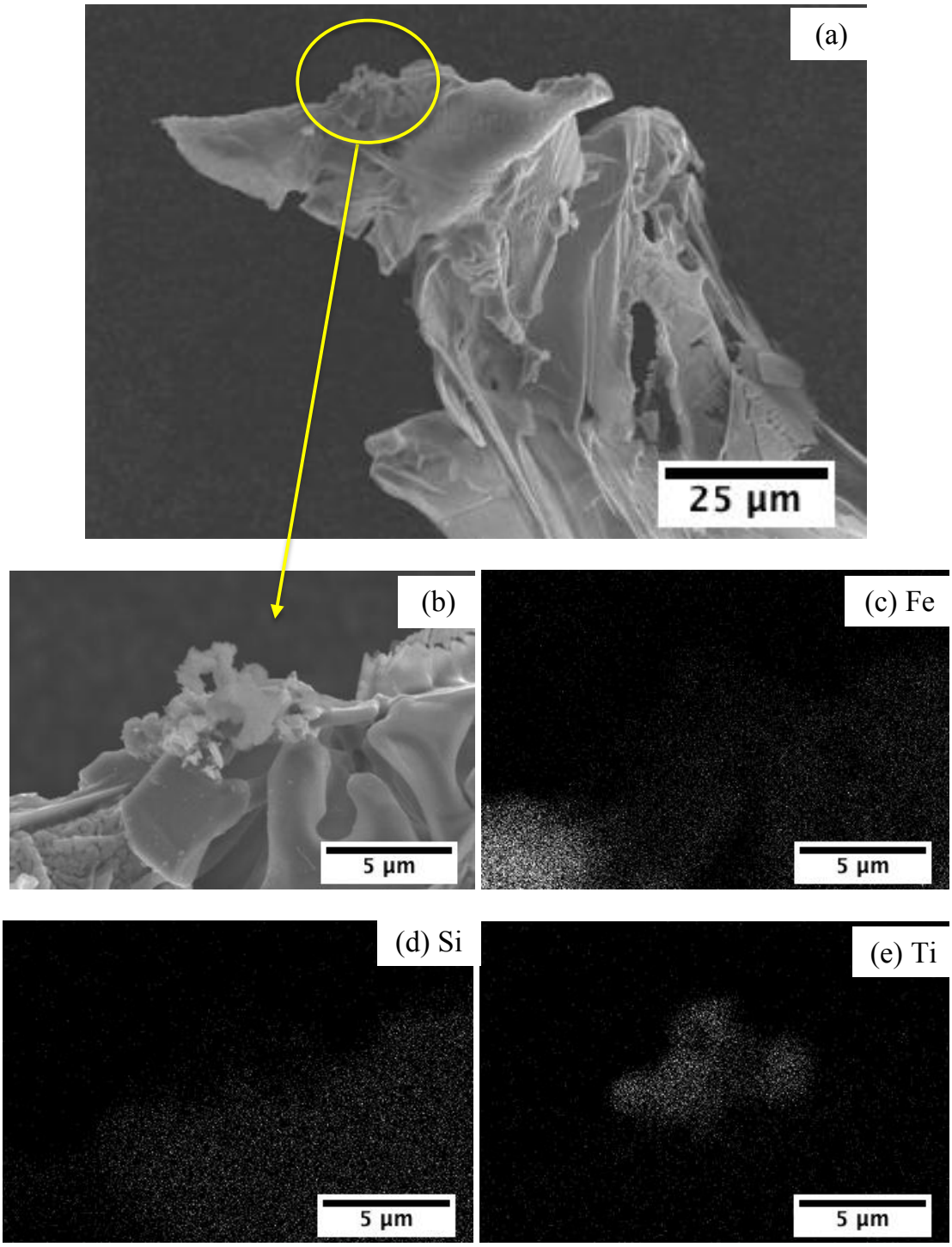


Figure 4.57: Two Ti-rich clusters were observed on this particle in GR200C: (a) SE micrograph of the overall intermetallic particle; (b) SE micrograph of the Ti-rich region at a higher magnification; and (c, d, e) element maps of the area. The Ti-rich cluster appears to be neither integrated nor isolated from the main intermetallic particle, but just in contact with the intricate intermetallic particle. Figure 4.58 shows the second Ti-rich cluster on this particle

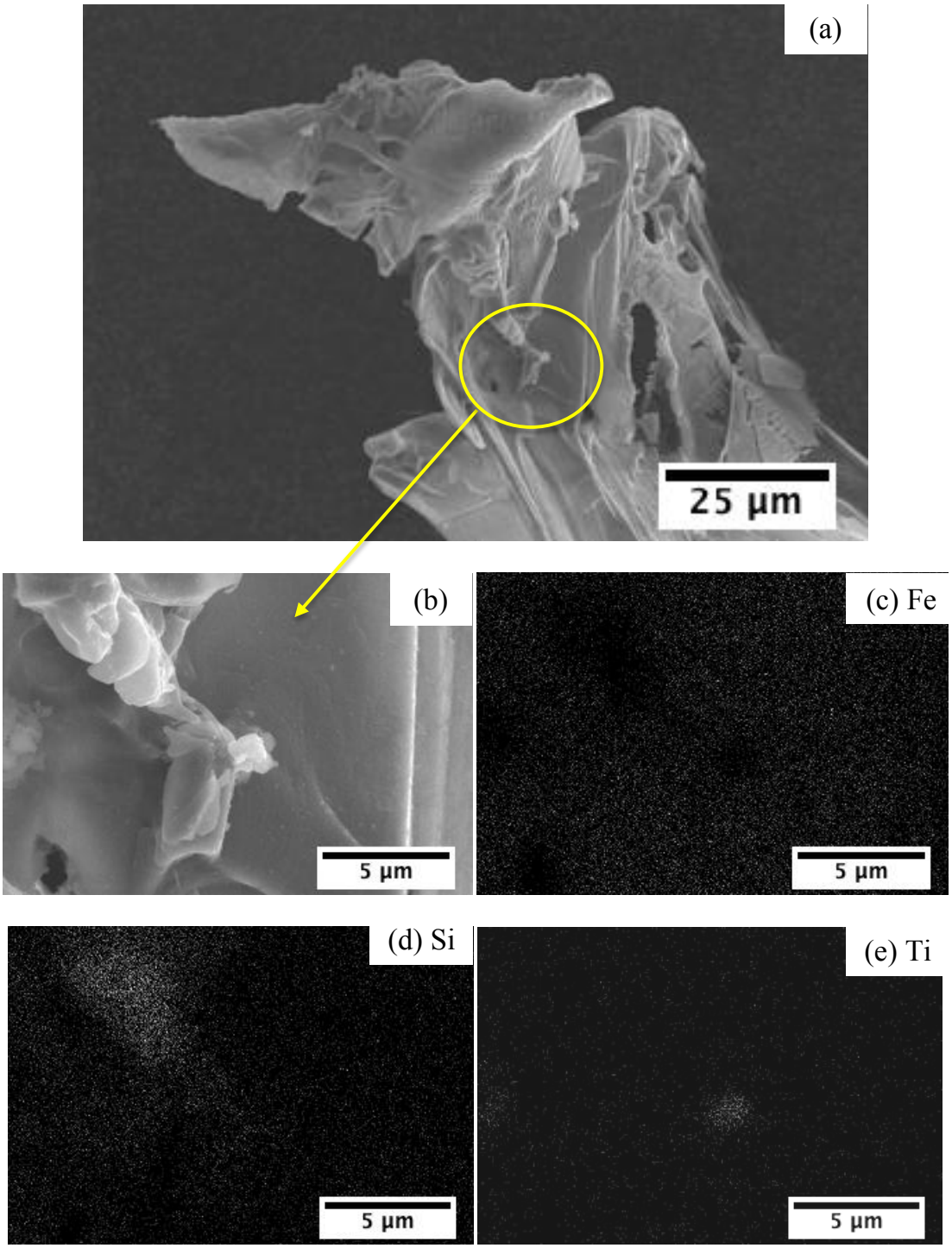


Figure 4.58: Second Ti-rich clusters that was observed on this particle in GR200C: (a) SE micrograph of the overall intermetallic particle; (b) SE micrograph of the Ti-rich region at a higher magnification; and (c, d, e) element maps of the area. This Ti-rich cluster appears to be integrated to the main particle; either growing on a raised edge or broken off from a further connected intermetallic particle

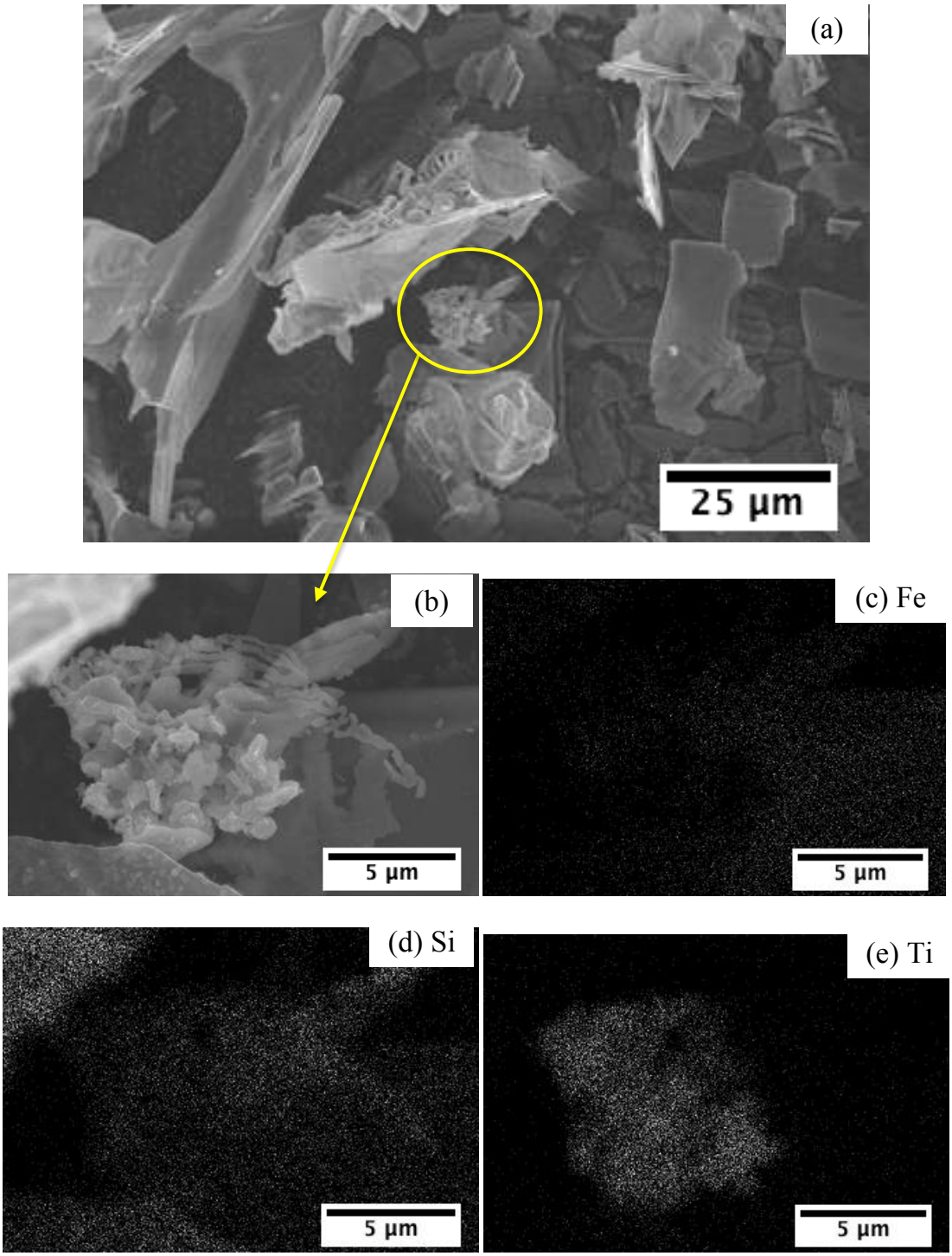


Figure 4.59: An example of Ti-rich clusters found in extracted intermetallic particles in GR200E where (a) shows SE micrograph of the overall intermetallic particle; (b) shows SE micrograph of the Ti-rich region at a higher magnification; and (c, d, e) shows the element maps of the area. A comparatively large Ti-rich cluster appears to be settled on a plate-like intermetallic particle surface

4.7.3 Extracted Intermetallic Phase Examination: Zr Added Alloy

Extracted intermetallic particles from ZR200C, ZR200E and ZR200B were observed to be very delicate, and crumbled more easily on contact than BA200 and GR200 samples. Thus attaching the samples as one piece to the carbon sticky tabs for SEM sample preparation proved to be very difficult. Most of the ZR200 samples were examined as crumbled intermetallic particles, shown in Figure 4.60. Once again the primary aluminium matrix was revealed through the well-defined pore structure, and the approximate diameters of the pores were 140±25μm, 180±20μm and 160±35μm for ZR200C, ZR200E and ZR200B respectively.

Pores in ZR200 were relatively equiaxed in the centre, with an average aspect ratio of 0.69 for ZR200C and 0.63 for ZR200B. The average aspect ratio of pores observed in BA200E was 0.48, indicating that the BA200 pore structures are more columnar in comparison. The intermetallic particle thickness was found to be less than 1μm.

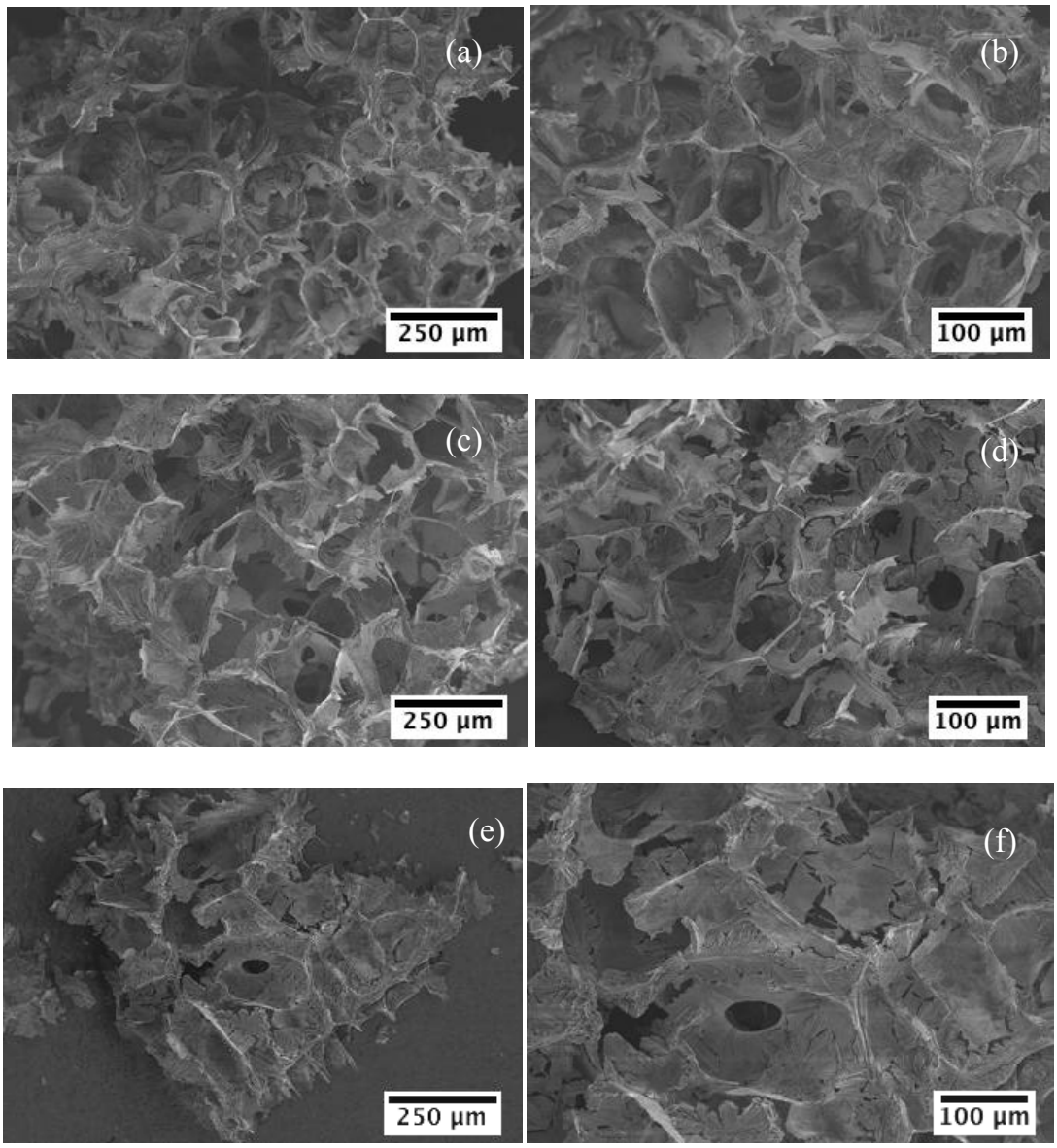


Figure 4.60: SE micrograph showing extracted intermetallic particles in (a, b) ZR200C, (c, d) ZR200E and (e, f) ZR200B

The surface structures of ZR200 samples, with regards to both intricate patterns and plate-like phases, were very similar to those observed in BA200 samples. Figure 4.61 shows some examples of the intricate patterns observed in ZR200 samples.

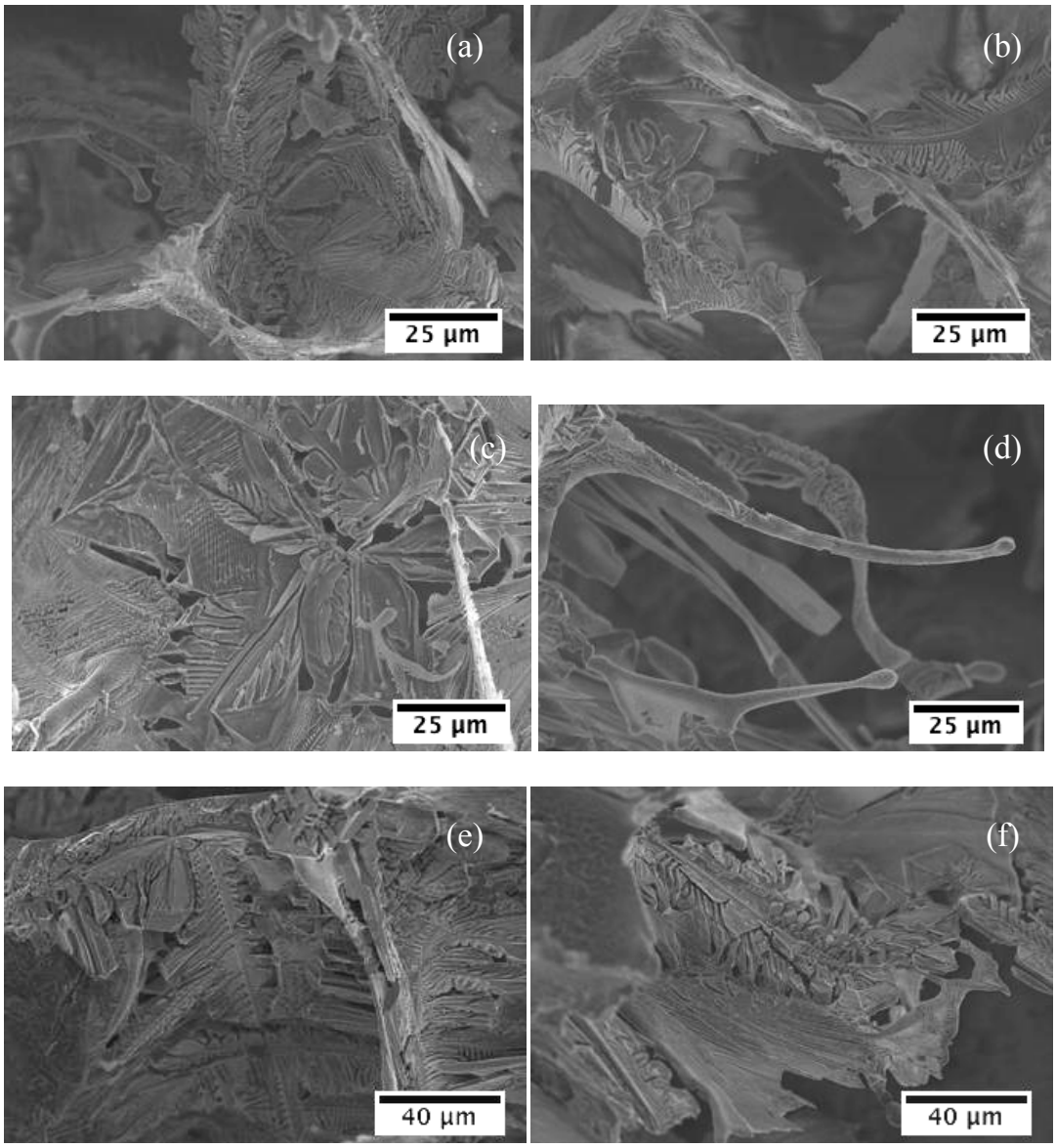


Figure 4.61: SE micrograph showing examples of extracted phases with an intricate morphology from (a, b) ZR200C, (c, d) ZR200E and (e, f) ZR200B

Plate-like intermetallic particles were very difficult to locate in all three ZR200 samples due to the very high frequency of intricately patterned intermetallic particles. Some examples of the plate-like morphologies observed in ZR200 samples are shown in Figure 4.62.

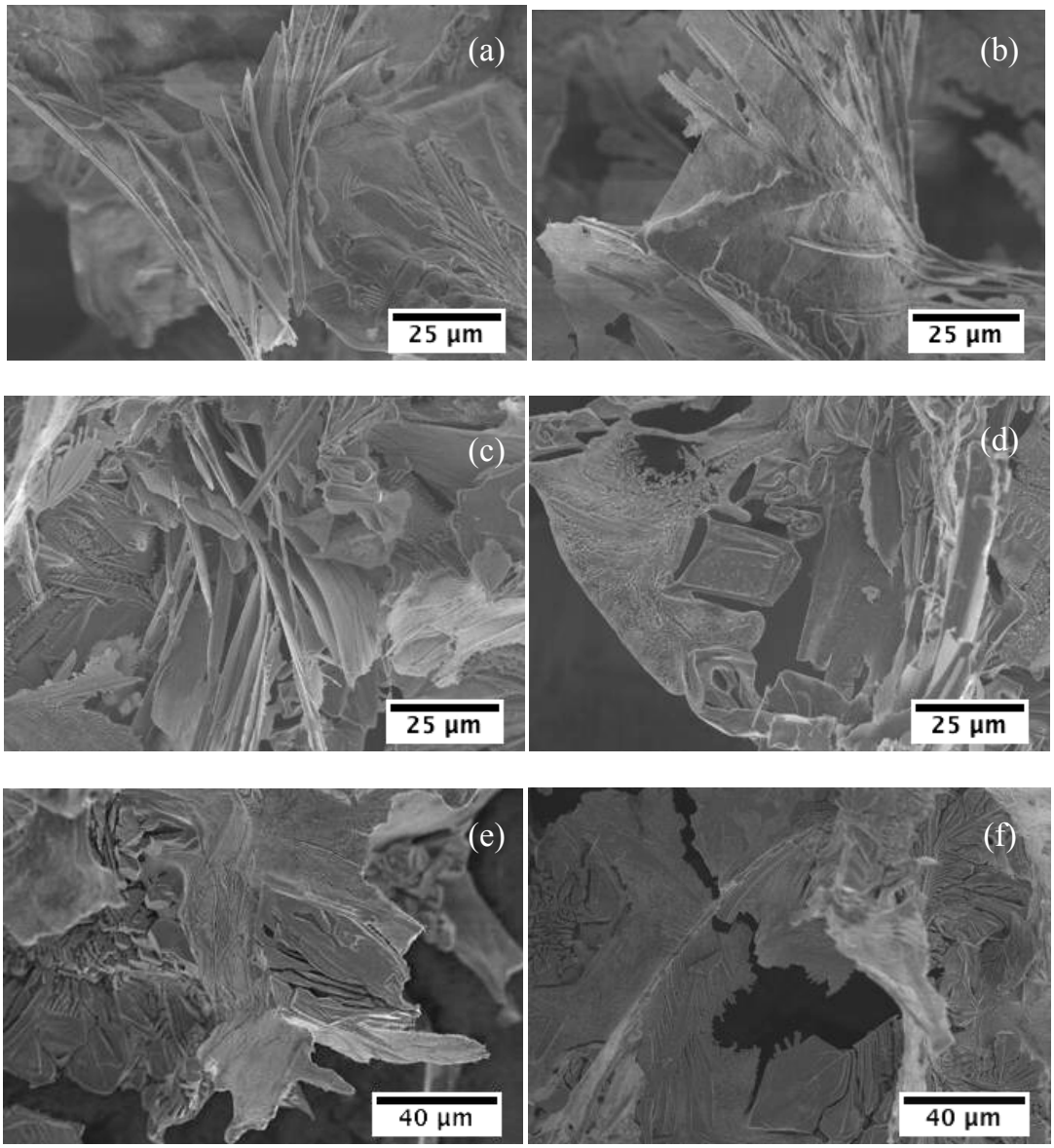


Figure 4.62: SE micrograph showing examples of extracted intermetallic particles with a plate-like morphology from (a, b) ZR200C, (c, d) ZR200E and (e, f) ZR200B

4.7.4 Summary

The extracted intermetallic phase morphology analysis revealed:

- Intermetallic phases from all three samples displayed a very interconnected 3D sponge like appearance;

- The 3D structures extracted from GR200 were sturdiest amongst all the samples and most interconnected, while the structures extracted from ZR200 were most delicate.
- All samples displayed combinations of intricate and plate-like morphologies;
- The intricate intermetallic phase morphology was more prevalent in BA200 and ZR200, while the plate-like morphology was more prevalent in GR200;
- 'Flower'-like intermetallic phase morphology was often observed in BA200 and frequently observed in GR200; and
- Ti-clusters could not be successfully located at the centre of the 'flower'-like intermetallic phases.

One of the objectives of the project was to maintain the α-Al grain size consistent between samples, which was achieved at the centre of the three alloys, BA200, GR200 and ZR200. Table 4.10 provides a summary of the microstructural characteristics observed at the centre.

Table 4.10: Summary of the various alloy characteristics at the centre

	BA200C	**GR200C**	**ZR200C**
Grain Size	290±25μm	170±20μm	220±25μm
Cell Size	140±10μm	120±5μm	150±15μm
Pore Size	150±15μm	120±10μm	140±25μm
Pore Aspect Ratio	0.75	0.72	0.69
α-AlFeSi Content	70wt.%	50wt.%	80wt.%
Predominant 3D Phase Morphology	'Chinese-script'	Plate-like	'Chinese-script'
Relative Frequency of 'Flowers'	Medium	High	Negligible

4.8 ThermoMechanical Analysis (TMA)

The thermomechanical behaviour of all the alloys were first analysed at temperature but under a small load of 200mN, and then the impact of load application was subsequently investigated. The solid fractions of GR200 and ZR200 were calculated using the Scheil model (shown in Figure 4.63), which was then compared with the extension of each sample tested.

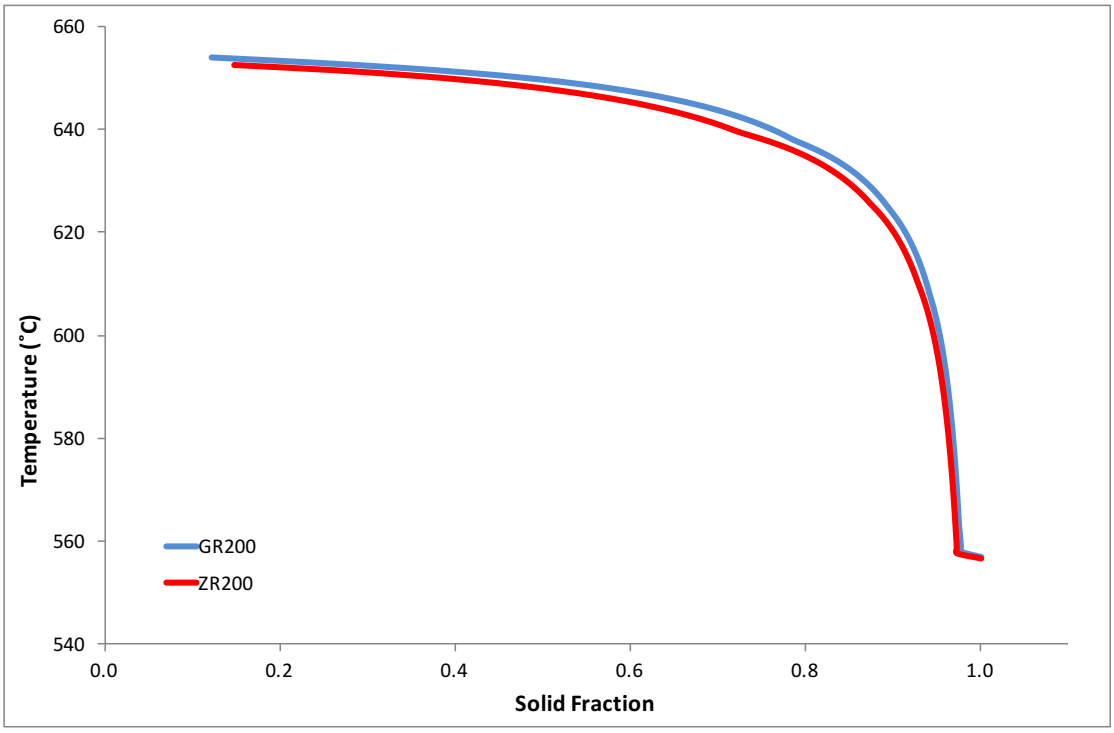


Figure 4.63: Solid fraction, calculations based on Scheil model, of GR200 and ZR200 against temperature change

4.8.1 GR200 (~50wt.% α-AlFeSi content)

The samples tested at the maximum temperatures of 610ºC (GR610) and 625ºC (GR625) fractured before experiencing any increase in load. To better understand the thermomechanical behaviour of the fracture mechanism, another set of samples were

tested at a maximum temperature of 595ºC (GR595), and the full load of 981mN was applied. Figure 4.64 shows the force against extension observed in GR200 samples, whereby suffixes _01 and _02 refer to the two samples that were tested at the same maximum temperature. It can be seen that the GR595 samples did not fracture or crack on completion of the entire test cycle, while the GR610 and GR625 samples fractured before any increase in load.

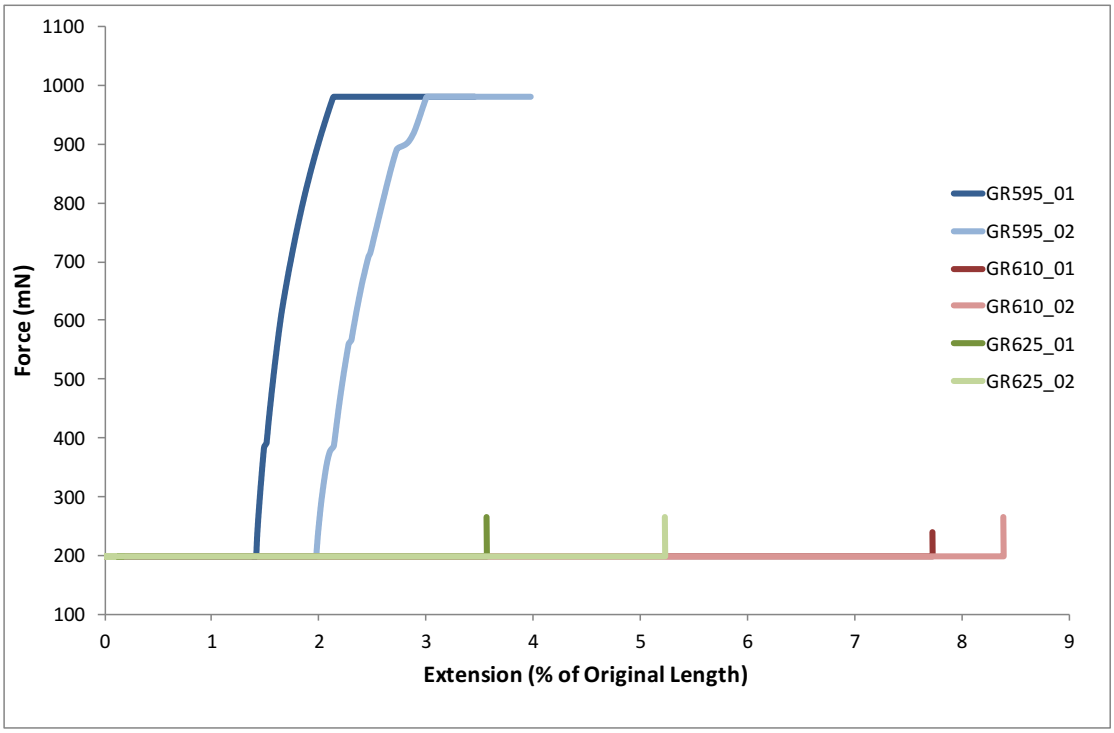


Figure 4.64: Force versus extension in GR200 samples

Temperature changes and extension over time are shown in Figure 4.65 and Figure 4.66, and the point where load application increased is identified. Figure 4.67 shows the extension and overall solid fraction of GR200 (calculated using Scheil model) over temperature. Table 4.11 summarises the thermomechanical behaviour of GR200 in tensile.

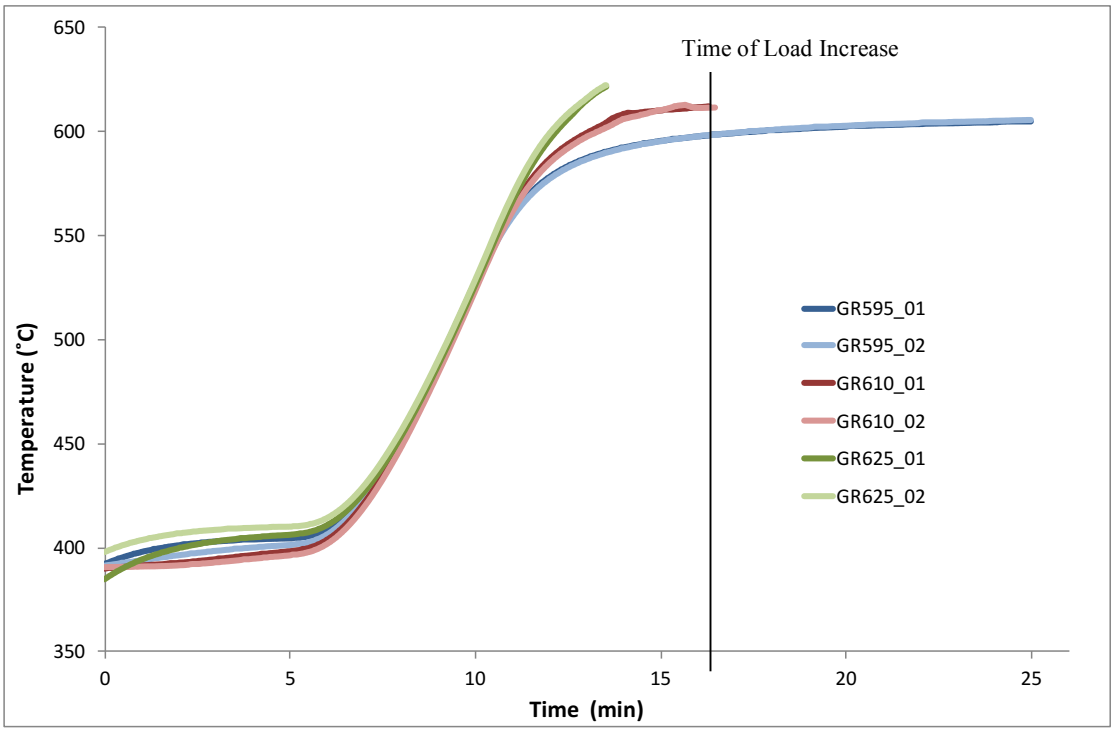


Figure 4.65: Temperature changes over time in GR200 samples

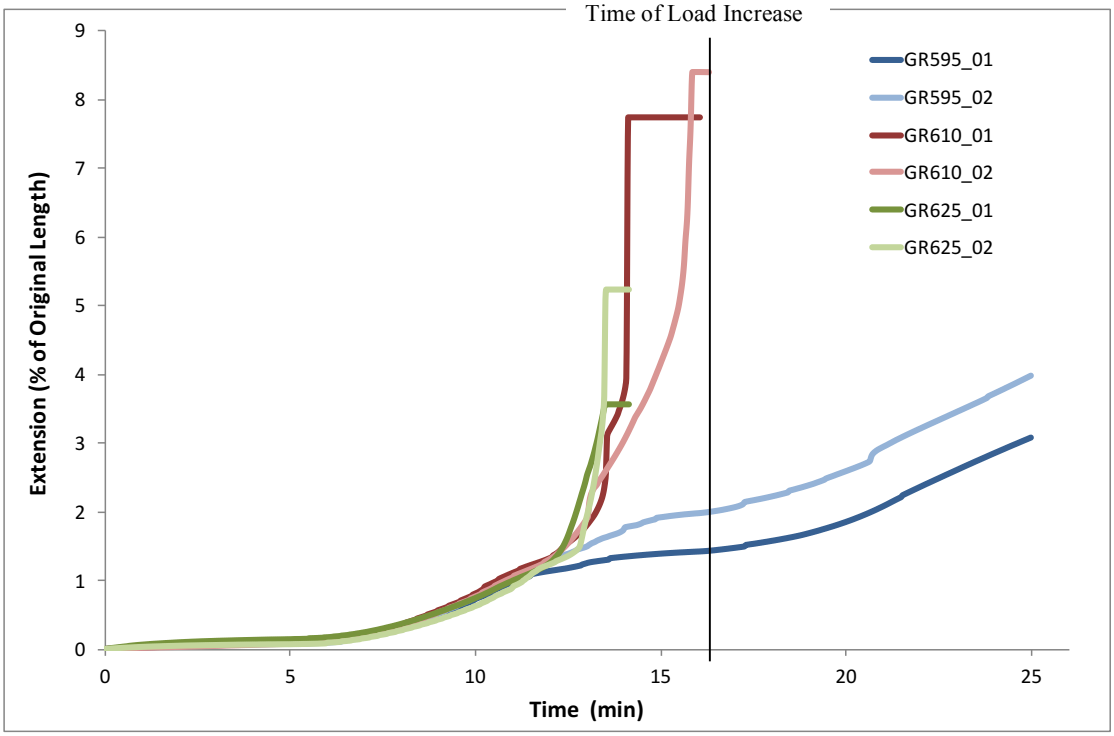


Figure 4.66: Extension over time in GR200 samples

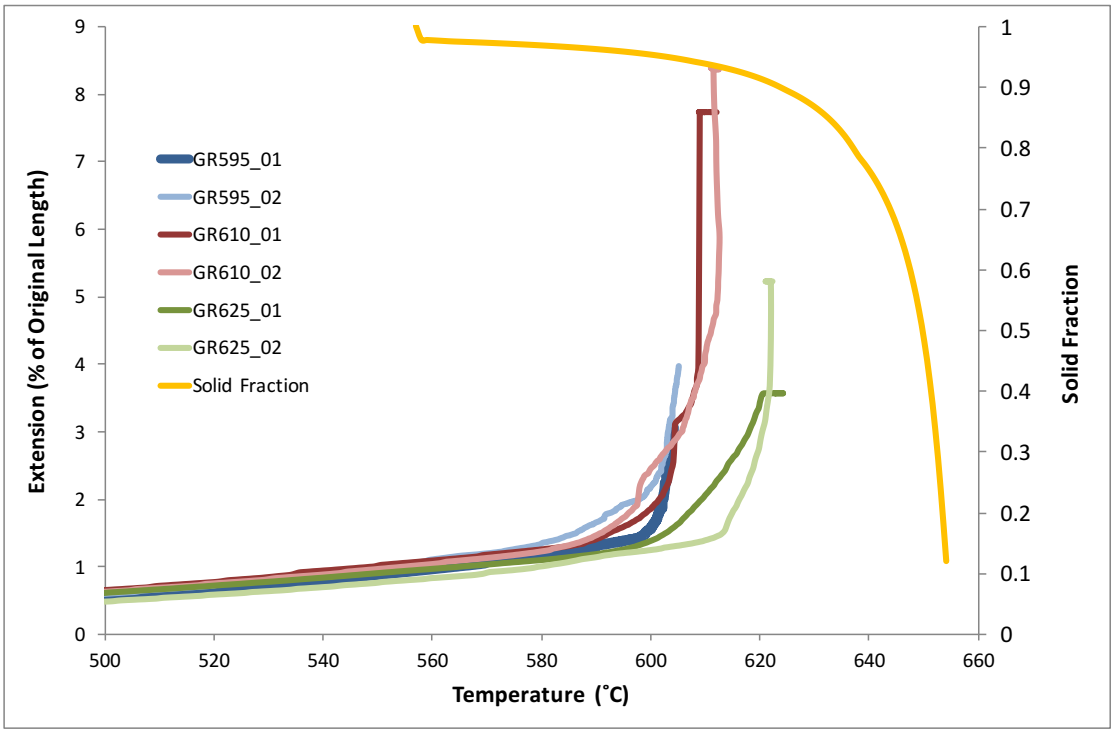


Figure 4.67: Extension and solid fraction (according to Scheil calculations) over temperature in GR200 samples

Table 4.11: Summary of thermomechanical behaviour of GR200 in tensile

Sample	Sample Fracture	Solid Fraction	Time at Max Temp.	Load at Fracture	Time at 981mN	Extension
GR595_01	–	–	5 min	–	10 min	3%
GR595_02	–	–	5 min	–	10 min	4%
GR610_01	608ºC	0.941	0 min	200 mN	0 min	8%
GR610_02	611ºC	0.936	0 min	200 mN	0 min	8%
GR625_01	620ºC	0.914	0 min	200 mN	0 min	3%
GR625_02	622ºC	0.906	0 min	200 mN	0 min	5%

4.8.2 ZR200 (~80wt.% α-AlFeSi content)

The elongations of ZR200 were tested at 595ºC, 610ºC and 625ºC, namely ZR595, ZR610 and ZR625 respectively. ZR595 fractured after the full load of 981mN had been applied, while ZR625 samples fractured before experiencing any increase in load. A small load was applied before ZR610 fractured. Figure 4.68 shows the force against extension observed in ZR200 samples. It can be seen that both ZR595 and ZR610 samples experienced increase in load application before fracture, while the GR625 samples fractured before any increase in load.

Temperature changes and extension over time are shown in Figure 4.69 and Figure 4.70, and Figure 4.71 shows the extension and overall solid fraction of ZR200 (calculated using Scheil model) over temperature. Table 4.12 shows the summarises the thermomechanical behaviour of ZR200 in tensile.

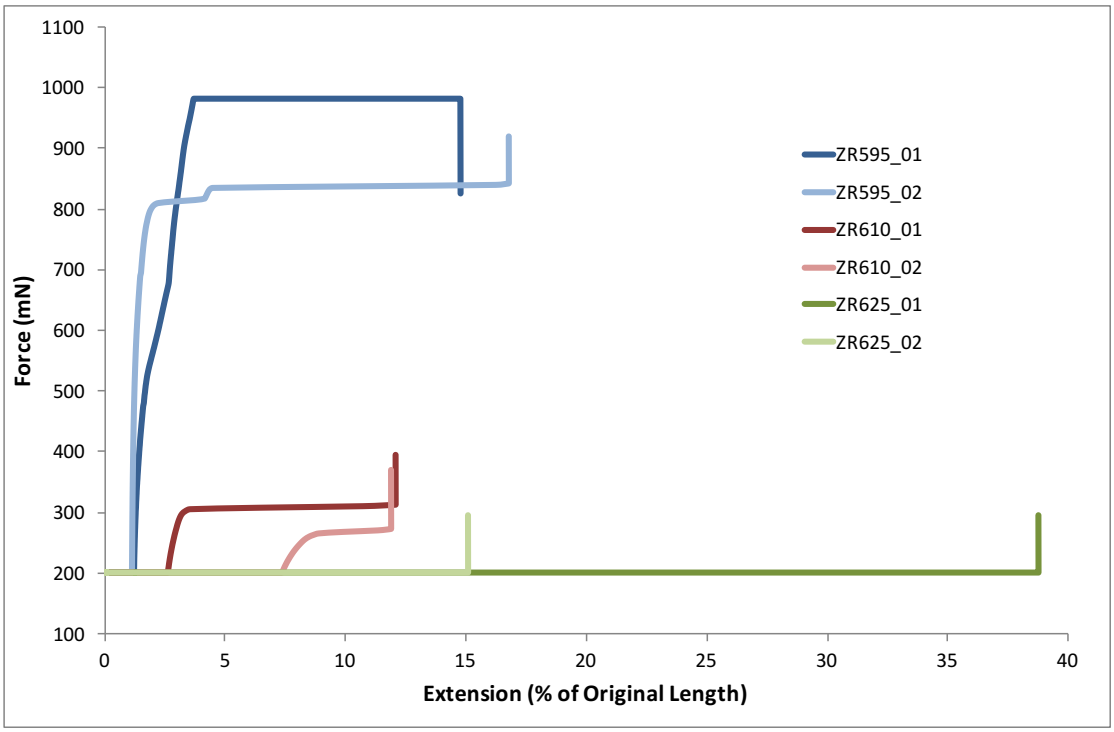


Figure 4.68: Force versus extension in ZR200 samples

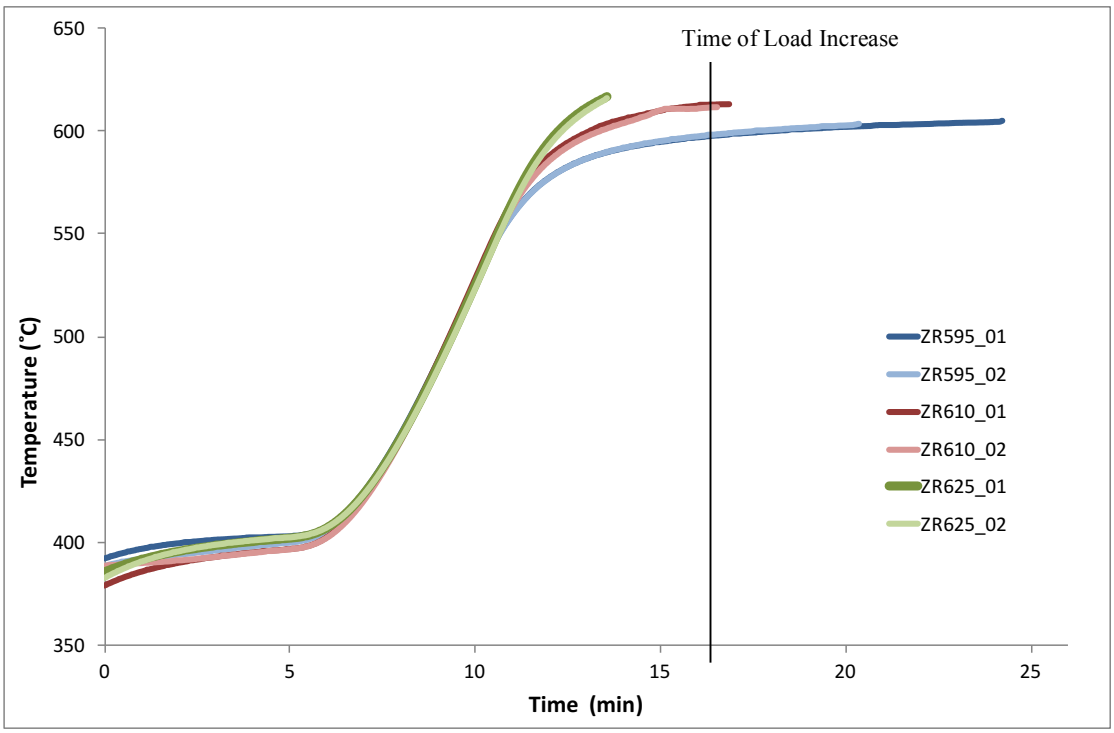


Figure 4.69: Temperature changes over time in ZR200 samples

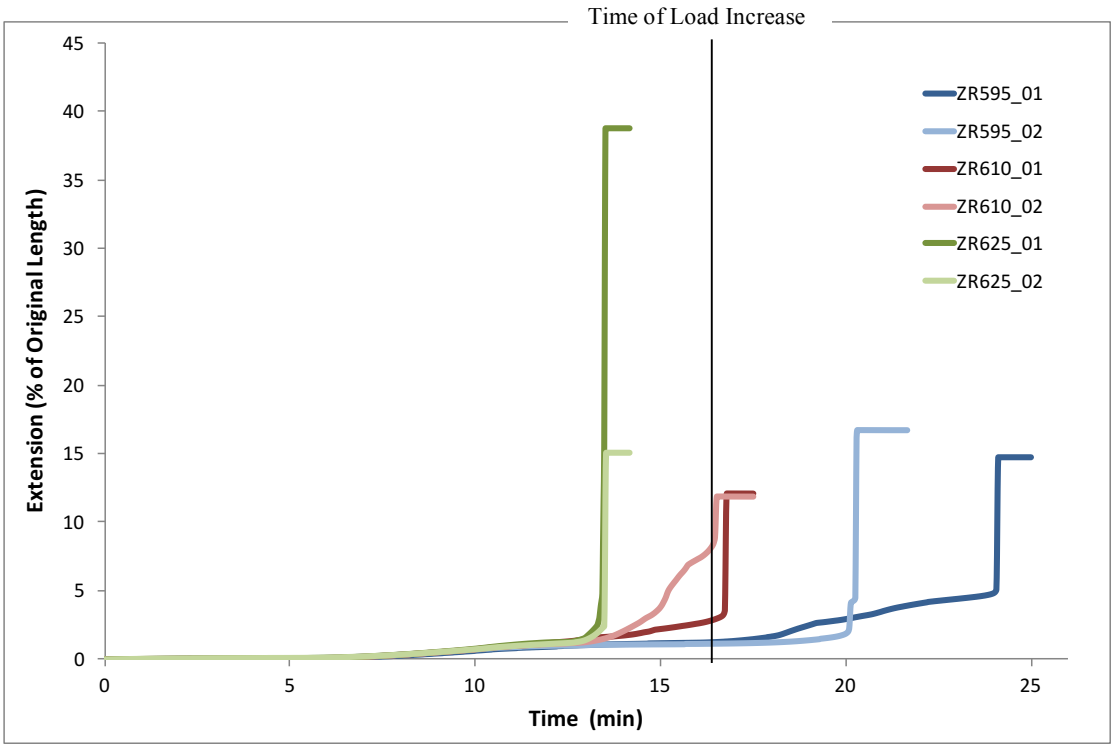


Figure 4.70: Extension over time in ZR200 samples

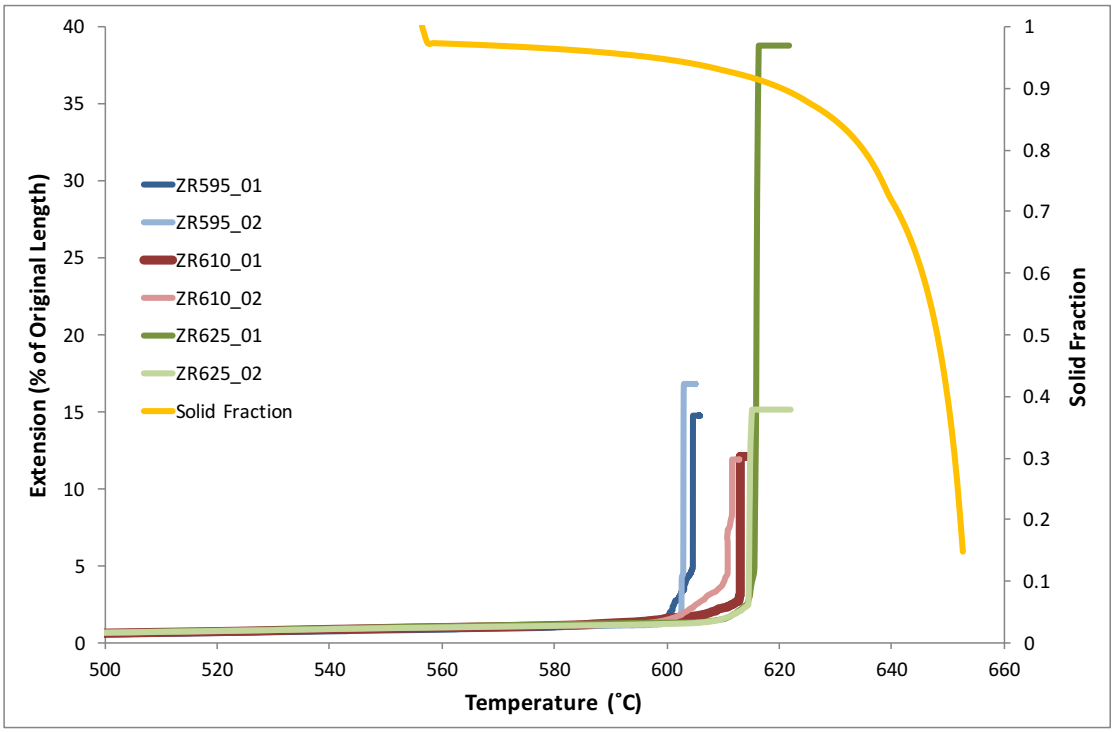


Figure 4.71: Extension and solid fraction (according to Scheil calculations) over temperature in ZR200 samples

Table 4.12: Summary of thermomechanical behaviour of ZR200 in tensile

Sample	Sample Fracture	Solid Fraction	Time at Max Temp.	Load at Fracture	Time at 981mN	Extension
ZR595_01	603ºC	0.941	14 min	981 mN	5 min	15%
ZR595_02	605ºC	0.937	10 min	842 mN	0 min	17%
ZR610_01	615ºC	0.915	6 min	313 mN	0 min	12%
ZR610_02	612ºC	0.923	6 min	275 mN	0 min	12%
ZR625_01	615ºC	0.915	0 min	200 mN	0 min	39%
ZR625_02	616ºC	0.912	0 min	200 mN	0 min	15%

4.9 Fracture Surface Analysis of TMA Samples

4.9.1 GR595

As mentioned previously, neither GR595 samples fractured or cracked on completion of the entire test cycle. Thus SEM examination was not carried out on these samples.

4.9.2 GR610

Only one side of the second test sample was examined for the fracture surface analysis. GR610 fractured before experiencing any increase in load, and the fracture surface is shown in Figure 4.72.

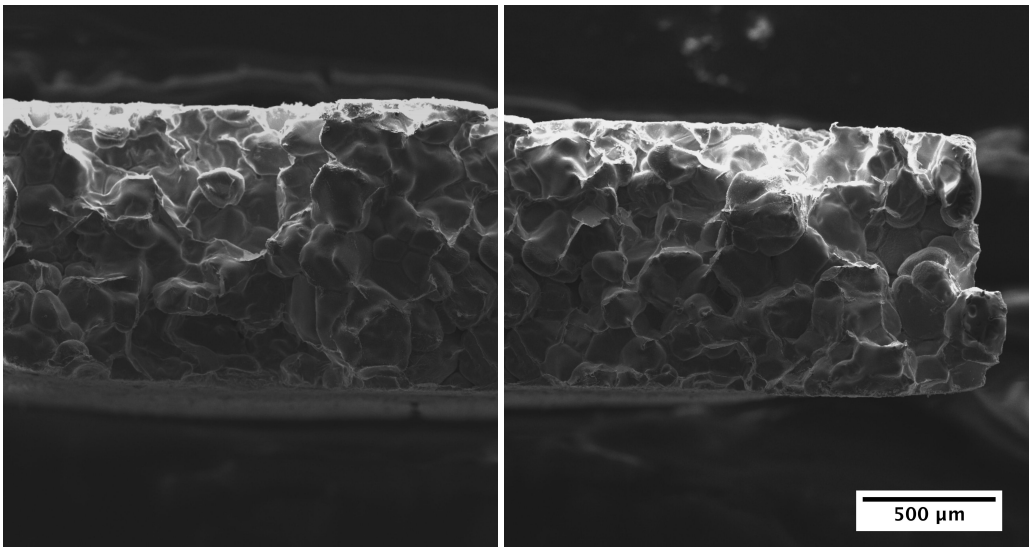


Figure 4.72: SE micrographs of the fracture surface of GR610 without load

The phase morphology observed, shown in Figure 4.73, was predominantly planar plate-like, with a very small percentage of intricate leaf-like structures. An oxide layer was also observed on the surface, interrupted by protruding intermetallic phases.

Element mapping and EDX confirmed the presence of one Ti-rich particle on the surface, which appeared to be associated with the intricate intermetallic particle from Figure 4.73 (b), as well as evidence of Mg rich zones.

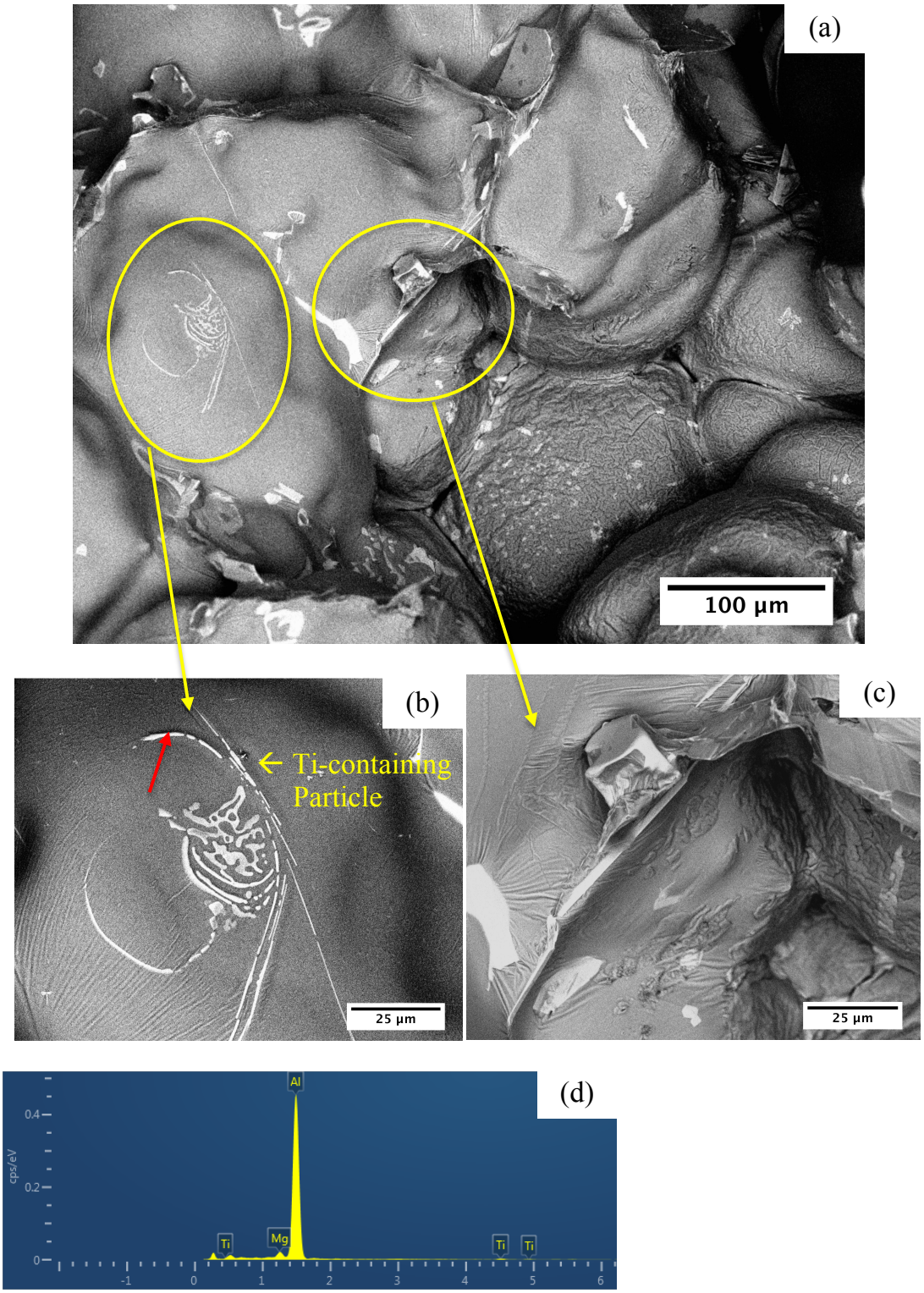


Figure 4.73: BSE micrographs of (a) section of the fracture surface of GR610, while (b and c) show some of the phases at higher magnification, (d) shows the EDX spectrum obtained from the location identified as a particle with Ti present. The red arrow identifies the very dark Mg_2Si phase, associated with the intermetallic phase

4.9.3 GR625

It was interesting to note that the fracture surface of GR625 which also fractured before experiencing any increase in load, shown in Figure 4.74, had a very similar appearance to that of GR610.

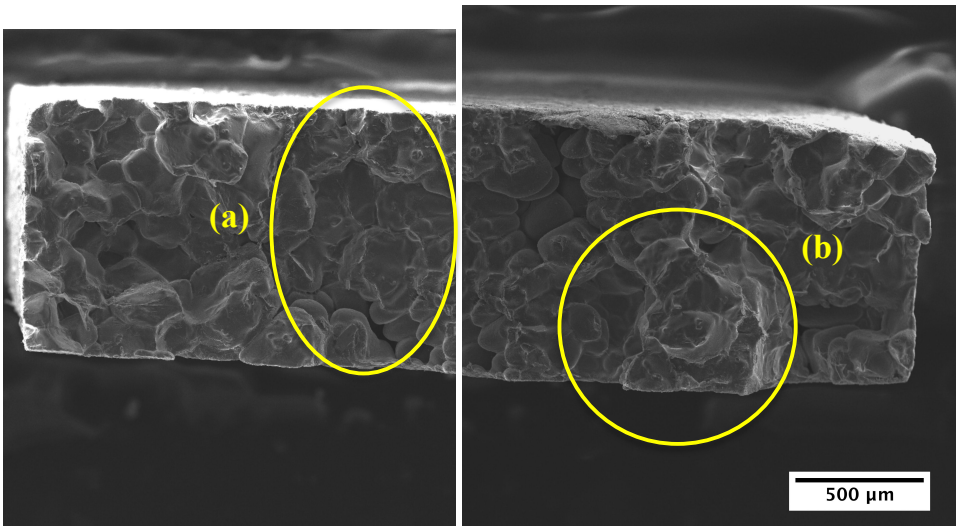


Figure 4.74: SE micrographs of the fracture surface of GR625 without load. The (a) depressed and (b) elevated features are identified with yellow ellipses highlighting the regions

On closer examination, the elevated and depressed regions, shown in Figure 4.75, appeared identical in terms of average candy-rock diameters, 175±20µm and 177±25µm respectively, and phase morphology.

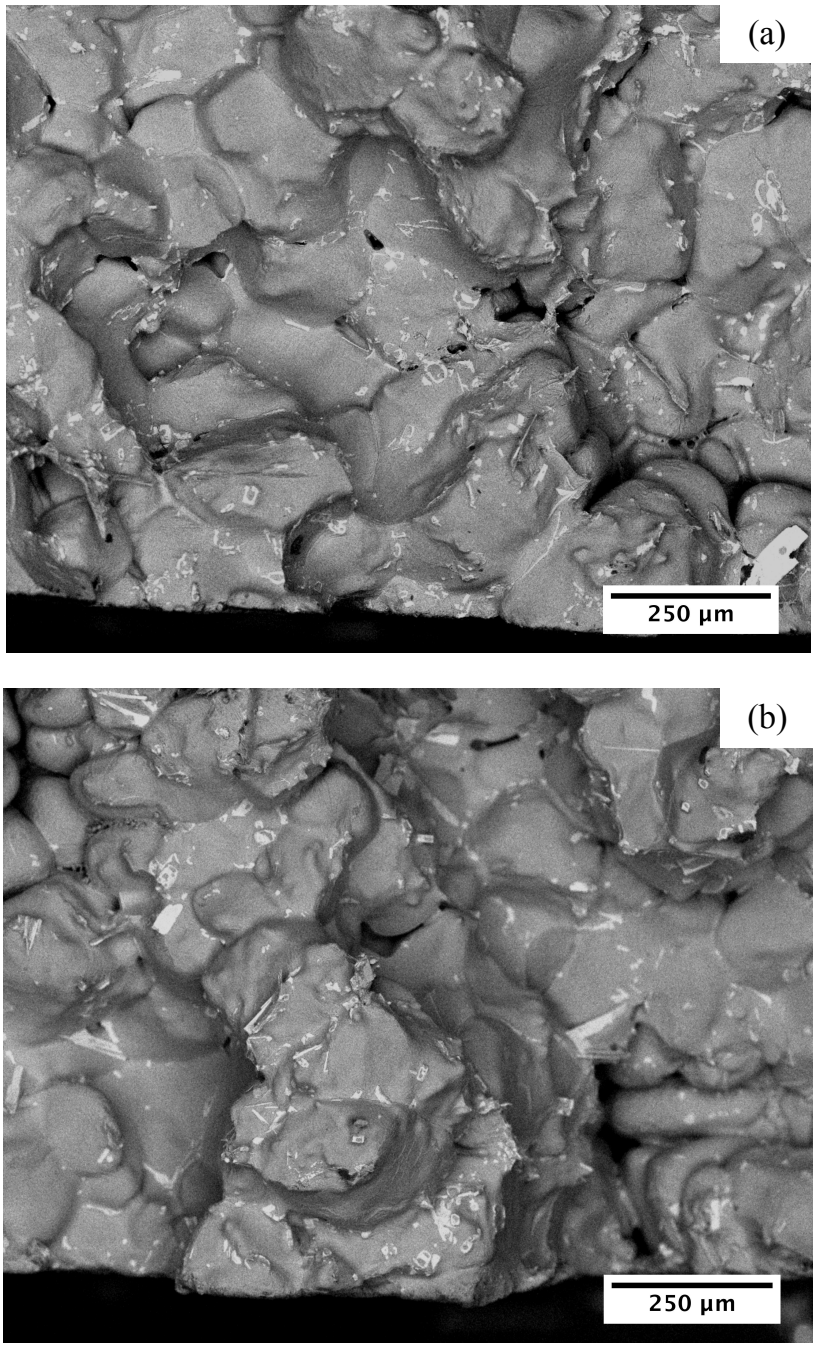


Figure 4.75: BSE micrographs of the (a) depressed and (b) raised regions of the fracture surface at higher magnification.

An example of the typical phase morphology observed in GR610 is shown in Figure 4.76. It was interesting to note, however, that there were several plate-like phases protruding out from the surface. Several examples of this feature are shown in Figure 4.77.

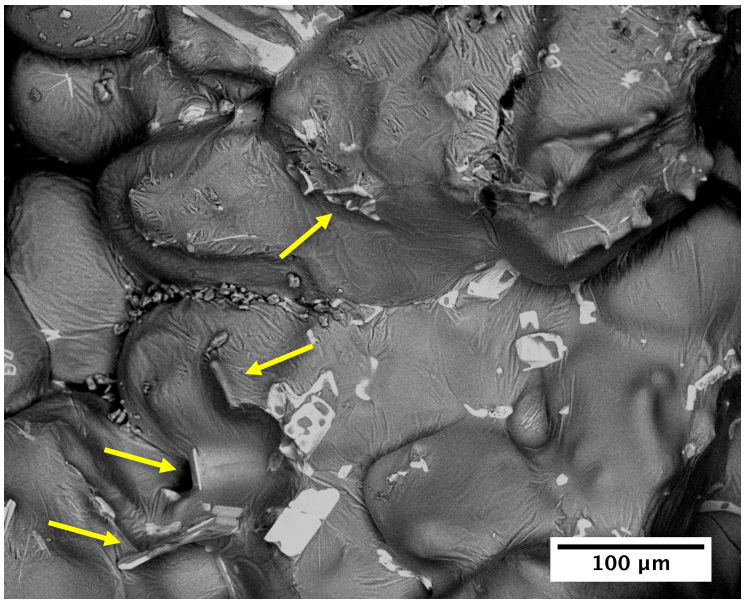


Figure 4.76: BSE micrograph of a section of the fracture surface of GR625, yellow arrows indicate plate-like phases protruding out.

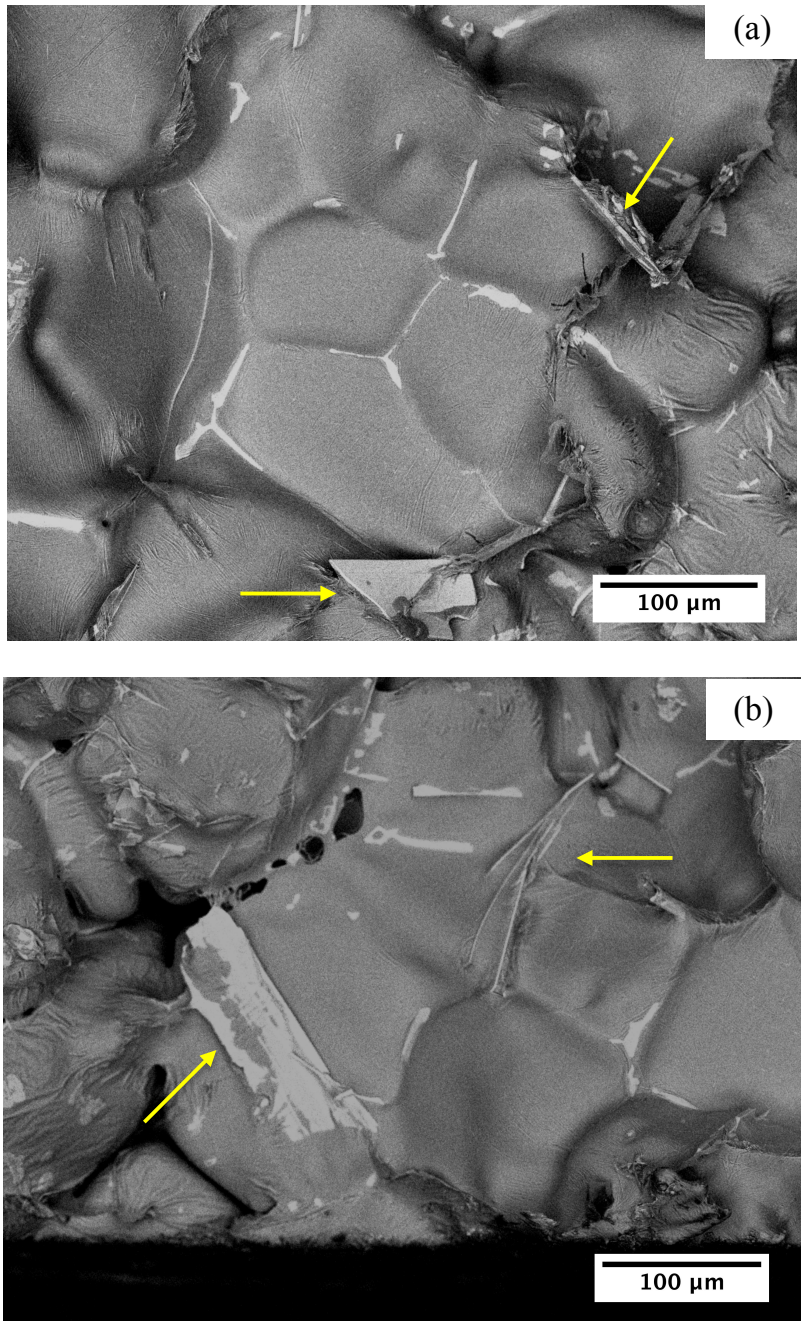


Figure 4.77: BSE micrographs of the fracture surface, showing plate-like planar intermetallic particles protruding out of the fracture surface (features identified with yellow arrows).

4.9.4 ZR595

As mentioned earlier, the sample fractured after the full load of 981mN had been applied. The fracture surface of the sample is shown in Figure 4.78; most of the surface

appears to have experienced a ductile fracture, except two distinct regions displaying brittle fracture features. No obvious initiation point could be determined.

Most of the surface displayed dimples, which are indication of microvoids – a characteristic feature of ductile fracture. Some secondary electron (SE) micrographs of the ductile fracture region, displaying dimples, are shown in Figure 4.79.

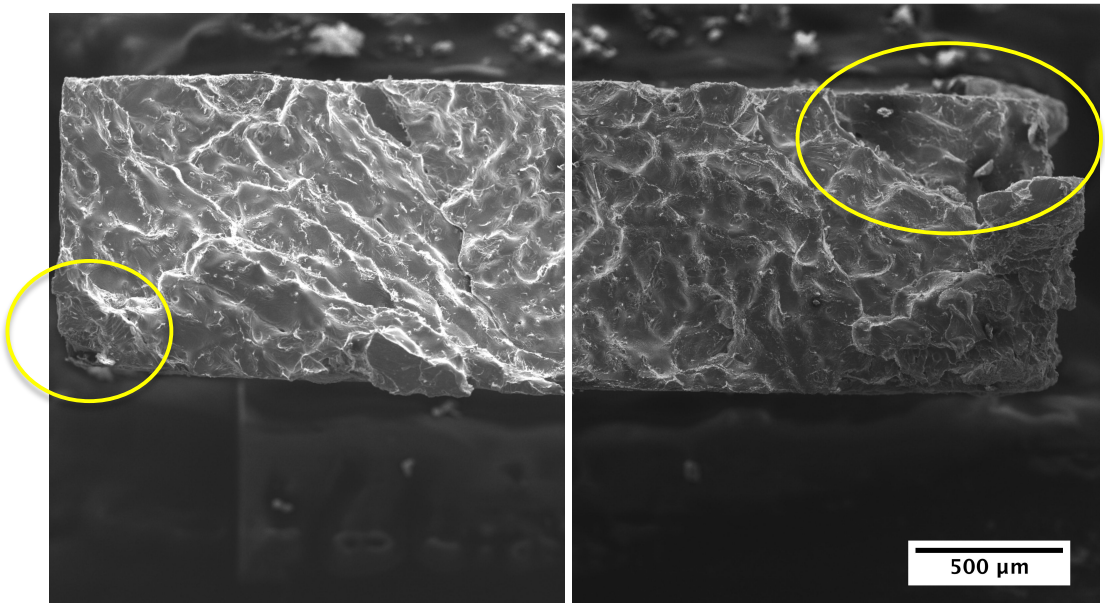


Figure 4.78: SE micrographs of the fracture surface of ZR595, fractured with an applied load of 981mN. The yellow ellipses highlight characteristic brittle fracture features

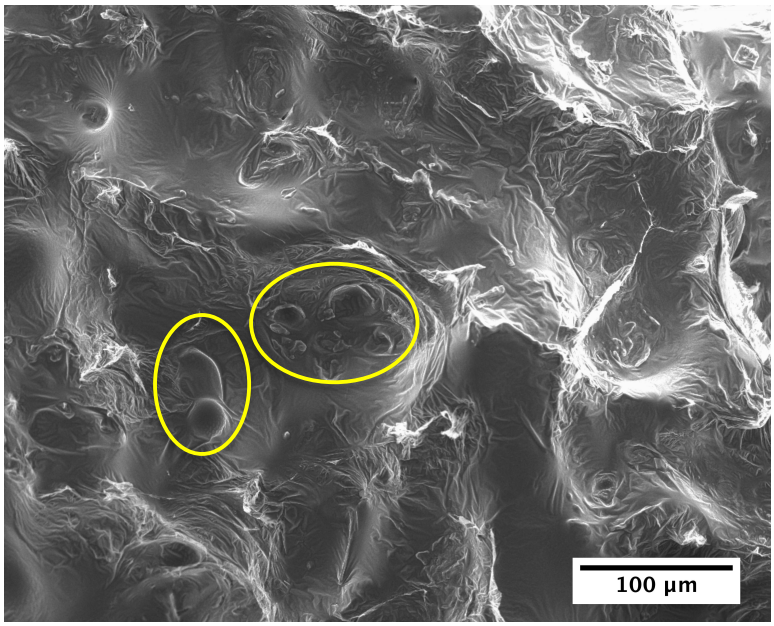


Figure 4.79: SE micrograph of the ductile fracture region in ZR595. The yellow ellipses highlight dimples within the larger dimples

The dimpled regions were further examined using backscatter imaging (shown in Figure 4.80 a) to ascertain the distribution of phases. Phases were observed on almost all the peaks in the region. The indication of microvoids at higher magnification (Figure 4.80 b) again displayed phases on the perimeter of the finer dimples, while the surface appeared to be covered in a layer of crumpled oxide.

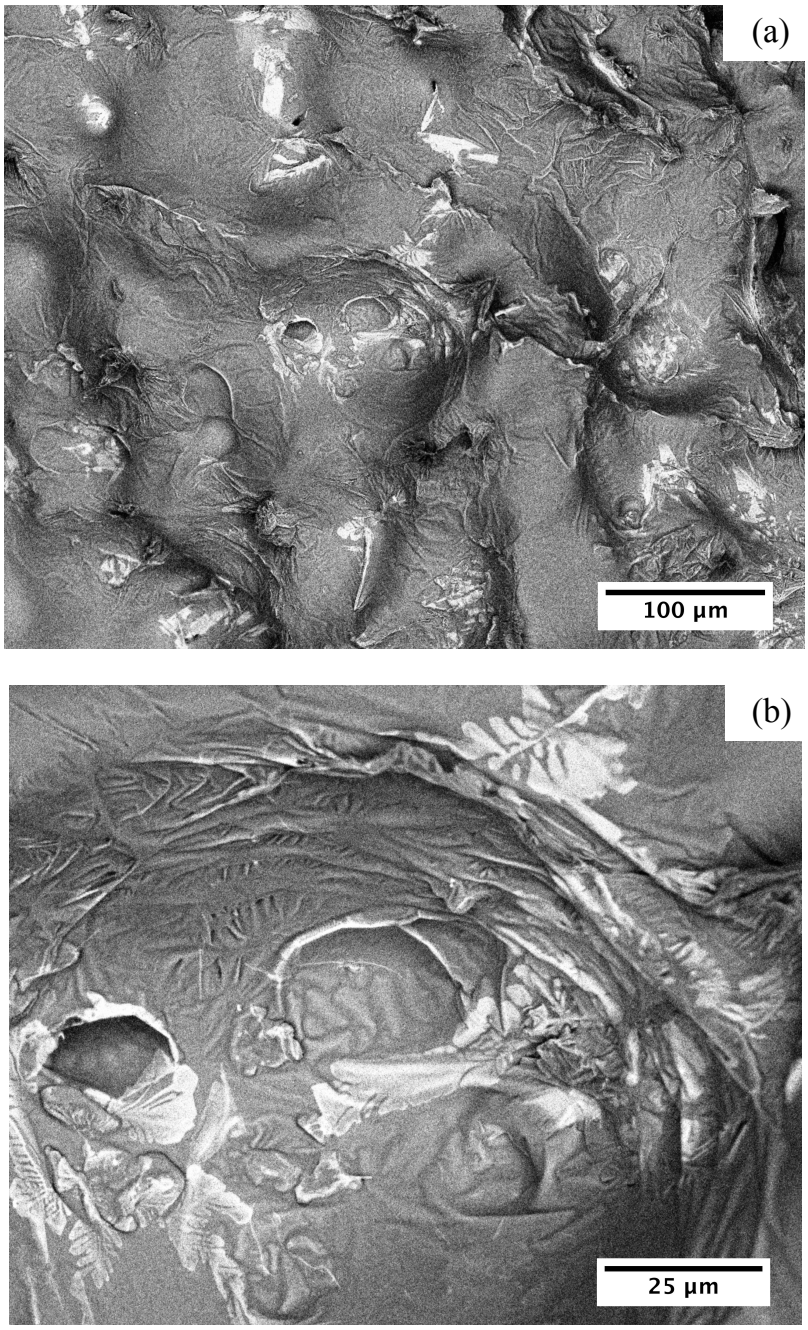


Figure 4.80: BSE micrographs of the (a) ductile fracture region in ZR595, and (b) a high magnification micrograph of one dimple

The regions with stepped features, characteristic of brittle fracture, were also examined using backscattered imaging, shown in Figure 4.81. Phases could once again be

observed on the higher regions, and the surface appeared to be covered with a crumpled oxide layer.

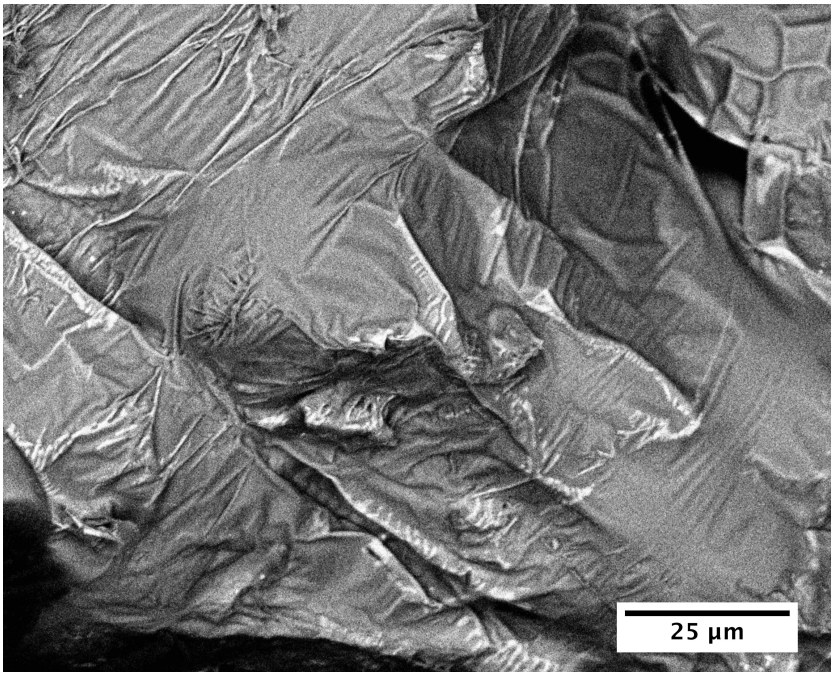


Figure 4.81: High magnification BSE micrographs of a brittle fracture region in ZR595. An oxide layer is visible covering the entire surface

4.9.5 ZR610

This sample fractured without experiencing any increase in load, and therefore it can be assumed that the predominant cause behind the fracture was the liquid/solid fraction of the sample. The fracture surface of the sample, shown in Figure 4.82, once again mostly displayed ductile fracture features, with a small region of brittle fracture (highlighted on the figure). A preferential direction of fracture was also observed on the fracture surface, but no obvious initiation point could be determined.

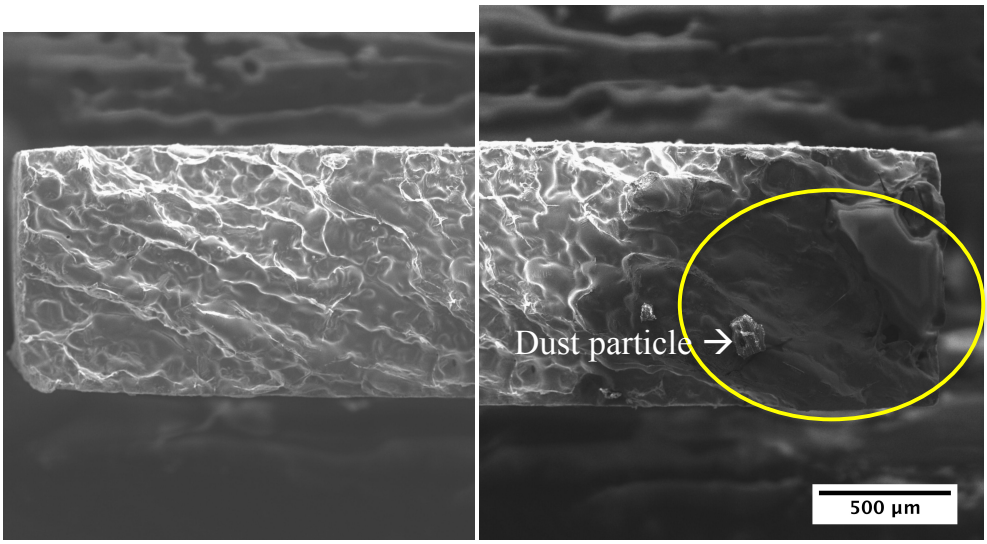


Figure 4.82: SE micrographs of the fracture surface of ZR610 without load. The yellow ellipse highlights characteristic brittle fracture features. The dust particles highlighted was an unwanted impurity, picked up while handing the fractured surface

The backscattered micrographs of the dimpled regions, and regions with brittle fracture features (Figure 4.83 and Figure 4.84 respectively), once again displayed the presence of phases on the raised regions, while the surface is wrapped with a rippled oxide film.

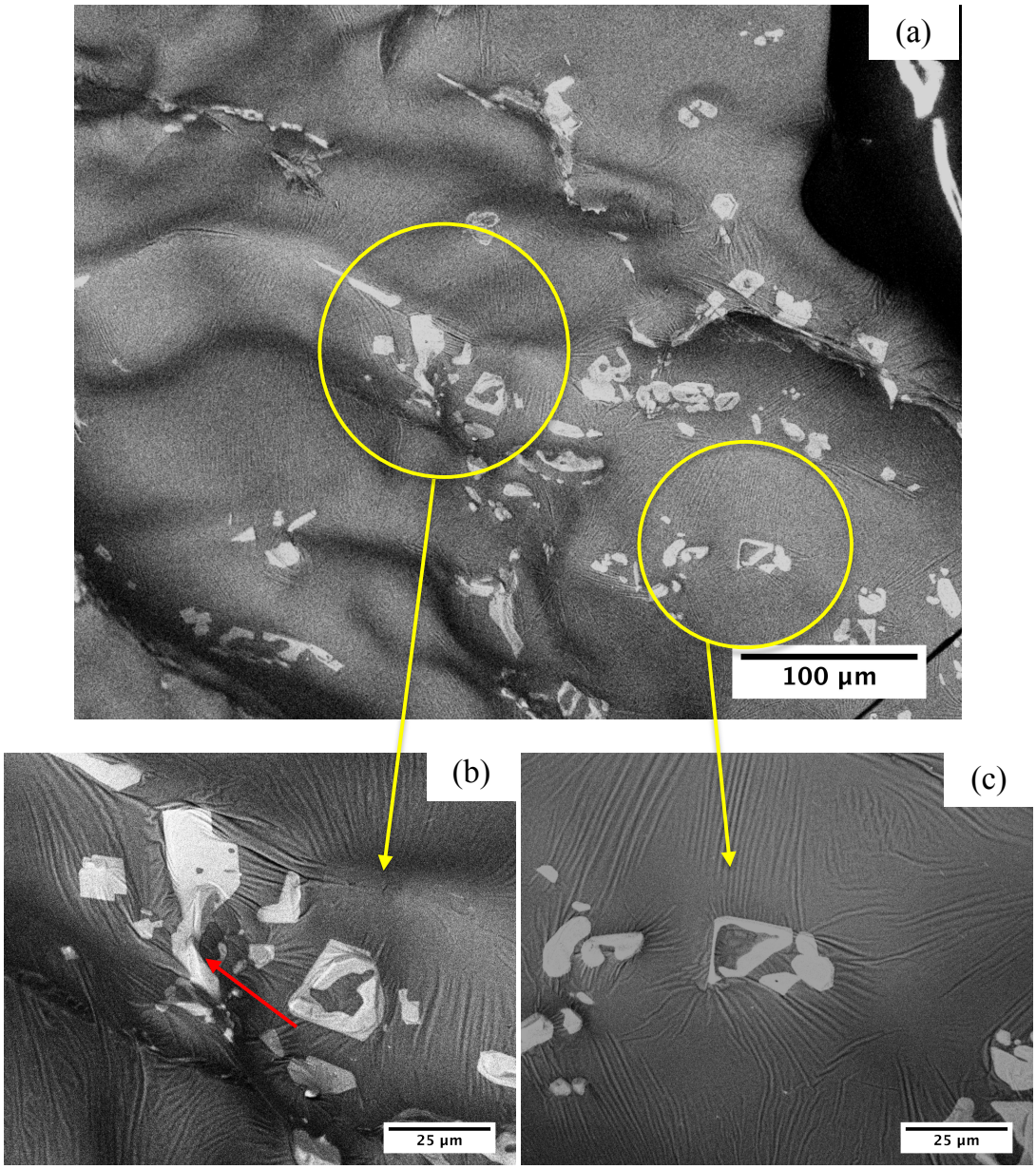


Figure 4.83: BSE micrographs of (a) section of the fracture surface of ZR610, while (b and c) shows some of the phases at higher magnification. The red arrow identifies the very dark Mg_2Si phase.

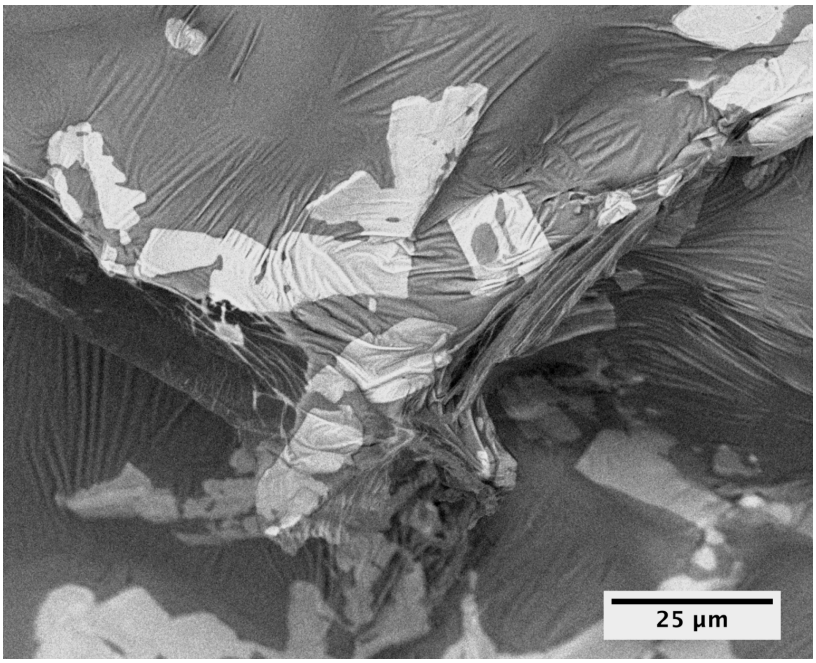


Figure 4.84: BSE micrograph of the fracture surface of the ZR610, without load

4.9.6 ZR625

Once again, this sample fractured without experiencing any increase in load. The fracture surface of the sample is shown in Figure 4.85.

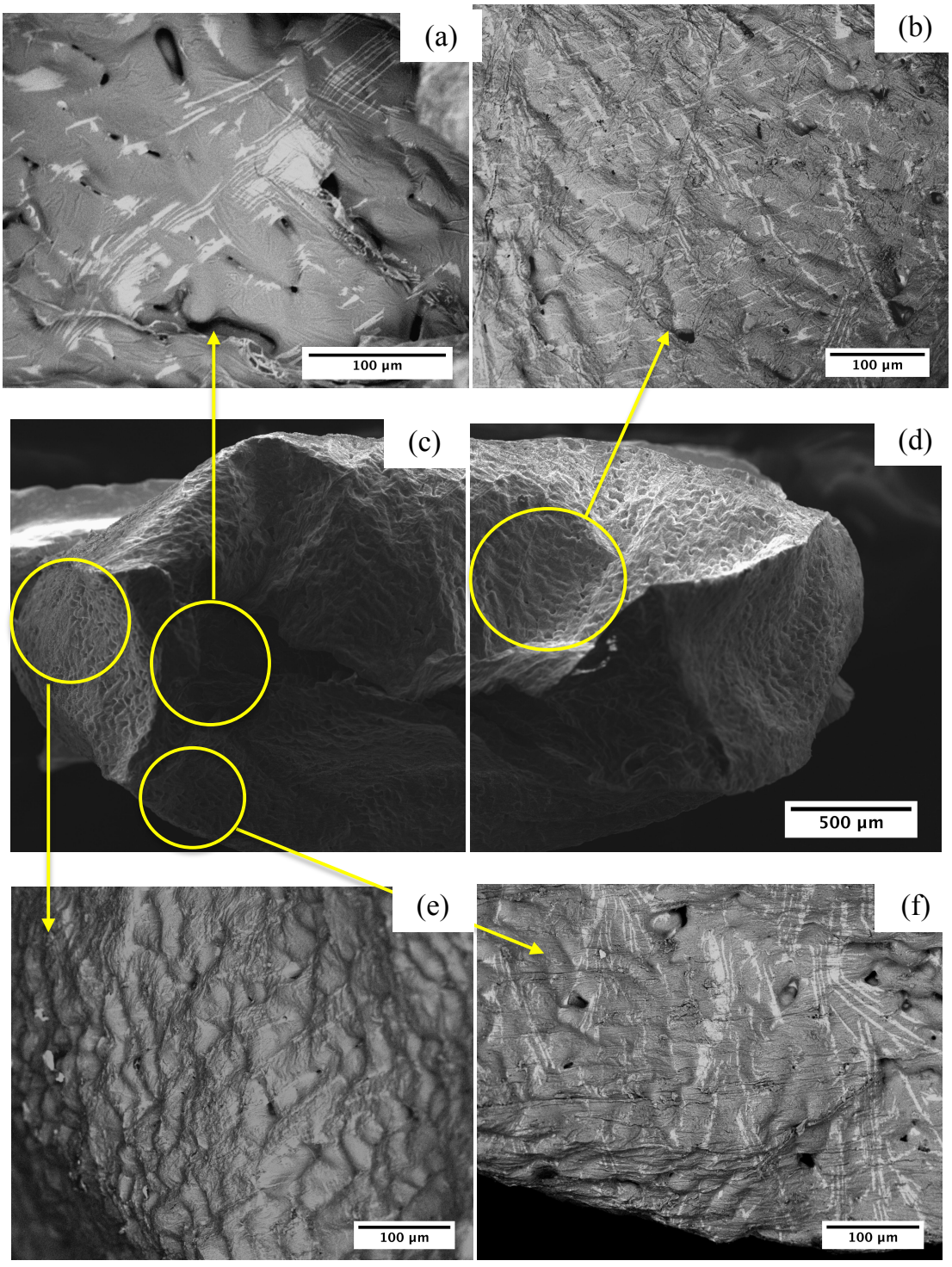


Figure 4.85: (c and d) Shows SE micrographs of the fracture surface of ZR625 without load, and (a, b, e, f) showing BSE micrographs of the various regions in higher magnification

Chapter 5 Discussion

This chapter will discuss the microstructures and phase selection of the base, grain refined and Zr containing alloys, followed by a summary of the overall trends observed. Based on the overall trends, it will then discuss the possible solidification routes that may have produced the resultant microstructures including the semisolid processing technique, the phase selection, and the phase morphology both for the as-cast alloy (2D) and as-extracted intermetallic particles (3D). The impact of different levels of α-AlFeSi and β-AlFeSi phases on the thermodynamic behaviours of the alloys produced through semisolid processing is also discussed in this chapter.

5.1 Primary Al Grain Size Analysis

In the images scanned from macro-etched surfaces, it was difficult to differentiate between grain boundaries and artefacts in the image caused by light diffraction, as well as grains and porosity. Thus, measurements taken from the anodised samples were considered to be a better representation of the overall microstructure.

It can be seen, however, from Figure 4.15 (section 4.3 a), Figure 4.19 (section 4.3 c) and Figure 4.23 (section 4.3 e) that the macro-etched grain sizes correspond closely to the average cell sizes measured from the anodised sample surface, indicating that the cell boundaries are displayed as visible contrast on the macro-etched sample surfaces. Thus, it can be assumed that the measurements carried out on the macro-etched sample surfaces were in reality the cell size measurements. This may have been caused by the phases encapsulating the cells, creating an impression of individual grains on visual inspection. The measurements from macro-etched sample surfaces were used to

compare microstructures of alloys cast with the semisolid processing technique with the steel enthalpy can preheated to 400ºC.

5.1.1 TP-1 Casting Process

As specified in section 3.1.6, TP-1 casts are the standard industrial test for assessing grain refiner performance for direct chill (DC) cast Al alloys. GRTP-1 displayed an average α-Al grain size of 160μm on the horizontal cross-section (Figure 4.19, section 4.3 c), which is significantly smaller than those of BATP-1, which averaged 790μm (see Figure 4.17, section 4.3 b). It was difficult to identify grain and cell boundaries on the ZRTP-1 anodised sample, which also displayed severely disconnected phases throughout the sample surface. Since ZRTP-1 had coarse grain size, such that even at low magnification used in the current optical microscopy it was difficult to get one full grain boundary in an image, therefore accurate grain size measurements could not be carried out using the anodised sample surface, and hence microstructural comparisons were limited to measurements taken from the macro-etched sample surface for this alloy. Although the average grain size of ZRTP-1, measured using the macro-etched surface, was 890μm on the horizontal cross-section (Figure 4.13, section 4.2 i), it was not representative of the overall microstructure as the grain sizes varied significantly, and were considerably larger than those of BATP-1 and GRTP-1.

The vertical and horizontal cross-sections of BATP-1 and ZRTP-1 resemble each other in terms of the microstructures, except that the grains in ZRTP-1 are significantly coarser in both length and width. Columnar grains (aligned at angles of 40^{o} and above) were observed on the vertical cross-sections of BATP-1 and ZRTP-1, which

interestingly extend to just about the 38mm horizontal plane. This might be a result of the faster cooling rate near the base of the TP-1 ladle, which is submerged into running water, acting as a thermal sink for the wider areas above containing more thermal energy. Since columnar grains form along the preferred thermal energy escape route, they form at the angle through which thermal energy escapes from the wider areas above towards the ladle base. Some columnar grains were also observed on the vertical sections of ZRTP-1 at the 38mm plane, which might be the result of the lower cooling rate near the edge, allowing time for the grains to grow longer along the preferred thermal energy escape route.

The microstructures of GRTP-1 remained identical in appearance in both the vertical and horizontal cross-sections; consistently fine and equiaxed. It can also be seen from Figure 4.9 section 4.2 (f) that there are no columnar grains on the edges of the sample surface. This can be attributed to two main mechanisms taking place:

– As mentioned section 2.3.2 (b), the growth restriction ability of Ti in aluminium (the Q value) is significantly higher than for the rest of the elements that were added to the alloy (Table 2.1); and

– TiB_2 is a potent nucleant which acts as an effective nucleation substrate for 99.97% of pure Al [32].

Thus, in the presence of Al-Ti-B type grain refiner, the various grain refinement mechanisms that take place are as follows:

- TiB_2 (the substrate) nucleates α-Al;
- The remaining Ti contributes to grain refinement at two stages:

- During initial solidification process, Ti disperses between the TiB_2-liquid interfaces and forms a single layer of Al_3Ti on the TiB_2, which in turn increases the nucleation potency of TiB_2;
- During the grain growth process, Ti disperses between the growing solid-liquid interfaces, which obstructs any/further dendrite growth. This growth restriction allows sufficient undercooling for the remaining TiB_2 in the vicinity to nucleate.

Thus, the addition of Al-Ti-B type grain refiner with Ti in excess reduces nucleation undercooling and suppresses columnar zone formation, resulting in a fine grain microstructure which is in agreement with previous studies [32]. It is also worth noting that unlike BATP-1, GRTP-1 displayed very little difference between the average grain and cell sizes, 160$\pm$10μm and 110$\pm$5μm respectively (shown in Figure 4.21, section 4.3 d).

The grain enlargement mechanism in the presence of Zr is not clear, but this phenomenon was also reported in a previous study [76]. The mechanism might involve Zr poisoning of solutes present in the alloy, causing their heterogeneous nucleation potency to either be suppressed or be delayed. It might also be possible that Zr causes an increase in the critical radius (r*) for grain growth. These concepts were not investigated any further as establishing the grain enlargement mechanism in the presence of Zr is outside the scope of this study.

Since α-Al grain sizes are very sensitive to processing technique, the purity of the aluminium master alloy, and the final chemical composition of the alloy, it is difficult to meaningfully compare grain sizes directly between investigations. Lui [76], however, carried out an examination on TP-1 casts of a 6xxx Al alloy, processed with the same technique, using the same master alloys, and with a very similar chemical composition (0.28wt% Si, 0.52wt% Fe and 0.37wt% Mg with trace amount of Ti, Ni, Cr, and V) as that of BATP-1. Thus comparisons in grain size and phase selection were made between these two alloys.

Lui [76] reported that the alloy grain sizes for:

(a) the control alloy, i.e. the base alloy without any chemical additions, ranged between 728 to 1309μm, and that α-AlFeSi was the predominant phase. Although the average grain size of BATP-1 is on the smaller end of this scale, it is still within range of those observed by Lui. He also reported observing columnar grains on some of the vertical cross-sections of his TP-1 samples, but no further details were provided.

(b) additions of 5:1 Al-Ti-B type grain refiner to the control alloy lead to fine equiaxed grain structures with grain sizes reduced to 125 to 175μm. The grain sizes were also observed to remain consistent across the cross-section. The average grain size of GRTP-1 is comparable to those observed by Lui. He also indicated that the β-AlFeSi became the predominant phase on additions of 5:1 Al-Ti-B, which is in agreement with GRTP-1 observations. Given the phase selection remained consistent in BATP-1 and BA200 despite the large differences between α-Al grain sizes, it can be assumed that the presence of grainer refiner played a significant role in the phase selection of GRTP-1.

(c) introduction of Zr to his control alloy 6063 (using Al-15wt%Zr waffle) with a chemical composition of 0.51wt%Si, 0.28wt%Fe, 0.37wt%Mg, 0.0026wt%Ni, 0.0016wt%Cr, and 0.09wt%Zr; displayed significantly larger grains compared to the control alloy. The average grain size of Lui's Al-Zr containing alloy was 1503μm. The microstructure of ZRTP-1 is comparable to Lui's observations. He also indicated that the presence of Zr always promotes the formation of α-AlFeSi phase, which is in agreement with observations made for ZRTP-1.

5.1.2 New Rheocasting Process

As mentioned earlier in section 5.1.1, the entire processing technique and the chemical composition of the alloy have significant effects on the alloy's grain size, and therefore direct comparisons between grain sizes between investigations are not always meaningful. Thus, the grain sizes of the alloys cast through the semisolid processing technique, which is not a standard process, have only been compared with each other and the TP-1 casts to examine the effects of the technique.

In this study, an attempt has been made for the first time to understand the influence of α-AlFeSi and β-AlFeSi phases on the hot tear properties of the 6063 alloy, independent of the α-Al grain size using the semisolid processing technique. On casting the same batch of alloys using the semisolid processing technique, although the average grain sizes of BA200, GR200 and ZR200 were around 620±110μm, 180±15μm and 350±70μm, the cell sizes were all comparable at an average of 180±15μm, 130±5μm and 160±10μm, respectively. It was interesting to note that GR is the only alloy where

the grain size is almost equal to the cell size, which in turn would have an impact on the mechanical properties of the material.

The α-Al grains of BA200 and ZR200 both display significantly finer, more consistent and more equiaxed grains compared to those observed in the corresponding TP-1 cast alloys. For example, in the case of BATP-1 and ZRTP-1, the vertical cross-sections of BA200 and ZR200 resemble each other in terms of the microstructures; both displayed a section of columnar grains near the edge, which rapidly reduced in size to become finer and more equiaxed grains near the centre. The columnar sections in BA200 and ZR200 extend to around 2mm and 5mm in width, which is relatively insignificant compared to the amount of bulk material containing fine equiaxed grains. Thus, the semisolid processing technique was successful in restricting columnar grain growth.

The microstructure of GR200 remained identical to that of GRTP-1, displaying grains that are very fine, consistent, equiaxed, and uniformly distributed throughout the cross-section. The microstructure did not exhibit any columnar grains. Thus, based on microstructural comparisons between the two processing techniques, it can be concluded that the processing technique of BA and ZR plays a significant role in determining the final microstructure of the alloys, while addition of 5:1 Al-Ti-B type grain refiner plays a bigger role in the microstructure determination of GR.

5.1.3 Microstructure of BA400, GR400 and ZR400

As mentioned section 3.1.2 (c), one set of alloys were cast through the semisolid processing technique but with steel enthalpy cans preheated to 400ºC to understand the

impact of enthalpy can temperatures on the microstructure and phase selection of each alloy.

In was interesting to note that the resultant microstructures were almost identical to their corresponding alloys cast with enthalpy cans preheated to 200ºC. The microstructures of BA200 and BA400 both displayed sections on the edge about 2mm wide with columnar grains, and the grains of both alloys reduced in size becoming more equiaxed past the columnar region. The same microstructual trend as BA was observed in ZR200 and ZR400, except the regions of columnar grains were around 5mm in width. GR200 and GR400 displayed fine equiaxed grains throughout the microstructure, with no columnar grains.

The average grain sizes of all the alloys measured from the macro-etched surfaces of the samples, were as follows:

- BA200 195±15μm and BA400 225±10μm;
- GR200 130±5μm and GR400 135±5μm; and
- ZR200 180±10μm and ZR400 280±25μm.

As mentioned in section 4.2 (g), the high level of porosity on the surface of ZR200 resulted in increased level of error margin in grain size measurements. Thus the macro-etched grain size calculation obtained for ZR200 were not analysed further.

The average grain diameters of BA400 and GR400 were ~15% and ~4% larger than those of BA200 and GR200, which can be attributed to the heat transfer rate from slurry

to atmosphere via the enthalpy can. The thermal gradient at the mould wall was higher for enthalpy cans heated to 200ºC than those heated to 400ºC. Thus it can be assumed that the enthalpy cans heated to 400ºC would allow more time for heat transfer from slurry to atmosphere, which in turn would allow more time for grain growth. This is in agreement with previous work carried out by Park [4], who indicated that the grain sizes of AA7032 processed with steel enthalpy cans preheated to 500ºC had larger grain sizes than the alloys cast with steel enthalpy cans preheated to 200-241ºC.

The insignificant change in average grain sizes between GR200 and GR400 reinforces the theory that the microstructure of GR is determined by the chemical composition and entirely unaffected by the processing technique.

5.1.4 Non-Dendritic Microstructure Formation Mechanism

The various steps of the semisolid processing technique may have each contributed to the transformation of dendritic grains observed in the TP-1 samples, to the fine uniform and equiaxed microstructures of the alloys produced using the semisolid processing technique.

The molten aluminium was ladled from the crucible holding the bulk material, to a preheated enthalpy can. During transfer the temperature of the melt dropped from ~730ºC to ~650ºC. At this point the solid fraction is expected to be ~50% according to the MTDATA calculations (see Figure 4.24), and therefore a large number of grains would be expected to have already nucleated and started growing under reasonably rapid cooling conditions. It has been suggested that solute enrichment can lower the

local melting temperature and melt away the dendrite arm roots causing grain multiplication as well as more non-dendritic grain structures. The thermosolutal convection would cause accelerated solute diffusion, thermal fluctuation and generate stress at the dendrite arm roots [37]. This theory was furthered by Liotti et al. [67], suggesting that the solid-liquid interface temperature (T^*) at the dendrite arm roots is a function of the freezing temperature of the alloy (T_f), the liquid composition in wt% at the interface (C^*_L), and the local curvature of the interface (K^*). Figure 5.1 shows the various components T^* is dependent on, where m represents the liquidus slope, and Γ is the Gibbs-Thomson coefficient.

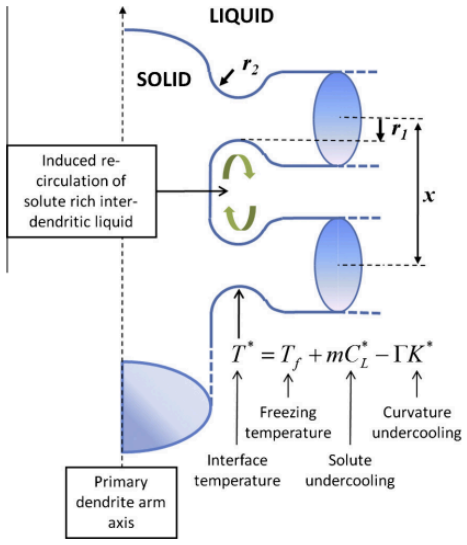


Figure 5.1: Schematic diagram of secondary dendrite arms, attached to the primary dendrite with spacing of x between them. r1 and r2 refer to the curvatures at the secondary dendrite arm root [67]

Liotti [67] observed that despite high solid fractions, movement of the liquid present between the primary and secondary dendrite arms can cause instabilities in T^* values,

which in turn can result in the dendrite arm roots re-melting. Thus, ladling the melt into the enthalpy can would have agitated the melt, which in turn would have caused turbulence in the inter-dendritic liquid present.

The steel enthalpy can is designed to create a more uniform temperature compared to conventional casting, giving rise to a more equiaxed grain structure in comparison. However, while cooling the alloys within the enthalpy can until the solid fraction reached 90vol%, the thermal gradient at the mould wall caused the formation of a small layer of non-dendritic columnar grains at the edges of BA200 and ZR200. These columnar grain sizes were restricted however because of the rapidly decreasing temperature gradient.

5.2 Intermetallic Phases

As mentioned section 4.5, it can be assumed that the phase selection remains fairly uniform throughout all the alloys. Although a small difference was noted in the approximate contents of α-AlFeSi phase in BA and GR alloys, it can be attributed to the local chemical composition of the solute-rich liquid or texturing. However, given this technique provides an approximation of the true value, the variation in α-AlFeSi phase content could be a result of data scatter.

On the XRD spectra of BA and GR alloys, an unidentifiable peak was observed at 37.25º 2θ, and another one observed at 19.05º 2θ for BA alloy only. It is possible that these peaks are caused by either varying lattice parameters and different crystal structures of the phases identified (see section 2.4.1.1), or entirely different phases.

However, since these phases are only observed in BA and GR alloys that contain 30% to 50% of metastable β-AlFeSi phase, it can be assumed that these peaks are caused by the transformations of β-AlFeSi intermetallic phase. The XRD database currently in use needs to be expanded to conclusively attribute any phases / crystal structures to the unidentified XRD peaks.

Based on the grain sizes, phase morphologies and phase identities between solidified slurries and TP-1 samples, it can be concluded that the chemical compositions during solidification play a more important role in phase selection compared to α-Al grain size.

5.2.1 Intermetallic Phase Selection Mechanism

Al alloys generally solidify by heterogeneous nucleation due to the intrinsic inclusions present. Due to the low solid solubility in solid Al of the alloying elements (Fe and Si) and trace elements, the solutes segregate into the liquid that remains between the grain and cell boundaries, and form various insoluble intermetallic compounds based on the local solute concentrations.

According to equilibrium phase diagram of the Al-Mg-Fe-Si alloy system (shown in Figure 2.18 (section 2.4.5), the phases $Al_{13}Fe_4$ (Al_3Fe), Al_8Fe_2Si (α-AlFeSi), Al_5FeSi (β-AlFeSi), Mg_2Si, Al_8Mg_5 and the quanternary phase $Al_8FeMg_3Si_6$ (π-AlFeMgSi) form as melts of various compositions that solidify [84]. In the current work, the solidification conditions of BA200, GR200 and ZR200 were non-equilibrium, and therefore thermodynamic calculations were carried out using MTDATA for the alloys

under both equilibrium (lever rule) and partial-equilibrium (Scheil rule) conditions (section 4.4).

According to the MTDATA lever rule calculations, α-Al forms first as the liquid solidifies, followed by $Al_{13}Fe_4$, α-AlFeSi, and β-AlFeSi. Calculations carried out based on lever rule indicate that only the phases α-Al, Al_3Fe and α-AlFeSi form directly from the liquid, while the Scheil calculations indicate that all of the above mentioned phases as well as Mg_2Si form from liquid. The interconnected sponge-like morphology of the extracted phases indicates that they formed from the liquid present in the grain and cell boundaries. Thus, it was assumed that the calculations carried out under Scheil conditions were more applicable for this investigation.

Based on the phases present in the XRD spectra and DSC heating curve analysis, it can be assumed that the possible reactions that caused the formation of α-AlFeSi, β-AlFeSi, Mg_2Si and $Al_{13}Fe_4$ phases are eutectic reactions 2.14, 2.15, 2.17, 2.19 and 2.20 given in section 2.4.4.

$L \rightarrow$ α-Al	dendritic network	(2.14)
$L \rightarrow$ α-Al + Al_{13} Fe_4	binary eutectic	(2.15)
$L \rightarrow$ α-Al + α-AlFeSi	binary eutectic	(2.17)
$L \rightarrow$ α-Al + β-AlFeSi	binary eutectic	(2.19)
$L \rightarrow$ α-Al + Mg_2Si	binary eutectic	(2.20)

XRD peak intensity and the relative sizes of the DSC peaks indicate that $Al_{13}Fe_4$ is present in very small amounts, significantly lower compared to α_c-AlFeSi, β-AlFeSi

and Mg_2Si phases (where applicable). This may be either due to $Al_{13}Fe_4$ quantity being just below the XRD detection level, or due to the quasi-peritectic reactions 2.16 and 2.21 took place.

$$L + Al_{13}Fe_4 \rightarrow \alpha\text{-}Al + \alpha\text{-}AlFeSi \qquad \text{quasi-peritectic} \qquad (2.16)$$

$$L + Al_{13}Fe_4 \rightarrow \alpha\text{-}Al + \beta\text{-}AlFeSi \qquad \text{quasi-peritectic} \qquad (2.21)$$

It has also been claimed high cooling rates restrict the nucleation of $Al_{13}Fe_4$ [86]. Thus, it is possible that the cooling rate of the alloys during solidification may have been to high for the formation of $Al_{13}Fe_4$.

This is agreement with the observations of Sha [71], who also reported that the solidification reactions 2.14, 2.15, 2.17, 2.19 and 2.20 were prevalent in forming the AlFeSi phases in a Bridgman solidified 6xxx Al alloy, with Al-Ti-B type grain refiner additions.

5.2.2 2D Phase Morphology

In the literature, 'needle'-like intermetallic structures were generally assumed to be the β-AlFeSi phase, and the 'Chinese script'-like structures were assumed to be the α-AlFeSi phase [12, 71, 134]. It is interesting to note, however, that contrary to the XRD results sections 4.5 (indicating α-AlFeSi phase to be predominant in BA200 and ZR200, while just 50wt% concentration in GR200), a higher proportion of the intermetallic particles displayed 'needle'-like structures on the surfaces of BA200 and ZR200, while a significantly higher proportion of 'Chinese script'-like phases were observed in GR200. This observation is in stark contrast with XRD analysis of the phases present,

and therefore it can be assumed that the 2D phase morphology is not representative of the AlFeSi phase identity and content in an alloy.

From the metallographic sample surface, it was observed that the phase interconnectivity was significantly higher in the alloys processed through semisolid technique, compared to those of TP-1 casts. The phases were very interconnected on all three quenched alloys (BA200, GR200 and ZR200), and created a clear outline of the cell boundaries in every case. The phases visible on the TP-1 casts however were not very interconnected and appeared scattered amongst the cell boundaries.

5.2.3 3D Phase Morphology of BA200, GR200 and ZR200

The concept that 2D phase morphology is not representative of the true phase identity and content was further reinforced on examining the extracted AlFeSi phases from all three alloys. Although exact proportions were not calculated, the extracted phases from BA200 displayed a significantly higher proportion of phases with 'Chinese-script'-like morphology, compared to the planar plate-like ones (Figure 4.46 to Figure 4.50). The same trend was true for GR200 and ZR200: higher levels of planar plate-like phases were observed in GR, while significantly high levels of "Chinese-script"-like phases were displayed by ZR. The trend displayed by the extracted phases corresponded closely to the XRD analysis, and therefore it was concluded that the AlFeSi phase identity cannot be determined from its 2D microstructure. Furthermore, based on the relative frequency of morphologies observed in the alloys and the XRD analysis of phase content, it can be concluded that the intermetallic particles with "Chinese-script"-

like morphology is most probably the α-AlFeSi phase, and the planar plate-like intermetallic particles are most probably β-AlFeSi phase.

The dimensions of the individual phases could not be measured due to the phases interconnecting into a sponge-like 3D structure, as shown in Figure 3.13. The extracted phases of GR200 displayed the highest interconnectivity, while extracted phases of ZR200 crumbled on the slightest contact, displaying the lowest level interconnectivity amongst the three alloys. Given all three alloys experienced comparable cooling conditions, the increased interconnectivity of GR200 can be attributed to the average grain size, which is significantly smaller in GR200 than the other two alloys, and therefore contained high amounts of cross-linking between the particles. The average grain size of ZR200 on the contrary was the largest amongst the three alloys, resulting in the encapsulating phases being longer with fewer triple-point junctions to strengthen the overall structure, and therefore increasing the fragility. This theory was further reinforced by the phase structures extracted from the TP-1 casts. Almost all of the extracted phase particles from TP-1 casts displayed a powder-like form, except the extracted phase from GRTP-1, which had a delicate 3D perforated structure, indicating that the cell size has a significant effect on the phase morphology.

The phase morphologies remained relatively consistent both along the radii and along the lengths of all three alloys, which is in agreement with the XRD observations. It was confirmed that a solute-rich liquid film encapsulates the cell during solidification since the pore size of the extracted phases (150$\pm$15μm) from BA200 was on average very similar to the cell size measured (140$\pm$10μm). This was also true in the case of GR200, where the average cell size of the bulk alloy (5mm from the edge to centre) and the

intermetallic pore size both equalled 120±10μm on average. The pore diameters of the extracted phases from ZR200 were 140±25μm near the centre and 180±20μm near the edge, while the cell sizes measured from the anodised samples were 150±15μm near the centre and 330±25μm near the edge. However, past the columnar grains, the average cell size of ZR200 near the edge is 195±40μm. The similarity in pore sizes from the extracted intermetallic particles and the cell sizes of the alloys further reinforces that the phases α-AlFeSi and β-AlFeSi form directly from liquid for all of these three alloys. The thicknesses of the phases in both the "Chinese-script"-like and planar plate-like morphologies were found to be <1μm for all three alloys, which again is in agreement with the literature [76].

It is possible that the needle-like phases on metallographic sample surfaces were the cross-sections of intermetallic particles across the thickness, which would explain the presence of mostly needle-like phases at the cell boundaries. The "Chinese script" morphology is predominantly observed at the triple-junctions of the cell boundaries, possibly displaying a slice through the submerged phase.

5.2.4 Phase Formation Mechanism

As discussed section 5.1.4, the effect of the enthalpy can is to create a more uniform temperature within the solidifying alloy compared to conventional casting, which in turn promotes a more equiaxed grain structure. This means the solute-rich liquid remains in the very well connected regions between the α-Al grains, giving rise to a very interconnected phase structure.

(a) Proposed Mechanism of α-AlFeSi Phase Formation

The various patterns observed on the phase surface in Figure 4.47 section 4.7.1 seem to indicate that they might be displaying the various stages of phase formation. Based on the SEM micrographs, it can be assumed that the solute-rich inter-cellular liquid begins to solidify as a rippled film, which most likely forms eutectically with Al, and therefore removing the primary and eutectic Al during extraction leaves stratified layers with gaps in between, creating the effect that can be seen in Figure 5.2. It can also be seen that the stratified phase layers can develop facets that do not align with the crystallographic relationship of its neighbours.

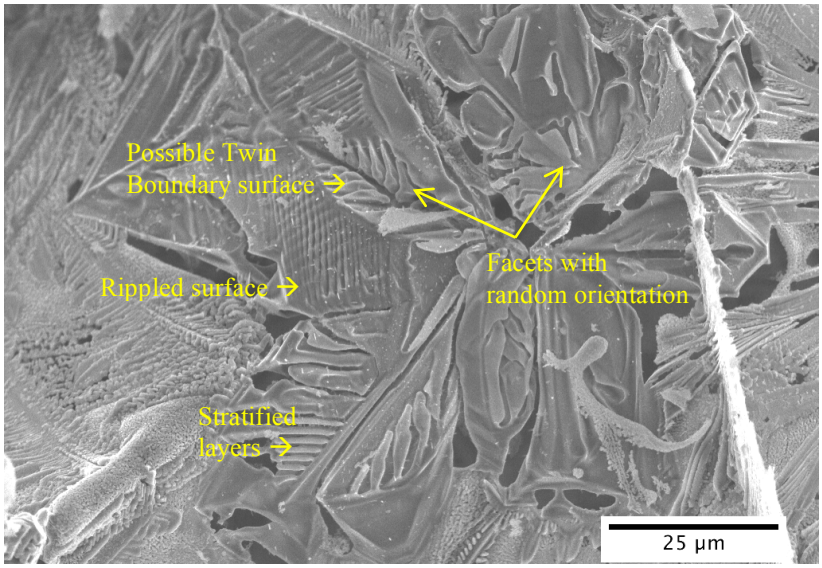


Figure 5.2: SE micrograph of the extracted phase from ZR200E, possibly showing the various stages of phase formation with an intricately patterned surface topography

The XRD spectra indicated that α_c-AlFeSi is the predominant phase in BA and ZR, with an α_c-AlFeSi content of 70wt.% and 80wt.% respectively. Both alloys displayed phases with an intricately patterned surface topography, frequently containing dendritic

morphology and possible twin boundaries. Thus, it can be assumed that the phases with intricately patterned surface topographies are α_c-AlFeSi, since the cubic lattice structure has the most symmetry elements.

(b) Proposed Mechanism of β-AlFeSi Phase Formation

XRD analysis of extracted phases indicate that GR alloys have 50wt.% of β-AlFeSi phase, which corresponded with the significantly higher levels of planar plate-like phases observed in GR compared to BA and ZR. It can be seen from Figure 5.3 that almost all the planar plate-like phase edges have a 90-95^o angle. Furthermore, Figure 5.4 shows that the surfaces of these plate-like phases are covered in growth steps and ledges, indicating high levels of growth anisotropy. Thus, it can be assumed that the phases with plate-like morphologies are β-AlFeSi, since the monoclinic lattice structure has very few symmetry elements and can cause high levels of anisotropy in different growth directions.

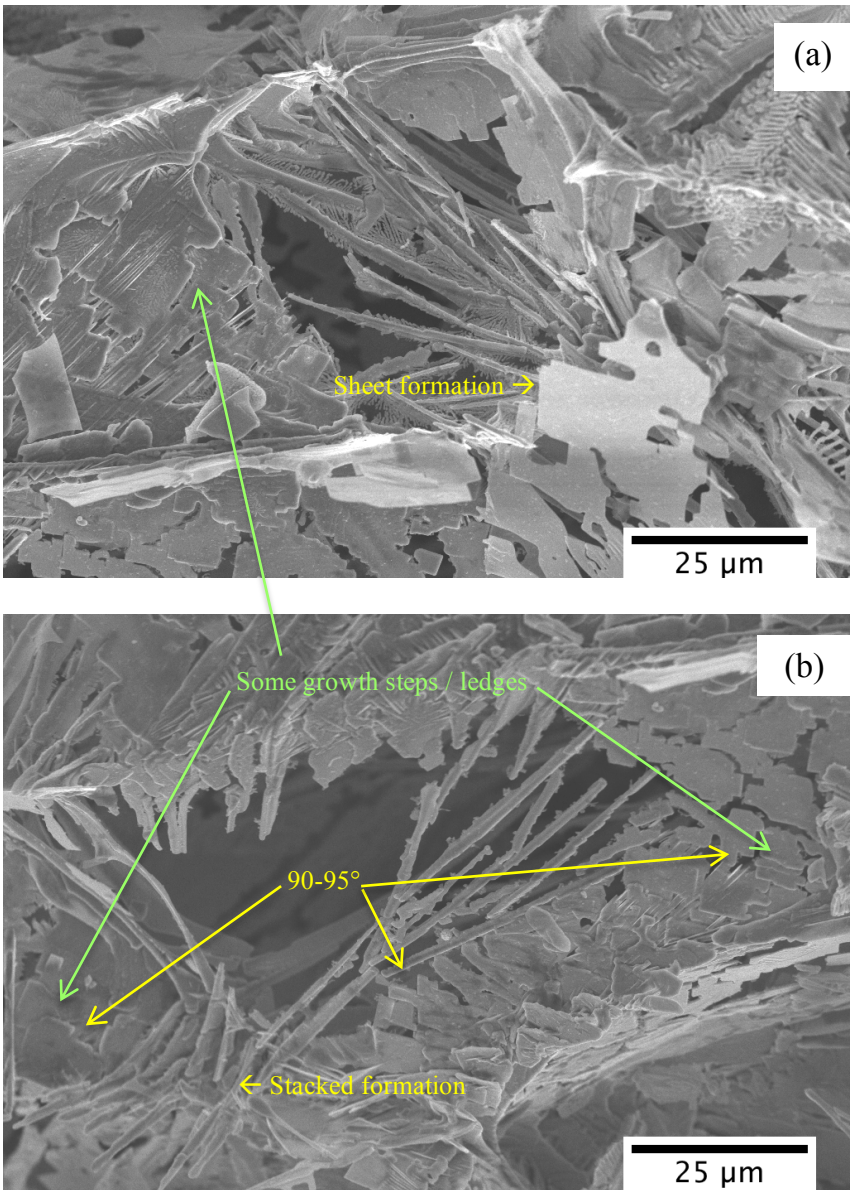


Figure 5.3: SE micrographs of the extracted phase from GR200C, showing examples of planar plate-like morphology

The plate-like phases were observed to form both as fine singular sheets, and as multiple layers stacked above each other (see Figure 5.3). As in Figure 4.53 section 4.7.2 and Figure 5.5, most of the plate-like phases that form in a stacked layer appear to be in a perpendicular plane to the cell surface. This might indicate the eutectic formation of β-AlFeSi phase with Al, and therefore leaving β-AlFeSi phase layers once the primary

and eutectic Al is removed during extraction. α-AlFeSi is sometimes observed growing on the surface of the planar β-AlFeSi phase, an example of which is shown in Figure 5.6.

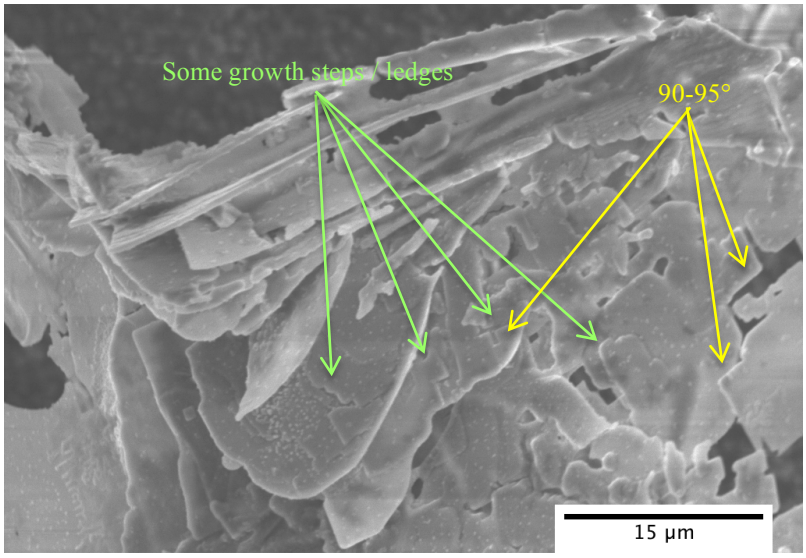


Figure 5.4: SE micrograph of the extracted phases from GR200E, showing the surface of a plate-like morphology particle covered in growth steps and ledges, while the edges display sharp angles of ~90°

Based on the SEM micrographs of the extracted phases, it can be assumed that the solute-rich inter-cellular liquid begins to either solidify eutectically with β-AlFeSi and Al forming the stacked layer effect, or solidifies into a single sheet of β-AlFeSi phase, which may sometimes form around the α-AlFeSi phase. Thus, it can be assumed that the phases can switch identity between α-AlFeSi and β-AlFeSi phases depending on levels of Si available in the local surrounding.

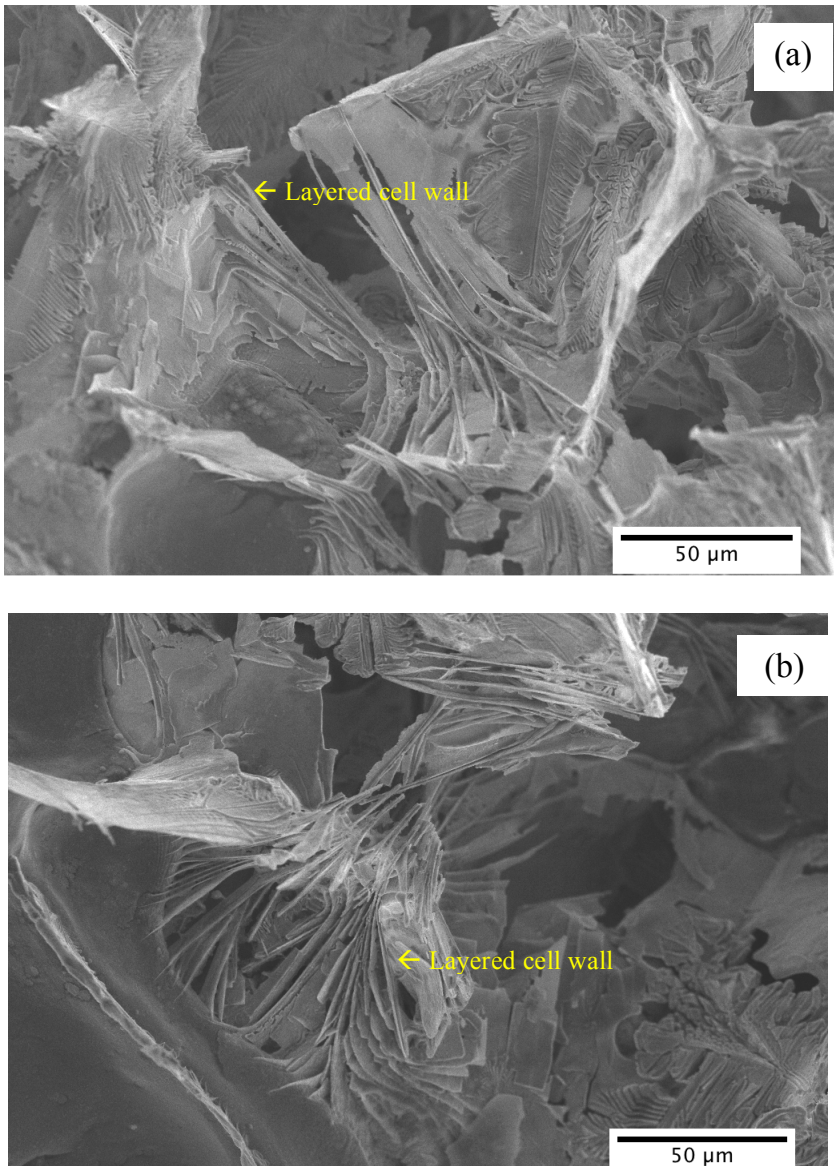


Figure 5.5: SE micrographs of the extracted phase from GR200E, showing α-Al cell structures outlined by stacked layers of plate-like phases

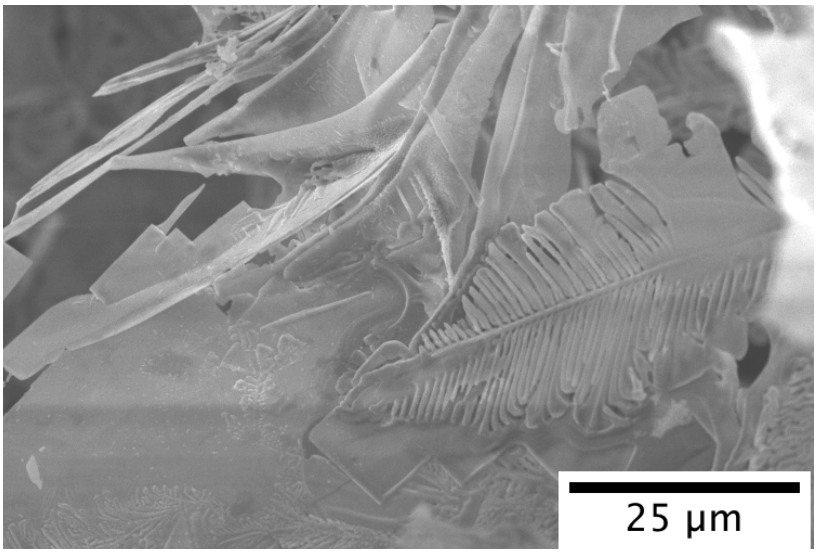


Figure 5.6: SE micrograph of the extracted phase from GR200E displaying a 'leaf'-like phase with secondary dendrite arms growing from a thin primary dendrite

(c) Flower-like Phases

Close observation of the 'flower'-like phases revealed that they display two distinctive structures:

- ***Type 1***: 'Flowers' that have been initiated either by a particle or a cluster of particles at the centre of the 'flower' structure. A secondary dendrite arm growing from a thin primary dendrite arm was always observed along the middle of the 'petals' (see Figure 5.7 a, b). There also appears to be a crystallographic relationship between the secondary dendrite arms on either side of the primary dendrite arm.
- ***Type 2:*** 'Flowers' with no clear indication of an initiation point, whereby the phase has also grown vertically upwards in the z direction (see Figure 5.7 c, d). The secondary dendrite arms with crystallographic relationship was not always observed in Type 2 'flowers'.

This even dendritic growth in all directions observed in both types of 'flowers' indicate that the temperature gradient was very low during the formation of these morphologies.

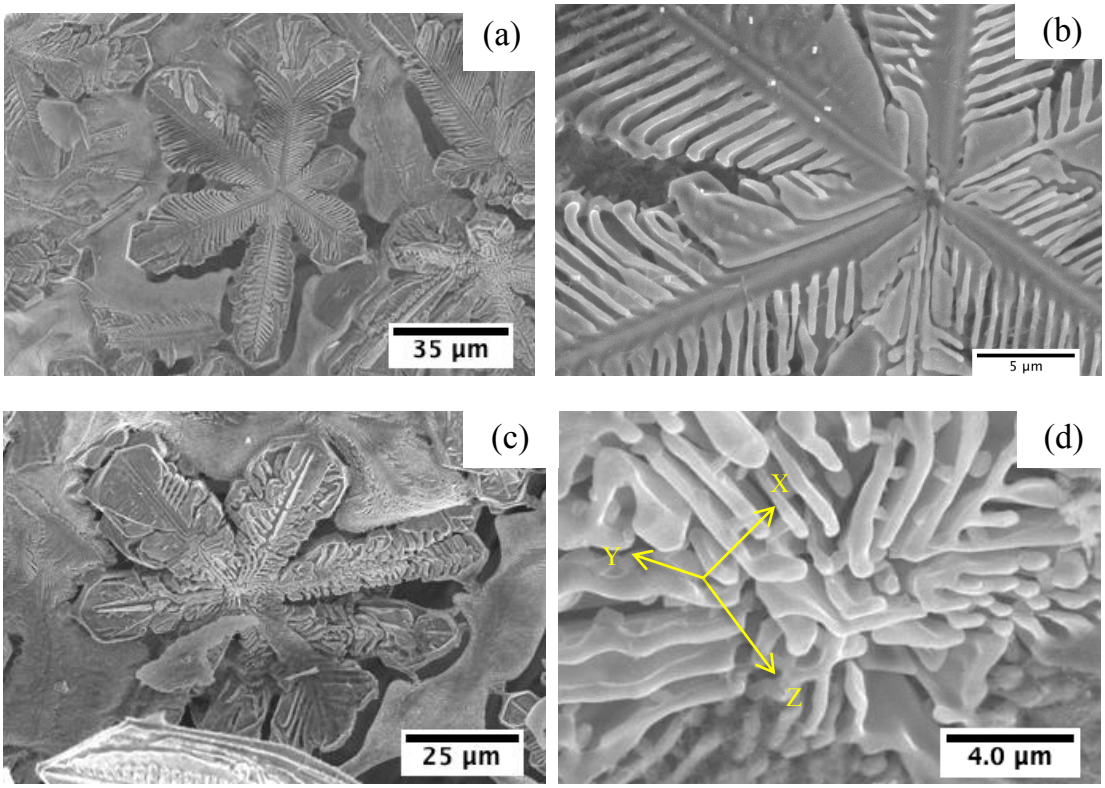


Figure 5.7: SE micrographs of the examples of extracted phases with a 'flower'-like morphology from GR200C, where (a, b) shows 'flower' Type 1 and (c, d) shows 'flower' Type 2

Most 'petals' of the 'flowers' displayed an angular feature at the tip. On average, the angles found at the tips were ~120^{o} (based on 25 'petal' measurements from 16 'flowers' of both BA200 and GR200). A very small group of 'petals' (7 out of the 32 'petals' examined) was also found with an average angle of ~92^{o} at the tip. To characterise the difference between the two sets of 'petal' tip angles, the angle at the 'petal' tip and the corresponding length of the 'petal' (where applicable) was measured

and compared (see Figure 5.8). Length measurements were only carried out on the 'petals' that were directly perpendicular to view.

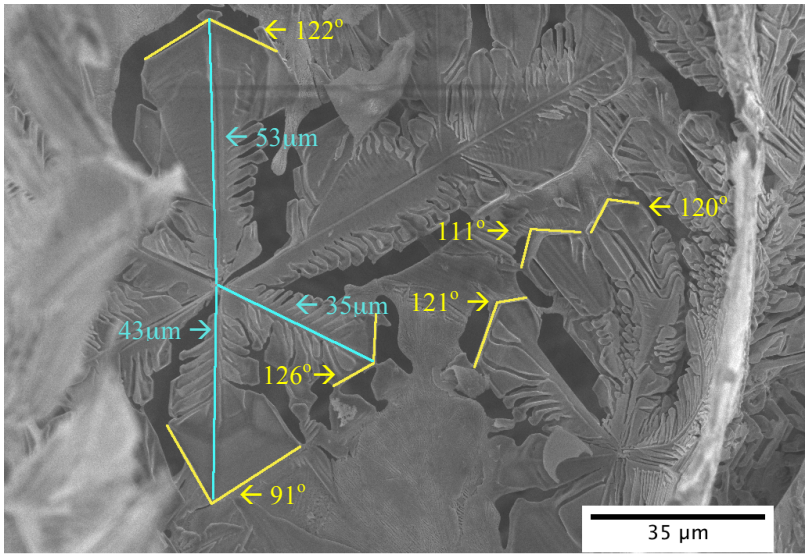


Figure 5.8: SE micrograph of the extracted phase with a 'flower'-like morphology from BA200C, showing how the 'petal' tip angles and 'petal' length measurements were carried out

The angles found at the 'petal' tips were plotted as a function of the corresponding 'petal' length, shown in Figure 5.9. Although no characteristic relationship could be observed between these two groups of 'petals', there is a slight indication that the 'petals' with ~92° tip angle tended to be shorter in comparison to the 'petals' with ~120° tip angle.

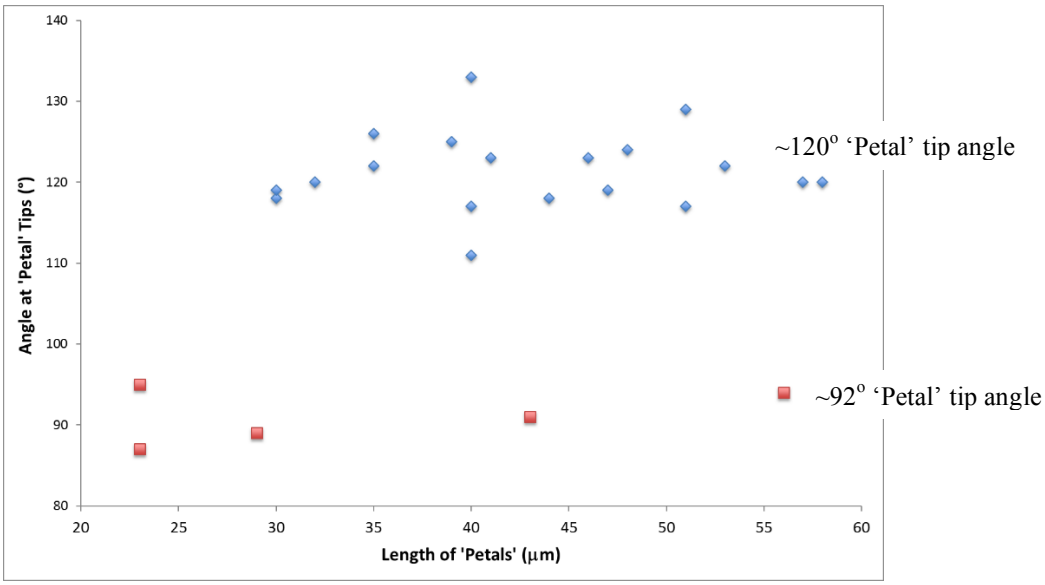


Figure 5.9: Angle at the 'petal' tip as a function of the corresponding 'petal' length revealed no significant correlation between the two parameters

It was clear from the SEM examinations that the 'flower'-like phases observed in BA200 had all been of Type 1, while the ones observed in GR200 were an almost equal mixture of both Types 1 and 2. Although 'petal'-like features were observed in ZR200 with the secondary dendrite arms with crystallographic relationship, no obvious 'flower'-like phases could be identified.

The angles of the facets were also measured from 10 'petals' that displayed clear stratified layers (see Figure 5.10 a), and it was observed that on average the facet angle was 123°, which is very similar to the 'petal' tip angle. This indicates that the 'petals' of 'flowers' mostly grow on a preferred orientation, particularly in the case of Type 1 'flowers'. A large number of Type 2 'flowers' and a rare few Type 1 'flowers' were observed to have surface facets that does not follow this angular pattern, as shown in Figure 5.10 (b).

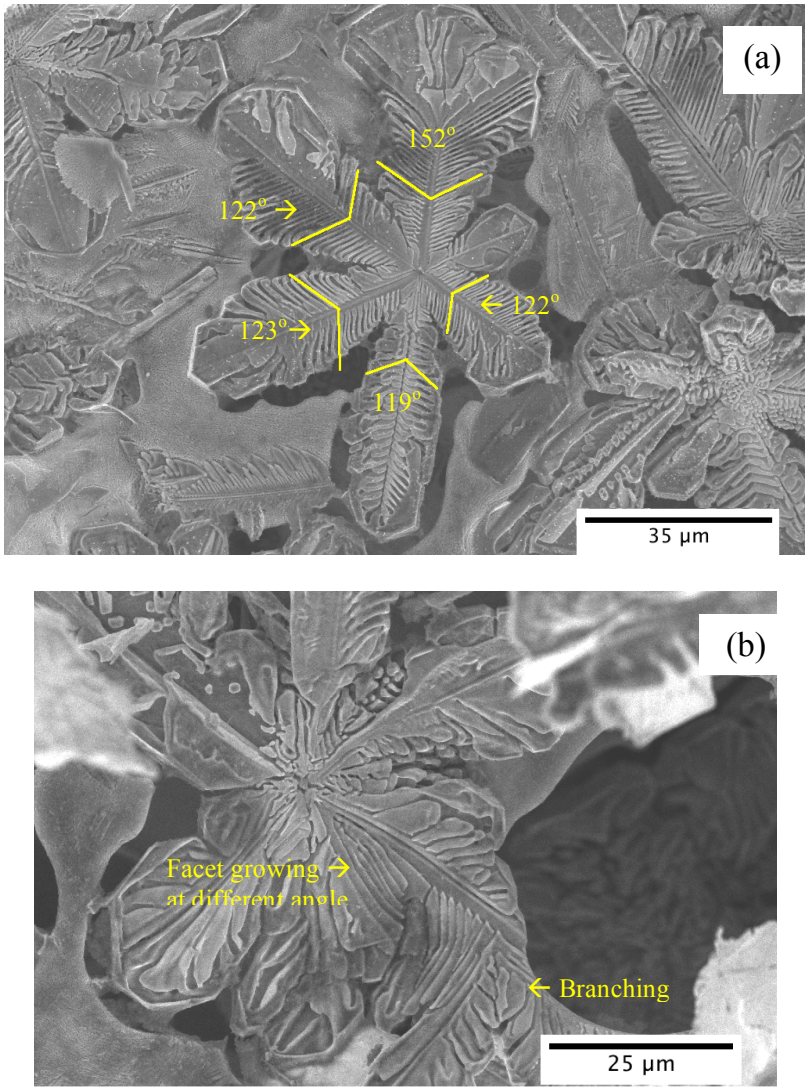


Figure 5.10: SE micrographs of the extracted phase from GR200C, showing (a) how the angles between the facets were measured and (b) an example of a 'petal' where the surface facets are following a different orientation to the rest

The numbers of 'petals' on 20 flowers were counted, and with the exception of three 'flowers', the remaining contained 6 'petals'. The shapes and sizes of the 'petals' seems to vary, possibly depending on the local solute content, inter-cellular liquid flow, α-Al

cell shape, etc. Some ‘petals’, as shown in Figure 5.10 (b), were also observed to be branching out to accommodate α-Al cells.

(d) Proposed Mechanism of Flower-like Phase Formation

The ‘flower’-like phases appear to have been initiated at the centre by the presence of solute(s) or inclusions. Since the extracted phases were several mm in height, attempts to identify the solute elements / chemicals present at the centre with EDX resulted in obtaining the spectrum for several layers, and therefore it was not possible to identify the cause of initiation. A second sample was prepared with a few broken particles from GR200C to further investigate the initiation point of the ‘flowers’, but the various element maps and EDX spectra failed to provide a conclusive indication of a possible initiation point.

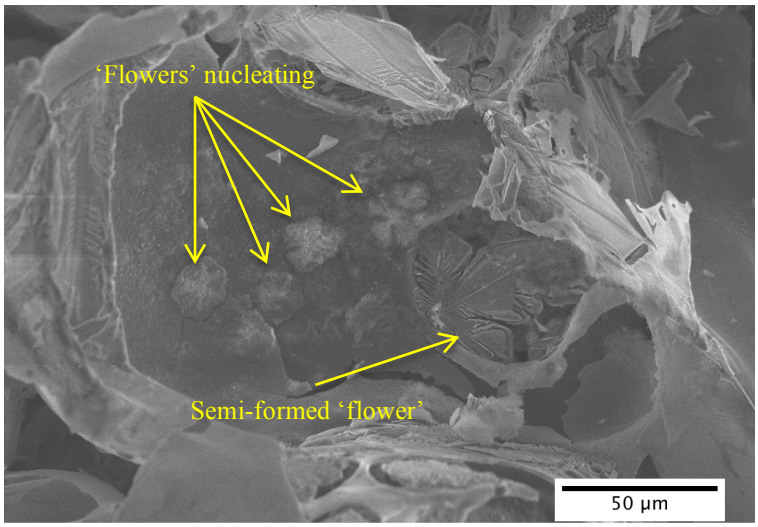


Figure 5.11: SE micrograph of the extracted phase from GR200E, showing possible nucleation of the ‘flower’-like phase morphology on the solidifying liquid film

Based on SEM observation (see Figure 5.11), it was assumed that the ‘flowers’ nucleated heterogeneously from the intrinsic solutes and inclusions in the liquid, growing into the multi-‘petal’ morphology as the liquid film solidified. As seen in Figure 5.12 (a), the ‘flower’ sizes are very much dependent on the inter-cellular liquid feed, whereby the surface facets have grown but the ‘flower’ size is stunted.

Given the thermal gradient at GR200E can be assumed to be higher than that at GR200C, the presence of more ‘flowers’ with planar ‘petal’ set at GR200E compared to those observed in GR200C indicate that the surface features of the ‘flowers’ are sensitive to cooling rate (see Figure 5.12 b).

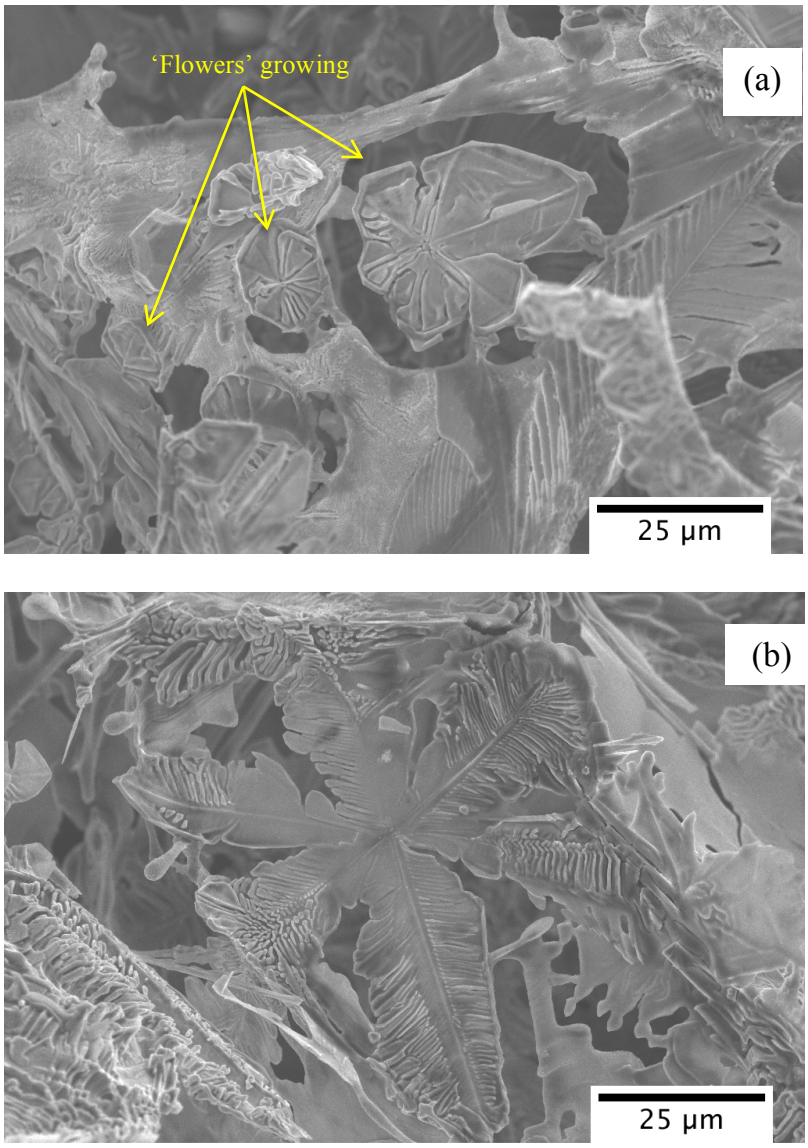


Figure 5.12: SE micrographs of the extracted phase from GR200E, (a) showing stunted 'flower' growth and (b) 'flower' with a planar surface, where the surface features have not fully developed yet

Due to the size and shape of the particles found in the centre of the 'flowers' (see Figure 4.54 section 4.7.2), and the angles involved in the 'petals' and surface facets, it is reasonable to assume that some of the six-petal morphology could be initiated by the hexagonal TiB_2 particles.

(e) Proposed Mechanisms of Other Phase Morphologies

A very fine phase that appears to have solidified from interconnected particles into a perforated sheet was observed in all three alloys. These perforated sheets were mainly observed as a layer connecting the various solid phases together, while some were observed on the surface of features. Examples of these sheets can be seen in Figure 5.13 to Figure 5.15.

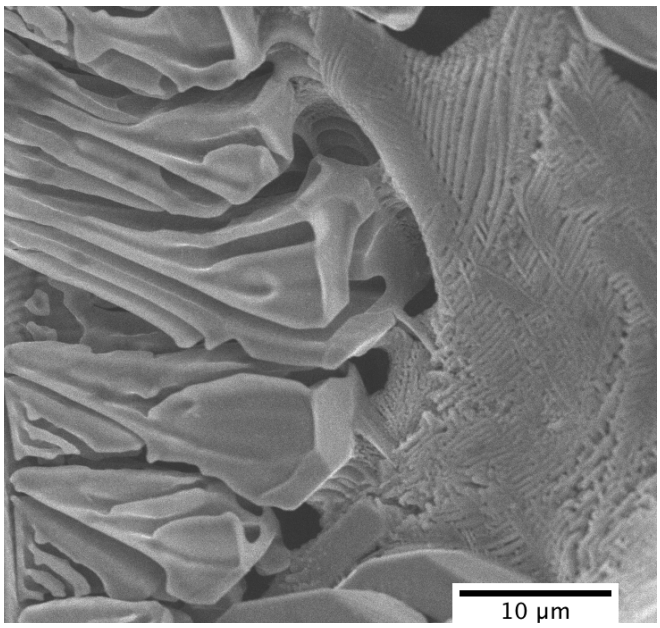


Figure 5.13: SE micrograph showing the perforated phase sheet from BA200C, that appear to have been feeding liquid into the 'petal' before solidification

These perforated sheets have also been observed to develop in the 'leaf'-like morphology with a skeletal backbone (shown in Figure 5.14 a) as well as dendrites (Figure 5.14 b).

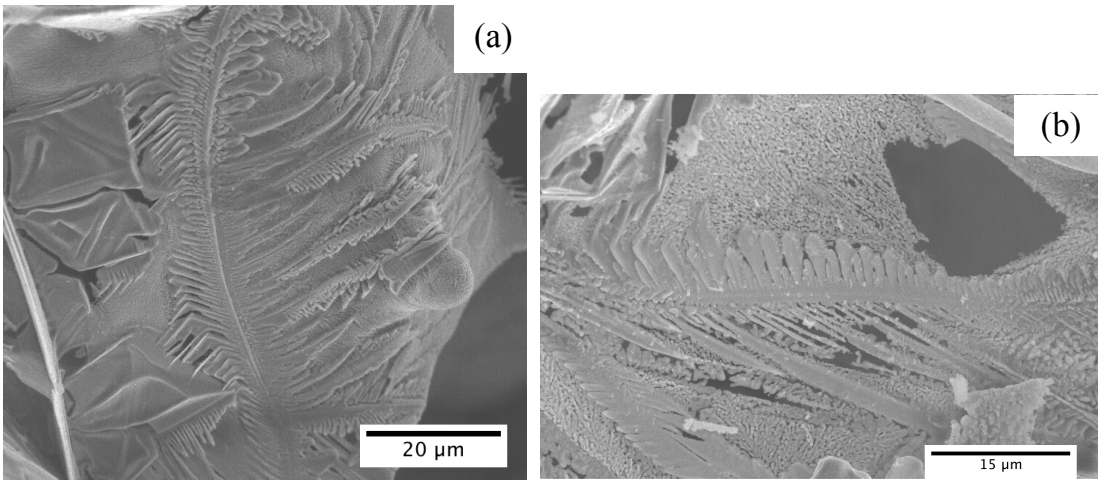


Figure 5.14: SE micrographs of the extracted phase from ZR200E, showing (a) the 'leaf'-like morphology with a skeletal backbone, and (b) the dendritic morphology

These perforated sheets have been observed with circular gaps, indicating the location of α-Al cells, as shown in Figure 5.15 (a, b). These perforated sheets were observed in all three alloys; most frequently in the samples near the edge, but relatively frequently in the samples near the centre too. It can be assumed that this phase morphology is a result of quenching the alloy during semisolid processing and causing a large thermal gradient. This theory is in agreement with previous work [135], which reports the presence of phases forming in complex eutectic structures at high cooling rates. Verma [136], while investigating the effect of increasing Mg content to 5wt.% on phase morphology, observed the presence of fibrous α-AlFeSi phase. Based on the XRD spectra and DSC analysis, it can be assumed that the phase identity of these fibrous structures is most likely to be α-AlFeSi phase as it was present in all three alloys.

The formation mechanisms involved in this fibrous intermetallic phase morphology is most likely that:

- The facetted particles nucleate away from the α-Al cells and grow towards the AlFeSi-phase dendrites and the α-Al cells until the alloy is quenched.
- During quenching, the growing particle tips further experience large undercooling and hence change in growth kinetics and results in this fibre-type growth.
- This altered type of growth continues until all the liquid between the α-Al and the facetted particle has been consumed.

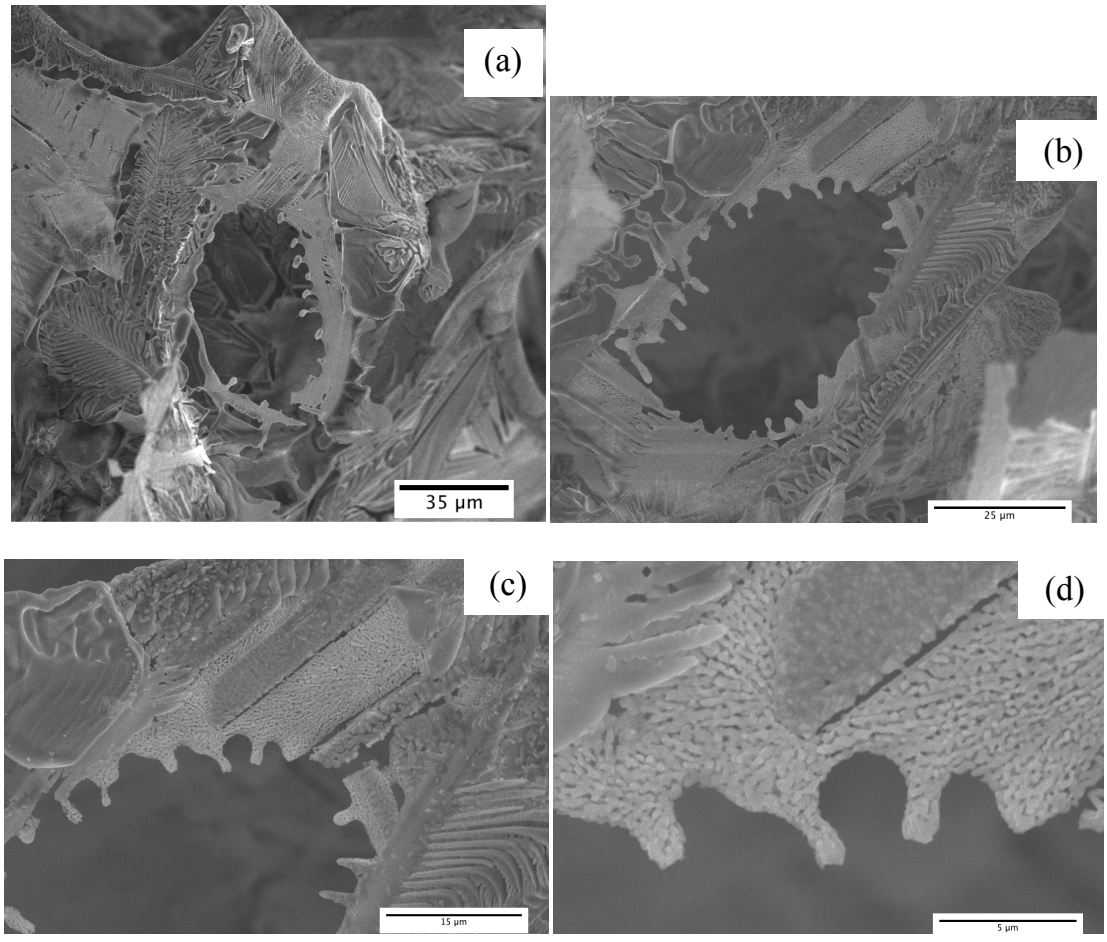


Figure 5.15: SE micrographs of the extracted phases from BA200C, showing (a, b) the inward growth of phases, and (c, d) the perforated sheet morphology growing around a much denser plate-like phase at higher magnification

5.2.5 Ti-Rich Particles and Clusters

The Ti-rich particles were observed both as individual particles and as clusters in the metallographic samples, and as clusters among the extracted phases. The individual particles were all less than 1μm in size, while the cluster sizes were much larger and ranged between 3-7μm.

The Ti-rich particles and clusters in the metallographic samples were always observed close to phases, but never in contact with the phase. However, on examining the extracted phases, it can be concluded that the Ti-rich particles are always observed as clusters, and that they were always found attached to phases. It was not possible to determine how many individual particles were in a cluster, and if their relative size had any effect on the surrounding phase morphology, since they could only be identified in broken phase structures.

It has been suggested in the past that the 'agglomerating agent' of TiB_2 particles can be attributed to a fine layer of Al_3Ti adsorbed on the TiB_2 particle surface [137]. Suggestions have also been made that the TiB_2 particles may have already formed clusters in the AlTiB master alloy, and the structure is mostly retained even after dissolution in the Al melt [76]. The examination of the TiB_2 clusters is outside the scope of this project, and no further consideration was given.

The Ti-rich cluster shown in Figure 4.55 (a) section 4.7.2 almost looks like the broken up centre of a 'flower'-like intermetallic particle with 'petals' branching out. The Ti-clusters shown in Figure 4.56 and Figure 4.57 section 4.7.2, however, were found in

the middle of a ‘leaf’/‘petal’-like intermetallic, and two random locations of an intermetallic particle with “Chinese-script” morphology. The Ti-rich clusters found in GR200E (Figure 4.58 and Figure 4.59 section 4.7.2) both appear to be located on plate-like intermetallic particles with a smooth surface.

Since only 1 out of the 6 Ti-rich clusters observed were structurally connected to the AlFeSi phases, it is difficult to determine whether these Ti-rich clusters actively nucleate AlFeSi phases. Furthermore, due to the lack of structural connection with the Ti-rich clusters and the surrounding phases, or any specific pattern given rise due to the presence of the Ti-rich clusters, it can be assumed that their location might simply be the result of these clusters being present in the solute-rich liquid channels as they solidified to form AlFeSi phases.

No Ti-rich particles were observed in BA and ZR in either metallographic samples or extracted phases, indicating that the ‘flowers’ observed in BA may have been initiated by solutes or inclusions other than Ti-rich particles.

5.3 ThermoMechanical Analysis

5.3.1 ThermoMechanical Behaviour

It is worth noting that (a) calculations for the solid fraction of ZR200 were carried out for the Al-Fe-Si-Mg component of the alloy due to Zr interactivity not being available in this MTDATA database; and (b) the amounts of Fe and Si were approximately 25% and 15% higher in ZR compared to GR.

According to the Scheil model, solid fraction ZR200 is consistently 0.009 lower than that of GR200 between 590ºC and 630ºC. Furthermore, Scheil calculations predict the presence of Mg_2Si phase for BA200 and GR200 only, although presence of Mg_2Si phase was evident in ZR200 on the DSC and XRD spectra, as well as 2D SEM microscopy. Thus, it can be assumed that Mg_2Si phase is present in ZR200.

Scheil calculations also predict the presence of 0.02% and 0.07% of $Al_{13}Fe_4$ to be present in GR200 and ZR200, respectively (see Table 4.7 and Table 4.8). However, based on XRD and DSC traces, only very small amounts of $Al_{13}Fe_4$ phases were observed, and therefore the calculated fraction of phases present was assumed to be an approximate value.

According to Scheil calculations, α_c-AlFeSi, β-AlFeSi and Mg_2Si phases start melting at 624ºC, 607ºC and 563ºC for GR alloys, while α_c-AlFeSi and β-AlFeSi phases start melting at 625ºC and 610ºC for ZR alloys. According to DSC traces obtained from a heating rate of 40K/min, Mg_2Si phase start melting at 566ºC in ZR alloys. Thus, Mg_2Si would have already melted in both alloys for tensile tests carried out at 595ºC, leaving only α_c-AlFeSi and β-AlFeSi phases in solid state. Tests carried out at 610ºC was expected have molten Mg_2Si and β-AlFeSi phases, leaving only α_c-AlFeSi phase in solid state. The tensile tests carried out at 625ºC was expected have all three phases melted.

It can be seen from the summary tables in section 4.8, that the α-AlFeSi-rich ZR595 samples are significantly more ductile compared to the GR595 samples when solid

fractions are comparable (f_s = 0.95 and 0.94 respectively). However, given the actual sample temperature during the tensile test was 605ºC, it can be assumed based on the DSC traces that the β-AlFeSi phase would have been transforming or had already transformed during these tests. Table 5.1 and Table 5.2 present the actual temperatures achieved during the tests, and the approximate fractions of each phase calculated to have formed in the alloys. This only provides an indication as it does not take phase transformations into account.

Table 5.1: Sheil calculation of fractions of phases present in GR during tensile tests

Sample	Sample Fail Temp.	Fraction of α-AlFeSi	Fraction of ß-AlFeSi	Fraction of Mg_2Si	Fraction of $Al_{13}Fe_4$	Solid Fraction
GR595_01	–	–	1.18×10^{-4}	–	–	0.95
GR595_02	–	–	1.18×10^{-4}	–	–	0.95
GR610_01	608ºC	8.62×10^{-5}	–	–	–	0.94
GR610_02	611ºC	1.05×10^{-4}	–	–	–	0.94
GR625_01	620ºC	2.12×10^{-4}	–	–	–	0.91
GR625_02	622ºC	2.55×10^{-4}	–	–	–	0.91

Table 5.2: Sheil calculation of fractions of phases present in ZR during tensile tests

Sample	Sample Fail Temp.	Fraction of α_c-AlFeSi	Fraction of ß-AlFeSi	Fraction of Mg_2Si	Fraction of $Al_{13}Fe_4$	Solid Fraction
ZR595_01	603ºC	–	1.10×10^{-4}	–	–	0.94
ZR595_02	605ºC	–	1.29×10^{-4}	–	–	0.94
ZR610_01	615ºC	1.57×10^{-4}	–	–	–	0.92
ZR610_02	612ºC	1.27×10^{-4}	–	–	–	0.92
ZR625_01	615ºC	1.57×10^{-4}	–	–	–	0.92
ZR625_02	616ºC	1.69×10^{-4}	–	–	–	0.91

The samples from both alloys tested at 610ºC and 625ºC fractured before experiencing any significant increase in load, and therefore their thermomechanical properties have been compared against solid fraction.

Table 4.11 and Table 4.12 that two sets of GR200 samples fractured before load application (GR610 at f_s ~0.94 and GR625 at f_s ~0.91), while only one set of ZR200 samples fractured without load application (ZR625 at f_s ~0.91). It is also clear that at f_s ~0.92 ZR200 still has some load carrying capability, while at f_s ~0.95 GR200 is able to carry the full load of 981mN for 10 minutes.

One other observable difference between the two alloys was the difference in extension before they fractured: ZR200 extended significantly more than GR200 before fracture at each temperature.

Summary

At 605ºC (GR200 $f_s = 0.95$ and ZR200 $f_s = 0.94$ respectively), ZR200 is x3 more ductile compared to GR200, while GR200 is significantly stronger than ZR200. The zero strength temperature (ZST) of GR200 correspond to f_s ~0.95 and for ZR200 it corresponds to f_s ~0.92, which is in agreement with Fabrègue et al. [104]. ZR200 extends 30-70% more than GR200 at $0.91 < f_s < 0.95$.

5.3.2 Fracture Surface Analysis

(a) GR200 with α-AlFeSi content of 50%

All the fracture surfaces displayed a layer of rumpled oxide covering the surface. The entire fracture surface of GR610 surface displayed candy-rock features, indicating that the fracture was caused because of a high liquid fraction in the sample. The average diameter of the circular rock-features, 170μm, was comparable to the grain and cell diameters of the alloy, indicating that the fracture may have been caused by intergranular liquid delamination.

Two interesting features were observed on the fracture surface:

- The surface displayed one intermetallic particle with the 'Chinese-script' morphology (shown in Figure 4.73), with a Ti-rich region.
- Transverse planar intermetallic particles protruding out of the fracture surface, further reinforcing the theory of liquid delamination from the phases.

The fracture surface of GR625 displayed a very similar surface structure to that of GR610, except the dimples were shallower indicating the presence of a higher volume fraction of liquid during fraction. The GR625 sample, like GR610, fractured before experiencing any increase in load application; the average diameter of the candy-rock structures were once again comparable to the grain and cell diameter (177μm on average); and almost all the phases observed had a planar plate-like morphology. Additionally, identified with yellow arrows in Figure 4.76 and Figure 4.77, several

planar plate-like intermetallic particles were positioned on the outer most layer of the primary aluminium matrix, further reinforcing the theory of decohesion at phases.

(b) ZR200 with α-AlFeSi content of 80%

The fracture surfaces of ZR200 samples tested at 595ºC and 610ºC both displayed characteristic ductile fracture features, with a small region displaying brittle fracture features, such as steps. Large amounts of secondary phases were observed on the fracture surface of all samples, mainly appearing in the raised regions. This indicates that the phases may have delaminated from the solute-rich inter-cellular liquid, which on solidification causes the fracture surfaces to display high levels of phases in the raised regions.

The phases observed in ZR595 on both the ductile and brittle fracture features all displayed intricate leaf-like morphology. It was interesting to note, however, that the phases observed in the ductile regions displayed the 'leaf'-like morphology (5-8μm wide) compared to the skeletal morphology (2-4μm wide) observed in the regions displaying brittle fracture features.

A large difference in morphology was observed between the phases that were observed in ZR595 and ZR610: the phases in ZR610 were not very intricate, more angular and plate-like in comparison. This difference can be attributed to the different temperatures the samples experienced. At 595ºC, ZR200 experienced a temperature much lower than the eutectic melting temperature of α-AlFeSi phase.

The fracture surfaces of ZR625 display clear signs of necking, and features of high liquid fraction. It can be assumed that the fracture was caused by high levels of intergranular liquid flow. The phases observed had a significantly different morphology compared to both ZR595 and ZR610. The phases are plate-like, mostly 5μm in width (with a few exceptions of 20-30μm wide), and all aligned along the direction of the fracture. This might be due to the phases themselves being in a semisolid region, and therefore being readily reshaped by the stressed primary aluminium in the semisolid state.

(c) Summary

The SEM micrographs of GR200 and ZR200 fracture surfaces indicated that GR200 samples failed through intergranular liquid delamination, while ZR200 samples displayed signs of ductile and brittle fracture. Intermetallic phases were also observed to be protruding out of the GR fracture surfaces, indicating formation of intercellular bridging.

5.3.3 Impact of Intermetallic Phase on the Hot Tearing Properties

It can be seen from section 4.8 that with increasing temperature there is a distinct reduction is mechanical integrity of both alloys, which in turn reduces their load carrying capabilities. This is agreement with previous findings [5, 113, 115].

It can be seen from Figure 5.16, directly comparing the grain and cell morphologies of ZR200 and GR200, that the grains and cells of both alloys are almost identical:

- The grains and cells of both alloy are globular and not-dendritic;

– The interconnectivity of the phases as observed in a 2D section of both alloys are almost identical; and
– The average grain and cell sizes near the centre of both alloys are very closely matched despite the significant difference in chemical composition. The average grain and cell sizes of ZR200 near the centre (220μm and 150μm) are around 21% larger than those of GR200 (170μm and 120μm). This difference in grain size is insignificant compared to the ~81% difference in grain sizes observed in ZRTP-1 and GRTP-1 (890μm and 160μm respectively).

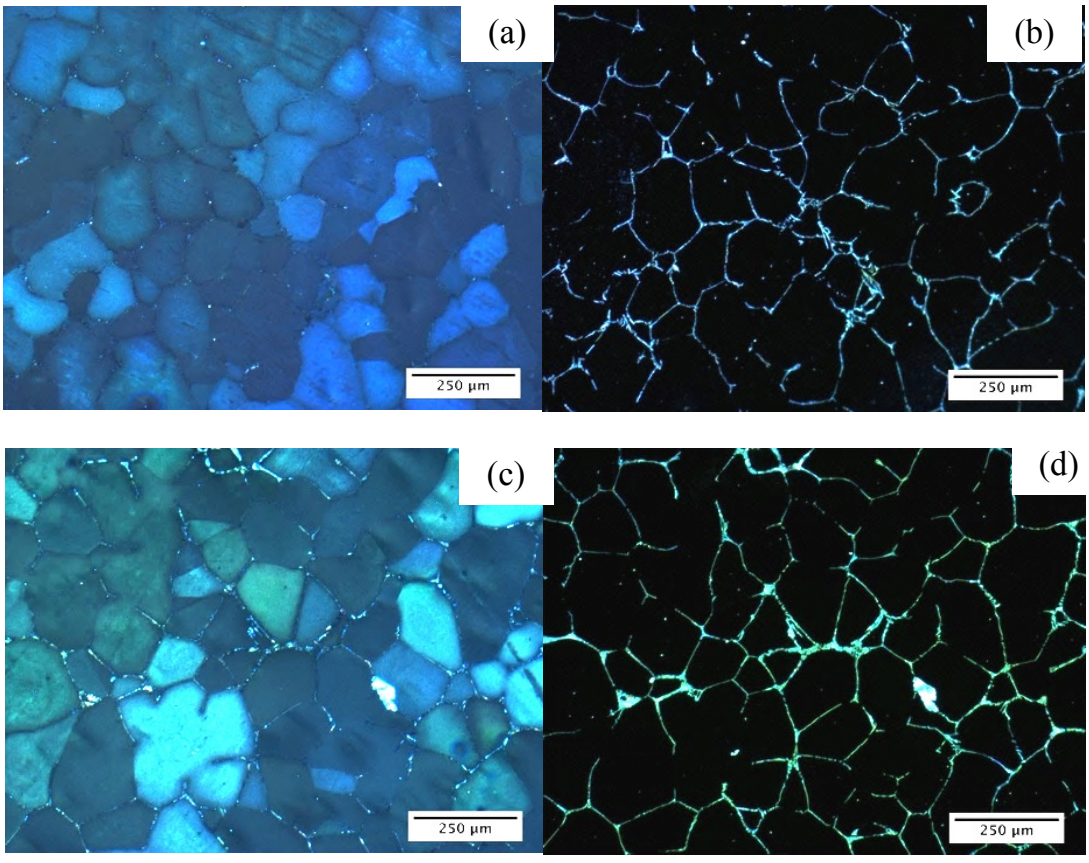


Figure 5.16: Optical micrographs of ZR200 and GR200, showing the grain and cell structures near the centre of (a, b) ZR200 with α-AlFeSi content of 80%, and (c, d) GR200 with α-AlFeSi content of 50%

Closer examination under the SEM, however, revealed that the phase thicknesses near the centre of ZR200 (1.25μm) is on average about 60% larger than those of GR200 (0.50μm), shown in Figure 5.17.

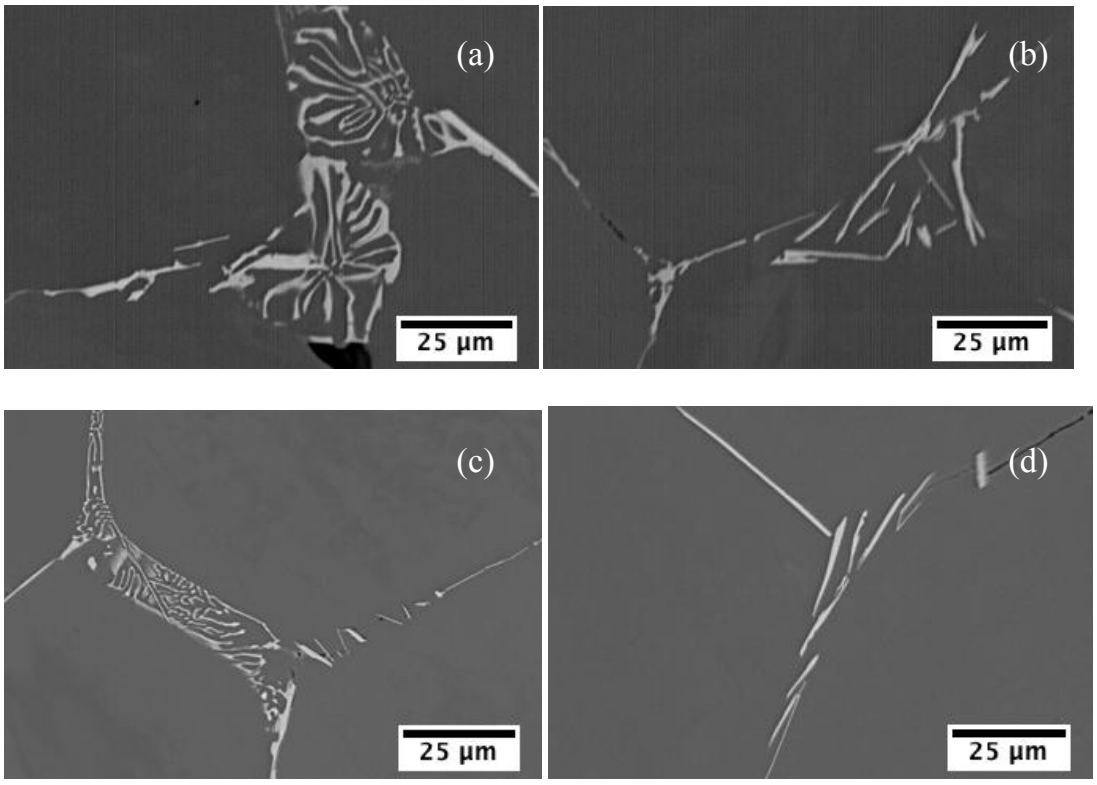


Figure 5.17: BSE micrographs of the 'Chinese script'-like morphology near the centre of (a) ZR200 and (c) GR200, and the 'needle'-like morphology near the centre of (b) ZR200 and (d) GR200

A significant difference was also observed on extracting the phases from their primary aluminium matrix: the phases from ZR200 were very delicate and crumbled more easily compared to the GR200 extracted phases, which were structurally much more robust and could be pressed onto a sticky carbon tab without causing much damage to the structure. Thus it was reasonable to conclude that the phase structures were more

interconnected in GR200 than in ZR200. This indicates that a high amount of the α-Al grains in ZR200 are in direct contact, enabling the grain boundaries to slide more easily and therefore improving the alloy ductility.

Furthermore, although both alloys contained a mixture of 'Chinese-script' and planar plate-like phases on extraction;

- ZR200 mostly exhibited the 'Chinese-script' morphology which possibly has better cohesion with the α-Al grains due to the intricately patterned surface structure, allowing a more diffuse interface;
- GR200 more frequently displayed the planar plate-like morphology which can delaminate causing premature fractures [79].

It is worth noting that the ZR200 samples extended 30-70% more than GR200 samples before failure at $0.91 < f_s < 0.95$. This difference may be attributed to the highly interconnected morphology of β-AlFeSi phase encapsulating the α-Al grains, whereby molten β-AlFeSi phase segregates the α-Al grains and as a result obstructs the grain boundary sliding mechanism. Since almost 50% of the total secondary phases present in GR200 is the planar plate-like β-AlFeSi, the samples failed through intergranular liquid delamination when tested around 610ºC and 625ºC.

It was also clear from Table 4.11 and Table 4.12 that the ZR200 samples had better mechanical integrity and therefore comparatively better load carrying capability than GR200 at $fs \leq 0.94$. This once again reinforces the concept that the intricate surface morphology of α-AlFeSi phase enables a more diffused interface with the aluminium

matrix, and therefore better cohesion compared to the planar β-AlFeSi phase [79]. It is also possible that the α-AlFeSi phase remaining in solid state around 610ºC helped maintain the mechanical integrity of the alloy.

At 595ºC, however, α-AlFeSi and β-AlFeSi phases are both in solid state, while Mg_2Si phase is molten. Mg_2Si phase was observed to be associated with the AlFeSi-based intermetallic phases on the grain boundaries [133] and was present in both alloy in this investigation. Thus, it can be assumed that the melting of Mg_2Si phase would create a liquid layer between the α-AlFeSi and β-AlFeSi phases and the α-Al grains, truly isolating their respective influences on the thermomechanical behaviour of the overall alloy.

GR200 was significantly stronger than ZR200 during tensile tests carried out at 595ºC (sample temperature of 605ºC), which can be either attributed to the β-AlFeSi phase being stronger, or its robust interconnected morphology. Furthermore, based on the intermetallic phases protruding out of the α-Al grains (see Figure 4.77), it can be assumed that at temperatures below the eutectic melting temperature of β-AlFeSi, the phase potentially strengthens the alloy by creating intracellular bridges.

It can be concluded that the differences in thermomechanical behaviours between the two alloys at $0.94 \leq fs \leq 0.95$ were mainly due to the morphology, interconnectivity, identity and thermodynamic properties of the α-AlFeSi and β-AlFeSi phases present in the alloys. Given hot tears are believed to occur above the solidus [98,138] caused by accumulation of strain [101], it can be concluded that GR200 is more susceptible to hot tears due to the presence of β-AlFeSi phase producing a solute-rich intercellular liquid

that obstructs the grain boundary sliding mechanism, and therefore inducing more strain on the surrounding α-Al microstructure.

A large amount of intermetallic phases was observed on the fracture surface of the tensile samples, some of which displayed uninterrupted oxide film extending into the matrix (see Figure 4.84 for example), while others displayed phases protruding out of the oxide layer (see Figure 4.77 for example). Since the samples were taken out as soon as the test cycle ended, there is a high possibility that the oxide layer could have formed after fracture rather than during casting. However, without further analysis, it is not possible to conclude whether these results support or contradict Campbell's suggestion [97] that hot tears are caused by aluminium oxide bi-films which form by the oxide folding onto itself on experiencing turbulence.

The intensity of intermetallic phases does support Lin [78] and Haaften's [5] findings. There may be two explanations for high levels of phases to be present on the fracture surface, especially along the raised regions:

- The phases could be causing decohesion from the aluminium matrix, aiding the propagation of the hot tears;
- The local concentration of phases could be causing the hot tear initiations.

However, it is also possible that due to the eutectic melting of β-AlFeSi phase, the surface is likely to be solute-rich liquid on fracture, which would then re-solidify on cooling, forming new phases at the surface.

Chapter 6 Conclusions and Suggestions for Future Studies

The main aim of this investigation was to understand the influence of AlFeSi-based intermetallic phases on the hot tearing and mechanical properties of 6063 alloy in the semisolid state.

6.1.1 Consistent α-Al Grain Size

One of the objectives to achieve that was to maintain a consistent α-Al/cell size between samples. α-Al grain size can be altered by varying the alloy chemical composition or through casting conditions.

A novel contribution of this investigation was the successful attempt in influencing the formation of α-AlFeSi and β-AlFeSi phases using chemical additions, while maintaining a comparable microstructure using the NRC processing technique.

The NRC technique was successful in restricting columnar grain growth. It was concluded from the microstructure observations of all the TP-1 and NRC process cast alloys that although chemical composition had a significant effect on the microstructure, processing technique was the overriding factor that determined the average grain size, except when AlTiB-type grain refiner was used. Casting the alloys through TP-1 casting and NRC had a significant effect on the microstructure of BA and ZR. The microstructure of GR, however, was completely unaffected, indicating that the chemical composition was the grain size determinant. The steel enthalpy can

temperatures of 200ºC and 400ºC during casting caused a slight increase in grain sizes, and did not have any noticeable effect on the phase selection for the given alloys.

The impact of quenching (creating a large thermal gradient) during NRC compared to TP-1 castings on the morphology of the α-Al grains and morphology of the phases were that:

- All the α-Al grains were more globular in the NRC alloys, compared to those of the TP-1 samples. The TP-1 grains were significantly more dendritic, and generally larger in diameter.
- The globular and generally smaller α-Al grains of the NRC alloys gave rise to very interconnected phases compared to those from the TP-1 casts. The interconnected sponge-like morphology of the extracted phases from NRC alloys indicate that they formed from the liquid present in the grain and cell boundaries.

6.1.2 Intermetallic Phase Identity, Quantity & Morphology Verification

The second objective was to determine the intermetallic phase identity, approximate quantity and morphology.

The XRD spectra obtained from the extracted phases of the three alloys reveal that phase selection is rather sensitive to the chemical composition of these alloys. α-AlFeSi and β-AlFeSi were the two main constituent phases that were observed in all alloys, alongside small amounts of Mg_2Si phase. Their respective proportions remained consistent despite the varying processing techniques, processing parameters, and

approximate grain and cell sizes. Additions of 5:1 Al-Ti-B type grain refiner promoted the formation of β-AlFeSi phases, while adding 0.1 wt% of Zr increased the formation of α-AlFeSi phases.

A novel contribution of this investigation was successfully establishing that the intermetallic phase identity remains consistent throughout the alloys processed through NRC.

It was established on all three alloys that the intermetallic morphologies observed through topographical examinations are not representative of the extracted morphology, and their respective proportions did not correspond to the approximate amounts of the α-AlFeSi and β-AlFeSi phases in the alloys. Due to the interconnectivity of the phases and the overlap of different phase morphologies, the exact proportions of specific morphologies could not be measured, and comparisons were made qualitatively.

Four different phase morphologies were observed after extraction:

- Dendritic 'petals'/'leaves' which had secondary dendrite arms on both sides, growing with a crystallographic relationship.
- Planar plate-like morphology which appear to grow either as sheets or as stacked layers.
- A novel contribution of this investigation was the identification of 'flower'-like intermetallic phases, and distinguishing them by their central point: one that appeared to have been initiated at the centre, and the second that displayed no clear indication of initiation point. It is reasonable to assume that some of the six-petal morphology could be initiated by the hexagonal TiB_2 particles.

– Fibrous sheets that are observed scattered throughout the microstructure, most likely to be the result of quenching the semisolid alloy, creating a large thermal gradient.

Chemically verified Ti-rich particles were successfully observed both as individual particles and as clusters in the metallographic samples, and as clusters among the extracted phases. The individual particles were generally less than 1μm in size, while the cluster sizes were much larger and ranged between 3-7μm.

6.1.3 ThermoMechanical Analysis

The final objective of this investigation was to understand the effect of α-AlFeSi and β-AlFeSi phases on the hot tearing and thermomechanical properties of a 6063 alloy.

The difference in morphology, interconnectivity, identity and thermodynamic properties of the phases present in GR and ZR alloys had an impact on the thermomechanical properties of the bulk alloy. The presence of β-AlFeSi phase made GR alloys more susceptible to hot-tears. This is because at semisolid temperatures, the β-AlFeSi phase produces a solute-rich intercellular liquid that encapsulates the α-Al grains and obstructs the grain boundary sliding mechanism, which in turn can induce additional strain on the surrounding α-Al microstructure causing hot tear formation.

At temperatures where GR $f_s = 0.95$ and ZR $f_s = 0.94$, ZR is x3 more ductile than GR, while GR is significantly stronger than ZR. Based on the TMA results, it was concluded that the ZST of GR correspond to f_s ~0.95 while for ZR it corresponds to f_s ~0.92.

During semisolid tensile tests, ZR extended 30-70% more than GR at $0.91 < f_s < 0.95$ before failure. Furthermore, the fracture surfaces of ZR alloys displayed features that can be attributed to ductile and brittle fracture, while fracture surfaces of GR appeared to be caused by intergranular liquid delamination.

A novel contribution of this investigation was to establish, in isolation of grain size, the effect of α-AlFeSi and β-AlFeSi phases on the hot tearing and thermomechanical properties of a 6063 aluminium alloy.

Chapter 7 Further Investigation

One of the limitations of this investigation was that the maximum heating rate that could be accurately obtained by the thermomechanical analyser used was 40K/min. Thus the effect of faster heating rates could not be investigated. This is important since some of the phases present in the alloy are metastable, and will therefore transform during the slower heating cycle. However, it can be concluded that the DSC traces and evidence from the fracture surfaces of GR200 indicate the transformation of metastable β-AlFeSi phase. Although some solid-state transformation may have taken place, it could not have gone to completion. Running the thermomechanical tests with varying cooling/heating rate could provide further proof to support the current findings.

One of the other limitations was the lack of control over the cooling of tensile test samples. Once the samples reached their test temperature, there were only two options for cooling them: 1) allowing the set up to cool down (at approximately 10K/min) before taking the sample out; or 2) taking the sample out into room temperature as soon as the test was complete, causing a large thermal gradient and therefore rapid cooling conditions. It has already been established that β-AlFeSi phase present in these alloys are metastable, and can transform during the thermal cycle given adequate time. Thus, the tensile samples were taken out as soon as the test was over, allowing them to cool at room temperature. This, however, may have resulted in altered primary aluminium microstructure, as well as the phase morphology and identity due to the altered micro-segregation and cooling conditions experienced. Observing a similar experiment in a synchrotron could provide a clearer understanding of the mechanism and interactions taking place between the behaviours of the two different phases.

The tensile samples in this project were just above 1mm in thickness, and were ground on all surfaces to eliminate any grooves or surface features that may initiate a crack under load. This process, however, could have introduced stresses within the sample, which in turn may have affected the test outcome. Preparing samples using a focussed ion beam (FIB) to polish the surface would ensure better control over the experimental variables.

Hot tearing is believed to develop during solidification, and as such, analysing the thermomechanical properties of these alloys during solidification would provide a thorough understanding in the impact of intermetallic phases on hot tear properties.

Despite great efforts to maintain the chemical composition of the base alloy constant in both GR and ZR, OES revealed that the chemical composition of ZR contained raised levels of various elements (0.45wt%Fe, 0.0080wt%Ni, 0.0076wt%Cr and 0.0064wt%V) compared to those of GR (0.34wt%Fe, 0.0029wt%Ni, <0.0010wt%Cr, and 0.0084wt%V). Investigating the individual impact of the trace elements on intermetallic phases could help improve understanding of the thermomechanical behaviours of the alloys.

Chapter 8 Bibliography

[1] I. J. Polmear and D. St. John; "Light Alloys: From Traditional Alloys to Nanocrystals", Butterworth-Heinemann, 2005

[2] D. G. Eskin; "Physical Metallurgy of Direct Chill Casting of Aluminium Alloys", CRC Press, 2008

[3] I. Davidson; PhD thesis, University of Oxford, 2006

[4] S. Park; PhD thesis, University of Oxford, 2008

[5] W. van Haaften, W. Kool, and L. Katgerman; Journal of Materials Engineering and Performances, **11**:537–543, 2002

[6] I. J. Polmear; "Light Alloys: Metallurgy of the Light Metals", Edward Arnold: London, 1989

[7] W. Hale; Journal of Minerals, Metals, and Materials Society, **52**:26–30, 2000

[8] http://hsc.csu.edu.au/engineering studies/aero eng/2580/aluminium alloys.html, Data Accessed on 07.02.2008

[9] Alcan. Metallurgy of Al-Mg-Si Alloys. Alcan Internationla Limited, 1972

[10] J.E. Hatch; "Aluminium: Properties and Physical Metallurgy", ASM International, 1984

[11] J. R. Davis; "Aluminum and Aluminium Alloys", ASM International, 1993

[12] C. Hsu, K. O'Reilly, B. Cantor, J. Titchmarsh, and R. Hamerton; Materials Science and Engineering A, **304-206**:119–124, 2001

[13] Y. Liu and S. Kang; Journal of Materials Science, **32**:1443–1447, 1997

[14] J. Zhang, Z. Fan, Y. Wang, and B. Zhou; Scripta Materialia, **42**:1101–1106, 2000

[15] L. Mondolfo; "Aluminium Alloys: Structure and Properties", Butterworths, London, 1976

[16] Y. Liu, S. Kang, and H. Kim; Materials Letters, **41**:267–272, 1999

[17] J. Hirsch, B. Skrotzki and G. Gottstein: "Aluminium Alloys", John Wiley and Sons, 2008

[18] M. Jarrett, B. Neilson, and E. Manson-Whitton. Solidification and Casting. CRC Press, 2002

[19] D. McCartney; Institute of Materials Reviews, **34**:247–260, 1989

[20] A. Lui; Master's thesis, University of Oxford, 2005

[21] G. Jones and J. Pearson; Metallurgical and Materials Transactions B, **7**:223–234, 1976

[22] A. Bunn, P. Schumacher, M. Kearns, C. Boothroyd, and A. Greer; Materials Science and Technology, **15**:1115–1123, 1999

[23] Z. Fan; International Materials Reviews, **47**(2):49-85, 2002

[24] H. V. Atkinson; Progress in Materials Science, **50**:341– 412, 2005

[25] D. A. Granger and J. Lid; Journal of Metallurgy, **35**(6):54-59, 1983

[26] D. A. Granger: in Proc. Int. Seminar on 'Refining and alloying of liquid aluminium and ferro-alloys', Trondheim, Norway, 231-244, 1985

[27] J. Patel, Y. Liu, G. Shao, and Z. Fan; Materials Science and Engineering A, **476**:341–349, 2008

[28] C. J. Quaak, L. Katgerman, W. H. Kool. In: D. H. Kirkwood, P. Kapranos, editors. Proc. 4th Int. Conf. Semi Solid Processing of Alloys and Composites, Sheffield, UK, 19–21 June 1996. Department of Engineering Materials, University of Sheffield; 1996. pages 35–39.

[29] K. Xia and G. Tausig; Materials Science and Engineering, **A246**:1-10, 1998

[30] H. Wang, D. St John, C. Davidson and M. Couper.; Materials Science Forum, **329-330**:449-454, 2000

[31] J. Yurko, X. Niu, and I. Pinwill; Journal of Materials Science Letters, **18**:1869-1870, 1999

[32] M. Easton, and D. St John; Metallurgical and Materials Transactions A, **30A**:1613-1623 and 1625-1633, 1999

[33] M. Kenney, J. Courtois, R. Evans, G. Farrior, C. Kyonka, and A. Koch; Semi-Solid Metal Casting and Forging, Volume 15. ASM International, 9th edition, 1988

[34] D. Kirkwood, and P. Kapranos (Editors). Proceedings of the 4th International Conference on 'Semisolid processing of alloys and composites', Sheffield, UK, The University of Sheffield, Pages 180-186, 1996

[35] G. Salvendy; "Handbook of Industrial Engineering", Wiley-IEEE, 2001

[36] http://www.azom.com/details.asp?articleid=1373, Data accessed on 07.10.2008

[37] D. Kirkwood; International Materials Review, **39**(5):173-189, 1994

[38] European patent ep 0745694a1, UBE Industries Limited

[39] M. Easton, H. Kaufmann, and W. Fragner; Materials Science and Engineering: A, **420**(1-2):135-143, 2006

[40] H. Kaufmann, R. Potzinger, and P. Uggowitzer; Light Metals Age, pages 56–61, 2001

[41] M. C. Flemmings; Metallurgical and Materials Transactions B, **22**:269–293, 1991

[42] R. E. Smallman and R. J. Bishop; "Modern Physical Metallurgy and Materials Engineering", Technology & Engineering, Butterworth-Heinemann, 1999

[43] M. C. Flemmings; "Solidification Processing", New York, McGraw-Hill, Pages 290-300, 1974

[44] D. R. Askeland, P. P. Fulay and W. J. Wright; "The Science & Engineering of Materials", Technology & Engineering, Cengage Learning, 2011

[45] J. Zeng, X. Wang and J. Hou; "Colloidal Hybrid Nanocrystals: Synthesis, Properties, and Perspectives", Nanocrystal, Dr. Yoshitake Masuda (Ed.), ISBN: 978-953-307-199-2, InTech, DOI: 10.5772/16418

[46] W. T. Kim and B. Cantor; Acta Metallurgica et Materialia, **42**(9):3115-3127, 1994

[47] B. Cantor; Philosophical Transaction of the Royal Society: A, **361**:409-417, 2003

[48] B. Cantor; Material Science and Engineering: A, **178**:225-231, 1994

[49] M. Kearns, S. Thistlethwaite and P. Cooper; "Recent advances in understanding the mechanisms of aluminium grain refinement by TiBAl master alloys", London & Scandinavian Metallurgical (LSM) Company Limited, Anaheim, California, 1996

[50] I. Maxwell and A. Hellawell; Acta Metallurgica, **23**:229-237, 1975

[51] A. L. Greer; Report 2 from MEBSP Sub-group 1 "Nucleation and Grain Refinement Processes", 2000

[52] A. L. Greer, A. M. Bunn, A. Tronche, P. V. Evans and D. J. Bristow; Acta Materialia, **48**:2823-2835, 2000

[53] P. Kolby; Proceedings of the 4th International Conference of Al Alloys, 1994, Atlanta, 2-17

[54] L. M. Carroll; D. Phil. Thesis, University of Oxford, 1999

[55] G. Sha; DPhil thesis, University of Oxford, 2001

[56] D. A. Porter and K. E. Easterling; "Phase Transformation in Materials", Chapman & Hall, London, 1992

[57] T. E. Quested and A. L. Greer; Light Metals, 945-952, 2003

[58] J. A. Spittle and S. Sadli; Materials Science and Technology, **11**:533-537, 1995

[59] A. L. Greer: Report 2 from MEBSP Sub-group 1 "Nucleation and Grain Refinement Processes", 2000

[60] T. Massalski; "Binary alloy phase diagrams", 2nd Edition; 1990, Metals Park, OH, ASM International

[61] P. Desnain, Y. Fautrelle, J. L. Meyer, J. P. Riquet and F. Durand; Acta Metallurgica Materialia, **38**:1513-1523, 1990

[62] R. Schmid-Fetzer and A. Kozlov; Acta Materialia, **59**:6133-6144, 2011

[63] M.A. Easton and D.H. StJohn; "Light Metals 2001", The Minerals, Metals and Materials Society, Warrendale, Pensylvania, 927-934, 2001

[64] A. Vogel, R. D. Doherty and B. Cantor; "Solidification and casting of metals", The Metals Society, London, 518–525; 1979

[65] O'Hara, S. and W.A. Tiller; Transactions of the Metallurgical Society of AIME, **239**:497-501, 1967

[66] R. D. Doherty, H. I. Lee, and E. A. Feest; Materials Science Engineering, 65:181-189, 1984

[67] E. Liotti, A. Lui, R. Vincent, S. Kumar, Z. Guo, T. Connolley, I.P. Dolbnya, M. Hart, L. Arnberg, R.H. Mathiesen, and P.S. Grant; Acta Materialia **70**:228–239, 2014

[68] S. Ji and Z. Fan; Metallurgical Materials Transactions, **33**(11):3511-3520, 2002

[69] P. Skjerpe; Metallurgical Transcripts A, **18**:189–200, 1987

[70] C. Allen, K. O'Reilly, B. Cantor and P. Evans; Progress in Materials Science, **43**:89–170, 1998

[71] G. Sha, B. O'Reilly, K.and Cantor, J. Titchmarsh, and R. Hamerton; Acta Materialia, **51**:1883–1897, 2003

[72] C. Sun and L. Mondolfo; Japan Institute of Metals, **95**:384, 1967

[73] A. Dons; Materials Research and Advanced Techniques, **75**:170–174, 1984

[74] H. Westengen; Materials Research and Advanced Techniques. **73**:360–368, 1982

[75] G. Phragmen; "Journal Institute of Metal", **77**:489, 1950

[76] A. Lui; DPhil thesis, University of Oxford, 2009

[77] S. Kumar, P. S. Grant and K. A. Q. O'Reilly; Transactions of the Indian Institute of Metals, **65**(6):553-557, 2012

[78] S. Lin, C. Aliravci, and M. Pekguleryuz; Metallurgical and Materials Transactions A, **38**:1056–1068, 2007

[79] K. B. S. Couto, S. R. Claves, W. H. Van Geertruyden, W. Z. Misiolek and M. Goncalves; Journal of Materials Science and Technology, **21**(2):263-268, 2005

[80] S. Zajac, L. Gulman, A. Johansson, and B. Bengtsson; Materials Science Forum, **217-222**:1193–1198, 1996

[81] S. Zajac, B. Hutchinson, A. Johansson, and O. Gullman; Materials Science and Technology, **10**:323–333, 1994

[82] N. Kuijpers, W. Kool, P. Koenis, K. Nilsen, I. Todd and S. van der Zwaag; Materials Characterisation, **49**:409– 420, 2003

[83] N. Kuijpers, W. Kool, P. Koenis, K. Nilsen, I. Todd and S. van der Zwaag; Materials Characterisation, **49**:409– 420, 2003

[84] T. Massalski; "Binary alloy phase diagrams", 2nd Edition, Metals Park, OH, ASM International, 1990

[85] H. Phillips; "Annotated Equilibrium Diagrams of Some Aluminium Alloy Systems", Institute of Metals, 1959

[86] M. Mulazimoglu, A. Zaluska, J. Gruzleski, and F. Paray; Metallurgical and Materials Transactions, **27A**:929–935, 1996

[87] C. Hsu; DPhil thesis, University of Oxford, 1999

[88] H. Kosuge; Journal of Japan Institute of Light Metals, **30**:1, 1990

[89] I. G. Davies, J. M. Dennis and A. Hellawell; Metallurgical Transactions, **1**:275-280, 1970

[90] H. Jin, T. Sagstad, J. Tafto and P. T. Zagierski; Materials Science Forum, **217-222**:241-246, 1996

[91] C. M. Allen, K. A. Q. O'Reilly, P. V. Evans and B. Cantor; Acta Materialia, **47**(17): 4387-4403, 1999

[92] W. Khalifa, F. H. Samuel, J. E. Gruzleski, H. W. Doty and S. Valtierra; Metallurgical and Materials Transactions: A, **36A**:1017-1032, 2005

[93] C. M. Allen, DPhil Thesis, University of Oxford, 1997

[94] Y. Langsrud, Key Engineering Materials, **44-45**:95, 1990

[95] D. Eskin, Suyitno, and L. Katgerman; Progress in Materials Science, **49**:629–711, 2004

[96] T. Clyne and G. Davies; British Foundry, **74**:65–73, 1981

[97] J. Campbell; "The New Metallurgy of Cast Metals: Castings", Elsevier: London, 2003

[98] L. Katgerman; Journal of Metals, **34**:46–49, 1982

[99] M. Rappaz, J. Drezet, and M. Gremaud; Metallurgical and Materials Transactions: A, **30A**:449–455, 1999

[100] W. Pumphrey; "Researches into the welding of aluminium and its alloys" Research Report 27, Aluminium Development Association, UK, 1955

[101] W. Pellini; "Strain theory of hot tearing", Foundry, **80**:125–140, 1952

[102] D. Eskin, Suyitno, and L. Katgerman; Progress in Materials Science, **49**:629–711, 2004

[103] A. Knuutinen, K. Nogita, S. McDonald and A. Dahle; Journal of Light Metals, **1**:241–249, 2001

[104] D. Fabregue, A. Deschamps, M. Suery, and J. Drezet; Acta Materialia, **54**:5209–5220, 2006

[105] N. Prokhorov; Russian Casting Productions, **2**:172–175, 1962

[106] I. Novikov; "Hot shortness of non-ferrous metals and alloys [in russian]", Nauka, Moscow, page 205, 1966

[107] U. Feurer; Mathematisches modell der warmriβneigung von binarer aluminiumlegierungen. Giesserei Forschung, 28:75, 1976

[108] C. Davidson, D. Viano, L. Lu and D. St John; International Journal of Cast Metals Research, **19**:59–65, 2006

[109] M. M'Hamdi, A. Mo, and C. Martin; Metallurgical and Materials Transactions: A, **33A**:2081–2093, 2002

[110] P. Ackermann and W. Kurz. Materials Science and Engineering, **75**:79–86, 1985

[111] W. van Haaften, B. Magnin, W. Kool, and L. Katgerman; Light Metals -Warrendale-, TMS: 829–834, 1999

[112] http://www.gleeble.com/3500.htm, Data Accessed on 18.09.2008

[113] J. Spittle, S. Brown, J. James, and R. Evans; Proceedings of 7th International Symposium on Physical Simulation, Tsukuba, Japan, pages 81–91, 1997

[114] W. van Haaften, W. Kool, and L. Katgerman; Materials Science and Engineering: A, **336**:1–6, 2002

[115] L. Colley, M. Wells, and D. Maijer; Materials Science and Engineering: A, **386**:140–148, 2004

[116] A. Singer and S. Cotrell; Journal Institute of Metals, **73**:33–54, 1946

[117] T. Nakagawa, T. Umeda, J. Murata, Y. Kamimura, and N Niwa; The Iron and Steel Institution of Japan International, **35**:723–729, 1995

[118] J. James, J. Spittle, S. Brown, R. Evans, and M. Keeble; "Asset - the advanced semi-solid elongation test for determining mechanical properties of alloys in the mushy zone", COMPASS 99, EMAS Ltd., Swansea, Wales, 73–80, 1999

[119] H. Nagaumi and T. Umeda; Journal of Light Metals 2, **2**:161–167, 2002

[120] A. B. Phillion, S. Thompson, S. L. Cockcroft and M. A. Wells; Materials Science and Engineering: A, **497**:388-394, 2008

[121] S. Instone, D. St John, and J. Grandfield; International Journal of Cast Metals, **12**:441–456, 2000

[122] Standard Test Procedure for Aluminium Alloy Grain Refiners: TP-1, Washington DC, The Aluminium Association, 1990

[123] L. Kaiser; Biometrics, **39**(4):965-976, 1983

[124] C. J. Simensen, P. Fartum and A. Andersen; Fresenius Z. Anal. Chem., **319**:286-292, 1984

[125] M. Cooper; Acta Crystallography **23**:1106-1107, 1967

[126] www.matweb.com, visited on 20th November 2015

[127] http://resource.npl.co.uk/mtdata/phdiagrams/almo.htm, visited on 20th November 2015

[128] http://www.periodictable.com/, visited on 30th January 2016

[129] L. Reimer; "Scanning Electron Microscopy: Physics of Image Formation and Microanalysis", 2nd edition, Springer-Verlag, 1998

[130] S. J. B. Reed; "Electron Microprobe Analysis", 2nd edition, 1997, Cambridge University Press

[131] TMA Instruction Manual

[132] International Centre for Diffraction Data 200, Advance in X-Ray Analysis, Volume 43

[133] S. Kumar, P. S. Grant and K. A. Q. O'Reilly; "Evolution of Fe bearing intermetallics during DC casting and homogenisation of an Al-Mg-Si Al alloy", *awaiting peer review* at International Centre for Diffraction Data 200, Advance in X-Ray Analysis, Volume 43

[134] C. Hsu, K.A.Q. O'Reilly, B. Cantor and P.V. Evans; Proceedings of the 4th Decennial International conference on solidification processing, Sheffield, 1997

[135] S. Kumar, N. Hari Babu, G. M. Scamans and Z. Fan; Materials Science and Technology, **27**(12):1833-1839, 2014

[136] A. Verma, DPhil thesis, University of oxford, ongoing

[137] P. Schumacher, A. L. Greer, J. Worth, P. V. Evans, M. A. Kearns, P. Fisher and A. H. Green; Materials Science and Technology, **14**(5):394-404, 1998

[138] I. G. Davies, J. M. Dennis and A. Hellawell; Metallurgical Transactions, **1**:275-280, 1970